Impact of long-wave climatic oscillations on the persistent hydrologic extremes

Ph.D. Thesis

by

Waqar ul Hassan

Under the supervision of

Dr. Mohd Farooq Azam

Internal supervisor

Dr. Munir Ahmad Nayak

External supervisor (Main)

Department of Civil Engineering

Indian Institute of Technology Indore

July 2022

Impact of long-wave climatic oscillations on the persistent hydrologic extremes

A THESIS

Submitted in partial fulfillment of the requirements for the award of the degree
of
DOCTOR OF PHILOSOPHY

by
Waqar ul Hassan

Under the supervision of
Dr. Mohd Farooq Azam
Internal supervisor
Dr. Munir Ahmad Nayak
External supervisor (Main)

Department of Civil Engineering
Indian Institute of Technology Indore
July 2022

INDIAN INSTITUTE OF TECHNOLOGY INDORE

CANDIDATE's DECLARATION

I hereby certify that the work which is being presented in the thesis entitled "**Impact of long-wave climatic oscillation on persistent hydrologic extremes"** in the partial fulfilment of the requirements for the award of the degree of **Doctor of Philosophy** and submitted in the **Department of Civil Engineering, Indian Institute of Technology Indore**, is an authentic record of my own work carried out during the time period from 26-December 2017 to 29-July 2022 under the supervision of internal supervisor, **Dr. Mohd Farooq Azam**, Department of Civil Engineering, Indian Institute of Technology Indore and external (Main) supervision of **Dr. Munir Ahmad Nayak**, Assistant professor, Department of Civil Engineering, National Institute of Technology Srinagar.

The matter presented in this thesis has not been submitted by me for the award of any other degree of this or any other institute.

Signature of the student with date
(Waqar ul Hassan)

This is to certify that the above statement made by the candidate is correct to the best of my/our knowledge.

Mohd. Farooq Azam

Signature of internal Thesis Supervisor
(Dr. Mohd. Farooq Azam)

Signature of external (Main) Thesis Supervisor
(Dr. Munir Ahmad Nayak)

Waqar ul Hassan has successfully given his/her Ph.D. Oral Examination held on 14 Feb 2023.

Mohd. Farooq Azam

Signature of internal Thesis Supervisor
(Dr. Mohd. Farooq Azam)

Signature of external (Main) Thesis Supervisor
(Dr. Munir Ahmad Nayak)

Dedicated to my parents

SUMMARY

Extreme weather and climatic events affect our society and the environment, particularly when several extreme events occur simultaneously in space and/or time –Compound events. Univariate extremes (e.g., droughts, heatwaves) have been thoroughly investigated in the last few decades and several indicators have been developed for quantifying and monitoring them. Although these indicators provide critical information for management and planning, they tend to underestimate the occurrence probability of compound extremes. Moreover, the current understanding of compound events is still blurred and unclear. Although, multivariate compound events –simultaneous occurrence of multiple extreme events over a region– are being investigated globally as a hot topic and multiple modelling and prediction frameworks have been developed to investigate their changes and impacts, spatially compound extremes –concurrent extreme events at multiple locations– which are more impactful, on the other hand, remain unexplored. This thesis explores spatial compounding in droughts, heatwaves, and compound droughts and heatwaves among the IPCC regions.

In this thesis after a comprehensive screening of the current literature on drought and heatwave monitoring and prediction approaches, a review article on drought monitoring and prediction over India was developed. In addition, we also developed a method to investigate heatwave characteristics in the regions with missing data. The analyses on spatially compound extremes (SCEs) revealed multiple significant concordances –IPCC region pairs that have statistically significant likelihood of co-occurrences– in droughts, heatwaves, and compound droughts and heatwaves. Noteworthy are the concordances that are more than 10,000km distant, which are referred here as teleconnections in extremes. The number of IPCC regions experiencing spatially compound extremes has been increasing at a significant rate over the last four decades. The results suggest, on an average, 50.0% risk of decreased global crop production during anomalous spatially compound heatwave (SCH) years in last 4 decades and an additional 50% increase in the population is exposed to SCHs post-2000. Composite anomalies of atmospheric dynamics for selected concordant pairs demonstrated El-Niño as the key driver of teleconnections in droughts, heatwaves, and compound drought and heatwaves. Other prominent climate oscillations, such as Pacific North America, North Atlantic Oscillation/Artic Oscillation, Atlantic Multidecadal Oscillation, Pacific Decadal Oscillation, and others also play a significant role in individual concordant pairs. ENSO is suggested as the primary driver of spatially compound CDHWs in the selected teleconnections by the logistic regression models. The model estimates a significant increase (from 0.5% to 90%) in the likelihood of SC-CDHW events from moderate El-Niño to exceptional El-Niño. The findings from this thesis are important in understanding spatially compound events, their changes, driver, and impacts.

LIST OF PUBLICATIONS

A. **Publications from PhD thesis work:**

a. Articles Published (journals)

1. Global teleconnections in droughts caused by oceanic and atmospheric circulation patterns; (2021) *Environ. Res. Lett.* **16** 014007. **Waqar Ul Hassan** and Munir A. Nayak:
DOI: https://doi.org/10.1088/1748-9326/abc9e2 **(I.F.=6.947)**

2. Recent changes in heatwaves and maximum temperatures over a complex terrain in the Himalayas; (2021) *Science of The Total Environment* **794** 148706. **Waqar Ul Hassan,** Munir A. Nayak, Rosa V. Lyngwa:
DOI:https://doi.org/10.1016/j.scitotenv.2021.148706**(I.F.=10.75)**

3. A synthesis of drought prediction research over India; (2021) *Water Security* **13**, 100092. Munir A. Nayak, **Waqar Ul Hassan**:
DOI: https://doi.org/10.1016/j.wasec.2021.100092 (**Cite score =4.5)**

b. Articles submitted or in preparation (journals)

4. Intensifying spatially compound heatwaves: implication to global crop production and human population; *Global Environmental Change.* **Waqar Ul Hassan**, Munir A. Nayak, and M. F. Azam: (***under review***) **(I.F.=11.16)**

5. Spatially compounding of multivariate hazards: role of climate oscillations and land-atmosphere interaction; **Waqar Ul Hassan**, Munir A. Nayak, and M. F. Azam. ***(In preparation)***

c. Refereed conferences

1. Hotspots of extreme compound drought and heatwaves: Role of feedback and climate oscillations; (2021) *EGU General Assembly 2021,* online, 19–30 Apr 2021, EGU21-11426. **Waqar Ul Hassan**, Munir A. Nayak: DOI:https://doi.org/10.5194/egusphere-egu21-11426, 2021

2. Role of climatic oscillations in causing spatially and temporally compound droughts and heatwaves; (2022) *EGU General Assembly 2022,* Vienna, Austria, 23–27 May 2022, EGU22-10344. **Waqar Ul**

Hassan, Munir A. Nayak: DOI: https://doi.org/10.5194/egusphere-egu22-10344, 2022

3. A Copula-based risk analysis of Hydrological extreme events in India: Droughts and Wet periods; (2020) *Roorkee Water Conclave*, 2020. **Waqar ul Hassan**, Munir A. Nayak.

4. Long-term hydro-climatic variability for Madhya Pradesh water resource systems; (2019) *8th APHW International Conference on Emerging Technologies in Urban Water Management,* 2019 **Waqar Ul Hassan** and Munir A. Nayak.

B. Other journal publications during PhD:

1. Atmospheric rivers as the major contributors to precipitation over Himalayan basins; *Journal of Climate.* Rosa V. Lyngwa, **Waqar Ul Hassan**, Munir A. Nayak, and M. F. Azam. ***(In revision)*** **(I.F.=5.38).**

ACKNOWLEDGEMENTS

Before beginning my thesis, I would like to express my gratitude to Almighty Allah (azzawajal) for his unlimited blessings, which includes my devoted parents, extended family, and beautiful friends. Secondly, I thank Almighty Allah (azzawajal) for the opportunity to be a member of IIT Indore community, which has greatly improved my professional and personal development. An overwhelming feeling of gratitude ties me to my advisors, Dr. Munir Ahmad Nayak and Dr. Mohd-Farooq Azam, for their guidance and support. Both of them are exceptional researchers. As a researcher, I appreciate their encouragement and support. They have provided me with good professional and personal guidance, and having them as mentors always inspires me to do better in life. Dr Munir Ahmad Nayak has been more than a PhD adviser to me throughout my time as a PhD student. I am pleased to name him my advising professor, research mentor, and personal friend. I owe Prof. Dr. Sandeep Chaudhary and Dr. Santanu Manna a debt of gratitude for their thoughtful remarks, recommendations, and encouragement while I completed my dissertation. In addition, I want to express my gratitude to the Civil Engineering Department, IIT Indore for all of its assistance with administrative tasks here at the institution. A special thank you to my close pals Zahoor, Junaid, and Uzma for all of their encouragement and support throughout my difficult times. I also like to extend my appreciation to my colleagues at IIT Indore and NIT srinagr, especially, Arif, Parvaiz, Rosa, Smriti, Mehvish, and Sakiba. I am very grateful to my parents for always allowing me to pursue my dreams. Their unwavering love and support have been an enormous source of strength and comfort to me throughout my life. I also want to express a sincere thank you to my family for their continual support, love, and care. Finally, I want to express my gratitude to everyone who has contributed, assisted, or supported me, both personally and indirectly.

TABLE OF CONTENTS

LIST OF FIGURES

Main text figures

Supplementary figures

LIST OF TABLES

ACRONYMS

CDHWs	Compound droughts and heatwaves
SCDs	Spatially compound droughts
SCHs	Spatially compound heatwaves
SC-CDHWs	Spatially compound compound droughts and heatwaves
SCEs	Spatially compound extremes
ENSO	El-Niño Southern Oscillation
EP-ENSO	Eastern Pacific ENSO
PDO	Pacific Decadal Oscillation
AMO	Atlantic multidecadal Oscillation
IOD	Indian Ocean Dipole
EQUINOO	Equatorial Indian Ocean Monsoon Oscillation
ISMR	Indian Summer Monsoon Rainfall
SLP	Sea Level Pressure
SST	Sea Surface Temperature
IMD	India Meteorological Department
NASA	National Aeronautics and Space Administration
NOAA	National Oceanic and Atmospheric Administration
CPC	Climate Prediction Centre
MLR	Multiple Linear Regression
SPI	Standardized Precipitation Index
scPDSI	self-calibrated Palmer Drought Severity Index

Chapter 1 : Introduction

1.1. Climate variability

Climate, in simple terms, is considered as the "average weather" and in broader sense, it is defined as the long-term statistics of weather conditions over a region (Seneviratne *et al* 2012). Climate is found to vary naturally on all timescales ranging from days to centuries. These variations in climate, often known as (natural) climatic variability (Trenberth 2001, Seneviratne *et al* 2012), have profound impact on our society and economy. The climatic variability can be broadly categorized into two major categories based on the source of the variation: (1) Internal climatic variability and (2) External or forced climatic variability.

Internal climate variability: This includes variations in the climate that are caused by the processes that are internal to the climate system, involving the interaction between different components of the system (i.e., via feedback) (Trenberth 2001, Mitchell 1976) for instance, from interactions between the atmosphere and ocean, such as ENSO (discussed in below). The processes resulting in internal variability are not deterministic, but rather probabilistic in nature, hence also known as internal stochastic variability (Mitchell 1976). Due to their stochastic nature, they are difficult to quantify and predict skillfully. As there is no external forcing involved, internal variability also occurs even in an unchanging climate (Mitchell 1976).

External or forced climate variability: As the name highlights, this type of variability is driven by the processes that involve forcings external to the climate system. These forcings are related to solar variability, volcanic eruptions, Orbital variability of Earth around Sun – the driving force behind the ice ages and interglacial eras, and various human influences on environment such as changes in aerosol loading (Mitchell 1976, Trenberth 2001). Since these processes are deterministic and are relatively predictable in longer intervals of time, the resulted variability would likewise be predictable in the same interval of time

(Mitchell 1976). Unlike internal variability, there is no involvement of feedback.

1.2. Climate Change

In contrast to climate variability, climate changes stand for any change in the statistics of the climate over a long period of time, which should not be less than 30 years. In statistical terms, climate change means the modification of the probability distribution (either in mean, amplitude or both) of a meteorological variable over time. According to United Nations Framework Convention on Climate Change (UNFCCC), climate change is defined as: "*a change of climate which is attributed directly or indirectly to human activity that alters the composition of the global atmosphere and which is in addition to natural climate variability observed over comparable time periods.*" This definition clearly makes a distinction between climate change attributable to human activities by changing the atmospheric composition (anthropogenic climate change), and climate variability attributable to natural causes. Intergovermental Panel for Climate Change (IPCC) in its Special report on extremes (SREX 2012) (Seneviratne *et al* 2012) defines climate change as "*a change in the state of the climate that can be identified (e.g., by using statistical tests) by changes in the mean and/or the variability of its properties and that persists for an extended period, typically decades or longer. Climate change may be due to natural internal processes or external forcings, or persistent anthropogenic changes in the composition of the atmosphere or in land use.*" In nutshell, climate change represents the long-term (decades to millennium) change in the statistics (particularly mean and variation), while as climate variability represents the changes in statistics (usually variation) over a relatively short term (days to years).

1.3. Modes of climate variability

The spatiotemporal structure of natural climatic variability follows repeating and/or recurrent patterns, often referred to as modes of climatic variability or climatic modes (Hernández et al., 2020). There are multiple definitions of climatic modes in the literature, however, the simplest definition is given by Hernández et al., (2020). They define a climatic mode as "*preferred spatial patterns and their fluctuations across different timescales, which represent a simplification of the complex spatial and temporal evolution of the climate system*". These climatic modes are typically identified through statistical analysis, mostly using empirical orthogonal functions (EOFs), of observational and model data, where they are represented by a characteristic spatial pattern and its associated timeseries (Christensen et al., 2013). Usually, most modes of variability are quasiperiodic and oscillatory, hence they are also known as "climate oscillations". The states of these climate oscillations are often monitored using so-called climate indices, which actually are the PCs (timeseries) of the corresponding EOF pattern. Some of the most common climate oscillations that significantly impact our climate system and climate extremes are El-Niño Southern Oscillation (ENSO; Philander 1983, Bjerknes 1969), North Atlantic Oscillation (NAO; Walker 1924, Lamb and Peppler 1987), Arctic Oscillation or Northern Annular Mode (AO/NAM; Lorenz 1951, Thompson and Wallace 1998), Antarctic Oscillation or Southern Annular Mode (AAO/SAM; Gong and Wang 1998), Pacific Decadal Oscillation (PDO; Mantua and Hare 2002), Atlantic Multidecadal Oscillation (AMO; Dijkstra *et al* 2006), Indian Ocean Dipole (IOD; Vinayachandran *et al* 2009), Pacific North America (PNA; Barnston and Livezey 1987), and others including East Atlantic (EA; (Wallace and Gutzler 1981)), East Atlantic West Russia (EA/WR; Wallace and Gutzler 1981), and Atlantic Niño (Latif *et al* 1996).

<u>El-Niño Southern Oscillation</u>: ENSO represents the natural variability of sea surface temperature (SST) and sea level pressure (SLP) in the equatorial Pacific Ocean. The term El-Niño refers to warming of the tropical Pacific with warm waters (warmer than normal) located in the central and eastern Pacific and occurs with an oscillation period of 2–7 years (Philander 1983). The opposite cold phase, i.e., when warm waters are in the western Pacific (warm pool), is known as La-Niña.

These anomalies in SST over eastern and western Pacific are linked with a large-scale east-west SLP seesaw, termed the Southern Oscillation, which represents the atmospheric counterpart of El-Niño and highlights the coupled nature ENSO phenomenon (Bjerknes 1969). Refer to Capotondi *et al* (2015), Wang and Picaut (2004), and Philander (1983) for further details.

Pacific Decadal Oscillation: PDO is the dominant mode of decadal SST variability in Northern Pacific Ocean (Mantua and Hare 2002). It is defined based on the leading mode (EOF 1) of detrended SST over the Pacific Ocean north of 20°N (Hernández *et al* 2020, Newman *et al* 2016). The positive phase of PDO (PDO+) is characterized by the warm waters/SST in the eastern Pacific towards west Coast of United States and cold waters in western Pacific near Japan and Korea. Reverse is the case during negative phase of PDO (PDO-). Refer Hernández et al., (2020); Newman et al., (2016); Wang et al., (2012) for more details.

North Atlantic Oscillation and Northern Annular mode: NAO is closely related to AO (Hurrell and Deser 2010), and is the leading atmospheric mode of climatic variability in the Northern hemisphere during the boreal winter. This climatic oscillation is characterized by a dipole in sea level (atmospheric) pressure with action centres located near Iceland and Azores. These action centres correspond to Icelandic low and Azores high. The positive phase of NAO (NAO+) is characterized by the anomalously and strong high (low) pressure above the action centre near Azores (Iceland), while as during negative phase of NAO (NAO-) the strength of pressure over the action centres are relative lower characterized by weak Azores high and weak Icelandic low. Although NAO is limited to Euro-Atlantic region, AO, its akin, is a planetary scale mode of climate variability over polar and sub-tropical northern hemisphere. For details refer (Hurrell and Deser 2010, Thompson and Wallace 2000, 2001).

Similar to AO/NAM in Northern hemisphere, SAM is the leading climate mode of atmospheric variability in Southern hemisphere (Fogt and Marshall 2020, Ho *et al* 2012).

Pacific North America: PNA is considered as 2nd leading atmospheric mode of climate variability in Northern hemisphere (Barnston and Livezey 1987). The spatial structure of PNA is like a quadrupole with four centres of action located near Hawaii, Western Canada, North Pacific, and Southeast United States. The positive phase of PNA (PNA+) is characterized by the above normal pressure over Hawaii and Western Canada and below normal pressure over North Pacific and Southeast United States. The reverse is the case during the negative phase of PNA (PNA-). For details refer (Dai *et al* 2017, Hurrell and Deser 2010, L'Heureux 2019)

Atlantic Multidecadal Oscillation: AMO is the major mode of SST variability in the Northern Atlantic Ocean with an oscillation period of 50–80 years (Dijkstra *et al* 2006). It is characterized by basin-wide fluctuations in SST. During the positive (warm) phase of AMO (AMO+) the Northern Atlantic is warmer than normal, while as during negative phase (AMO-) Atlantic is cooler than normal. Details can be seen from (Dijkstra *et al* 2006, Li *et al* 2009, Wyatt *et al* 2012)

Indian Ocean Dipole: This mode of climate variability is linked with coupled ocean-atmosphere variability in Tropical Indian Ocean (Vinayachandran *et al* 2009). During the positive phase (IOD+) the Eastern Indian Ocean becomes unusually cold compared to Western Indian Ocean, which is warmer than normal, making the winds blow from west to east. In contrast, during negative phase, the reverse happens and represents the intensified normal phase. Details can be found in (Vinayachandran *et al* 2002, 2009)

1.4. Climate extremes

Climate extremes often pose severe impacts on agriculture, humans, infrastructure, and terrestrial ecosystem and contribute to about 90% of all impactful disasters (UNISDR 2015). According to the IPCC

SREX, weather or climate extreme is defined as *"the occurrence of a value of the weather or climate variable above (below) a threshold value in upper (lower) tail of the distribution of the observed values"*; however, the definition of the threshold varies depending of the perspective (Seneviratne *et al* 2012). In general, threshold values that have relatively less likelihood of occurrence (e.g., 10% or lower probability during a reference period) are preferred for defining extremes (Seneviratne *et al* 2012). In other cases, absolute thresholds are also employed for climate extreme identification, for example, critical temperature beyond which humans develop heat strain. There is no precise or universal definition of a climate extreme and the definition of an extreme event varies from region to region; for example, a hot day ($35°C$) in the mid-latitudes will be considered a normal day in the tropics. Droughts and heatwaves are among the top 5 disastrous climate extremes that impart substantial impacts on society and global economy (UNISDR 2015).

1.4.1. Drought

Droughts– defined as deficit in available water– are one the most disastrous climate extreme as they impact our society and environment in multiple aspects. Bryant (1991) ranked droughts as the first among all natural hazards based on the characteristics and impacts of the hazards. In contrast to other climatic hazards, droughts begin prior to developing any symptoms like a disease (Ault 2020). Droughts occur globally in all climatic zones and hence are considered "the most far-reaching of all the natural disasters" on Earth (UNCCD 2022). Drought is the most feared, and fatal natural disaster for living beings as they jeopardize the environment, economy, agriculture, and social security, leading to displacement and deaths besides detoriating the quality of life (AghaKouchak 2015, Kelley *et al* 2015, Nicholson 2014). In addition to direct impacts, droughts deliver several indirect impacts such as dust storms, wildfire, and vector-borne diseases (Berman *et al* 2017, Bifulco and Ranieri 2017, Vins *et al* 2015).

Drought is a creeping phenomenon with no clear onset and termination, making it challenging to monitor and predict them accurately (Wilhite and Glantz 1985). Drought severity, which depends on the duration, intensity, and geographic extent, is even more difficult to determine. The multiplicity of the drought characteristics and its impacts hinder making reasonable estimates of their socio-economic effects (Haile *et al* 2020). Although a drought may last a season or a year, its impacts on society linger for many years depending on the society's vulnerability to drought (Ding *et al* 2011).

In the simplest terms, drought is defined as a deficit of water as compared to the climatological average. In general terms, IPCC defines a drought as a *"prolonged absence or marked deficiency of precipitation"*, or a *"deficiency of precipitation that results in water shortage for some activity or for some group"* or a *"period of abnormally dry weather sufficiently prolonged for the lack of precipitation to cause a serious hydrological imbalance"* (Heim 2002, Trenberth *et al* 2007). Droughts can appear in different forms, such as deficits in precipitation, lack of soil moisture, deficits of streamflow, lack of snowfall, among others, and corresponding stresses to the natural ecosystem can emerge, for example, agricultural stresses are most clearly reflected in soil moisture deficits (Lu *et al* 2017, Mishra and Cherkauer 2010). Drought is a "temporary" condition of water shortage and should not be confused with aridity, low flows, water scarcity or desertification, which are permanent characteristics of arid and semi-arid regions (Haile *et al* 2020). Droughts are not specific to the dry seasons only, however, they may occur during any season and are often associated with relatively higher temperatures (Mishra and Singh 2010, Dai 2011b).

1.4.1.1. Drought definitions and types

Droughts nearly occur in all regions of the globe with varying frequency and the associated socio-economic and ecological impacts, which vary spatially and temporally depending on the societal context of drought (Wilhite 2000). A universal definition of drought is thus unrealistic anticipation because drought definition should reflect the spatiotemporal variability and stochastic nature of water demand and socio-economic factors (Wilhite and Glantz 1985). Scores of definitions of drought have been developed across multiple disciplines according to their perspectives of droughts and their impacts. These definitions of droughts are broadly categorized either as conceptual definitions –which offer a general qualitative idea of drought without considering onset, termination, and severity– and operational definitions –that attempt to identify and quantify the key characteristics of droughts including onset, termination, and severity (Wilhite and Glantz 1985, Wilhite 2000). Operational definitions are mainly aimed at providing an early warnings of drought onset and severity (Mishra and Singh 2010, Dai 2011b). Drought definitions also vary based on the variable or context (indicator) used to describe them and are mainly divided into 4 major categories (Mishra and Singh 2010, Wilhite and Glantz 1985, Dai 2011b): (a) meteorological drought (b) hydrological droughts (c) agricultural droughts (d) socio-economic drought. Meteorological drought is defined as a period of months to years of deficit in precipitation (Gibbs 1975, Eltahir 1992) and are often augmented by above-normal temperature and high potential evapotranspiration (Dai 2011b). Meteorological droughts most often proceed and trigger other kinds of droughts. Hydrological drought is defined as a period with below-normal surface and sub-surface water levels (Tallaksen and Van Lanen 2004, Van Loon 2015), while agricultural drought is a period with inadequate soil moisture to sustain crop growth (Rickard and Fitzgerald 1969, Wu and Wilhite 2004). Finally, socio-economic drought arises when the demand for water and related socioeconomic goods and services exceed its supply due to meteorological and hydrological scarcity of water (Council 2004, Mishra and Singh 2010). Besides these, ecological drought –is defined as *"an episodic deficit in water availability that drives ecosystems beyond thresholds of vulnerability, impacts ecosystem services, and triggers feedbacks in natural and/or human systems"*(Crausbay *et al* 2017). Flash drought –defined as rapid onset and intensification drought (Christian *et al* 2019), and snow drought –

defined as lack of winter precipitation and/or higher temperatures in snow-dominated regions (Harpold *et al* 2017) have recently emerged in the scientific literature.

In the human-modified world, i.e., anthropocene, a new cause-based definition of drought is adopted, where drought is defined as a climate-induced drought if it is solely caused by climatic variability, while human-induced drought is caused by human influence on the water cycle by excessive farming, and human-modified drought that is caused the combination of human influence and climatic variability (Van Loon *et al* 2016).

1.4.1.2. Drought indices and drought identification

Droughts are multivariate/multiscalar events mainly described on the basis of hydro-meteorological variables (indicator variables). Drought indices are the prime metric for identifying and characterizing a drought event. A collection of multiple drought indices (about 150 indices) have been developed over the recent decades to identify and characterize different kinds of droughts, each having its advantages and limitations in monitoring and forecasting droughts (Vicente-Serrano *et al* 2012, Zargar *et al* 2011, Keyantash and Dracup 2002, Quiring 2009). These indices are actually the functions of the indicator variable or combinations of various indicator variables and measure the departure of the indicator variable from its normal conditions (i.e., climatological average). Among them, the most common are the Palmer drought severity index (PDSI; Palmer 1965), crop moisture index (CMI; Palmer 1965), surface water supply index (SWSI; Doesken *et al* 1991), standardized soil moisture index (SSMI; Hao and AghaKouchak 2014), standardized precipitation index (SPI; McKee *et al* 1993), soil moisture drought index (SMDI; Sohrabi *et al* 2015), standardized precipitation evapotranspiration index (SPEI; Vicente-Serrano *et al* 2010), Integrated Drought Index (IDI; (Shah and Mishra 2020)), Effective Drought Index (EDI; Byun and Wilhite 1999), Normalized Difference Vegetation Index (NDVI; Peters *et al* 2002), Evaporative Stress Index (ESI; Anderson *et al* 2016), soil water storage (SWS; Martínez-Fernández *et* *al* 2015), standardized runoff index (SRI; Shukla and Wood 2008), streamflow drought index (SDI; Vicente Serrano *et al* 2012), self-calibrated palmar drought severity index (scPDSI; Wells *et al* 2004). The most commonly used drought indices to characterize, monitor, and forecast droughts are briefly discussed in Table 1.1.

Yevjevich (1967) proposed theory of runs to identify drought characteristics, which include identification of drought duration, severity, and intensity, based on the drought indices. The most basic element for identifying drought characteristics is the threshold level; also termed as drought characterization factor (Haile *et al* 2020). A positive (negative) run is defined as the continuous period during which the drought index values (X_i) are above (below) the threshold (X_o). Figure 1.1 represents the theory of run method for drought identification where each negative run represents a drought event. The major properties of a drought event are (1) drought onset: time at which index value becomes lower than threshold, (2) duration termination; time at which index value becomes higher than threshold, (3) drought duration; time period between drought onset and termination. (4) drought intensity: it is the average value of the drought index drought a drought event, (5) drought severity: is the sum of index values over the drought event. It is also given by the product of intensity and duration.

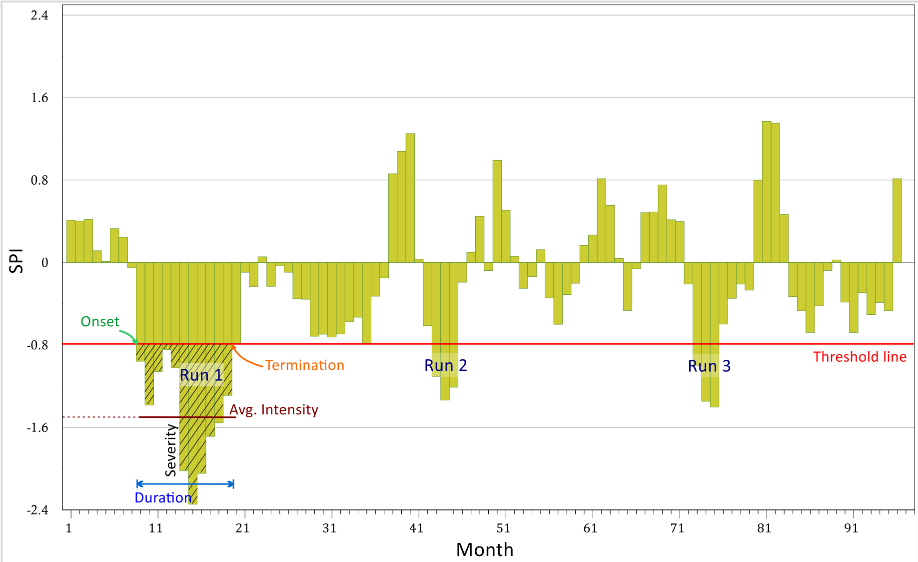

Figure 1.1. *Illustration of theory of runs for identification of drought characteristics. The bars show 3-month SPI at a randomly selected grid cell (30°N,62°E). X-axis represents the month number from Jan 2000. Red line is the drought characterization factor (drought threshold). Severity, which is product of duration and average intensity, is given by the hatched area.*

__Table 1.1__. List of some most common drought indices used for drought monitoring and prediction and their advantages and limitations.

Drought Index	Drought Variable	Advantages	Limitations	Calculation procedure	Drought categories
SPI	Precipitation	• Flexible time scale • Relates to probability of occurrence • Symmetric for both dry and wet spells	• Requires long-term data • Does not consider evaporation, temperature, soil water holding capacity, etc. • Assumes other variables as stationary • May give misleading results in regions with small seasonal precipitation	Measures the normalized anomalies of corresponding drought variables. The index values are computed by fitting the variable values to a parametric probability distribution and then transform the non-exceedance probabilities into a standard normal distribution.	Generally, less than -0.5 = Normal -0.5 to -0.8 = Mild -0.8 to -1.2 = Moderate -1.2 to -1.6 = severe -1.6 to -2.0= Extreme below -2 = Exceptional
SPEI	Climatic water balance anomalies: i.e., difference of precipitation and potential evapotranspiration	• Flexibility of timescale • Simple calculation (same as SPI) • Uses both precipitation and evapotranspiration	• Requires long-term data • Sensitive to the method of evapotranspiration calculation • May be sensitive to the probability distribution fitted		
SSMI	Soil moisture	• Flexible time scale • Uses probability distributions to	• Requires long-term data • May be sensitive to the probability distribution fitted • Uses soil moisture only		

		standardize soil moisture • Suitable for agricultural droughts			
SRI/SSI	Runoff	• Flexible time scale • Probability-based standard values • Incorporates climatic influence of seasonal lag on streamflow • Considers snowmelt	• Requires long term data • Sensitive to the nature of probability distribution • May require complex hydrological model to compute runoff (for SRI)		
PDSI/scPDSI	Hydro-climatic moisture departure (d): defined as difference of observed precipitation (P) and climatically expected precipitation (P')	• Considers both water supply (precipitation) and demand (evapotranspiration) • Besides precipitation, it also considers the temperatures and soil moisture changes • Takes precedent conditions into account	• Calculations are more complex than other indices • Inherent fixed time scale 9 to 12-month • Assumes all precipitation as rain • Does not work well in mountains and snow areas • Renormalization is needed for PDSI values	Multiple water balance coefficients are computed from a generic two-layer soil-moisture model, which is then used to compute the expected normal precipitation Moisture departures ($d = P - P'$) are then scaled with climate and duration coefficients to get PDSI values.	less than -1 = Normal -1 to-2 = Mild -2 to-3 = Moderate -3 to -4 = severe -4 to -5= Extreme below -5 = Exceptional

1.4.1.3. Causes of Drought

Droughts are the prolonged periods of deficit in moisture supply and are usually natural in occurrence. Atmospheric circulations, which carry the moisture from oceanic basins and terrestrial evaporation and distribute it across the globe, are found to be the major driver of droughts (Dai 2011b, Ault 2020). These circulations are often driven and modulated by long-range teleconnections of the tropical SST and remote forcing or atmospheric pressure patterns (Mishra and Singh 2010). Also, there are several anthropogenic causes of drought which include excess water demand by irrigation, deforestation, and soil degradation, and altered global weather patterns and teleconnections in response to anthropogenic climate change (Van Loon *et al* 2016).

Most naturally occurring droughts are related to anomalies in the atmospheric circulations such as atmospheric blocking or persistent high pressure that stays over a region for longer than normal duration (Mishra and Singh 2010). These anomalous circulations are often part of the large-scale atmospheric oscillations or circumglobal wave patterns (Ault 2020, Dai 2011b, Wang *et al* 2015b, Röthlisberger *et al* 2019, Swain *et al* 2017). Persistent highs block the moisture-laded winds and thus suppress the precipitation in the region (Wang *et al* 2015b, Black *et al* 2004). For example, the "ridiculously resilient ridge" near the west coast of United States blocks the moisture travelling from north-western Pacific and diverts it to North Canada resulting in the precipitation deficit and drought in California (Seager *et al* 2015, Seager and Henderson 2016). Similarly, Atlantic-European blocking is responsible for majority of the European droughts (García-Herrera *et al* 2019, Hanel *et al* 2018). Studies over Australia also found persistent high pressure over the eastern coast during the droughts in eastern Australia (Hirsch and King 2020, King *et al* 2020). Recent studies also found persistent high pressure as the major cause of Amazon droughts (Coelho *et al* 2016, Nobre *et al* 2016).

Climate oscillation –recursive patterns of climate variability (discussed in detail in section 1.4)– are often considered as the modulators of these synoptic-scale atmospheric circulation anomalies as they have the potential to alter the global climate system including the atmospheric circulations (Kenyon and Hegerl 2008, Hernández *et al* 2020, Wang and Picaut 2004, Kao and Yu 2009). Studies have explored the role of climatic oscillations in causing droughts at regional and global scale (Coelho *et al* 2016, King *et al* 2020, Wang *et al* 2015b, Mo and Schemm 2008, Vicente-Serrano *et al* 2011, Mares *et al* 2002, Fogt and Marshall 2020, Dai 2011b). ENSO –the dominant mode of global climate variability– impacts the global precipitation and temperature at interannual scale (New *et al* 2001, Dai 2011b). ENSO is found to cause precipitation deficit and drought over majority of global land in different seasons by altering the global precipitation pattern via "atmospheric bridges" (Vicente-Serrano *et al* 2011, Dai 2011b, New *et al* 2001). El-Niño is found to be the principal driver of droughts in South Africa, South Asia, Northern south America, Australia, parts of America and Europe (Dai 2011b, Vicente-Serrano *et al* 2011). La-Niña –the opposite phase of El-Niño– is found to be the major tropical, remote forcing for droughts in the western United States (Wang *et al* 2015b). Other climate oscillations, such as PDO, AMO, NAO, IOD, PNA and others have been associated with droughts regionally. For example, positive NAO (negative NAO) results in higher probability of droughts in southern (northern) Mediterranean region (Mares *et al* 2002, Vicente-Serrano *et al* 2011). Most of the droughts in western United States are found to occur during the negative PNA (Seager *et al* 2015). PDO is the major decadal variability in Pacific SST and has global impact on drought occurrence when in phase with ENSO (positive ENSO [El-Niño] during positive PDO) (McCabe *et al* 2004, Newman *et al* 2016). AMO influences droughts in Europe, Africa and East America (McCabe *et al* 2004, Wyatt *et al* 2012, Masih *et al* 2014). IOD –SST variability in Indian Ocean– has a significant impact on drought occurrence and severity in Australia and Indian sub-continent (Ummenhofer *et al* 2011, Gadgil *et al* 2004, Vinayachandran *et al* 2009, King *et al* 2020, Reddy *et al* 2022). More frequency of drought in Australia and India is observed during positive IOD and El-Niño.

Besides climate variability, land-atmospheric feedback is an important driver for propagation of mild dry conditions to severe droughts (explained in detail in sections 1.2.2 and 1.3.2). Furthermore, the intensive agricultural activities both at regional and global scales create an imbalance in supply and demand of water that results in higher risks of droughts and hence could be a potential driver of droughts (Van Loon *et al* 2016). Furthermore, the recent global warming led by anthropogenic forcing is responsible for unabated rise in global temperature leading to disruption in evaporation and rainfall patterns that causes unusual droughts (Mo and Schemm 2008, Dai 2011b, Mukherjee *et al* 2018, Ault 2020). Climate change also alters large-scale climatic oscillations that modifies the prevailing weather patterns globally and causes frequent extremes (Dai 2011b).

1.4.1.4. Impacts of Drought

Droughts affect the society and ecosystem in various ways, and many affect living beings and the environment (Van Loon and Laaha 2015). Drought impacts are non-structural and hard to evaluate even though they are environmental, economic, or social. Drought impacts vary with intensity and duration; however, same intensity droughts might have distinct effects at different times and locations. Although droughts affect all communities but more vulnerable are rural communities and agro-based businesses. Water shortage occurs practically in all economic sectors when the deficiency of water persists in a hydrological system, and in extreme circumstances, it may restrict freshwater supply (Tokarczyk 2013). As a consequence of drought and lack of water, agricultural productivity, food, and livelihoods decline (Muller 2014). Global water usage has more than doubled over the last decade, increasing drought intensity by 10–500% (Wada *et al* 2013). If water supply and demand are imbalanced, drought can lead to devastating effects (Tallaksen and Van Lanen 2004, Sheffield *et al* 2012). Wada *et al* (2013) found that human water usage alone increased worldwide hydrological drought frequency by 27%, with irrigation responsible for intensifying ~56% of droughts. Limited supply of water significantly reduces crop productivity by impacting the growth of plants. For instance, the 2011 Texas drought was the worst 1-yr drought in Texas history,causing $7.62 billion in losses in the agricultural sector alone (Guerrero 2012).

Recent studies have recognized that droughts may have major health implications via environmental, economic, and social degradations (Berman *et al* 2017, Vins *et al* 2015). Berman *et al* (2017) discovered for the first time that drought severity significantly affects public health. As the drought conditions worsened, Australia saw a 15% spike in working group suicide deaths (Hanigan *et al* 2012). High-frequency drought areas have increased mortality and cardiovascular disease risks (Berman *et al* 2017). Increased airborne dust and particle air pollution may aggravate asthma, allergies, and airway disorders (Page *et al* 2002, Hanigan *et al* 2012, Bifulco and Ranieri 2017). During severe droughts, rural mortality was four times higher than in cities (Berman *et al* 2017). Drought-related suicides and mental health issues were worse in rural agricultural areas (Hanigan *et al* 2012) with about 9% of working group male fatalities drought-related (Hanigan *et al* 2012). Droughts raise farmers and rural communities mental stress as a consequence of the unanticipated loss of animals and crops. For example, The droughts of 1876-78, the Global Drought, significantly reduced crop productivity and resulted in the Great Famine (worst famine world has wintnessed) and caused 50 million casualities (Singh *et al* 2018). In addition, the droughts in 1983, caused the largest global maize failure in modern history (Anderson *et al* 2019).

1.4.2. Heatwave

Heatwaves are defined as multi-day events of excessive heat or anomalously high temperatures (Perkins and Alexander 2013a), however, in extreme cases, these may last for weeks. They are one of the most impactful weather extremes that cause substantial impacts on human health (McMichael and Lindgren 2011, Matzarakis and Nastos 2011), environment (McKechnie *et al* 2012, Xu *et al* 2020), infrastructure (Zuo *et al* 2015), and agriculture (Lobell and Field 2007, Im *et al* 2017a), including other natural and anthropogenic systems (Rübbelke and Vögele 2011, Jones *et al* 2020). For example, in July 2010 Russia observed the deadliest heatwave of the century (Hoag 2014) that claimed 55,000 lives, resulted in 25% of crop failure, more than a million hectares of burned area and an economic loss of ~15 billion US dollars (Barriopedro *et al* 2011). In 2003, European heatwaves were responsible for 70,000 deaths, making it the most lethal heatwave for mankind (Poumadere *et al* 2005). Indeed, heatwaves are tagged as 'silent killers'(Loughnan 2014) as they impact human health in multiple ways but not instantaneously. For example, heat strokes usually increase the severity and complexity of the underlying medical conditions (usually in elderly people, children, and field workers) resulting in the death after few days. Heatwaves also increase the risk of cardiovascular and respiratory distress (McMichael and Lindgren 2011). The impacts, however, are more pronounced in developing countries due to lack of adaptive capacity and cultural constraints (Kjellstrom 2016).

Although extreme heatwaves generally occur during summer season, mild heatwaves are also noted in spring and autumn (Perkins 2015). Recent studies have differentiated heatwaves from warm spells where heatwaves are defined as "a period which is hot in absolute sense" and warm spells are defined as "a period which is hot in relative sense" (Perkins *et al* 2012). According to this distinction, warm spells can occur any time of the year whereas heatwaves are limited to occur during hot summers. In climatic terms, heatwaves are exceptionally hot temperatures (absolute values) whereas warm spells are unusually high-temperature anomalies (with respect to climatological average). However, in climate research, they are being used synonymously (Perkins-Kirkpatrick and Lewis 2020, Fischer and Schär 2010).

Heatwave consequences are projected to escalate in a warmer environment, where more frequent, intense, longer, and larger heatwaves are expected if climate change continues unrestrained. (Im *et al* 2017a, Perkins *et al* 2012). At the regional scale, the climate change impacts are more intense compared to global scale (Seneviratne et al., 2016), which together with higher temperature variability results in more intense and longer heatwaves (Dosio *et al* 2018). In addition to climate change, the global and regional changes in heatwaves are driven by the changes in synoptic systems (Meehl and Tebaldi 2004), and land-atmosphere feedback (Hirsch *et al* 2019) and natural modes of climate variability (Perkins et al., 2015).

1.4.2.1. Heatwaves definitions and indices

Like droughts, there is no universal definition for heatwaves. The world meteorological organization (WMO) defines a heatwave as *"a period of five or more consecutive days during which the daily maximum temperature exceeds the climatological average by $5°C$"*. The United States national weather services define a heatwave as *"a spell of abnormally and uncomfortably hot and unusually humid weather spanning two or more days"*. Indian meteorological department (IMD) declares a heatwave, *"if the daily maximum temperature exceeds its normal conditions by* $5-6°C$ *for 3 or more days"*. WMO has recently recognized dry heatwaves and wet heatwaves as two distinct kinds of meteorological heatwaves. Clear sky and high amount of sun radiation describe dry heatwaves; by contrast, oppressive humidity and even nighttime cloud cover characterize moist heatwaves (McGregor *et al* 2015). Moist heatwaves are found to be more impactful on human health compared to dry heatwaves as they impart additional stress on metabolic activities (Schär 2016). Additionally, multiple definitions of heatwaves have been developed across multiple disciplines depending upon meteorological variables or impacts of interest (Perkins and Alexander 2013a). These definitions are either percentile (e.g., 90th percentile of daily maximum temperature) or fixed threshold based (e.g., $40°C$).

Heatwaves are usually characterized by their duration, intensity, frequency, timing and spatial extent, which are often used to measure their potential to impact (Perkins 2015). In order to quantify/identify these characteristics of heatwaves, multiple heatwaves indices are developed considering a single indicator variable or a combination of the variables (Perkins and Alexander 2013a, Nairn and Fawcett 2015).

Temperature is often considered as the best indicator variable for heatwaves due to its near-ubiquitous observations; however, use of apparent temperature –a function of temperature and humidity– is becoming popular nowadays for identification of moist heatwaves. Some of the most commonly used index-based heatwave definitions are: (1) A heatwave is a period of six or more consecutive days with daily T_{max} greater than the local 90th percentile based on 15-day centred window (Fischer and Schär 2010). This definition was later modified (Perkins and Alexander 2013, Perkins *et al* 2012) by reducing the minimum number of days to three and representing it as CTX90pct. (2) CTN90pct– same as CTX90pct but based on minimum temperature. (3) Excess heat factor (EHF)– developed by Nairn and Fawcett (2015) based on three-day averaged daily mean temperature that actually measures the excess heat accumulated during the three-day period, which is not dissipated during the night. EHF is based on two excess heat indices (a) Significance index (EHI_{sig})–measures the excess heat with respect to climatological 95th percentile. This represents whether the three-day period is warmer than the normal annual climate or not. For a heatwave to be present EHI_{sig} is required be positive. (b) acclimatization index (EHI_{acc})– measures the excess heat with respect to recent past (one month). The minimum value of EHI_{acc} is limited to 1 in order to constraint that EHF must have the same sign as EHI_{sig}.The mathematical formulation of EHF is as follows:

$$EHI_{sig} = (T_i + T_{i-1} + T_{i-2})/3 - T_{95} \quad [1.1]$$

$$EHI_{acc} = (T_i + T_{i-1} + T_{i-2})/3 - (T_{i-3} + T_{i-4} + \cdots + T_{i-32})/30 \quad [1.2]$$

$$EHF = EHI_{sig} \times max(1, EHI_{acc}) \quad [1.3]$$

Other heatwave indices used for heatwave analysis include: Wet bulb temperature (WBT; Stull 2011, Budd 2008), Apparent heatwave index (AHWI; Russo *et al* 2017), universal thermal climate index

(UTCI; Bröde *et al* 2012, Błażejczyk *et al* 2013) and others (see (Perkins and Alexander 2013a, Fischer and Schär 2010)),

1.4.2.2. Causes of Heat waves

Although heatwaves last less than a week, the exceptional 2010 Russian heatwave lasted more than a month (Barriopedro *et al* 2011). All heatwaves over the globe had a common atmospheric feature –a high-pressure synoptic system associated with them. These high-pressure systems (or anticyclones) are typically known as blocking highs or persistent highs (Charney and DeVore 1979) and they remain stationary over a region longer than usual (Hong *et al* 2011). These blocking or persistent highs block a region from the zonal jet stream movement for days (Egger 1978, Pezza *et al* 2012) and prevent cooler air from the poleward side to interact with hotter air on the equatorial side, therefore heated air builds up. When such high-pressure systems persist for multiple days, they generate and extend a heatwave by adverting warm, dry air to the area and downwelling hot air (Hirsch *et al* 2019, Dong *et al* 2018b). Blocking/persistent highs have caused several intense heatwaves, including the 2010 Russian heatwave (Hong *et al* 2011, Matsueda 2011), the 2003 European heatwave (Black *et al* 2004, Vautard *et al* 2013), the 1995 Chicago heatwave (Meehl and Tebaldi 2004), and the southeastern 2009 event (Parker *et al* 2014, Hudson *et al* 2011).

Besides these high-pressure systems that are important for heatwave conditions, land-atmosphere coupling is more important for maintaining the heatwave conditions (Miralles *et al* 2019). When the soil is moist, more incoming solar radiation is converted to latent heat fluxes, whereas during dry conditions more radiation converts to sensible heat fluxes (Hirsch *et al* 2019). This increased sensible heatwave during dry conditions increases the surface air temperature and if the dry conditions persist for a longer time it results in a heatwave. Studies on the relationship between the land surface and extreme temperature indicate that interactions between soil moisture and temperature increases summer temperature fluctuation and extreme temperatures are more prevalent during dry conditions (Seneviratne *et al* 2006, Lorenz *et al* 2010). Although the strength and impact of the land-atmosphere feedback depend on multiple aspects, it was a key factor in the "mega heatwaves" across Europe in 2003 and Russia in 2010 (Black *et al* 2004, Miralles *et al* 2014, Fischer *et al* 2007). Moreover, advection of hot air from an upwind drought area could also cause heatwave conditions by continuous supply of hot air (Schumacher *et al* 2019).

Climate oscillations drive the heatwaves by modulating the global temperature pattern and the atmospheric pressure patterns through atmospheric bridges (Alexander *et al* 2002). Multiple studies have noted higher temperatures over most of the global land during El-Niño phase of ENSO (Kenyon and Hegerl 2008, Arblaster and Alexander 2012, Alexander *et al* 2009). El-Niño has been linked to heatwaves over most of the tropics, South Africa, parts of Europe and America (Perkins-Kirkpatrick and Lewis 2020, Luo and Lau 2020, Sun *et al* 2016, Herceg-Bulić *et al* 2017). North Atlantic Oscillation drives the extremes of high temperatures over Eurasia (Sun *et al* 2016, Li *et al* 2020). ENSO and IOD play a significant role in causing heatwaves over Australia (White *et al* 2014). SAM+ results in heatwaves in eastern Australia by developing a high pressure near the region (King *et al* 2020).

1.4.2.3. Impacts of Heat waves

Heat waves– multiday high-temperature events– have disastrous impacts on humans (McMichael and Lindgren 2011, Khosla *et al* 2021) and the surrounding environment including agriculture (Kornhuber *et al* 2020, Lesk *et al* 2016), infrastructure (Rübbelke and Vögele 2011), vegetation(Xu *et al* 2020), and other natural and anthropogenic systems (Rübbelke and Vögele 2011, Barriopedro *et al* 2011). Extreme heat events represent a substantial danger to worldwide agricultural production systems, with consequences for food security and pricing (Lesk *et al* 2016, Ray *et al* 2015). In addition, vegetation disturbance from excessive heat often affects net ecosystem productivity and may exacerbate positive climate-carbon cycle feedbacks, particularly in combination with drought (Fernández-Martínez *et al* 2019). Extreme heat events may also directly impact terrestrial ecosystems by harming or killing species, and indirectly by increasing their susceptibility to following disturbances like disease, pests, fire, and drought. Moreover, heat events strain power-producing stations and transmission infrastructure, thus increasing the chance of power outages when the loss of air conditioning might have the most effect on human mortality (Rübbelke and Vögele 2011, Sigauke and Nemukula 2020).

The adverse health effects of heatwaves include sunburn, heat stress, and heatstroke, as well as renal failure and heart attacks (Kovats and Kristie 2006, Khosla *et al* 2021, McGregor *et al* 2015). Heat waves may result in an increase in hospital emergency admissions, ambulance dispatches, illness, and death (Wang *et al* 2012b, Nitschke *et al* 2011). They are a significant cause of weather-related deaths in Australia (Herbst *et al* 2014) and the United States (Robinson 2001). During the 2009 heat wave in Australia, mortality rose by 62% in Melbourne and 10% in Adelaide and caused an $800 million economical loss (Zuo *et al* 2015). This heatwave event in Melbourne had a severe influence on the peak power demand, which caused the explosion of a power grid supply transformer (Boston 2013). The 2003 heat waves in southern Europe killed 15,000 in France alone and 25,000-70,000 throughout Europe (Robine *et al* 2008). In 2018, heatwaves in multiple regions across the northern hemisphere resulted in 4–11% reduction in crop productivity regionally (Kornhuber *et al* 2020).

1.4.3. Compound weather or climate extremes

Weather or climate extremes occurring simultaneously and/or sequentially in space and/or time are referred to as compound extremes (Zscheischler *et al* 2020), and often result in exponential impacts as compared to the isolated univariate extremes (e.g., droughts or heatwaves) (Wahl *et al* 2015, Haqiqi *et al* 2021, Feng *et al* 2019). Until the 2nd decade of the 21st century, majority of the studies on the risk assessment and impact analysis of extreme events considered univariate extremes. In 2012, the Inter-governmental panel for climate change (IPCC) for the first time introduced the concept of "compound event/extremes" in the Special Report on Climate Extremes (SREX) for better estimation of the associated risk and impacts. (Seneviratne *et al* 2012) According to IPCC a compound event can be defined to occur if:

"(1) two or more extreme events occurring simultaneously or successively, (2) combinations of extreme events with underlying conditions that amplify the impact of the events, or (3) combinations of events that are not themselves extremes but lead to an extreme event or impact when combined. The contributing events can be of similar (clustered multiple events) or different type(s)"

Later Leonard *et al* (2014) defined compound events as *"an extreme impact that depends on multiple statistically dependent variables or events".* Their definition, emphasized on requirement of multiple variables/events, extremeness of impact rather than variables/events, and statistical dependence between the variables. In 2018, Zscheischler *et al* (2018) modified this definition for weather and climate events by defining compound weather and climate extreme as *"the combination of multiple drivers and/or hazards that contributes to societal or environmental risk".* In climate science, a driver can be any process or climate-related variable or phenomenon that spans over multiple spatiotemporal scales. A hazard, on the other hand, is a climate-related event that usually results in negative impacts. The characteristics of these drivers and hazards are often affected by the modulators (e.g., low-frequency modes of climate variability such as ENSO). Based on the above-discussed definitions of compound weather and climate events, multiple studies have been carried out to rationally estimate the risk and impacts arising from these events and their changes in the warmer world (Lee *et al* 2017, Wahl *et al* 2015).

1.4.3.1. Types of compound extremes

The impacts of compound weather or climate events usually result from causally interrelated hazards and/or drivers. The correlation between multiple hazards is usually due to (1) common external forcing factor or modulator, (2) mutual reinforcement of events via system feedback, and (3) conditional dependence of occurrence (Seneviratne *et al* 2012). From the definitions, discussed above, it is evident that compound events can be a result of multi-hazards occurring over a region within a specific time period (i.e., either at same time or with some lag) or over multiple regions but simultaneously. Based on this concept, Zscheischler *et al* (2020) categorized compound weather and climate events into four major classes viz (1) pre-conditioned events, (2) multi-variate events, (3) temporally compound events, and (4) spatially compound events; however, the boundaries of these classes are subjective and not fixed.

Pre-conditioned events: In pre-conditioned events, a pre-existing climate-driven condition causes or amplifies the impact of one or more hazards occurring over a geographical region. In multi-hazard literature, such kind of compound events are often referred to as "change condition" types (Tilloy *et al* 2019); however, in case of compound weather and climate, both precondition and hazard(s) are caused by climate drivers though they need not be always causally related (Zscheischler *et al* 2020). For example, rain-on-snow flood in Bernese Alps, on 10 October 2011, which resulted in damage of ~90 million Swiss franc, is a typical example of pre-conditioned compound extremes (Rössler *et al* 2014). This event resulted from the extensive snow cover (precondition), caused by the sustained snowfall (driver of precondition), and the atmospheric river that subsequently brought warm and moisture laded air, resulting in extreme precipitation and warmer temperatures that raised the freezing line by 1700m in 24 hours, driving snowmelt. This combination of snowmelt and intense rainfall gave rise to the flood (hazard). In addition, false-spring events also fall in this category where the early vegetation growth and early blooming during warming event towards the end of winter corresponds to precondition and the following frost event represents the hazard (Marino *et al* 2011).

<u>Multivariate events</u>: The co-occurrence of multiple climate drivers and/or hazards in the same geographic region that results in an impact are termed as multivariate compound events (Zscheischler *et al* 2020). For a multivariate event, a single driver could result in multiple correlated hazards or multiple drivers can cause a single or multiple hazard(s). Typically, the drivers of multivariate events are casually related through associated weather patterns (the modulator). Multivariate events include all kinds of concurrent extremes occurring in the same location and are referred to as "compound hazards" in multi-hazard literature (Tilloy *et al* 2019, Liu *et al* 2016). Moreover, it is important to note, that multivariate events incorporate extreme climate anomalies that are not necessarily extreme in univariate variables, but could cause large impacts (Sadegh *et al* 2018). The two typical and most commonly studied examples of multivariate events are compound coastal flooding and compound drought and heatwaves. For example, a low-pressure system (the modulator) during February 2015 produced a storm surge and heavy precipitation (the drivers) that resulted in the compound flooding (the hazard) in multiple coastal river catchments in Ravenna, Italy, thereby, causing widespread damage of tens of millions of euros (Bevacqua *et al* 2017). On the other hand, concurrent droughts and heatwaves that generally lead to tree mortality, crop failure, human mortality and morbidity, wildfires, and hydropower plant failure. Such compound events are attributed to persistent high-pressure or anticyclonic circulation (the driver) that are often modulated by the remote tropical SST forcing (the modulator) (Aghakouchak *et al* 2020, Feng *et al* 2019, 2021). For example, the La-Niña-like SST pattern in Pacific during 2011 (the modulator) promoted a stationary Rossby wave (the driver) that caused compound drought and heatwave over Texas (Hoerling *et al* 2013). These dry and hot conditions were further intensified by the land-atmosphere interaction, resulting in the statewide record-breaking agricultural loss, wildfires and commercial timber loss.

<u>Temporal compounding events</u>: The successive occurrence of same or different hazards affecting a given geographical location that results in an impact or amplifies the impact are referred as temporally compound events (Zscheischler *et al* 2020). Similar to multivariate events, the hazards are generated by one or multiple drivers which intern is caused by a modulator. The successive hazards could be casually related through the same driver (also referred as cascading hazards) or could occur by chance (Tilloy *et al* 2019); however, distinguishing them is difficult due to limited sample size and incomplete understanding of the system. One of the typical examples of temporal compounding is the temporal clustering of heavy precipitation events on sub-seasonal scale. The multiple successive heavy-rainfall events (the drivers), over southern Switzerland, caused by the upper-level Rossby wave breaking (the modulator) resulted in extreme lake flooding (the hazard) and associated damage (Barton *et al* 2016). As mentioned above, consecutive occurrence of different hazards is also included in this category. For example, the consecutive occurrence of floods and heatwaves (the hazards) in Japan during East Asian monsoon (the driver) has resulted in 300 deaths and substantial economic loss (Wang *et al* 2019b).

Spatially compounding events: Spatially compound events refer to the occurrence of same or different hazards at multiple geographical locations simultaneously or within a limited time window, thus resulting in an amplified impact (Zscheischler *et al* 2020). Such events are always established by a system capable of spatial integration and usually act as a modulator. The drivers and the hazards are often caused by the modulator, which is capable of creating a physical link among multiple locations (Steptoe *et al* 2018). The globally synchronized –spatially compound at a global scale– occurrence of hazards and associated impacts often arise from large-scale modes of climate variability, such as the ENSO (Singh *et al* 2018, Anderson *et al* 2019), atmospheric teleconnections (Boers *et al* 2019) or are driven by circumpolar wave patterns (Kornhuber *et al* 2019). For example, the strong El-Niño of 1983 (the modulator) fueled the heatwaves and droughts in majority of maize-producing nations including South Africa, North America, Brazil, and Southeast Asia (the hazards), resulting in the world's largest synchronized crop failure in the modern history (Anderson *et al* 2019). In addition, the concurrent heatwave of 2018 in multiple regions of Northern hemisphere including North America, Europe, and Asia (the hazards) was driven by the circumpolar Rossby wave pattern of wave number 7 (modulator) (Kornhuber *et al* 2019).

Although previous studies on compound events have considered multiple combinations of hazards for the investigation of compound events, this thesis, however, is limited to investigation of multivariate events and spatially compound events. Droughts and heatwaves are considered as univariate hazards (extremes) in this thesis. The further discussion on the compound events will be focused on compound droughts and heatwaves [CDHWs] (Multivariate event) and spatially compound extremes, which are (1) spatially compound droughts [SCDs], (2) spatially compound heatwaves [SCHs], and (3) spatially compound CDHW [SC-CDHWs].

1.4.3.2. Causes of compound extremes

Compound droughts and heatwaves are the first and most commonly studied multivariate events in the compound weather and climate extremes literature. This type of compound event is often represented by the precipitation deficit and warmer temperatures that are often promoted by the atmospheric circulations (Feng *et al* 2021). In addition, precipitation and temperature are closely associated with each other through a well-defined thermodynamic relationship. Recent studies have noted a negative dependence between precipitation and temperature over most of the global land (Trenberth and Shea 2005, Zscheischler and Seneviratne 2017). The occurrence of CDHWs is attributed to two major physical mechanisms. The first and the most important driving mechanism is the presence of the persistent ocean-atmospheric circulation anomalies that often result in drought and heatwave. These large-scale and persistent atmospheric circulation anomalies, which include blocking highs, atmospheric stagnation events, and subtropical highs, stay over a region longer than usual and increase the temperature, evapotranspiration and divert the cold and moist air thereby suppressing precipitation. For example, the subtropical high/anticyclonic pattern is found to be responsible for compound droughts and heatwaves over East Asia, and North America by driving the droughts and heatwaves (Kong *et al* 2020b, Ryu and Hayhoe 2015). In addition, during the 2010 Russian heatwave, the compound drought and heatwave were a result of persistent high pressure over the region (Hong *et al* 2011). Such anticyclonic circulations are often part of quasi-stationary Rossby waves or planetary waves, which are most often established and modulated by anomalous sea surface temperatures (SSTs) and teleconnections of remote forcing, e.g., large-scale climate oscillations such as ENSO (Hoerling and Kumar 2003, McCabe *et al* 2004, Seager and Henderson 2016, Swain *et al* 2017, Wang *et al* 2015b, Dai 2011b). Other climate oscillations are also known for their role in causing CDHWs by assisting in the formation of such high-pressure regimes and stationary blockings (Hao *et al* 2019, Hong *et al* 2011, Mukherjee *et al* 2020, Wu *et al* 2019).

Besides large-scale circulation patterns that are responsible for the onset of droughts and heatwaves, land-atmosphere feedback is often used to explain compounding of droughts and heatwaves (Hirsch *et al* 2019, Miralles *et al* 2019). Droughts are often associated with atmospheric moisture deficit and have clear skies that increase solar irradiation (Hirsch *et al* 2019). The dry soil, during an abnormally dry condition, limits or ceases the evapotranspiration, thereby limiting the latent heat fluxes (Miralles *et al* 2019). Consequently, any additional incoming radiation is used as sensible heat flux that increases the temperature leading to or exacerbating the heatwave condition. These anomalies in energy budget are often associated with lower-level wind divergence and anticyclonic cyclonic that block the moist-air influx leading to prolonged drier conditions and provide sufficient time for heatwave to develop and amplify as a compound drought and heatwave (Mukherjee *et al* 2020).

The co-occurrence of droughts and/or heatwaves at multiple locations –spatially compound events– are often linked to circumglobally teleconnections (Hassan and Nayak 2020, Singh *et al* 2021, 2018) and Rossby waves (Kornhuber *et al* 2019, Röthlisberger *et al* 2019, Kornhuber *et al* 2020). These atmospheric teleconnections modulate and are modulated by the SST anomalies in Pacific, Atlantic, and Indian oceans via atmospheric bridges (Wang 2019, Cai *et al* 2019a). For example, in a global but event-specific study on spatially compound droughts of 1876–1878, Singh et al., (2018) noted compound droughts in South East Asia, East Brazil, and North and South Africa and linked their occurrence to the record-breaking El-Niño, AMO, and Indian Ocean Dipole (IOD). In addition, the simultaneous warm spells over Europe, North America, and the western North Atlantic in summer 1994 resulted from synoptic-scale recurrent Rossby wave (Röthlisberger *et al* 2019). More often than not Rossby waves of wavenumbers 5 and 7 are observed hovering during concurrent heatwaves over central North America, Eastern Europe, and eastern Asia and central North America, Western Europe, and western Asia, respectively (Kornhuber *et al* 2020).

1.4.3.3. Impacts of compound events

Droughts and heatwaves impact our society and ecosystem in multiple ways and most of them are associated with living beings and their surrounding environment (Haqiqi *et al* 2021, Zuo *et al* 2015, Bifulco and Ranieri 2017, Rathore and Maini 2008). These impacts, however, amplify and are more extreme when droughts and heatwaves co-occur in a region (Feng *et al* 2019, Haqiqi *et al* 2021). During a CDHW event, the deficit in the available water results in water stress in all components of ecosystem and the heatwave further amplifies the stress by increasing the water demand in crops and living beings (Wu and Jiang 2022, Wu *et al* 2021). This increased demand under a limited supply of water results in the wilting, and in extreme cases death of plants thereby significantly reducing crop productivity . In addition, the abnormally high temperatures not only over-stress energy sectors but also decrease the quality of life and in extreme cases could lead to morbidity and mortality in living beings including humans (McGregor *et al* 2015, Khosla *et al* 2021). Furthermore, the extremely dry soil and atmosphere lead to a higher likelihood of wildfires and dust storms that reduce the quality of air in the region (Jones *et al* 2020). For example, the summer 2010 Russian heatwave, which was induced by the extreme drought conditions over the region, caused widespread wildfires by burning over a million hectares of land, destroying 25% of region's crop yield, killing 55,000 people, and costing the country \$15 billion (Barriopedro *et al* 2011). In another event in July 2003, most of Europe was engulfed by a compound drought and heatwave event that resulted in burnt area of 739,000 hectares, 30% reduction in gross primary productivity, and 40,000–70,000 deaths (Poumadere *et al* 2005, Le Tertre *et al* 2006). Feng *et al* (2019) noted an increase of 23% in the probability of maize yield reduction when droughts or heatwaves transform to compound droughts and heatwaves.

These impacts are more pronounced and disastrous when the droughts and/or heatwaves occur simultaneously in multiple regions (Kornhuber *et al* 2020, Singh *et al* 2018, Anderson *et al* 2019). Such occurrences of connected extremes could result in collapse of global food system and lead to economic crisis. For example, during 1875–1878, a multi-year compound drought in South East Asia, East Brazil, and North and South Africa, also known as the Great Drought, resulted in more than 50 million fatalities, and the Great Global Famine (Singh *et al* 2018). Anderson *et al* (2019) noted that spatially compound droughts and heatwaves of 1983, resulted in the largest synchronized crop failure in modern history. Spatially compound heatwaves (SCHs) in northern mid-latitudes have reduced the overall crop productivity by 4% and up to 11% at regional-scale based on regions defined using event coincidence analysis (Kornhuber *et al* 2020).

1.5. Climate variability and climate extremes

As mentioned in the previous sections, climate variability is considered as the major cause of the occurrence or initiator of climate extremes across the globe; however, climate change is found to have a significant impact on changing the characteristics of extremes (Diffenbaugh *et al* 2015, Jones *et al* 2020, Aghakouchak *et al* 2020). Multiple studies have been performed to understand the changes in extremes during the last few decades (drought, heatwaves and compound extremes) due to climate change and changes in climate variability (Byrne 2021, Seneviratne *et al* 2012, Diffenbaugh *et al* 2015, Wu *et al* 2021, Russo *et al* 2017, Chapman *et al* 2019, Goswami *et al* 2006b). For example, Mazdiyasni & AghaKouchak, (2015) noted an increase in the risk of concurrent drought and heatwaves (CDHW) in United States. These studies have noted a significant increase in the frequency, intensity, duration of droughts, heatwaves and CDHWs and attribute these changes to the anthropogenic climate change. However, the interannual variability in the extremes is mainly driven by the modes of natural climate variability (Perkins-Kirkpatrick *et al* 2017, Kenyon and Hegerl 2008). Since this thesis is more inclined towards understanding the role of climate oscillations, further discussion will be limited to impact of climate oscillations on the occurrences of droughts, heatwaves and compound extremes.

1.5.1. Climate oscillations and droughts

Climate variability or climate oscillations are often associated with extreme weather and climate conditions such as droughts, heatwaves, floods, and cyclones (Vicente-Serrano *et al* 2011, White *et al* 2014, Lau and Kim 2012, Perkins-Kirkpatrick *et al* 2017, Seager and Henderson 2016). ENSO, the dominant mode of interannual variability of global climate, has profound impact on the precipitation and temperature patterns across multiple regions via Atmospheric teleconnection (White *et al* 2014, Mo and Schemm 2008, Singh *et al* 2020, Hao *et al* 2018). The ENSO phenomenon explains 6.3% of the precipitation variability globally (New *et al* 2001) and is also useful to explain the climatic (precipitation and temperature) variability in multiple regions in Northern hemisphere (Mo and Schemm 2008, Kumar *et al* 1999, Sun *et al* 2016, Ju and Slingo 1995). El-Niño is often linked with the precipitation deficit and drought conditions across Maritime Continents, parts of India, Southwest North America, West Africa, and, Brazil, and Australia (New *et al* 2001, Singh *et al* 2022, Vicente-Serrano *et al* 2011). For instance, Gore et al., (2020), Masih et al., (2014), and Pomposi et al., (2018) have found that El-Niño strengthens the Walker Circulation resulting in the reduced moisture supply to south Africa causing severe drought over the region. Multiple studies on droughts over Australia have highlighted that El-Niño and positive IOD favors the precipitation deficit that later translates to drought (Ummenhofer *et al* 2011, 2009, Kiem *et al* 2016, King *et al* 2020). King *et al* (2020) also noted a significant influence of SAM on Australian droughts. Keshavamurty (1982) and Kumar *et al* (1999) noted that most of the severe droughts over India have happened during the El Niño phase of the ENSO and of negative phase of Equatorial Indian Ocean Monsoon Oscillation (EQUINOO) (Surendran *et al* 2015), which is atmospheric counterpart of negative IOD (Gadgil *et al* 2004, Maity and Kumar 2006). Other regional droughts studies over South America, Southern North America, Southeast Asia, Iran, and parts of China have observed higher drought activity during El-Niño. In contrast, La-Niña is often linked to large-scale flooding in these regions; however, causes severe drought over Western North America by developing a high-pressure ridge over the west coast of United States (Wang *et al* 2015b).

Indeed, ENSO is the major driver of dry conditions globally, but it only explains 4.6% variability in global PDSI (index for wet and dry conditions) (Dai 2011b). Recent regional and continental studies including studies over Africa, United States, Amazon and Australia (Lee and Zhang 2011, Masih *et al* 2014, McCabe *et al* 2004, Ummenhofer *et al* 2009, 2011, Vicente-Serrano *et al* 2011, Kong *et al* 2020b) have noted that droughts can be attributed to direct or indirect influence of other low-frequency modes of climate variability, such as PDO, AMO, PNA, NAO, and AO. The Euro-Atlantic region is less impacted by ENSO and mainly influenced by climate modes in Northern hemisphere i.e., NAO, AO, and PNA including other modes in

Atlantic region. López-Moreno & Vicente-Serrano, (2008), Mares et al., (2002), and Vicente-Serrano et al., (2011) noted that NAO+ is associated with drought conditions over southern Europe, Turkey, and Northwest Africa, while NAO- causes drought in northeast Africa and Northern Europe. PNA, which usually impact Northern America, leads to drought condition in North America, particularly in Southwest United States, when in negative phase (Hubeny J. Bradford *et al* 2011, Van der Schrier and Barkmeijer 2007).

Besides, ENSO and IOD+ that often cause failure of monsoon in India and results in drought, Goswami et al., (2006), and Srivastava et al., (2002) highlighted important role of NAO for drought occurrence in India. Later Borah *et al* (2020) noted that most of the non-El-Niño droughts occurred when North Atlantic Ocean is relatively cold (i.e., AMO-). Abdul Malik & Brönnimann, (2018) and Ashok Singh et al., (2020) observed that AMO- and PDO+ reduce the ISMR through their influence on ENSO and NAO patterns. Ganguli and Reddy (2014) found that 60% of dry years in India have occurred during negative phase of AMO. Furthermore, large-scale Rossby waves are also found to cause severe sub-seasonal decline in the monsoon rainfall over India, mainly during late-season (Borah et al., 2020).

1.5.2. Climate oscillations and heatwaves

Similar to large-scale ENSO–drought relationship, ENSO remarkably impacts the extreme temperatures globally and regionally in Australia, Southeast Asia, India, Europe, Southern America, Southern Africa, And China (Arblaster and Alexander 2012, Kenyon and Hegerl 2008, Lin *et al* 2018, Murari *et al* 2016, Sun *et al* 2016, Wang *et al* 2016, White *et al* 2014). Studying the impact of climatic oscillation on heatwave characteristics in Australia, (Parker *et al* 2014, Perkins *et al* 2015), noted higher frequency, areal extent, and intensity of heatwaves in northeast Australia during El-Niño and positive IOD; however, the ENSO impacts were weak over Southwestern region (Arblaster and Alexander 2012, Parker *et al* 2014, Perkins *et al* 2015, White *et al* 2014). Marshall et al., (2014) also highlight higher heatwave occurrence in northeastern Australia during negative SAM due to persistence of the high pressure blocking near Tasman (Fogt and Marshall 2020, Marshall *et al* 2014). El-Niño is often associated with higher probability of longer and hotter heatwaves in Indian sub-continent during pre-monsoon season due to high pressure over the region that weakens moist Southeasterlies in Arabian sea, and increases the number of clear sky days (Murari *et al* 2016, Ratnam *et al* 2016). Ratnam et al., (2016) noted that the north-central heatwaves in India are associated with the high pressure blocking in North Atlantic Ocean.

Cold phase of ENSO, i.e., La-Niña, is usually linked with more heatwave days over Europe by developing a PNA-like pattern over North Pacific and North America that modifies the atmospheric circulation pattern over Atlantic and Europe and forms a persistent atmospheric block over the European region (Schneidereit *et al* 2012, Sun *et al* 2016). La-Niña has also been linked as the major driver of the 2010 Russian heatwave by Schneidereit *et al* (2012) and Sun *et al* (2016). Multiple studies on European heatwaves have highlighted the significant role of NAO+ (NAO-) in developing the heatwaves over the northern (southern) parts of the region (Castro-Díez *et al* 2002, Tan and Unal 2003). Moreover, Li et al., (2020) found that the NAO+ leads to the formation of European blocking that is quasi-stationary and more persistent compared to other kinds of blocks, hence resulting in more extreme heatwaves. Recent studies have also highlighted role of other climate oscillations in regional heatwaves, for instance, ENSO, AMO, PNA modulation of north American heatwaves (Grotjahn *et al* 2016, Meehl *et al* 2007, Ruprich-Robert *et al* 2018), NAO impacts on 2010 Russian heatwave (Wright *et al* 2014), and of impact of ENSO and other climate oscillation during south African heatwaves (Lyon 2009, Reason 2017).

1.5.3. Climate oscillations and compound events

CDHWs are often caused by the strong negative dependence between precipitation and temperature (Zscheischler and Seneviratne 2017) that is often triggered by the negative land-atmosphere feedback and/or large-scale climate oscillation (Hao *et al* 2013, 2018). ENSO, which often causes drought and heatwaves in multiple regions around the globe, is also found to affect the precipitation–temperature dependence and lead to concurrent occurrence of hot and dry conditions (Hao *et al* 2018, Zscheischler and Seneviratne 2017). ENSO plays a significant role in the occurrence of summer season CDHWs in tropical regions of America, Central and Southern Africa, Southeast Asia, and Australia during El-Niño; while as wetter and cooler conditions prevail during La-Niña (Alexander et al., 2009; Hao et al., 2018). Perkins et al.,

(2015) and Ummenhofer et al., (2011) separately investigated the role of ENSO and IOD in causing heatwaves and drought over Australia and highlighted higher extreme event activity when the two oscillations are in phase. Due to lack of regional study on CDHWs and climate modes, based on the above studies it could be hypothesized that of CDHWs are more likely during IOD+ and El-Niño in Australia. In a recent study on variations in compound precipitation and temperature extremes over China, Wu et al., (2019) found statistically significant positive correlation between spatial extent of compound extremes and AMO during both winter and summer seasons. They also noted significant role of NAO- and EA/WR-, but ENSO failed to show any impact. Hao et al., (2019) developed a logistic model to predict the CDHWs globally and found that ENSO skillfully predicted the spatiotemporal variability in CDHWs. They added that PDO and NAO are important at regional scale and could be used to improve the predictability skill of the model. NAO shows the negative correlation with the CDHW over most of Europe highlighting higher occurrences of CDHWs during NAO+ (Hao *et al* 2019). Although some studies have explored CDHWs in view of climate variability but, overall, there is limited literature available on how, when, and which climate oscillation impact CDHWs and in which region?

Spatially compound events, which affect multiple regions simultaneously, are usually triggered by large-scale atmospheric circulations (Kornhuber *et al* 2017, 2019). The concept of spatially compounding in weather and climate extremes is new and gained popularity after a recent study by Kornhuber et al., (2017) that highlighted co-occurrence of high-temperature extremes over Western United States, Western Europe, and Western Central Asia. Although there were a few studies that hinted at the co-occurrence of extremes in multiple regions, they did not explicitly investigate them as spatially compound events. For examples, the co-occurrence of 2010 Russian heatwave and Pakistan flood (Lau and Kim 2012) and; Global drought of 1876 (Singh *et al* 2018). After Kornhuber et al., (2017) few more studies on spatially compound heatwaves were developed, however, they were either limited to Northern hemisphere or event specific for instance concurrent heatwaves of 2018 (Kornhuber *et al* 2019). Spatially compound droughts, on the other hand, remained unstudied, with only two event-specific but global studies: Singh et al., (2018) investigated the Global drought during the great Global Famine of 1875–1878 and found that the simultaneous drought conditions in South East Asia, East Brazil, and North and South Africa were caused by the atmospheric teleconnection of El-Niño and IOD+. In another study, Anderson *et al* (2019) found that during El-Niño major food-producing countries including Brazil, South Africa, India, and southern North America experienced drought and heatwave conditions, resulting in crop failure at global level. Moreover, they find that 1983 El-Niño was extreme and resulted in the largest global crop failure in modern history.

In a nutshell, climate variability plays an important role in the occurrence of droughts and/or heatwaves regionally and globally. Although droughts and heatwaves have been explicitly explored in the context of climate variability both at global and regional scales, their role in causing and changing compound extremes is unclear.

1.6. Research gaps

Droughts and heatwaves always lead to negative impacts on society, and the ecosystem; however, these impacts multiply when droughts and heatwaves co-occur in space and/or time. The impacts of CDHWs are relatively localized i.e., impacts are limited to the region and its neighbouring nations compared to spatially compound drought and/or heatwaves, which are more disastrous and have global implications, as multiple regions get impacted simultaneously. In addition, SCEs are an emerging topic in the science of weather and climate and have gained popularity due to the potential impacts they impart on global food security, water resource systems, insurance industries, and economy, for instance, globally-synchronized crop failure during spatially compound droughts of 1983 (Anderson *et al* 2019).

Multivariate compound extremes, such as CDHWs, have been explored extensively in the last decade and have been linked to multiple large-scale climate oscillations (such as ENSO) (Hao *et al* 2018), local land-atmosphere feedback (Schumacher *et al* 2019), and persistent high pressure (Coumou *et al* 2018). However, spatially compound extremes, on the other hand, remains understudied with only a few studies over northern hemisphere or for a specific extreme event. For example, the spatially compound heatwaves in northern hemisphere during Rossby waves 5 and 7 (Kornhuber *et al* 2017, 2019a). Compound drought in southeast Asia, east Brazil, and North and South Africa during El-Niño of 1876–1878 (Singh et al., in 2018). The worst globally-synchronous maize crop failure of 1983 was caused by compound drought conditions across multiple regions due El Niño event (Anderson *et al* 2019). This limited available literature and blurred understanding of compound events, their causal mechanisms, change and impacts, hint toward a much-needed global assessment of spatially compound droughts and/or heatwaves, understanding their mechanisms, changes and associated impacts.

1.7. Objectives

Based on the research gaps and the motivation highlighted in the previous section following objectives were framed for this thesis with the intention to answer the following research questions.

Objective 1. Understanding drought characteristics over India.

Objective 2. Understanding heatwave characteristics over a complex terrain of the Himalayas.

Research questions*: - How to estimate heatwave day frequency from temperature data with some missing entries? How are heatwaves and maximum temperatures changing over complex Himalayan terrain? Develop a model to separate the contributions of global* *climate change from local forest cover change towards these changes in maximum temperature?*

Objective 3. Investigating the large-scale teleconnection in droughts and their attributions to large-scale climatic oscillations.

Research questions*: - Do spatially-compound droughts happen? if yes, where? Can they be attributed to large-scale climatic oscillations?*

Objective 4. Estimating the changes in spatially compound heatwaves and their impacts on crop productivity and humans.

Research questions*: - How are observed spatially compound heatwaves changing? What are their impacts on crop production and humans? What are the roles of climatic oscitations?*

Objective 5. Investigating and modelling the role of large-scale climate oscillation in causing spatially compounding of multivariate extremes.

Research questions*: - How often do we see spatial compounding of CDHW? What regions have more likelihood of such events? What are the contributions of different climate oscillations? Develop a model to estimate the probability of SCE given the climatic conditions?*

To make this thesis coherent with other global climate studies, the global landmass, excluding Antarctica, is divided into 25 and 44 reference regions as defined in IPCC AR5 and AR6, respectively.

1.8. Thesis organization

Chapter 1. Introduction

In this chapter, a brief discussion about the definitions, types, metrics causes and impacts of droughts, heatwaves, and compound extremes is presented. An overview of the climate oscillations (climate variability modes) is also given and that are differentiated from climate change. This chapter also provides a comprehensive and detailed review of all the available literature (recent) on droughts, heatwaves, and compound extremes. An extensive review of the studies on the role of climate variability (climate oscillations) and climate change on climate extremes is also included. Towards the end of this chapter, the major research gaps are highlighted and the thesis objectives are defined.

Chapter 2. Understanding regional droughts and heatwaves

In this chapter, (A) we review multiple approaches used for monitoring and predicting droughts. India is selected as the study area for this case study. (B) In order to understand the heatwave characteristics, a smaller region in the complex Himalayan terrain, the Kashmir Valley, is selected as a case study. A novel method is developed to separate the contribution of local forest cover changes from global climate change towards the changes in maximum temperature and heatwaves. Furthermore, this chapter highlights how to estimate the heatwave characteristics if missing data is present.

Chapter 3 Spatially-Compound Droughts

In chapter 3 the likelihoods of SCDs among the IPCC AR5 reference regions are quantified. Sc-PDSI computed using monthly precipitation and temperature data from CRU, ERA5, and MERRA2 for the period 1980–2017 is employed to identify the region pairs that show robust spatially compounding in droughts. Two robust pairs are selected for further investigation on casual factors/physical mechanisms that result in spatial compounding in droughts in these regions. Phase of standard climate indices is also investigated during the SCDs in the selected pairs to highlight the role climate oscillations in causing them.

Chapter 4. Spatially-Compound Heatwaves: Role of ENSO

In chapter 4, based on daily maximum temperature from NOAA CPC, changes spatially compound heatwaves during the period 1979–2020 are shown. The region pairs that have significantly higher likelihood of experiencing spatially compound heatwaves are highlighted. The changes in crop productivity and population exposure in response to changes in SCHs are also assessed. Spearman's rank correlation coefficient between the global and regional spatial extent under heatwaves and monthly climate indices is estimated to evaluate the role of climate oscillation in causing large-scale compound heatwave events; however, role of ENSO was explicitly explored in explaining the interannual variability of compound heatwaves.

Chapter 5. Spatially compounding of multivariate extremes: Role of climatic variability

Chapter 5 discusses the changes in number of IPCC AR6 regions that experience CDHWs (multivariate compound extremes) simultaneously. Using weekly total precipitation and mean maximum temperature (obtained from daily data) from NOAA CPC, we identify the dominant season for occurrence of concurrent drought heatwaves for each IPCC AR6 region and then estimate the likelihood of spatially compound CDHWs for each pair of regions that have same dominant season. Two pairs with significantly higher likelihood in SC-CDHWs are selected for in-depth analysis. Transitional probabilities are computed to understand the propagation from one extreme to other extremes. A logistic regression model is also developed to identify the drivers (climatic oscillations) that significantly impact the compound of extremes and estimate probability of spatially compound extremes for any specific weather regime.

Chapter 6. Conclusions

The detailed conclusions from the thesis work are presented in Chapter 6. This chapter also highlights several implications of our results and provides multiple avenues where the results from the thesis can be extended to further understand and model compound weather extremes.

Chapter 2 : Understanding droughts and heatwaves

Executive summary

Chapter 1 discusses the brief concept of droughts, heatwaves and compound extremes and highlighted the main research gaps in our present understanding of extreme events. Chapter 2 aims at monitoring and predicting droughts and heatwaves, by selecting India and Kashmir Valley as the case studies, in two separate sub-headings 2A and 2B, respectively. Chapter 2A discusses in detail all the methods and procedures used to monitor and predict various kinds of droughts in India. Multiple drought indices have been developed to define drought and its characteristics in India and globally. Drought prediction in India is being performed using both statistical and dynamical approaches. IMD highly relies on its multiple linear regression model for ISMR predictions. We discover that large-scale climatic modes and regional hydrometeorological factors are crucial to understanding and forecasting drought occurrences. In chapter 2B, which is related to the heatwave identification over the Kashmir Valley, a method is proposed to compute heatwave day frequency for the regions with missing data. In addition, this sub-chapter also highlights the role of forest cover loss in changes in temperature over Himalayan terrain by developing a model to segregate the temperature changes due to global climate change and local changes in forest cover.

A. Understanding droughts

After: Munir Ahmad Nayak and ***Waqar Ul Hassan****; A synthesis of drought prediction research over India; (2021) Water Security,13, p.100092. https://doi.org/10.1016/j.wasec.2021.100092*

Abstract

A major section of India's economy is directly linked with water-dependent food and energy systems. Skilful predictions of droughts play a pivotal role in sustainable water management and evading serious damages to agriculture production and economy of a region. Recent decades have witnessed valuable advances in scientific understanding and prediction of droughts in India. In this review, we synthesize major sources of drought predictability over different regions in India. We find that a few large-scale atmospheric and oceanic circulation patterns and regional-scale hydrometeorological variables are key to understanding and predicting drought occurrences. We also present a concise summary of major statistical and dynamical forecasting-based modelling efforts in drought predictions. Although major strides have been taken in drought prediction in the recent decades, important gaps still remain in understanding the onset and spatiotemporal dynamics of droughts.

Further, many opportunities of improving the skill of drought prediction over India are envisaged, and many impending challenges are highlighted. The overall picture is that significant efforts and investments are critical for understanding and predicting droughts over India.

2.1. Background

Drought over a region is defined when water availability in the region is significantly lower than the normal. Among the most complex natural eco-hydrological processes, droughts can occur at temporal scales of weeks to years and spatial scales of cities to continents (Van Lanen and Peters 2000, Sheffield *et al* 2009). Droughts can appear in different forms, such as deficits in precipitation, lack of soil moisture, deficits of streamflow, lack of snowfall among others, and corresponding stresses to the natural ecosystem can emerge, for example, agricultural stresses are most clearly reflected in soil moisture deficits (Lu *et al* 2017, Mishra and Cherkauer 2010). Many drought definitions have evolved over the years and corresponding indices or metrics have been proposed to quantify drought intensities (discussed in detail in Section 2.2).

The all-India Summer (June-July-August-September) Monsoon Rainfall (ISMR) variability is generally used to distinguish drought and wet years in India. Agricultural yield in India is highly correlated with ISMR and droughts can reduce the Gross Domestic Product (GDP) of the country by 2 to 5% through crop failure (Gadgil and Gadgil 2006). ISMR drought of 1987 (Figure 1.1) affected the agriculture activities in roughly 59 million hectares crop area (46% of the total all-India crop area), and resulted in severe deficits in drinking water in large parts of the country (GoI, 1989). Accurate seasonal predictions of droughts can help in early preparedness efforts and better management, thereby saving lives and the economy. Sub-seasonal predictions are most useful to farmers who have to decide and manage the necessary investment options in crop production before the cropping season (Shah *et al* 2017, Saseendran *et al* 2002, Rathore and Maini 2008). Over the past few decades, there have been significant advances in drought prediction over India, and most of the state-of-the-art models show promising skill in forecasting ISMR tendency more than a month ahead. However, significant gaps remain in explaining the ISMR annual and sub-seasonal variability, and hence in prediction of droughts.

In this work, we discuss the major large-scale climatic teleconnections that are shown to explain the majority of ISMR variability, followed by different approaches that have evolved in the recent years to predict droughts, including various statistical and dynamical approaches. And finally, we highlight some of the emerging challenges and future research directions that can help in advancing models for drought predictions over India.

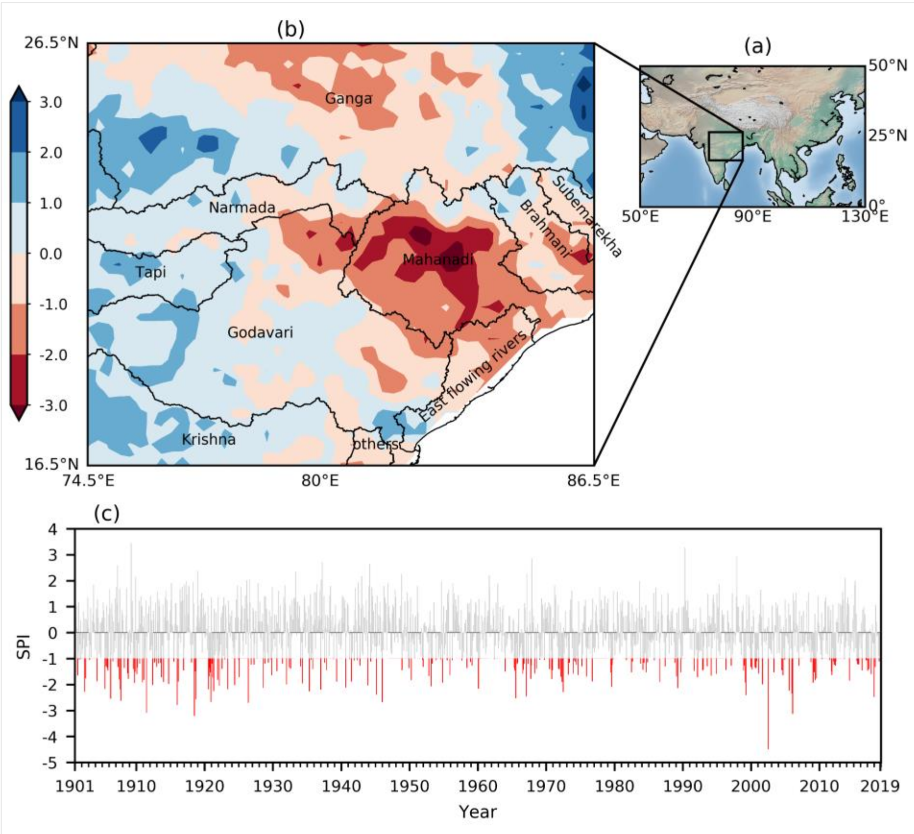

Figure 2.1. *Spatiotemporal variability of droughts over central India. (a) Location of the Indian monsoon region defined by Goswami et al (2006b) (b) Spatial map of 3-month SPI (SPI_3) on Aug 1987. Blue and red shadding represent wet and dry conditions. (c) Average SPI_3 over the monsoon region during the last 118 years. The red color bars represent the months which have SPI<-1 (moderate to extreme drought).*

2.2. Drought definitions

Droughts nearly occur in all regions of the globe with varying frequency and the associated negative impacts on economy, society, and ecosystems, which vary spatially and temporally depending on the societal context of drought (Wilhite 2000). A universal definition of drought is thus unrealistic anticipation because drought definition should reflect the spatiotemporal variability and stochastic nature of water demand and socio-economic factors that are functions of climate regimes (Wilhite and Glantz 1985). Scores of definitions of drought have been developed across multiple disciplines according to their perspectives of droughts and their impacts. These definitions of droughts are broadly categorized either as *conceptual definitions*−offer a general qualitative idea of drought without considering about onset, termination, and severity, and *operational definitions*−that attempt to identify and quantify the key characteristics of droughts including onset, termination, and severity (Wilhite and Glantz 1985, Wilhite 2000). Operational definitions are formulated as drought indices that can be used to analyze the frequency, severity, and duration of a given drought event to provide an early warning system (Mishra and Singh 2010, Dai 2011b). The drought definitions also vary based on the variable or context used to describe them and are hence divided into 4 major classes (Mishra and Singh 2010, Wilhite and Glantz 1985, Dai 2011b): (a) meteorological drought (b) hydrological droughts (c) agricultural droughts (d) socio-economic drought. Meteorological drought is defined as a period of months to years that are deficit in precipitation (Gibbs 1975, Eltahir 1992) and are often augmented by above-normal temperature and high potential evapotranspiration (Dai 2011b). Meteorological droughts most often proceed and trigger other kinds of droughts. Hydrological drought is defined as a period with below-normal surface and sub-surface water levels (Tallaksen and Van Lanen 2004, Van Loon 2015), while agricultural drought is a period with inadequate soil moisture to sustain crop growth (Rickard and Fitzgerald 1969, Wu and Wilhite 2004). Finally, socio-economic drought arises when the demand for water and related socioeconomic goods and services exceed its supply due to meteorological and hydrological scarcity of water (AMS 2004, Mishra and Singh 2010). A collection of multiple drought indices have been developed over the recent decades to identify and characterize different kinds of droughts, with each having its own advantages and limitations in monitoring and forecasting droughts (Vicente-Serrano *et al* 2012, Zargar *et al* 2011, Keyantash and Dracup 2002, Quiring 2009). The most commonly used drought indices to characterize, monitor, and forecast droughts in India are given in Table 1.1 (Complete table can be found in the published paper).

2.3. Data-driven approaches

Data-driven statistical models and empirical models have served as powerful tools in understanding and forecasting climatic variables. IMD heavily relies on statistical models for long-range operational forecasting of ISMR. With the most recent statistical models, developed and updated with efforts of many years, IMD issues two long-range forecasts, first in the mid-April for the ISMR, and then an updated forecast in June for JAS all-India rainfall (Rajeevan *et al* 2007). The details of IMD multiple linear regression models can be found at https://mausam.imd.gov.in/imd_latest/contents/seasonal_forecast.php#. In most cases, data-driven models for drought prediction are physics-driven, where the predictor variables are selected based on their influence on ISMR variability through some atmospheric or oceanic physical processes. In this section, we summarize the most important predictors for ISMR and droughts, challenges in developing models, and different modelling attempts in the recent years to forecast droughts, including purely time-series analysis-, linear regression-, and artificial intelligence-based approaches.

2.3.1. Use of Standard Climate Indices

Most of the recent work in statistical approaches has been devoted to understanding the influence of large-scale climatic oscillations on ISMR, and how they can be used to predict droughts. A major lead in statistical forecasting of Indian summer monsoon rainfall (ISMR, definition JJAS) happened when it was found that the eastern Pacific El Niño Southern Oscillation (EP-ENSO) plays a significant role in driving a major fraction of the monsoon variability (Ju and Slingo 1995, Rasmusson and Carpenter 1982). Most of the severe droughts over India have happened during the El Niño (warmer SST in eastern Pacific) phase of the ENSO (Keshavamurty 1982, Kumar *et al* 1999).

SST anomalies over the Indian Ocean affect the variability of ISMR through the Indian Ocean Dipole (IOD), and recent works have demonstrated that the atmospheric component IOD called the Equatorial Indian Ocean Oscillation (EQUINOO) is more correlated with ISMR (Gadgil *et al* 2004, Maity and Kumar 2006) and can be a better predictor of droughts. The negative phase of EQUINOO is comprised of negative and positive convection anomalies over the western and the eastern Equatorial Indian Ocean, respectively, and westerly wind anomalies in the Equatorial Indian Ocean and a suppressed ISMR. The anomalies reverse during the positive phase of EQUINOO. Many droughts have occurred during the negative phase of EQUINOO, and most of the droughts over India are well explained by co-occurrence of negative EQUINOO and negative ENSO (i.e., El Niño) (Surendran *et al* 2015).

Apart from the Pacific and Indian Oceans, other distant regional climates are also believed to influence the variability of ISMR. Of particular interest are the SST anomalies in the North Atlantic Ocean that affect the snow cover over the Eurasia. In anomalous snow winters, when the snow cover is large, the Eurasia does not heat up strongly during spring and summer. The decrease in the temperature gradient between Indian Ocean and Eurasia landmass decreases the strength of Indian summer monsoon (Fu and Fletcher 1985). Hence, SST anomalies over the North Atlantic Ocean as depicted by the North Atlantic Oscillation (NAO), for example, can be important predictors of droughts over India (Goswami *et al* 2006a, Srivastava *et al* 2002).

Other large-scale low-frequency oceanic oscillations, such as the Atlantic Multidecadal Oscillation (AMO) and the Pacific Decadal Oscillation (PDO), are thought to influence the ISMR through their influence on the strengths of ENSO and NAO patterns (Malik and Brönnimann 2018, Singh *et al* 2020). For example, Ganguli and Reddy (2014) found that higher fraction (~60%) of rainfall deficit years happened when AMO was in negative phase. Borah *et al* (2020) noted that most of the non-El-Niño droughts occurred when North Atlantic Ocean is relatively cold. Furthermore, large-scale Rossby waves are also found to cause severe sub seasonal decline in the monsoon rainfall over India, mainly during late-season (Borah *et al* 2020)

2.3.2. Search of Precursors

Instead of the predefined standard climate indices, for example, Niño3.4 for ENSO, which are metrics for major states of the climate, it is prudent to search for specific regional climates that are linked with ISMR through teleconnections (Capua *et al* 2019, Rajeevan and Pai 2007, Wang *et al* 2015). If a few leading regional climates are found to be linked with ISMR, these can be considered as the precursors of the ISMR and can be utilized for months-ahead drought prediction. Much of the research in this area has relied on developing correlation maps of ISMR with months-ahead sea level pressure (SLP) and/or SST fields over the globe, and it is hoped that a few significantly correlated regions will appear from the maps. The IMD operational statistical models for ISMR forecasts (Rajeevan *et al* 2007) use multiple predictors that are 1- to 4-months lead time climates in different regions around the globe, including the North Atlantic and North Pacific SSTs, Equatorial South Indian Ocean SST, East Asia SLP, and Eurasia land surface temperature, among others.

It is likely that some of the precursor regions in the correlation maps are interrelated and hence do not add independent skills to drought forecasting. Based on 4 and 5-month lead times SLP and air temperature, Capua *et al* (2019) obtained a set of five independent precursors by removing correlated precursors using partial correlations. Besides the Pacific and Atlantic regions, the authors found two precursors of ISMR in the Arctic and one in Indonesia. Similarly, based on correlation fields, Wang *et al* (2015) showed that central Pacific warm SST anomalies ahead of the summer affect the ISMR, which is supported by Sahastrabuddhe *et al* (2019), who found central and eastern Pacific warm SST anomalies (El Niño events) during wide-spread monsoon rainfall deficit years. It should be noted, however, that predictors found through correlation may not have a physical relationship with ISMR, thus the list of predictors needs to be scrutinized to remove those that show spurious correlations.

2.3.3. Spatial heterogeneity in ISMR

There is a large degree of spatial variability in summer rainfall over India (see drought of 1987 in Figure 2.1), part of which can be attributed to local factors, such as orography and the land cover type, but a significant portion is related to the large-scale climatic teleconnections (Ghosh *et al* 2012, Mishra *et al* 2012, Parthasarathy and Pant 1985, Yadav *et al* 2018). The spatially varying correlation of climatic teleconnections with summer rainfall suggests multiple avenues in the context of drought prediction or, in general, ISMR prediction. The use of lumped average rainfall over India may confound regional prediction skills of the climatic teleconnections, resulting in lower skill of ISMR prediction. On the other hand, the use of regional or finer-scale rainfall anomalies can produce global precursors for drought prediction more conspicuously. Even by using the standard climate indices, prediction of droughts over India can be improved by considering regional or finer scale anomalies rather than all-India rainfall. Indeed, finer-scale predictions are more directly useful for regional-scale planning and management. Sahastrabuddhe *et al* (2019) identified nine spatial patterns of Indian summer monsoon using K-means clustering algorithm and found some distinct precursors for the patterns that showed wide-scale rainfall deficits. They noted that climatic teleconnections can provide important information on the spatial distribution of monsoon rainfall, in addition to the lumped all-India summer rainfall. Predictions at regional scale, considering climatically homogenous regions, is performed in many recent studies (Dutta and Maity 2018, 2020a, Kashid and Maity 2012, Rajeevan *et al* 2004, Saha *et al* 2017)

2.3.4. Multiple-Modelling frameworks

A basic and powerful statistical modelling approach that uses multiple predictors to predict droughts in a region is multiple linear regression (MLR) framework given as:

$$Y = \alpha + \beta_1 X_1 + \beta_2 X_2 + \cdots + \beta_p X_p + \epsilon \quad [2.1]$$

where Y is the drought series (in terms of a drought index) and X_1 to X_p are the predictors, α is the intercept term, $\beta_1$to β_p are the corresponding coefficients, and ϵ is the residual term. The most simplistic linear regression framework utilizes the rainfall anomalies from a few previous months to predict future droughts; these include autoregression-based models, such as Autoregressive Integrated Moving Average (ARIMA) models. Mishra *et al* (2007) and Mishra and Desai (2005) found that for Kansasbati River Basin (area 4265km^2) in West Bengal, the correlation skill (given as the correlation coefficient between the forecasted drought indices and the observed values) was small (~0.35) at lead times of 4-months. Tiwari and Mishra (2019) considered lagged accumulated rainfall, SPI, and SPEI over past months to forecast storage anomalies in 91 reservoirs over India. The results showed that lagged rainfall provides a high correlation skill (> 0.7) in predicting 1- to 3-months ahead reservoir anomalies, and it was found all the four major drought months from 2002 to 2017 were primarily related to below-average monsoon in the previous year. It was further noted that lagged SSI, when available, can improve upon SPI and SPEI in forecasting reservoir anomalies.

IMD stage1 linear regression model with multiple precursors showed a correlation skill 0.82 for 1.5-months ahead ISMR forecasts for the period 1981–2004 (Rajeevan *et al* 2007), though the correlation equation used in the analysis is not correct (Equation 6 in their paper). For the same forecast period, Capua *et al* (2019) showed moderate correlations of ~0.35 based on IMD precursors used in Rajeevan *et al* (2007) for longer leads of two and four months. Maity and Kumar (2008) used a composite index of lagged ENSO and EQUINOO to predict monthly rainfall anomalies over India. Copula framework was used to model the dependence between ISMR and the composite index, while the uncertainty between the dependence was utilized to estimate the uncertainty bands of the predicted ISMR. The model performed significantly better than the linear regression-based models; however, a visual analysis of forecasts of drought months suggests that most of the drought months (16 out of 25) were outside the 90th percentile uncertainty bands. Ganguli and Reddy (2014) used ENSO, IOD, and AMO to predict up 1- to 3-month lead time six-monthly SPI (SPI6) in western Rajasthan using Support Vector Regression (SVR). Then Copula framework was used to develop joint probability distribution of the observed and SVM-predicted SPI6, which was then used to simulate the ensembles of droughts conditional on the predictions from SVM, giving the uncertainty of the predictions. In their work, most of the droughts were within the 95th percentile prediction intervals, though the prediction intervals in many cases were wide covering wet-range (SPI6 > 1). It is also noted that summer months showed larger uncertainty in predictions as compared to the winter seasons. Wang *et al* (2015) observed smaller and negative correlation skill of IMD operational forecasting system in predicting ISMR for 1989 to 2012 period. Surendran *et al* (2015) developed a linear model with ENSO and EQUINOO indices for summer as predictors that is able to explain more than half of the variance in ISMR, and the one-month ahead lead-time predictions showed ~0.5 correlation skill with ISMR.

Another approach that has been found useful is to decompose the drought index into multiple independent components that can be predicted with better accuracy without significant loss of information. Maity *et al* (2016) used wavelet-based decomposed series to predict transitions of meteorological drought to agricultural and hydrologic drought in Upper Mahanadi basin in Chhattisgarh. With lesser assumptions than wavelet decomposition, Adarsh and Reddy (2019) employed an empirical mode decomposition technique to decompose the original SPI series into multiple independent components for meteorological drought prediction over Kerala, Telangana, and Orrisa. These studies showed marginal prediction skill improvements of artificial intelligence (AI-) based models over MLR-based models.

Drought processes do not necessarily follow a linear relationship with the lagged index values and exogenous predictors, especially for short-term droughts, such as one-month (SPI1) or three-month (SPI3) (Adarsh and Reddy 2019, Maity *et al* 2016, Mishra *et al* 2007). Due to their capability to capture non-linear relationships, AI-based models to predict droughts have received significant attention recently (Malik *et al* 2019, Sahai *et al* 2000, Singh and Borah 2013). For Kansasbati River Basin, Mishra *et al* (2007) found better performance of hybrid ARIMA-Artificial Neural network (ANN) model than ARIMA model. Malik *et al* (2019) compared models based on MLR, co-active neuron fuzzy inference system (CANFIS), and Multiple Layer perceptron Neural Networks (MLPNN) to predict droughts over two small watersheds of the Ganga river. It was observed that CANFIS and MLPNN performed better for smaller-scale droughts than MLR, and all the models performed competitively for longer-scale (6 months) droughts. Ganguli and Reddy (2014) employed support vector regression using ENSO, IOD, and AMO indices as predictors for droughts over Western Rajasthan and found a moderate correlation skill of ~ 0.55 for 3-month lead time drought. Kashid *et al* (2010) used climate teleconnections (ENSO and EQUINOO) and local covariates, e. g. outgoing long-wave radiation (OLR), to predict weekly streamflow for summer season over Mahanadi River using Genetic Programming. They observed a reasonable streamflow forecast skill, NSE of roughly 0.67; in general, however, streamflow in low-flow weeks and months were overestimated consistently in most of the 13 summers analyzed from 1990 to 2003. Similar results can be observed in their later studies Maity and Kashid (2010, 2011). Sahoo et al (2019) compared Recurrent Neural Networks (RNN) and Long Short-Term Memory-RNN (LSTM-RNN) to predict 1-month ahead lower quantile monthly streamflow at Basantpura station of Mahanadi River. The results showed high forecasts skill of both modelling frameworks, and it is found that LSTM-RNN only marginally improves over RNN (NSE values of 0.878 and 0.843).

Besides the standard climatic indices, regional precursors using correlation maps have been used as predictors for ISMR. Capua *et al* (2019) used 4- to 5-months ahead temperature and pressure anomalies of five independent precursor regions in an MLR-based model to predict ISMR variability. The model yielded a modest, albeit better than operational IMD forecasts, correlation of 0.4 for 1981–2004 forecast period; however, based on IMD definition of drought of rainfall 10% below the long-term mean, none of the four drought years in the period were predicted accurately. From the physical understanding of the monsoon and climate teleconnections and correlation maps, Wang *et al* (2015) developed an ISMR prediction model based on spring season temperature and pressure anomalies in four precursor regions. The model showed an improved correlation skill of ~0.64 for the 1921–2012 forecasted period.

2.4. Physically-based approaches

Besides statistical approaches of weather predictions, which only consider physically based empirical relationships between the predictors and predictand without accounting for the detailed underlying physical mechanisms, dynamical approaches are mostly based on the physical processes in the atmosphere, ocean, and land surface. Dynamical predictions rely on Climate models (Global or/and Regional) and/or hydrological models that imitate the physical processes by a set of numerical equations. These climate models represent and simulate the physical and thermodynamical processes either in the atmosphere only (AGCMs) or oceans (OGCMs) or coupling of both (Coupled ocean-atmosphere). Since dynamical models are physically based, they have the ability to capture nonlinear interaction of climate systems and thus are capable of predicting unprecedented conditions even under non-stationary climate. Besides uncertainty in initial conditions, inaccurate knowledge of evolutionary mechanisms of weather processes introduces uncertainty in the model, termed as “model uncertainty”. Charney and Shukla (1981) hypothesized a “*second kind of predictability*” that stems from the low-frequency variations of boundary forcing anomalies such as sea surface temperature (SST), ice cover, and soil moisture and act as the basis for seasonal predictability. Several post-processing techniques such as bias-correction methods, multi-model ensemble (MME) technique, and downscaling procedures have proved fruitful in improving the forecast skill (Acharya *et al* 2013a, Kulkarni *et al* 2012, Ratna and Sikka 2011). The use of GCMs for prediction of Indian Summer Monsoon rainfall (ISMR) started in the early 1990s when different modelling groups tried to simulate 1987 and 1988 monsoon features under the Monsoon Numerical Experimental Group program (Palmer *et al* 1992) and Atmospheric Model Inter-comparison Project (AMIP) and highlighted that models show incongruity in simulating the interannual variability of monsoon even though forced with observed SST (Sperber and Palmer 1996, Gadgil and Sajani 1998).

2.4.1. Meteorological droughts prediction using AGCMs

Out of 30 AGCMs from AMIP, only 11 models performed realistically in simulating the mean rainfall and interannual variation of monsoon over India and the skill was high during ENSO-associated seasons, though their performance was poor for extremes years (Gadgil and Sajani 1998). In addition to better skill in weekly rainfall forecasts, reasonable skill scores (probability of detection(POD), threat score, and others>0.5) were also reported for excess and scanty categories of weekly rainfall over multiple regions of India (Saseendran *et al* 2002). Mean ensemble technique has been satisfactorily implemented in simulating the essential features of ISMR such as climatology, intra-seasonal variability, and successfully validated against observation for the drought year 2002 (Sajani *et al* 2007). A reasonable agreement between model simulations from National Centre for Environmental Prediction's T170/L42 model and observation was found in key features of ISMR such as Climatology, monsoon circulations, etc., for the period 1985–2004, however, differences were evident in the magnitude of interannual and intra-seasonal variability (Ratna *et al* 2011). Moreover, models' forecasts skill was poor in predicting droughts and excess monsoons, for example, droughts of 1987, 2002 and excess of 1994, which were later on efficiently simulated (except 1994) by averaging the member ensembles with similar seasonal numbers of below and above average pentads by Ratna and Sikka (2011). The skills of five different AGCMs were evaluated under the 'Seasonal Prediction of the Indian Monsoon' project by forcing them with either observed SST forcing for the period 1985–2004 or persistent April SSTs for 1987, 1988, 1994, 1997, and 2002. Results from observed SST forcing simulations showed that only two models successfully predicted the sign of seasonal rainfall anomalies during the drought and excess years with one model reasonably predicting the magnitudes also (correlation coefficient=0.4) (Gadgil and Srinivasan 2011). The bias identified in simulations could be either due to irrational oversensitivity of models to ENSO or inability to simulate Equatorial Indian Ocean Oscillation (EQUINOO) or both (Gadgil and Srinivasan 2011, Ratna and Sikka 2011). Precipitation forecasts from Global Ensemble Forecast System's (GEFS) at a lead of 7-days for the period 1985–2010 have shown higher skill in precipitation forecasts during non-monsoon season (correlation=0.6) compared to monsoon season (correlation=0.5) though no significant improvement was observed after post-processing (Shah & Mishra, 2016). This low skill of monsoon forecasts was attributed to the inability of the model to simulate the intra-seasonal variability specifically active-break phases during monsoon.

2.4.2. Need for Coupled ocean-atmosphere GCMs

Multiple studies found that most of AGCMs fail to predict droughts, in general, ISMR variability with a reasonable skill (Gadgil *et al* 2005, Gadgil and Sajani 1998, Ratna *et al* 2011, Gadgil and Srinivasan 2011), although improvements have been seen in AGCM forecast. The actual predictability skill of AGCMs is much lower than the potential skill of 0.65 estimated by the "perfect model", which showed improvement when AGCMs were forced by simulated SST (Kumar *et al* 2005). Despite improvements from post-processing techniques, the performance of AGCMs is relatively poor as compared to coupled Ocean-Atmosphere models in predicting seasonal precipitation (correlation=0.2) (Kulkarni *et al* 2012, Mohanty *et al* 2019) because of misrepresentation of air-sea interactions over warm pool region and Indo-West Pacific Ocean; however, AGCMs forecast with better skill at lead 0 (forecast started in June for June–September rainfall) (Singh *et al* 2012a). These deficiencies of AGCMs and the ability of coupled models to better capture the intra-seasonal and interannual variability of ISMR endorse the need for coupled ocean-atmosphere models for monsoon prediction (Kumar *et al* 2005, Rajeevan *et al* 2012, Wang *et al* 2005a).

2.4.3. Meteorological droughts prediction using Coupled models

In general, the forecasts from AGCMs have improved globally and regionally over the last few decades (Li *et al* 2019, Song and Zhou 2014, Zhang *et al* 2018) but their predictability skill and use in operational mode is still a topic of discussion, particularly for monsoon regions (Kumar *et al* 2005, Ratna and Sikka 2011). Preethi *et al* (2010) used 7 coupled models from Development of European multi-model Ensemble System for Seasonal-to-interannual prediction (DEMETER) and reported a positive but weak predictability skill for monsoon forecasts at 1-months lead; however, multi-model ensemble (MME) performed better in 1980s but failed afterwards. MME of six-coupled models from ENSEMBLES were found to have higher skill compared to MME of DEMETER in forecasting ISMR, and efficiently simulated droughts of 1972, 1974, 1982, and excess year 1961, but failed to capture the recent decline in ENSO–monsoon relationship (Kumar *et al* 1999), which resulted in a reduction in actual skill from 0.3 for 1960-1979 to 0.1 for 1980-2005 (Rajeevan *et al* 2012). Comparing the skill of 6 GCMs (4 coupled and 2 AGCMs) in simulating ISMR at three different leads (0-month, 1-month, and 2-month), it was found that coupled models and AGCMs exhibit higher predictability at 1-month and 0-month lead, respectively, and the predictability skill decreases as lead time increase (Singh *et al* 2012a, Shrivastava *et al* 2018). Shrivastava *et al* (2018) considered 20 days ahead forecasts of rainfall from 44 ensemble members of Indian Institute of Tropical Meteorology

(IITM) climate forecast system and global forecast system models' over central India to predict 1-month SPI, 1-month SPEI, and PDSI. In their results they found that model based probabilistic predictions of drought occurrences (months with SPI<-1) were in good agreement with observation (Hit rate> false alarm rate; Skill coefficient>0.5). The predicted SPEI and PDSI also showed reasonable agreement with observations and efficiently captured 2002, 2009, and 2014 drought (Shrivastava et al 2018). In addition, they also noted that the raw ensemble members forecasts have large biases and, variance-based bias correction improves the ensemble mean drought forecasts resulting in high hit and smaller false alarm rates. The results from the comparison of monsoon season predicted SPI from 9 GCMs (3 AGCMs and 6 coupled GCMs) and IMD for the period 1982–2010 concluded that all models' predictability skill is low with maximum skill for GML and CFSv2 (correlation>0.54, index of agreement>0.7) at all India scale; however, none of the models predicted droughts effectively, for example, CFSv2 predicted the maximum, 3 out of 6 observed droughts (2002, 2000, 2009) (Acharya *et al* 2013b). Weighted mean MME technique showed noticeable improvement in the skill of SPI forecasts compared to arithmetic average MME and individual models. Jain *et al* (2019) were able to achieve a skill of about 0.6 at seasonal lead times using multi-model average of 8 prediction systems from Climate Historical Forecast System, which was found to improve by spatial averaging over a larger area because of extended spatial coherence of monsoon variability. An increase was noted in the better representation of mean state of the Indian monsoon, its variability, and predictability skill with higher-resolution CFSv2 model (T382) configuration ($\rho = 0.55$) compared to low-resolution configuration (T126) ($\rho = 0.49$) (Ramu *et al* 2016). Moreover, increased skill in high-resolution was attributed to the significant improvement in IOD–monsoon relationship (reduction in bias) and ENSO–monsoon teleconnection (strengthening of teleconnection), but both configurations failed to capture the correct phase of ISMR in 7 years (1985, 1989, 1990, 1991, 1992, 1993, and 1997) (Ramu *et al* 2016, 2017). In a recent study, Köhn-Reich and

Bürger (2019) found that the removal of the erroneous year (such as 1997) from the analysis could greatly improve the skill of forecasting. In addition, CFSv2, SEAS4, and multi-model ensemble realistically simulated droughts and excess years during the period 1982–2005. Consistent with previous studies multiple recent studies have highlighted that the errors/underestimation of precipitation during missing ENSO–monsoon link, for example, 1997 monsoon are due to the super-sensitivity of models to ENSO rather than IOD–ENSO relationship and mean rainfall bias (Jain *et al* 2019, Köhn-Reich and Bürger 2019). Multiple improvements were made in the CEFSv2 model equations and algorithm, for example, improvements in parameterization of convection, land surface processes, improved ocean model, improved cloud microphysics, and other improvements, have been useful in enhancing the model prediction skill (Ramu *et al* 2017, Srivastava *et al* 2017, Pillai *et al* 2018), and skill score (Pearson's correlation) improved from 0.55 to 0.67 (0.118 to 0.326) over extended central India defined (central India) region $[65° - 95°\mathrm{E}, 5° - 35°\mathrm{N}]([70° - 90°\mathrm{E}, 10° - 30°\mathrm{N}])$ (Pokhrel *et al* 2018). IMD, under the Monsoon Mission program, successfully predicted two consecutive monsoon droughts of 2014 and 2015 at 3-month lead using CFSv2-T382 model, which outperformed the IMD's operational forecasts (statistical model) in terms of forecast skill by about 0.18 (Rao *et al* 2019). However, (Srivastava *et al* 2020) proposed one month gain in the predictability of Indian rainfall by using burst initialization (i.e., perturbated initial conditions) in the atmospheric conditions. Ignoring the false alarms of 2006 and 2016, all major droughts during the period 2003–2017 were successfully simulated.

2.4.4. Prediction of Hydrological and Agricultural droughts

Predictions for soil moisture and runoff anomalies are simulated in a hydrological model driven by climate forecasts, and other land variables with the skill dependent on both climate forcing and initial hydrological conditions (IHC). The soil moisture and total runoff for India were successfully simulated at 7-day lead by running Variable

Infiltration Capacity (VIC) (Mishra *et al* 2014) model forced by raw and corrected GEFS forecasts with IHCs generated using observed IMD forcing on 14-February and 14-July each year (Shah & Mishra, 2016). The results highlighted the dominating role of IHCs in soil moisture forecast at 7-day lead time because of persistent high soil moisture compared to runoff simulations, where persistence of both soil moisture and hydrological variables are important. Droughts in non-monsoon season were predicted with a higher skill ($POD_{avg} \geq 0.7$) compared to monsoon ($POD_{avg} = 0.5$) but no significant improvement was observed in POD using bias-corrected forcing. The weekly drought prediction system based on soil moisture index (SMI) successfully reproduced the spatio-temporal structure of drought during 2002, 2004, 2005, and 2009 with some minor inconsistencies. Forecasts from CFSv2 and 4 high-resolution models from the Indian Institute of Tropical Meteorology (IITM) have been successfully used to stimulate agricultural and hydrological droughts at 45-day lead time (Shah *et al* 2017). Bias corrected IITM ensembles forcing and calibrated VIC model successfully reproduced the observed spatiotemporal pattern of soil moisture and runoff anomalies at 45-day lead with better skill (Critical Success Index (CSI)=0.71 for runoff and 0.67 for soil moisture) compared to raw IITM ensemble (CSI=0.63 for runoff and 0.6 for soil moisture) and CFSv2.

2.5. Challenges and future perspectives

From the above studies, it can be recognized that significant improvements have been made in ISMR prediction in the past few decades; there is, however, a large fraction of ISMR variability yet to be explained and, hence, a large scope for improvements in seasonal prediction of ISMR and droughts.

Charney and Shukla (1981) found that "predictability of second kind" may contribute to better prediction of Indian monsoon over large spatiotemporal scales but it should be noted that these simulations are highly unreliable for shorter spatiotemporal scales (Ratna *et al* 2011).

Although mean rainfall bias impacts the seasonal prediction skill (Goswami and Goswami 2017) but ENSO–monsoon relationship is more important for the seasonal predictability of Indian monsoon and is overestimated by most of the climate models resulting in erroneous predictions (Ratna and Sikka 2011, Köhn-Reich and Bürger 2019, Kumar et al 2005). Also, the IOD–monsoon relationship is not simulated correctly and is opposite to the observed relationship in some models (Kumar *et al* 2005). Hence, remaining skill ($\text{potential} - \text{actual}$) in predictability can be achieved only by improving the models' ability to capture the pacific SST of erroneous years like 1997, IOD–monsoon relationship, and Monsoon–El-Niño Modoki relationship efficiently by improving model parameterizations and representation of physical processes (Abhilash *et al* 2014a, Jain *et al* 2019, Kumar *et al* 2005, Ramu *et al* 2016, Vishnu *et al* 2019). Decadal predictions, those at 10 to 30-year time scale as per Smith *et al* (2007), are often full of uncertainty that mainly stems from internal variability and model variability, which are the spreads of the climate predictions of same model but with different initial conditions (different realizations of the same model) and predictions from different models (also known as inter-model uncertainty), respectively (Strobach and Bel 2017, Akhter *et al* 2018, Hingray and Saïd 2014). At a longer time scale, such as centennial projections, uncertainties linked to likelihood of future forcing are more important. Akhter *et al* (2018) found that the internal variability (defined as standard deviation of detrended variations or simply noise in simulations) accounts for about 70–80% of total uncertainty in precipitation projections and dominate the inter-model variability (defined as standard deviation of multi-model projections at a particular time) [20-30% of total uncertainty]. This contribution reduces to 60% and 50% by the end of the century under RCP 4.5 and RCP 8.5, respectively. They also noted higher model spread for changes in precipitation in 3 future periods (2006-35, 2036–65, 2066–95) under RCP 8.5 (~14%, 17%, 23%) compared to RCP 4.5 (13%, 15%, 20%) (Akhter *et al* 2018). In contrast to internal variability, which is inherent to models and can hardly be reduced by ensemble method, inter-model uncertainty can be reduced by weighing the model based on past performance and bias correction of models (Strobach and Bel 2017, Akhter *et al* 2018, Singh and AchutaRao 2019). Furthermore, GCMs operate at coarse resolution that limits their ability to capture and reproduce the finer scale processes at the regional and local scales (Shashikanth *et al* 2014, Singh *et al* 2019). Multiple statistical and dynamical downscaling approaches though help in obtaining high-resolution data introduce uncertainties in the projections (Dibike and Coulibaly 2005, Ghosh and Katkar 2012, Singh *et al* 2017).

2.5.1. Finer-scale spatial and temporal predictions

Some large-scale climatic oscillations are associated with rapid changes in SST and SLP anomalies, causing unprecedented changes in the ISMR at sub-seasonal scales (Borah *et al* 2020). Correlations of rapidly changing pressure and temperature anomalies over northern Asia with ISMR have grown significantly during the recent decades (Wang *et al* 2015, Capua *et al* 2019). Rapid changes in the Pacific SST anomalies during 2012 were related to the decrease of forecast skill in the model developed by Sahastrabuddhe *et al* (2019). Severe deficits of rainfall in any month of the summer may eventually result in a drought year, even when the rainfall received in the rest of the three months of the season is near-normal (Borah *et al* 2020). For improved droughts forecasts, it is imperative to understand the drivers of the sub-seasonal variability of summer rainfall. In this context, active-break predictions can be a valuable approach, especially for extreme breaks following a lower-than-normal preceding active period. Wang *et al* (2005b) suggest that the monsoon oscillation (active followed by break period and so on) are induced locally and the cycle continues due to large-scale upper-level convergence in the eastern Equatorial Indian Ocean (EIO) left by previous monsoon cycle end phase. This suggests that suppressed connection over EIO can be a precursor of break periods. With this knowledge, Ding and Wang (2009) used OLR over southern India, representing convection activity, and 200hPa heights, representing circulation anomalies, to predict extreme active and break periods of monsoon. It was shown that extreme break phases can be predicted at a high hit rate of 72% and false alarm rate of 62% at lead times 6–7 days. Borah *et al* (2013) developed a probabilistic model based on self-organizing maps to predict active and break phases. The model yielded a high hit rate of 70% and a small false alarm rate of 30% for 5-day lead time, and it is seen that short breaks (~5 days) are predicted more accurately than longer breaks at all the lead times ranging from 5 to 20 days. Some other important studies on active-break prediction are (Goswami and Xavier 2003, Abhilash *et al* 2014b, 2013).

As noted earlier, the spatial heterogeneity of ISMR and its correlations with climatic teleconnections is one of the important factors responsible for low-skill forecasts. Owing to this, many recent studies have performed analysis at regional scale considering a set of homogenous regions in India (Dutta and Maity 2020a, 2018, Kashid and Maity 2012, Saha *et al* 2017, Rajeevan *et al* 2004). However, a finer-scale analysis, without predefining homogenous regions based only on the regional climate, can be more valuable in finding the precursor regions and improving the forecasts.

The higher resolution CFSV2 T382 (~38 km) performed better in representing the monsoon intra-seasonal oscillation (MISO) and also reduced the climatological bias in June–September precipitation compared to a lower resolution CFSv2 T126 (~100 km) (Sahai *et al* 2015). Multiple studies have noted improvements in prediction skill by using regional climate models (either stand-alone or coupled) (Mishra *et al* 2021, Di Sante *et al* 2019, Singh *et al* 2019), and downscaled GCMs (Sinha *et al* 2013, Singh *et al* 2017). Shah et al (2017) noted a negative correlation, high mean absolute error, and small critical success index (defined as the ratio of hits and sum of hits, miss, and false events; CSI<0.2) between the observations and model forecasted 7-day accumulated rainfall over the hilly and complex terrains of Himalayan foothills. The skill reduced with the increase in forecast accumulation time (15-days, 30-days, and 45-days). Similar results were found by Sridevi *et al* (2020) with GFS model at T574 and T1534 resolution (Hit score ≤ 60), though the skill was better with T1534 resolution. The critical success index of predicting droughts based on SPI (SPI<-0.5) and SSI (SSI<-0.5) also highlighted the lower skill over hilly terrains (CSI$\leq$0.1) compared to plains (CSI$\geq$0.3) (Shah and Mishra 2015). Other important studies featuring the impact of topography on prediction skills include (Singh *et al* 2012b, Sinha *et al* 2013, Mandal *et al* 2007).

2.5.2. Non-stationarity and climatic interactions

It has been observed that the influence of large-scale teleconnections is not consistent on the variability of ISMR; for example, a majority of droughts have occurred during El Niño periods, many El Niño years, however, have resulted in near-normal ISMR (Kumar *et al* 2006, Surendran *et al* 2015). Conversely, the IMD predictions of normal ISMR for severe drought years during moderate El Niño events of 2002 and 2004 questioned our understanding and modelling of Pacific SST effects on ISMR (Ashok *et al* 2007a, Gadgil *et al* 2002, 2005). Depending on the background large-scale low-frequency variations in the climate, ISMR interaction with teleconnections may appear contrasting; for example, the strong El Niño of 1997 did not result in severe deficits over India (Kumar *et al* 2006). The SST anomaly pattern in the Pacific, for example, fluctuates the precursor regions for ISMR (Capua *et al* 2019). Further, recent studies have shown that the interaction of ENSO with the Indian Summer monsoon is not stationary (Azad and Rajeevan 2016, Kumar *et al* 1999) and that, due to global warming, the warm eastern Pacific precursor of droughts (EP-El Niño) has shifted to the central Pacific (CP-El Niño) (Kumar *et al* 2006, Lee and McPhaden 2010). Wang *et al* (2015) found significant correlations of the central Pacific SST anomalies with ISMR in recent decades and suggested a central Pacific dipole region as one of their two new precursors for predicting ISMR.

A dynamic linear regression model was proposed by Maity and Kumar (2006) to predict ISMR at a lead time of one month using ENSO and EQUINOO, in which the model parameters are updated through

Bayesian posterior updating using all the information (in terms of observations) available up to the time of forecast. This captured the non-stationary relationship between ISMR variability and the two indices. In general, the model performed reasonably over the prediction period of 1986 to 2003; droughts, however, were underestimated generally. Recent works (Dutta and Maity 2018, 2020a, 2020b) suggest a more rigorous way to incorporate non-stationarity in predicting droughts. In Dutta and Maity (2018), a time-varying SVR and Copula-based model are proposed for ISMR prediction, in which the model inputs change after every τ years (τ is roughly between 3 to 5 years and is estimated through optimization of forecast skill). Accordingly, calibration and validation period continuously slide by τ years. Input covariates (among various lags of ENSO and EQUINOO) for each period were obtained through Graphical Modelling that allows identifying conditionally independent covariates that are directly associated with the ISMR. The results showed that the time-varying model predicted summer droughts more accurately than the stationary model, in which the association between ISMR and ENSO and EQUINOO was kept stationary. The results also suggested that the 90th percentile prediction intervals covered almost all droughts. The same approach was applied at regional scale over five homogenous regions of India for the prediction of 5-month lead ISMR (Dutta and Maity 2020a). In this case, however, many other large-scale climatic indices were searched for the best model inputs in different sliding calibration periods. However, the performance of regional models (for example, in terms of RMSE) did not improve over the pan-India ISMR models developed in Dutta and Maity (2018), and many of the droughts in different regions were under predicted. (i.e., rainfall anomaly predicted was smaller than observed anomaly). The approach was further adopted in Dutta and Maity (2020b) for one-month ahead monthly streamflow prediction of Bhadra Dam Basin in Karnataka. The results showed that the time-varying models predicted streamflow more accurately than the time-invariant models for the testing period of 2001 to 2003. However, the models seem to generally overestimate the low-flows, and severe low-flows were generally out of the 80th percentile prediction interval. In addition to non-stationary nature of natural climate forcings, they also interact with each other through their causal pathways such as interbasin interactions (Cai et al 2019), tropical-extratropical interactions and coupled ocean-atmosphere interactions. These causal pathways are not always in phase and hence could either amplify or mute the remote influence of the forcing (Cai et al 2019). Based on these observations, it is crucial to explore the influence of these interbasin interactions on ISMR at seasonal and sub-seasonal and also evaluate their potential in improving the forecasting skill ISMR and droughts in India

Clearly, these work1s suggest that the operational statistical models need to be updated to embrace the changes associated with global warming. An understanding of the changes to climatic interactions with ISMR will help in identifying new, non-stationary precursors required to improve the forecast skill in the coming decades.

2.5.3. Recent advances in drought science

As mentioned above, sudden transitions in the climate state can reverse the direction of ISMR within weeks, from positive anomaly to negative anomaly. Sudden onset and intensification of droughts, termed as *flash droughts*, have received significant attention recently, owing to their large societal impacts mainly attributed to our lack of preparedness in managing these events (Otkin *et al* 2018, Pendergrass *et al* 2020). The mechanisms of flash drought intensification relies on deficits of rainfall and above-average temperatures and result in feedbacks that potentially enhance drought intensity further (Miralles *et al* 2019, Herrera-Estrada *et al* 2019, Schumacher *et al* 2019, 2020). Understanding of flash drought evolution, feedback mechanisms involved, and their incorporation in sub-seasonal drought forecasting systems are important research areas for advancing drought science in India.

Winter precipitation and temperature in snow-dominated mountainous regions control water availability in the low-lying downstream watersheds in later seasons–lack of precipitation or higher temperatures during winter can severely reduce the water security in the downstream regions in ensuing spring and summer. Due to the alterations of precipitation and temperature regimes in a warmer climate, the concept of *snow drought,* defined as lack of winter precipitation and/or higher temperatures in snow-dominated regions, has recently emerged (Harpold *et al* 2017, Huning and AghaKouchak 2020). Many basins in India, including the Indus and Ganga, are dominated by snow and glaciers in the Himalayas; serious considerations should be given to the global warming-driven changes in snow-droughts and the resulting water availability in the basins.

B. Understanding heatwaves

Heatwaves are defined as the period of abnormally high temperatures that last few days to weeks. Over the recent two decades a plethora of indices have been developed to define and identify the heatwaves. All these indices quantify heatwaves in terms of some characteristics of heatwaves which include heatwave day frequency (HWF), Number of heatwaves (HWN), heatwave amplitude (HWA), heatwave duration (HWD), and average heatwave magnitude (HWM).

1. HWF is defined as the sum of the heatwave days –there or more consecutive days that satisfy the definition of heatwave– per year.
2. HWD is defined as the duration (in days) of the longest heatwave event in a year.
3. HWA is defined as the peak daily intensity (or peak) of the hottest heatwave event in a year.
4. HWN is defined as the number of heatwave events per year i.e., heatwave frequency.
5. HWM is defined as the average daily intensity of all the heatwaves events in a year.

Based on different heatwave definitions, multiple studies have estimated these aspects of heatwaves both at regional and global scale. However, these aspects have been measured from daily and complete data i.e., no missing data.

In the Himalayas regions, where the topography is really complex and the observations of temperature are limited or have lot of missing data, heatwave analysis has not been performed extensively. The gridded observations or reanalysis data available over Himalayas are not accurate and are biased (Kanda *et al* 2020, Mishra 2015). In addition, the grid resolution of these datasets is coarse to capture the spatial variability in temperature over these complex terrains. Moreover, the satellite data, which is available at a finer resolution of 5km×5km, could capture the spatial variability of temperature over these terrains.

As a part of this thesis, to understand the concept and characteristics of heatwaves, a case study of changes in heatwaves (particularly in HWF) and maximum temperature over a smaller region in Himalayas (the Kashmir Valley) was performed. Satellite data, which potentially could be the best dataset for heatwave analysis in Himalayas, also had lot of missing data. So, in this chapter 2B, an algorithm is developed to estimate the heatwave characteristics (HWF) over himalayan complex terrain despite of having missing temperature data.

❖ Heatwave analysis over complex terrains of Himalayas

*After: **Waqar ul Hassan**, Munir Ahmad Nayak, Rosa Vellosa Lyngwa: Recent changes in heatwaves and maximum temperatures over a complex terrain in the Himalayas; (2021) Science of The Total Environment 794, 148706; https://doi.org/10.1016/j.scitotenv.2021.148706*

Abstract

The temperature response to anthropogenic global warming and forest cover changes is dependent on regional climatic characteristics. It is challenging to segregate the impacts of two anthropogenic changes on local temperatures and heatwaves over complex mountainous regions. Here we present estimates of regional and local heat stress responses to the recent global climate change and local forest cover loss in complex terrain in the Himalayas using a satellite-based high-resolution land-surface temperature dataset. We find large-scale decreasing trends in the observed frequency of heatwaves and heat days, and localized increases in urbanized and high-elevation regions. Our results show large-scale significant decreasing trends in annual maximum and mean surface temperatures over the period 2003−2019. In locations that have witnessed large-scale forest losses, the declines in the surface temperatures were steeper compared to no-loss regions.

We develop a regional multiple linear regression model to estimate the regional and local temperature responses to global climate change and to segregate them from the response to forest cover losses. Our model estimates a regional decrease of about 2.0 $°C$ in annual maximum temperature over the recent 2003–2019 period, which is locally modulated by the extent of urbanization, forest cover, and elevation. At the locations of intense deforestation, our model

successfully predicts a steeper decrease in maximum surface temperature, and estimates the temperature response due to forest loss, after controlling for elevation and initial forecast cover. The local cooling effect due to deforestation was reaffirmed by comparing the regions with contrasting forest cover losses. The results suggest that forest clearing amplifies the anthropogenic climate change over the region.

2.6. Background

Recent decades have witnessed changing frequency of extreme weather and hydrologic events throughout the globe (Yin *et al* 2018, Rummukainen 2012, Meehl and Tebaldi 2004), with growing concerns of temperature extremes, e. g., heatwaves and associated heat stress, in many regions (Chapman *et al* 2019, Perkins *et al* 2012). Significant increases in heatwave frequency and intensity are witnessed in recent decades in Europe, Mediterranean, California, Southern Africa, and India etc. (Hulley *et al* 2020, Christidis *et al* 2015, Russo *et al* 2016, Perkins-Kirkpatrick and Lewis 2020, Rohini *et al* 2016, Mishra *et al* 2017). This increase in heatwaves in India made more population vulnerable to heatwave and heat stress impacts resulting in more premature mortality and higher heat-related health issues, mainly in rural areas (Mishra *et al* 2017, Rohini *et al* 2016, Murari *et al* 2015, Murari and Ghosh 2019). The distribution of the changes in extremes, however, is not spatially homogenous with regions observing decreases in heat stresses, such as southeastern United States (Grotjahn and Huynh 2018). Many of these changes are shown to have happened concurrently with changes in diurnal variations in temperatures (Kueh *et al* 2017).

Indeed, pumping large quantities of CO_2 into the atmosphere has led to significant non-stationary changes in the global climate (Zickfeld *et al* 2012, Davis *et al* 2010). Modulating the impact of anthropogenic global warming are the regional anthropogenic changes to land use land cover that have led to unimaginable changes in the regional and local climates. The complex interactions and feedbacks among the local land cover changes and global warming have made it challenging to predict changes and trends in local temperatures. Major difficulties are in isolating the temperature response of deforestation from that of regional changes due to global warming. Temperature response to forest clearing is dependent on many interacting geo-biophysical factors.

2.6.1. Factors affecting response to deforestation

Globally, forests act as a large-scale sink for carbon, hence are the main inhibitors of global warming (Luyssaert *et al* 2008, Fernández-Martínez *et al* 2019). In general, the regional cooling effect of forests is location-dependent and happens mainly through evapotranspiration and heat transfer to the atmosphere through turbulent mixing. Temperature response to deforestation is complex. Deforestation generally leads to following two major changes that regulate land-atmosphere feedback. The first major change is lowering of turbulent mixing level, which reduces the exchange of surface heat, when available, with the atmosphere. Its effect, however, is dependent on the extent of deforestation and land use following deforestation. With large-scale deforestation, sensible heat increases on bare soils and small vegetation, resulting in increases in local temperatures. However, even moderate shifts to water-intensive agriculture, such as paddy, are expected to result in discernable decreases in temperature due to increased evaporative cooling (Mishra *et al* 2020, Nayak and Mandal 2019a). The second major change due to deforestation is change in albedo. For bare-dry soils and green vegetation, increased albedo can be expected to decrease the temperature, whereas, for wet soils, changes may not be apparent (Snyder *et al* 2004). Again, water-intensive land use can store more heat energy due to higher absorption of sunlight, increasing evaporative cooling and possibilities of decreases in temperature (Bonan 2001, Nayak and Mandal 2019b). In cold regions, increased snow-cover area due to forest clearing results in increased albedo and may decrease the temperature. All these potential changes in surface temperature due to deforestation are dependent on solar irradiance; hence the magnitude of changes, even to the same type of cover change after deforestation, is latitude and season dependent.

Several recent studies have observed that changes in the forest cover play an important role in local temperature variability of the region (Wang *et al* 2019a, Alkama and Cescatti 2016a, Nayak *et al* 2021). Over the last two decades, physics-based paired models (Bala *et al* 2007, Davin and Noblet- 2010, Lean and Warrilow 1989, Snyder *et al* 2004) and data-driven model (Lee *et al* 2011, Li *et al* 2015a, Zhang *et al* 2014a) have been widely used to understand the bio-physical effects of land use land cover changes (deforestation and afforestation). Moreover, most of the studies have emphasized on the idealized case of large-scale forest cover changes, and impacts of climate (Bala *et al* 2007, Lee *et al* 2011, Li *et al* 2015a) but a few have quantified the effect of existing forest cover changes on local climate (Lee *et al* 2011, Li *et al* 2016). In a recent study, Alkama and Cescatti (2016) attempted to separate the global climate signal and local climate signals due to forest cover changes by comparing the temperature changes at two locations within 50 km but with contrasting forest cover changes (i. e., one location has significant forest loss and the other with small losses (<2%)) (see Alkama and Cescatti (2016) for more details). However, they did not control for the effects of differences in altitude and forest cover, which have a significant impact on local climate particularly in the regions with complex terrains and steep slopes, for example, Himalaya, where our study area lies.

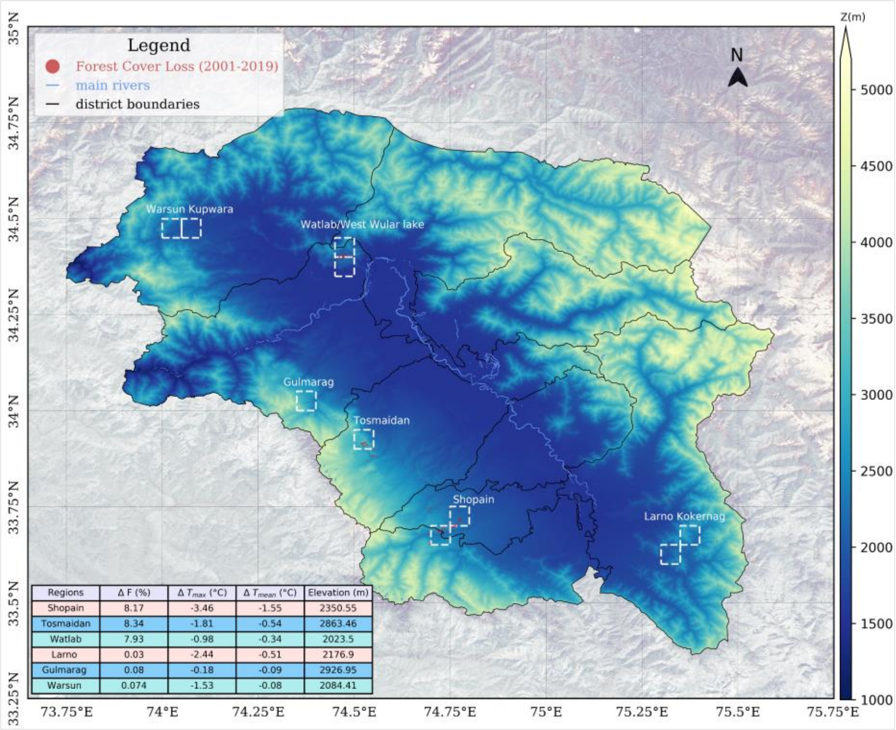

Figure 2.2. *Map of the study area with districts (black colored boundary lines) in Kashmir valley. The elevation (m) for the area is shaded as shown by the colorbar on the right. CartoDEM Version 3 R1 from Bhuvan, India, is used that is openly accessible at https://bhuvan-app3.nrsc.gov.in/data/download/index.php. Locations of selected regions for analysis are highlighted in white (dashed) colored boxes (of* $0.05^\circ \times 0.05^\circ$*) with their corresponding names. Details of each region are shown in the Table on the left bottom corner.* ΔF *gives the fraction of forest cover loss from 2001–2019;* ΔT_{max} *and* ΔT_{mean} *are the changes in annual maximum and mean temperatures* $(^\circ C)$ *for the period 2003 to 2019; the elevation (m) represents the average elevation for each region.*

2.6.2. Recent literature over the study region

This study focuses on the Kashmir valley, a highly complex topographic region in Himalayas located between $33.25°N$ to $35°N$ and $73.65°E$ to $75.75°E$ (Figure 2.2). There are only a few recent studies that have analyzed changes in temperature over the study area. Shafiq *et al* (2019a) observed increases in annual maximum, mean, and minimum temperatures for the recent period of 1980–2014, with a sudden jump in 1997 that resulted increasing trend during the period. For the period 2000–2016, Shafiq *et al* (2019b) noted decreasing trend in the annual mean temperature and maximum temperature at six meteorological stations. On comparing the Land Surface Temperature with air surface temperature Rafiq *et al* (2016) observed a negative and positive trend in summer and winter maximum temperature, respectively, in both datasets. Zaz *et al* (2019) used monthly averages of daily maximum and minimum temperatures and observed increasing trends in annual maximum and minimum temperatures ranging from $0.6°C$ to $1.3\ °C$ over a period of 37 years from 1980–2016. These studies also note a significant decrease in annual precipitation at all the six stations.

In all the above studies, the data are aggregated to monthly scales for trend analysis. However, monthly and spatially sparse data may not be representative of the annual maximum or mean of the local daily temperature distribution, and such analysis may mask important local changes in temperatures and their spatial variation.

2.6.3. Objectives

In this study, we aim to evaluate the recent changes in heatwaves and temperature in a highly complex topographic region using high-resolution remote sensing-based land surface temperature and forest cover products. We show that the daily gridded data provide important insights into the spatial variability and local dependence of changes in temperatures and heatwaves, which is not apparent in sparse monthly-aggregated station data. In this study, we hypothesize that climate signal in response to local scale forest cover changes, which may amplify or dampen the global climate signal, significantly contribute to the local climate change. We propose a novel regression-based model that can isolate temperature changes due to local forest cover changes and those due to regional changes under global warming, after controlling for local topographic characteristics.

2.6.4. Study area

Kashmir valley consists of 10 districts (outlined in Figure 2.2) with an overall geographic area of about 15,960Km^2. The valley is enclosed within the geologically younger mountains of the Himalayan belt, Pir-Panjal range on the west and Greater Himalayas on other sides, (Raina 2002), and the altitude (elevation above mean sea level) varies between $1000\ m$ in the center of valley (plain areas) to $5250\ m$ in the mountainous areas mainly in the north-eastern part of Kashmir valley. The mountain ranges act as the buffer (barrier) to summer monsoon circulation that originates from the Indian Ocean and to cold but moisture-laded air masses coming from eastern Siberia and the Mediterranean Sea (colloquially known as the western disturbances). However, western disturbances are less obstructed by the lower elevation mountains of the Himalayas as they cross the valley from west or north-west of greater Himalayas (Bhat *et al* 2017). The climatology and interannual variations in the climate of Kashmir valley are distinct compared to surrounding regions, including India, Azad Kashmir, Ladakh, and Jammu (Shafiq *et al* 2019a). The precipitation over Kashmir follows a bimodal distribution with peaks in mid-February–April i.e., winter/spring precipitation, and in July–August, i.e., summer precipitation. Temperature achieves its minimum and maximum in December–January and July–August respectively (Supplementary Material Figure S2.1). The mean annual temperatures in Kashmir valley vary between $7.29°C - 19.27°C$ with annual average precipitation of 840 mm. The daily minimum temperatures can drop to $-10°C$ in winters and maximum temperatures can shoot up to $38°C$ in summers (Figure S2.1), and their spatial variation is mainly governed by altitude, insolation, precipitation, and forest cover (Husain 1987, Raina 2002).

The forest in Kashmir ranges from subtropical to temperate to alpine (Government of Jammu and Kashmir Department of Forest and India Water Portal, 2011). The main lifeline of the region is the River Jhelum, which drains through the center of the valley and deposits important nutrients to increase the fertility of the soil in the region. The vegetation in the region varies greatly with altitude; agriculture and horticulture dominate the lower elevations below $2000m$, while at moderate altitudes up to $2800m$, dense evergreen coniferous forests are more dominant. Regions at elevations in the range of $2800m$ and $3800m$ are covered with alpine pastures and scrubland, and those above $3800m$ elevation are devoid of tress and are mostly rocky, glaciers, and extensive snow covers (Dar and Khuroo 2020). Most vegetation do not flourish when soil temperatures are below 5˚C (Rabenhorst 2005), and this can be observed in Kashmir Valley when we compare the elevation data in Figure 2.2 and the forest cover in Figures S2.2 and S2.13. Considering this forest type and elevation dependence, we divide the region into three categories; lower elevation ($<2000\,m$), Moderate elevations (2000–2800 m), and higher elevation ($>2800\,m$) and understand some of our results later according to this classification.

2.7. Data and Methods

2.7.1. Temperature observations

We used the daily observations of maximum temperature of a meteorological station from the Global Historical Climate Network (GHCN) over the Kashmir valley (https://www.ncdc.noaa.gov/ghcnd-data-access; Menne *et al* 2012, Peterson and Vose 1997)). GHCN has precipitation and temperature data from a total of 30 meteorological stations over Kashmir, and only one station, located in Srinagar city, has long-term consistent daily maximum temperatures at 2m height for the last 20 years. The data at Srinagar station was further scrutinized for missing days during 2000−2019, and it was found that more than 330 days of observations were available each year up to 2015, and less than 15 days of observations were available afterwards, therefore in this study, we have used GHCN temperature data for the period 2000–2015.

2.7.2. Satellite-based temperature observations

The Moderate Resolution Imaging Spectroradiometer (MODIS) provides multiple products of land surface temperature (LST) with different spatial and temporal resolutions and retrieval times. MODIS sensors are onboarded on two helio-synchronous, near-polar satellites, the Aqua and the Terra (Justice *et al* 2002). The equatorial crossing local times of Aqua satellite are 13:30 (south to north) and 01:30 (north to south), whereas Terra satellite crosses the equator at 10:30 (south to north) and 22:30 (north to south) local time. Both satellites provide two readings for a day, one daytime LST and one nighttime LST. Here we used daytime LST observations from Aqua MODIS, as the LST values at 1:30 pm local time act as the best proxy for daily maximum LST for the location (Crosson *et al* 2012, Sharifnezhadazizi *et al* 2019, Sims *et al* 2008). Among the multiple products of MODIS Aqua LST, we selected a cloud-free daily LST product–MYD11C1 Collection 6 (Wan, *et al.*, 2015) from January 2003 to December 2019. Several studies have highlighted the improved accuracy and performance of Collection 6 compared to predecessor Collection 5 and other earlier products (Duan *et al* 2019, Prakash *et al* 2018), which are mainly attributed to the improvements in the retrieval algorithm (Duan *et al* 2019, Wan 2008). MODIS MYD11C1 product is available globally at a high spatial resolution of $0.05° \times 0.05°$, roughly $5.6\ km \times 5.6\ km$ at the equator. This dataset, maintained by NASA (National Aeronautics and Space Administration), contains LST observations of day and night, their quality control indicators, viewing times, viewing angles, and other emissivity observations, and is openly available at (https://lpdaac.usgs.gov/products/myd11c1v006/). The viewing times over our study area were in between 1:30 pm and 2:30 pm local time.

2.7.3. Forest Cover Data

Forest cover data and their changes over time are needed at a high spatial resolution to understand and evaluate the local changes in land use due to human activities and evaluate their impacts on the local temperature extremes. For this purpose, we used the high-resolution $30m \times 30m$ forest cover, forest cover loss, and forest cover gain data from the Global Forest Change Datasets (Version 1.7) derived from global Landsat imageries by Hansen *et al*., (2013). Forest in the dataset is defined as tree cover with a minimum height of 5m, without distinguishing among the primary or non-primary forest, commercial forests, pulp plantations, oil palms, eucalyptus, etc., and have together been considered here as land cover (Hansen *et al* 2014). Each $30m \times 30m$ Landsat pixel scale contains forest cover as percent of area in the pixel for year 2000, annual forest cover loss from 2000–2019, and forest cover gain is available as the total gain for 12 years from 2000–

2012 only. Forest cover loss in a Landsat gridcell ($30m \times 30m$) is defined as the complete removal of forest canopy from the gridcell, and the gain is defined as the transition to forest from a non-forested area.

Landsat 7 Enhanced Thematic Mapper Plus (ETM+) sequences are used for the period 2001–2012 in Version 1.1 (Hansen *et al*., 2013) and Landsat 8 Operational Land Imager (OLI) from 2013–2019 for forest cover loss maps in the updated Version 1.7 (Global Forest Change (earthenginepartners.appspot.com)). Hansen *et al*., (2013) classified forest cover, forest cover losses, and forest cover gain using decision tree generated from a comprehensive set of training data and Landsat imageries in Google Earth Engine (Gorelick *et al* 2017).

Notice that the satellite-based forest cover and temperature data are of different lengths and spatial resolutions, hence we need upscaling of forest cover data to LST resolution for some of our analysis.

2.7.4. Heatwaves and heat days

Climate change has resulted in significant changes in heatwaves in different regions of the globe (Fischer and Schär 2010, Perkins-Kirkpatrick and Lewis 2020, Schär *et al* 2004). A heatwave is defined when a heatwave index (usually computed with temperature or a combination of temperature and relative humidity) is greater than a certain threshold for three or more consecutive days. While heat stress is defined as the level of discomfort experienced due to exposure to extreme heat. Heatwaves usually measure the atmosphere-related heat stress rather than actual heat stress perceived by humans. When heatwave is estimated using both temperature and relative humidity, it provides better measures of discomfort and physiological stress (heat stress) experienced by humans than pure temperature-based indices (Mishra *et al* 2017). We note, however, some studies have successfully used pure temperature indices to explore the heat stress risk in India and South Asia (Mishra *et al* 2017, Im *et al* 2017b). In this study, we use daytime LST as the heat stress variable and daily varying 90th percentile of LST as the threshold, which is computed based on a 15-day window centered on the calendar day; for example, the 90th percentile threshold for calendar day 8th June is computed as the 90th percentile (T_{90}) of LST values from 1 June to 15 June of all years (i.e., sample size of the distribution = 15 days$\times$ no. of years). The calculation of heatwaves requires continuous daily temperature with no missing data. The gridded LST data from MODIS have many missing days (on an average of 125 days and 27 days annually and during summers (JJA), respectively), using which results from heatwaves analysis can be ambiguous and may provide misleading statistics about the changes in them. For LST data here, as a proxy to heatwaves, we have considered daily based "*heat days*", which are expected to provide better estimates of changes in heat stresses than the heatwaves obtained from missing data. We understand that the results from heat day analysis will not perfectly conform with heatwave observations, but with the given LST data, heat days appear to be the best possible representations of heatwaves.

There are multiple approaches to defining a heat day based on mean, maximum, minimum temperature; some are based on a fixed threshold (for example, a threshold of $35°C$ without considering the climatology of the region) others are percentile-based (for example, 90th percentile computed from data). Since day-time MODIS LST can be used as the proxy to maximum daily air temperature (Good *et al* 2017), we adopted a heat day definition based on moving threshold of 90th percentile of daily maximum temperature distribution introduced by Perkins and Alexander, (2013). With this, we define a day as "heat day" when the LST for the day is greater than the 90th percentile of daily maximum LST (see Figure S2.3 for 90th percentiles of six selected regions) of the calendar day. Adopting the moving window accounts for temporal variations in temperature and provides a reasonable sample size for threshold estimation.

Since we are mainly interested in changes in the frequency of temperature extremes and heat days, we use heat days as our main metric to represent heat stress and to overcome the uncertainty and ambiguity in the annual frequency of heatwaves due to missing data. At each

MODIS LST grid cell, we first compute the ratio of number of heat days to total number of days for which data are available for each year and then multiply the ratio by total number of days in that year (i.e., 365 for non-leap year and 366 for leap year) (Equations 2.2 and 2.3). This will be an estimate of the annual frequency of heat days. An assumption is made here that the missing data at each grid cell are uniformly distributed over the study period (among the years), which is validated at the 10 grid cells covering the 6 selected regions (figure not shown).

$$Heatday\ ratio\ for\ i^{th}\ year\ = \frac{No.of\ heatdays\ in\ i^{th}\ year}{No.of\ days\ with\ LST\ observations\ in\ the\ i^{th}\ year} \quad [2.2]$$

$$Annual\ heatdays\ in\ i^{th}\ year = Heatday\ ratio\ for\ i^{th}\ year \times 365 \quad [2.3]$$

Temporal changes in heat days were estimated as the slopes β of simple linear regressions of annual frequency of heat days with time (year) at each grid cell, and Pearson's correlation coefficient (ρ) between the annual frequency of GHCN and LST datasets is computed as an estimate of degree of agreement. The slope and correlation values were tested for statistical significance at a 5% significance level. The hypothesis for slope and correlations can be stated mathematically as given in Equations 2.4 and 2.5, respectively.

$$Linear\ regession;\ \ H_0: \beta = 0;\ \ H_1: \beta \neq 0 \quad [2.4]$$

$$Correlation;\ H_0: \rho = 0;\ \ H_1: \rho \neq 0 \quad [2.5]$$

where H_0 and H_1 are the null and alternatives, respectively

Further, the six selected regions highlighted in Figure 2.2 (discussed in the next section) were investigated for comparisons of changes between regions that observed forest cover loss and those that did not observe any significant losses. For the regions with two grid cells, such as Shopian, we used the averaged time series (average of the two grid cells) of LST for heat days calculations. We also note that when

LST observation for one of the two grid cells was missing for any day, the LST for the region on that day was taken as the LST of the second grid cell alone. The change in the frequency of heat days over the 17 years from 2003 to 2019 was defined and computed as the product of trend (slope of linear regression) and duration (17 years). Similarly, the trends and changes in the annual frequency of heat days are estimated for GHCN observations for the available period 2003–2015.

2.7.5. Forest cover losses

For our analysis, we have selected three regions, Shopian, Tosmaidan and Watlab/West Wular Lake in Kashmir valley, where significant forest cover losses were observed over the period 2001–2019 (shown in Figure 2.2, highlighted in white dashed boxes), to demonstrate the impact of losses in forest cover on maximum LST. These regions are bounded by MODIS grid cells of size $0.05^\circ \times 0.05^\circ$ ($\sim 5.6\ km \times 5.6\ km$), to make the results comparable with LST data. Two grid cells were considered for regions Shopian and Watlab (Figure 2.2) as major forest cover losses were observed in multiple surrounding areas, and one grid cell was considered for Tosmaidan. Additionally, three regions with similar number of grid cells were carefully selected, Larno Kokernag, Gulmarag and Warsun Kupwara (shown in Figure 2.2), that do not have appreciable forest cover losses. The stable (no forest loss) regions will be used for comparison with the above forest-loss regions. The two sets (in total six regions) were selected in consideration of matching elevations, initial forest cover fractions (i.e., in the year 2000), low urban density, no glacier cover, and the latitudes (Alkama and Cescatti 2016a), so that meaningful comparisons for changes in LST can be obtained. It is usually unclear how forest cover changes at local scale impact the local temperature due to inter-connected relationships with other biophysical processes (such as evapotranspiration and albedo) (Davin and Noblet 2010, Lee *et al* 2011). The high spatial heterogeneity of biophysical responses can result in an increase or decrease of LST as mentioned in the Introduction section (Li *et al* 2015a).

The fractional forest cover losses for each of the six selected regions (shown as percentage in Figure 2.2, table) was computed as the average fractional forest cover loss over all the grids in the region, where fractional forest cover loss in each grid was computed as the ratio of forest cover loss (total forest cover loss during 2000–2019) to the initial forest cover in the year 2000 (Equation 2.6). If within a selected region forest cover was lost at multiple pixels, the forest cover of reference percent tree cover (2000) at the corresponding pixels were entirely removed, if no appreciable forest gain offsets it.

$$\Delta F\ \% = \frac{Forest\ cover\ (area) loss\ from\ 2000\ to\ 2019}{Total\ forest\ cover\ (area) in\ 2000} \times 100\% \quad [2.6]$$

ΔF % gives the percent forest cover lost in each of the six regions as compared to the forest cover in those regions initially in the year 2000. The forest cover in 2000 and 2019 upscaled to $0.05° \times 0.05$ resolution are shown in Figure S2.2 (a) and (b) as the percent forest cover per grid cell (i.e., 100 × ratio of forest cover area to the total area of the pixel).

2.7.6. Temperature changes and regional regression model

The changes in maximum and mean LST for the period (2003–2019) were estimated as the slope of the temperature v/s year linear regression line, (in $\text{°C}/year$), multiplied by the total number of years in the study period (17 years). As mentioned in the Introduction section, it is difficult to accurately segregate the local signal in temperature change due to forest cover change without considering the background climate and bio-geological features (such as vegetation and topography) of the region (Pitman *et al* 2011). Here we provide a novel methodology to estimate and segregate the individual effects of forest cover loss and global climate change on local temperature change. A multiple linear regional regression (MLRR) model is developed to model the changes in annual maximum LST (ΔT_{max} ($°C$) hereafter, computed above) with the forest cover loss, elevation, and forest cover. The regional regression model used here has an inherent assumption of independent predictors, and spatial independence within each predictor. A strong non-linear relationship was noted between elevation and forest cover (Figure S2.4), i.e., forest cover is the highest for moderate elevations of about 2500m and declines for both higher and lower elevations. The inter-dependence between forest and elevation suggests the introduction of an additional interaction term (between elevation and forest cover) in the regression model and the modified model equation is given below in Equation 2.7. The spatial correlation is ignored in the present work and is hoped to be considered in our future works.

$$\Delta T_{max} = \alpha + \beta_{\Delta F}\Delta F + \beta_Z Z + \beta_{Fc} FC + \beta_{Z*FC} \times Z * FC + \epsilon \qquad [2.7]$$

where ΔF, Z, and FC are forest cover loss (m^2), elevation (m) and forest cover (m^2), respectively. α is intercept and ϵ is the random normally distributed error term; $\beta_{\Delta F}$, β_{Z}, and β_{FC} are the main effects corresponding to forest cover loss, elevation, and forest cover, respectively. β_{Z*FC} is the interaction effect. The main effect is the change in predictand (say ΔT_{max}) due to unit change in one predictor (say Z) while keeping others constant, and the interaction effect is change in predictand due to change in the predictor (Z) that also depends on another predictor (FC). We also assessed the model for multicollinearity by computing the variance inflation factor (VIF), and the results showed severe multicollinearity for forest cover and the interaction term, which is avoided by standardizing the predictor variables (Marquardt 1980). Standardizing of predictors not only helps in removing the multicollinearity but also in making the coefficients more interpretable, without changing the coefficient of determination R^2 value and predictions.

The partitioning of ΔT_{max} between the regional impact of global climate change and local forest cover losses is achieved by modeling changes in annual maximum LST (ΔT_{max}) in two different scenarios using MLRR: in the first scenario, we predicted ΔT_{max} by running the model using the observed elevation, forest cover of the year 2000, and forest cover changes during 2000 and 2019 in each grid cell. These model predictions are expected to estimate the total changes in T_{max} that is due to the combined regional impact of global climate change and local forest cover changes. In the second scenario, the model was run using the observed elevation and forest cover of each grid cell but fixing forest cover changes, ΔF = 0m^2, i.e., the model will simulate the changes in T_{max} for conditions when there is no change in forest cover. Therefore, the changes in LST under second scenario will represent the regional impact of global climate change on changes in LST, assuming that local changes due to higher aerosol and greenhouse gas emissions are part of global climate change. The impact of local-scale forest cover loss is then separated from total change by subtracting the ΔT_{max} due to global climate change from ΔT_{max} simulated under the first scenario. The procedure used in partitioning of ΔT_{max} is mathematically given in Equations 2.8–2.10.

$$\begin{aligned} Total\ \Delta T_{max} &= \Delta T_{max}(Global) + \Delta T_{max}(Forest\ loss) \\ &= senerio\ 1\ MLRR\ model\ predictions \end{aligned} \qquad [2.8]$$

$$\Delta T_{max}(Global) \rightarrow senerio\ 2\ MLRR\ model\ preditions \qquad [2.9]$$

$$\begin{aligned} \Delta T_{max}(Forest\ loss) &= Total\ \Delta T_{max} - \Delta T_{max}(Global) \\ &= scenerio\ 1 - scenerio\ 2 \end{aligned} \qquad [2.10]$$

Hence, using MLRR we can partition the total change in maximum LST after controlling for elevation and forest cover, which has been one of the main challenges in the previous studies, as discussed in the Introduction section.

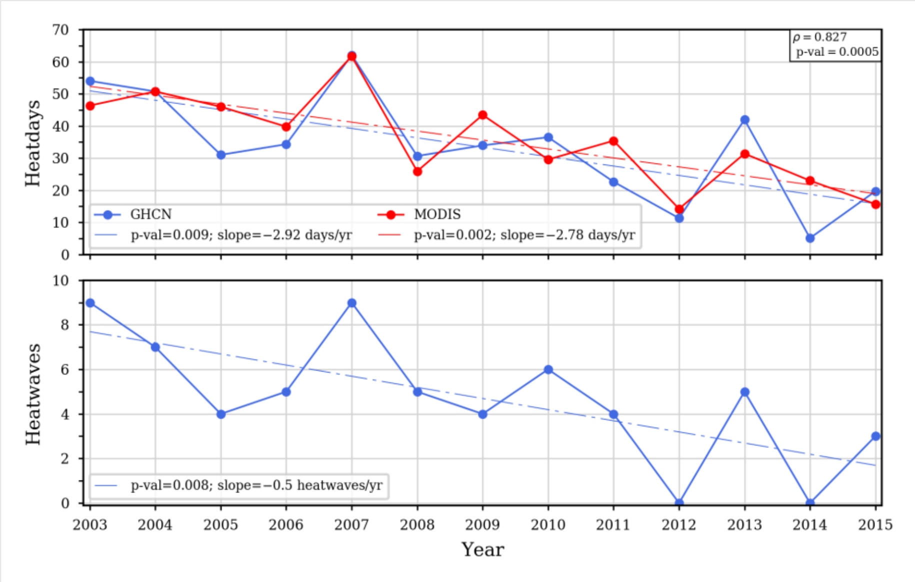

Figure 2.3. *Changes in the annual frequency of heatwaves and heat days over the last 13 years (2003–2015). a.) Heat days from GHCN station daily maximum and MODIS Land Surface Temperature (LST) day-time temperature b.) annual variation of heatwave frequency from GHCN data; see text for details.*

2.8. Results and discussion

2.8.1. Changes in heatwaves and heat days

Figure 2.3 shows the annual variation in the frequency of heat days for GHCN data and MODIS LST at GHCN grid cell. There is a statistically significant (at 1% significance level) decrease in the frequency of heatwaves at GHCN station (Figure 2.3b), and a sharp decrease in the number of heat days in both GHCN and MODIS datasets. This decrease in the heat days can be directly related to decreasing trend in annual maximum, mean, and quantiles of maximum temperatures (shown in Figure S2.5 and discussed in SM text S2.1). Strong agreements are observed in the estimates of heat days between the GHCN and MODIS LST at GHCN grid cell and heat days and heatwaves in the GHCN data (correlation coefficient > 0.80, significant at 1%). This suggests that MODIS LST and heat day are reasonable representations of the heatwave stresses at the GHCN location, which we assume to be true at all the grid cells in the region.

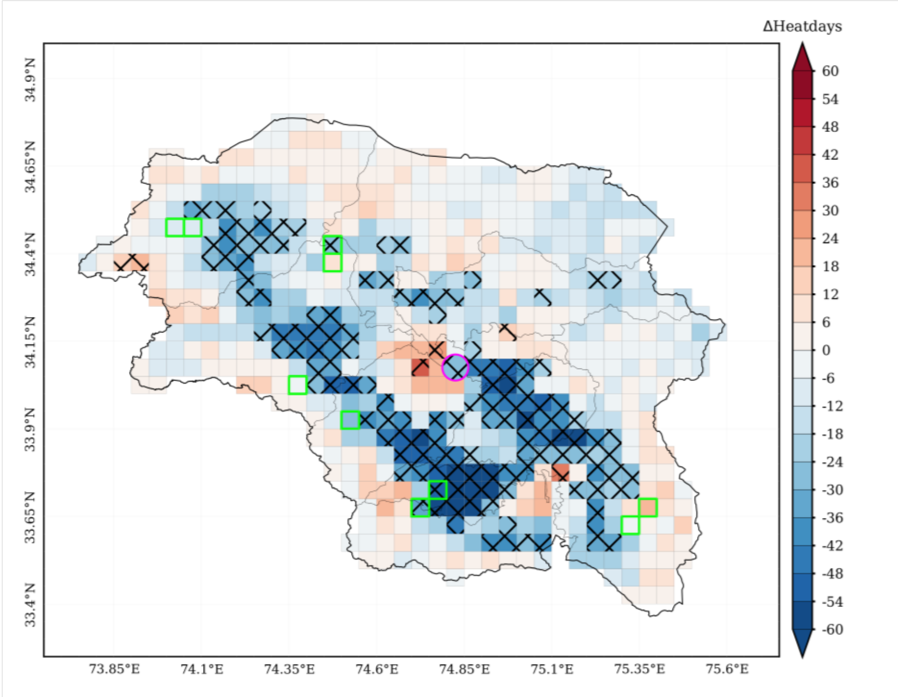

Figure 2.4. *Changes in heat days for 2003–2019 using the MODIS LST data. Hatched grid cells show significant changes at 10%. The encircled grid cell at the center of the map with a pink outline corresponds to the GHCN station grid (i. e., grid cell where GHCN station is located). The green boxes show the six selected regions.*

Figure 2.4 illustrates the spatial variation of the change in annual frequency of heat days over the period 2003–2019. Changes in heat days at GHCN grid cell and the six selected regions are highlighted by pink and green color, respectively. It is found that grid cells at high altitudes (elevation $>2800m$) show a mild decrease in annual frequency of heat days (decreasing trend) except for the grid cells with higher fraction of forest cover ($>$ 40%), where an increase is observed; however, the changes were not significant at 10% level. An intense and significant decrease in the annual frequency of heat days is observed over moderate elevations ($2000 - 2800m$), which is independent of the forest cover. At lower elevations ($< 2000\ m$), similar large-scale decrease in heat days is evident in rural and moderately urbanized areas, and an increase is noted in urbanized areas of Anantnag and Srinagar city, except the areas surrounding Dal Lake, which can be attributed to the evaporative cooling over the lake surface. Besides that, a latitudinal dependence is also observed in the magnitude of decrease, for example, in south

Kashmir, a decrease of about 60 days is observed at most of the grid cells compared to north Kashmir where a maximum of 40 days decrease is observed. In rural and moderately urbanized areas, the cooling effect of evaporation from the partially/fully saturated agricultural land (Bonan 2001) and intensified agricultural practice (for example, paddy fields) (Oleson *et al* 2004) plays an important role in decreasing the temperature and number of heat days, in addition to large scale cooling trend over the valley. (discussed in next section). Nayak and Mandal (2019a) also noted cooling trend over India in response to the conversion of dry barren land/grassland/shrubs to agricultural land due to enhanced evapotranspiration. Consistent with the previous studies of Kumar *et al* (2017), Veena *et al* (2020), Schatz and Kucharik (2015), and Stone *et al* (2010) the increased frequency of heatdays in the urban areas is clearly an indication of urban heat island effect where the conversion of the agricultural land and small vegetation to built-up areas leads to increase in the sensible heat fluxes and reduction in evapotranspiration. The spatial variation also suggests larger decreases within the valley, followed by mild increases and then decreases outside the valley, over both the Greater Himalayas on the east and Pir-Panjal on the west side. These results suggest that changes in heat days are mainly forest- and elevation-dependent. In addition to that shift of land use and land cover type also plays an important role in the changes of temperature (Nayak and Mandal 2019b).

The interannual variation in annual frequency of heat days at the selected regions is further investigated as shown in Figure 2.5. A decreasing trend is observed at all locations except Larno, where a mild increasing trend is observed because of an increase in temperature (discussed in the next section sections). The decrease in the number of heat days is more intense and strong in the region with a significant forest cover loss (significant at 5% for Shopian) compared to the region with no change in forest cover, which can be attributed to the cooling effect of local-scale deforestation in the mid-latitudes (Lee *et al* 2011, Zhang *et al* 2014a). The smaller decrease in frequency heatdays at

Watlab in comparison to Shopian and Tosamaidan can be attributed to the lesser forest cover and the fractional change in forest cover.

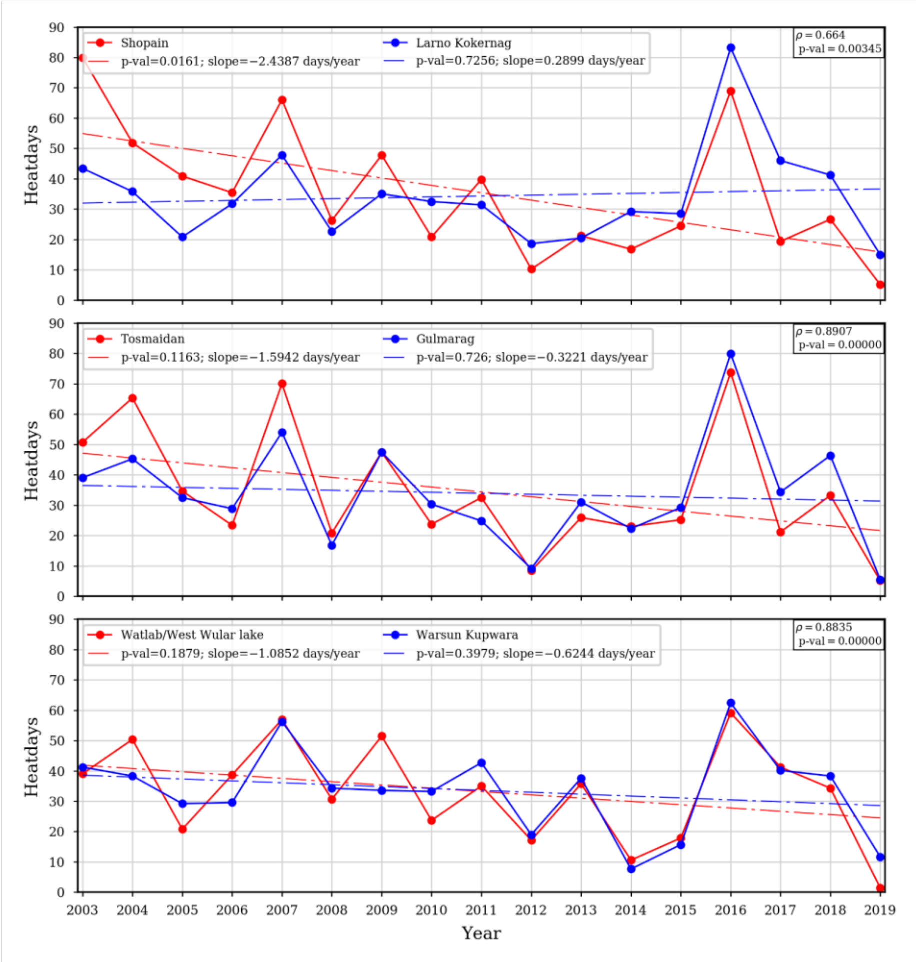

Figure 2.5. *Temporal variation of annual frequency of heat days in the six selected regions over Kashmir valley.*

2.8.2. Changes in temperature

Figure 2.6a shows the spatial variability of changes in maximum LST over the period 2003–2019. A mild to strong large-scale decrease in annual maximum temperature is observed over most parts of the valley particularly in the moderate elevation areas, where the forest cover is generally higher. The changes, however, are not spatially uniform. The decreasing trend over majority of the region is statistically significant at 10% in most of the moderate elevation areas, and a steeper decrease is observed in the southern part compared to the northern part, which may be suggestive of its latitudinal dependence. An increase in snowfall and snow cover area observed over the north-western

Himalayas in the recent years (Sakai and Fujita 2017, Shafiq *et al* 2019b) increases the albedo, and hence decreases the temperature. Since our study area is not completely snow-covered during summers but the topsoil in forests and pastures at higher altitudes is highly saturated because of recently melted and continuously melting snow, that increase the evapotranspiration and turbulent mixing from forest and direct evaporation from exposed saturated soil, which locally cools the forest and may cause rain in the nearby areas depending on other factors (Muluneh *et al* 2017) Studies have also found that a small scale localized deforestation in a forested area can act as a focal point of localized convection which can increase the local precipitation and thus reduce the local temperature (Sturm *et al* 2005). A more plausible cause of temperature decreases in the lower and mid-elevations may be related to evaporative cooling due to increases in precipitation and water-intense agricultural practices (mainly paddy) (Bonan 2001, Shafiq *et al* 2019b); however, further studies are required to estimate the contributions from different mechanisms.

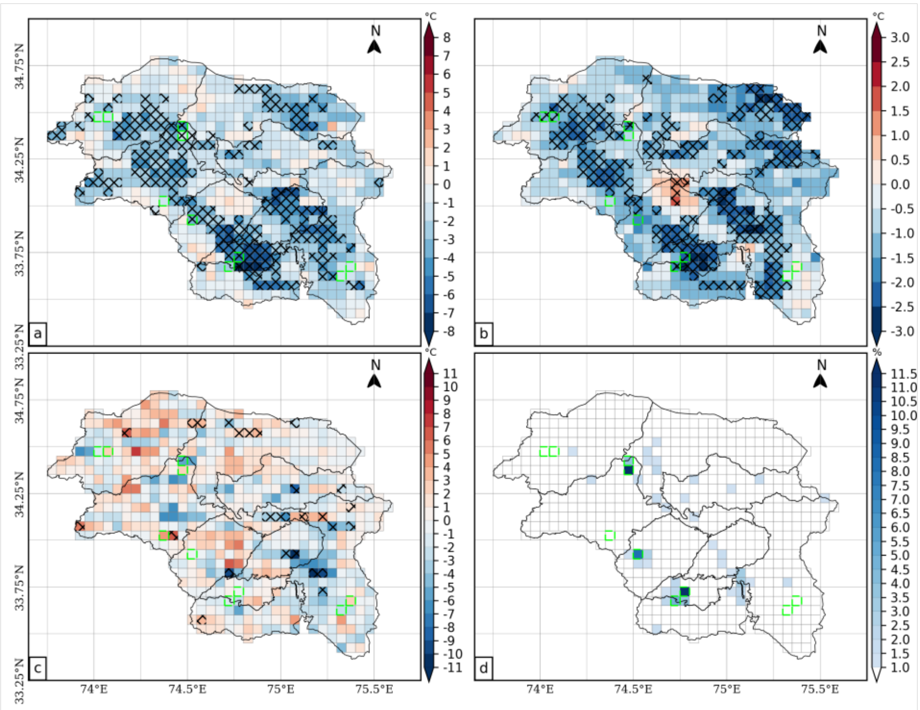

Figure 2.6. *Changes in temperature over Kashmir Valley. a) Changes in annual maximum temperature (ΔT_{max} ($°C$)) (b) Changes in annual mean temperature (ΔT_{mean} ($°C$)) (c) Changes in annual minimum*

temperature (ΔT_{min} ($°C$)) for the period 2003−2019; the changes in grid cells that are significant at 10% are hatched by dark solid lines (d) fractional forest cover loss over 2001 to 2019 period, the grid resolution in the figure is 0.05°×0.05°.

An increasing trend is observed in the central regions of the study area (uptown Srinagar), Anantnag, and mild increases in some high elevation areas, where the forest cover is relatively small (Figure S2.2). In the areas of Srinagar and Anantnag, there has been significant growth in urbanization (Habib 2017), which implies increases in impervious surfaces, such as concrete buildings and asphalt roads, etc., and increases in CO_2 emissions. The changes result in higher heat absorption (Nasipuri *et al* 2006; Stone *et al* 2010) and maybe one of the reasons for increasing trends observed in the mean and maximum LST in these regions. In addition, the removal of available forest or small vegetation by built-up areas may have resulted in urban heat island (Hu and Jia 2010, Jamei *et al* 2019). At higher elevations, bare rocks heat up faster than the forest area during summers when snow cover is less, thereby increasing the land surface temperature.

Figure 2.6b shows the annual mean LST changes for the period 2003–2019. Similar to maximum LST, a large-scale decreasing trend is observed almost throughout the valley, except at a few higher elevation grid cells near the periphery of the study region and uptown area of Srinagar and main town Anantnag, where an increasing trend is apparent. Shopian and upper grid cell of Watlab showed significant decreasing trends (at 10%; cross hatches in Figure 2.6b) for the period 2003–2019. The other selected regions showed a mild decreasing trend except for the upper grid of region Larno that showed a mild increasing trend. The decreasing trends in both maximum and mean LST are steeper (mostly significant at 10%) in moderate elevation and higher forest cover regions, and the decrease is less pronounced as we increase or decrease the elevation. As in the case of heatwaves and heat days, we observe spatially non-uniform trends in maximum and mean LST in the Kashmir valley, which are mainly governed by forest cover, elevation, and urbanization extent.

The changes in annual minimum LST show an increase in higher latitudes of Kupwara and Bandipora, central Budgam, and scattered grid cells in many other districts during the recent period 2003–2019 (Figure 2.6c). A localized decreasing trend is also evident in lower elevations of Anantnag and Pulwama and Dal Lake area of Srinagar. However, the changes in minimum temperature were statistically significant at a few grid cells only (see Figure S2.6). A similar increasing trend in the winter temperatures (i.e., annual minimum temperature) over Kashmir is observed by Rafiq *et al* (2016).

The forest covers for 2000 and 2019 upscaled to grid resolution $0.05^\circ \times 0.05^\circ$ are shown in Figure S2.2 (a and b). Figure 2.6d shows the forest cover losses from 2000 to 2019, which is computed as the difference in forest cover between 2019 and 2000. The change of forest cover is shown as the percentage of $0.05^\circ \times 0.05^\circ$grid cell area. There were small decreases in forest covers (0.2%) in the whole study area, but significant changes are observed in a few grid cells: the two grid cells in Shopian showed forest cover changes from 45.24% to 43.01% and 17.31% to 15.33%, respectively. Tosmaidan reduced from 27.53% to 25.23%. Watlab also showed a decrease from 49.5 to 47.1 %. These losses appear rather small, the percentage loss of forest is roughly 8% (Figure 2.2 and 2.6d), the impact of which on local maximum temperature may be significant.

We further analyzed the LST at the three regions along with three other no-loss regions, i.e., where forest cover losses are insignificant. Figure 2.7 shows percent cumulative forest cover loss (ΔF_L) per year from 2001–2019 (solid lines, cumulative), using Equation (2.5), and the changes in maximum LST for the period 2003–2019 (dashed lines) taken with respect to the maximum temperature of 2003. Large-scale deforestation of about 8% is observed in Shopian, Tosmaidan, and Watlab from 2001 to 2013, and as desired, the other no-loss regions, Larno, Gulmarg, and Warsun, have minor losses of less than 0.1% over the 2001–2019 period. An interesting observation is the change in maximum LST with respect to forest cover changes. Decreasing trends are observed in maximum LST in all the six regions; however, the decreases were more pronounced and consistent after 2007, especially in Shopian and Tosmaidan, shown in Figure 2.7a and 2.7b. For example, for Shopian the change in temperature after 2009 range between $-2.57°\mathrm{C}\ to - 7.7°\mathrm{C}$, while Larno showed much smaller decreases that range between $0.16°\mathrm{C}\ \ to - 5.3°\mathrm{C}$. The average changes over the period 2003–2019 are shown in the inset Table of Figure 2.2. Since the pairs of regions are located in comparable latitudinal extents, have similar initial forest cover areas, and elevations, the magnitudes in the decreasing trends of maximum LST can be mainly attributed to the forest cover changes. Hence, it can be assumed that the forest cover losses result in significant changes in local temperatures within one or two years after, if no appreciable forest gain offsets the changes.

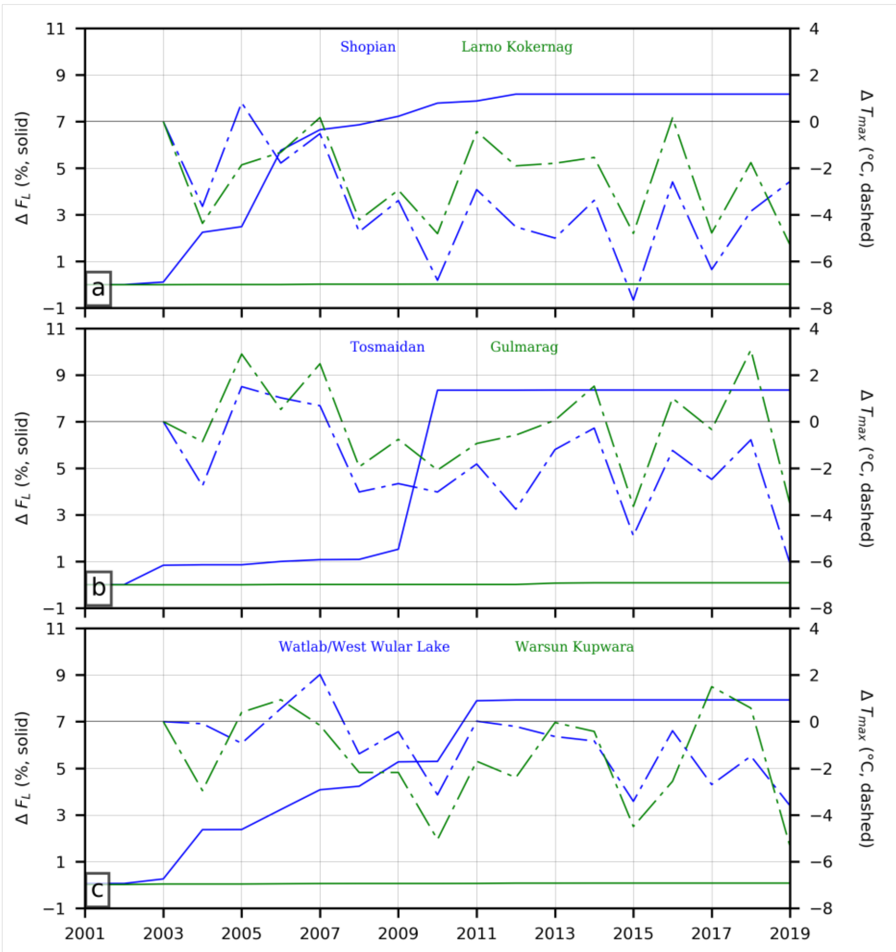

Figure 2.7. *Annual variation of forest cover loss (ΔF_L, in percentage) from 2001−2019 for (a) Shopian and Larno near Kokernag (b) Tosmaidan and Gulmarag and (c) Watlab/West Wular Lake and Warsun*

Kupwara. Also shown are the variations of annual maximum temperature changes (ΔT_{max} ℃, averaged spatially) in the regions. The annual maximum temperature change for each year is computed by subtracting the annual maximum temperature from that of 2003.

For the regions of Watlab and Warsun Kupwara, the annual maximum LST showed marginally different variations (Figure 2.7c) as compared to the above Shopian and Tosmadian cases, even though both regions are located in the same latitudinal extent with comparable forest cover and elevation. Upon closer examination of the region, upper grid of Watlab has more than 75% forest cover, while the lower grid has only ~36% forest cover (Figure S2.2). The land cover in the lower grid is found to have established towns at multiple locations, agricultural land, burnt forest and bare soil, likely causing an increase in the maximum LST, affecting the average maximum LST variation of the region. These results suggest that the impacts of forest cover losses are dependent on the land use following the loss. Similar but less intense changes are observed for mean temperature and the changes are shown in Figure S2.7.

The analysis on changes in maximum, mean, and 90th percentile showed a decreasing trend in all regions (see Figure S2.8–S2.10 for interannual variation), and the decrease in LST were generally higher and statistically significant (at 5%) for the regions with forest cover loss (except for annual mean at Tosamaidan and Watlab) compared to regions with no forest cover loss.

Deforestation at mid and high latitudes unmasks the high albedo snow layer and causes cooling by decreasing the shortwave absorption; however, there is a decrease in evapotranspiration and surface roughness at the same time which tend to increase Bowens ratio and thus increases temperature (Davin and Noblet 2010, Noblet *et al* 2012). The net effect of cooling due to high albedo and warming due to increased Bowen's ratio depends on the local bio-geophysical factors (Davin and Noblet 2010, Lee *et al* 2011). The cooling effect at locations of large-scale deforestation in Shopian, Tosamaidan and Watlab may be due to increased evaporation from saturated soils during summers. Several studies have also highlighted a cooling trend in mid and high latitudes in response to local and large-scale deforestation (Lee *et al*, 2011; Li *et al*, 2015; Zhang *et al*, 2014). The melting of snow during spring and summers swells the soil and increases the available moisture for evaporation, which intensify local evaporative cooling in these regions. Conversion of high forest cover to water-intensive crops also significantly increases the evaporating cooling (Bonan 2001). An increase in water-intensive paddy crops, especially in plain areas surrounding the Jhelum River, up to elevations of 3200m is observed in recent years (Fayaz *et al* 2020). In addition, an increase in the precipitation and snowfall also assists the decrease in temperature (Sakai and Fujita 2017, Shafiq *et al* 2019b). However, further studies are needed to ascertain the causes behind the changes in maximum temperature over the three deforested regions.

2.8.3. Partitioning of temperature change

The estimated regional regression model is given in Equation 10 (adjusted $R^2 = 0.17$), the coefficients of which are all significant at 1% level. This means that we have strong evidence that changes in annual maximum LST (ΔT_{max}) are dependent on forest cover loss, elevation, and forest cover, and can be estimated with reasonable accuracy.

$$\Delta T_{max} = -1.99 + 0.17 \times \Delta F + 1.047 \times Z + 0.20 \times FC + 0.76 \times Z * FC + \epsilon \qquad [2.11]$$

On examining and interpreting the model coefficients, we find that there is a decrease of roughly $2°C\ in\ T_{max}$ corresponding to the regional change. As we have seen a large-scale decreasing trend in annual T_{max} in most parts of the valley (Figure 2.6a) which suggests a regional decreasing trend due to global climate change, the MLRR model correctly estimates the regional decrease of $2°C.$ All predictor variables were found to increase ΔT_{max} when they are above mean and cause further decrease in ΔT_{max} when lower than mean. Controlling for elevation and forest cover at mean values, the loss of forest cover by one unit (i.e., $0.051 km^2$) causes a decrease of roughly $0.172°C$ in ΔT_{max}, and the reverse is true for forest gain. Similarly, there is an increase of about $1.05°C$ and $0.2°C$ with a unit increase elevation (835.5 m) and forest cover ($4.37 km^2$), when controlling for others. However, these changes in ΔT_{max} due to changes in $Z \, and \, FC$ are under the independence condition. In our case, the total change in ΔT_{max} because of a unit change in $Z \, and \, FC$ are approximately $1.05 + (0.764 \times FC) \, °C$ and $0.2 + (0.764 \times Z)°C$, respectively.

The simulation estimates of changes in maximum LST due to global climate change (green circles, error bars showing the 95% confidence interval) and the combined impact of climate change and forest loss (red circles, error bars showing the 95% confidence interval) at the 3 regions where the changes in forest cover were significant are shown in Figure 2.8. The observed changes are also shown (black stars) to evaluate the accuracy of our model in simulating the observed changes in T_{max}. From Figure 2.8, we note that the observed changes in T_{max} at the regions of forest cover loss are more negative than the changes caused by global/regional climate change, that means deforestation or forest cover loss has a cooling effect in Kashmir valley, except for G1 of Watlab region (lower grid), where it seems that forest cover loss increases the temperature, which is explained in the previous section. Our model successfully captures the cooling effect of forest cover loss at the selected grid cells (red circles show more negative values than green circles), though there are differences in the model estimates and the observed values. It can be assumed that the temperature of the region depends on multiple meteorological factors such as humidity, precipitation, cloud cover, soil moisture, and others which were not considered to avoid the complexity of the model, and our main interest in partitioning between impact global/regional climate change and impact of forest cover loss.

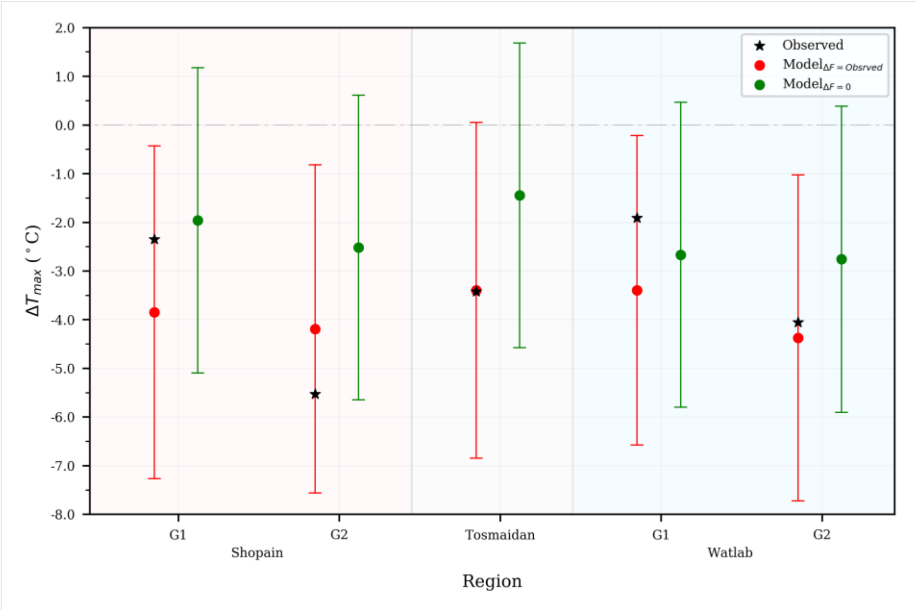

Figure 2.8: *Observed and model predictions of change in maximum temperature (ΔT_{max}) in the grid cells in the selected regions that have changed in forest cover. Blue stars, Brown circles, and green circles represent the observed ΔT_{max}, model predicted ΔT_{max} considering observed forest cover change, and model predicted ΔT_{max} when forest change is zero, respectively. Golden and green bars represent the 95% prediction interval at the grid cells. Shopian G1 and Shopian G2 are the two grid cells of region Shopian, similarly Watlab G1 and Watlab G2 from Watlab region.*

To understand the effect of elevation and forest cover on temperature changes, we divided the elevations into three classes (mentioned in methods) and analyzed the changes in ΔT_{max} with forest cover as we are more interested in forest cover and its changes, rather than elevation. The variations of ΔT_{max} with the forest cover from the model and observations are shown in Figure S2.11. Both model and observations are showing an increase in ΔT_{max} with the increase in forest cover at higher elevations (Z>2800m), though the observations are more scattered. From the observations, it can be seen that most of the high elevation grid cells with lower forest cover of about 15% ($4\,km^2$) show a decrease (mean = $-1.5°C$), some, however, show positive changes. Whereas high forest cover grids (> $4km^2$) mostly show increases or changes close to zero (mean = $-0.1°C$). The grid cells at lower elevations (Z < 2000m) show a pronounced decrease with the increase in forest. Note, however, that only a few grid cells have forest cover more than $8 km^2$ (30%). Both model and observations agree in showing the decreasing trend in ΔT_{max} and with increasing forest cover. Even though the relationship between ΔT_{max} and forest cover at moderate elevations (2000m<Z<2800m) is more complex, the model predicted a statistically significant increase in ΔT_{max} with increase in forest cover, as is seen in the observations. The observations highlight that lower forest cover grid cells at moderate elevations show the highest decrease in temperature and smaller decreases with the increase in forest cover area. We found that the grid cells with the highest forest cover of $> 16 km^2$ showed almost similar change in both model and observation; however, the differences between model and observations were more pronounced in lower forest cover range. Overall, if we consider changes in ΔT_{max} due to forest cover change, our model efficiently and accurately simulated the observed changes in maximum temperature.

2.9. Conclusions

A spatially non-uniform large-scale decreasing and localized increasing trends were observed in the annual frequency of heat days, mean LST, and maximum LST over the Kashmir valley. Warmer trends are observed over highly urbanized areas such as regions surrounding Srinagar and Anantnag and over higher elevations regions, devoid of forests. Even though at global scale temperatures are rising, the regional changes are variable and depend on the climatic characteristic of the region (Mascioli *et al* 2017, Partridge *et al* 2018). Unlike India, which experiences an increase in heatwaves and extreme temperatures (Mishra *et al* 2020, Rohini *et al* 2016, Murari *et al* 2015, Mishra *et al* 2020), we observed a regional decreasing trend in annual maximum, mean temperature and heatdays over Kashmir in the recent period. Small to moderate, and mostly statistically significant, increases in annual minimum temperatures were observed over much of the study region. On further investigating the selected regions, it was found that the decrease in heat days and annual maximum temperature at the regions of significant forest loss was more pronounced compared to the regions with no forest loss and similar bio-geophysical characteristics. Changes in forest cover appear to be the main driver of the pronounced decrease of LST, likely through other biophysical processes, such as evaporative cooling.

Both the observations and the regional regression model agree that annual maximum temperature increases with increase in forest cover at higher elevations, and it decreases with increase in forest cover at lower elevations. In addition, both observations and regional regression model simulations showed that the variations in annual maximum temperature are complex, as they depend on multiple interacting bio-geophysical factors such as forest cover, forest cover changes, elevation, geolocations, precipitation, and others. The temperature dependence on forest cover is more complex and uncertain in moderate elevations, where the model was reasonably successful in capturing the observed variations for relatively higher forest covers. Moreover, our model successfully and efficiently simulated the observed changes in temperature, particularly at the grid cells where forest cover loss was significant. As in the observations, the proposed model highlighted a sharp decrease in ΔT_{max} at those grid cells.

Partitioning of the changes in temperature between the impact of global climate change and local changes due to forest cover changes highlighted that global climate change decrease the temperature throughout the valley, i.e., climate change is negative, and the local change due to forest cover loss, which is also negative (i.e., cooling effect), amplifies the global climate change. Further studies are required to estimate the contributions from different factors to decreases in heatwaves and enhanced decreases due to forest cover losses. An implicit assumption in this study is that the annual maximum series from the partially complete satellite LST data is an unbiased estimate of the true maxima series. In addition, in our MLRR model, we assumed that the changes in annual maximum temperature are dependent on forest cover, forest cover changes, and elevation, and other likely affecting factors are ignored.

Due to the non-availability of high-resolution AST data and a closer relationship of LST with land use changes (Mildrexler et al 2011), we used LST for estimation of changes in maximum temperature (tmax) and heatwaves. Further, multiple studies have observed a strong positive correlation between AST and LST (Rafiq *et al* 2016, Alkama and Cescatti 2016, Mildrexler *et al* 2011). The use of LST for heatwave changes seems the best choice here. However, we note that the results from LST may vary from those based on AST. In addition, there are lot of uncertainties associated with satellite-based products, which we did not estimate in this study. As result, it is critical to evaluate these uncertainties in future studies when using satellite-based products like LST here. Regardless of these limitations, our results provide a simple and easy way to segregate the global climatic change signal from the local climate signal in response to land cover changes in the complex terrains of Himalayas. In order to perform risk assessment and to predict societal impact due to the changes in maximum temperature and heatwaves observed here, we emphasize the need of comprehensive studies through collaborative efforts. Furthermore, more robust modelling efforts are recommended to improve our mechanistic understanding of these temperature changes in response to deforestation in complex topographic regions like upper Indus valley.

APPENDIX-A: Supporting Information

Supplementary text

2.1. Comparison of MODIS-based LST with GHCN station data

On examining the MODIS LST, we found minor inconsistencies in the spatial and temporal availability, which necessitated the validation of the LST data with observed GHCN temperature data. Though the GHCN observations of maximum air temperature at 2m height are expected to be slightly different from maximum LST observations due to differences in specific heat capacities of air and land and time of observation, the annual maximum, mean, and other quantiles should show agreement in variations and trends over time (Sobrino *et al* 2020). To validate the MODIS LST data, we compared the trend and correlation for annual maxima, mean, median, 90th and 10th percentiles of daily GHCN observations and MODIS LST over the grid pixel, where GHCN Srinagar station is located, for the GHCN period of 2003−2015. We used Pearson's correlation coefficient (ρ) between the GHCN and LST datasets, and slope β of linear regression of temperature with time (year) as an estimate of temporal trend. The slope and correlation values were tested for statistical significance at 5% significance level. The hypothesis for slope and correlations can be stated mathematically as given in Equations S2.1 and S2.2, respectively.

$$Linear\ regession;\ \ H_0\!:\beta = 0;\ \ H_1\!:\beta \neq 0 \qquad \text{[S2.1]}$$

$$Correlation;\ H_0\!:\rho = 0;\ \ H_1\!:\rho \neq 0 \qquad \text{[S2.2]}$$

where H_0 and H_1 are the null and alternatives, respectively

The comparison between GHCN maximum temperature and day-time MODIS LST at GHCN grid cell is shown in Figure S2.5. We see that both datasets show a similar decreasing trend in annual maxima, mean, median, 90th and 10th percentiles, and the degree of agreement, estimated by the correlation coefficient, varies from 0.392 (for median) to 0.8178 (for 90th percentile), all of which are statistically significant at 5%, except for median and maximum (Figure S2.5). However, the biases and differences in the magnitudes can be attributed to the difference in thermal inertia of air and land surface, observation recording time, and the fraction of missing data in both datasets. MODIS LST showed the maximum decrease of $0.21°C/year$ for annual maximum and the lower decreases of $0.111°C/year$ and $0.114°C/year$ for annual median and 10th percentile, respectively, while as GHCN observations showed the highest and the lowest decreases of $0.292°C/year$ and $0.066°C/year$ for annual median and annual 90th percentile, respectively (Figure S2.5). Though not similar in magnitude, the trends in the higher quantiles (90th percentile and annual maximum) in both datasets were decreasing (Figures S5 (T_{max} and T_{90})). In addition, both the high quantiles in MODIS were almost always higher than GHCN. Though we do not have observations at all the grid cells, these results suggest that MODIS LST is a reasonable proxy to daily maximum temperatures at local scales, as is also noted by many other studies (Mildrexler *et al* 2011, Urban *et al* 2013, Zhang *et al* 2014b). On comparing LST with AST over Kashmir, Rafiq *et al* (2016), Romshoo *et al* (2018) noted a strong correlation of about 0.9 between LST and AST which gave us the confidence to use LST as a surrogate to AST.

Supplementary Figures

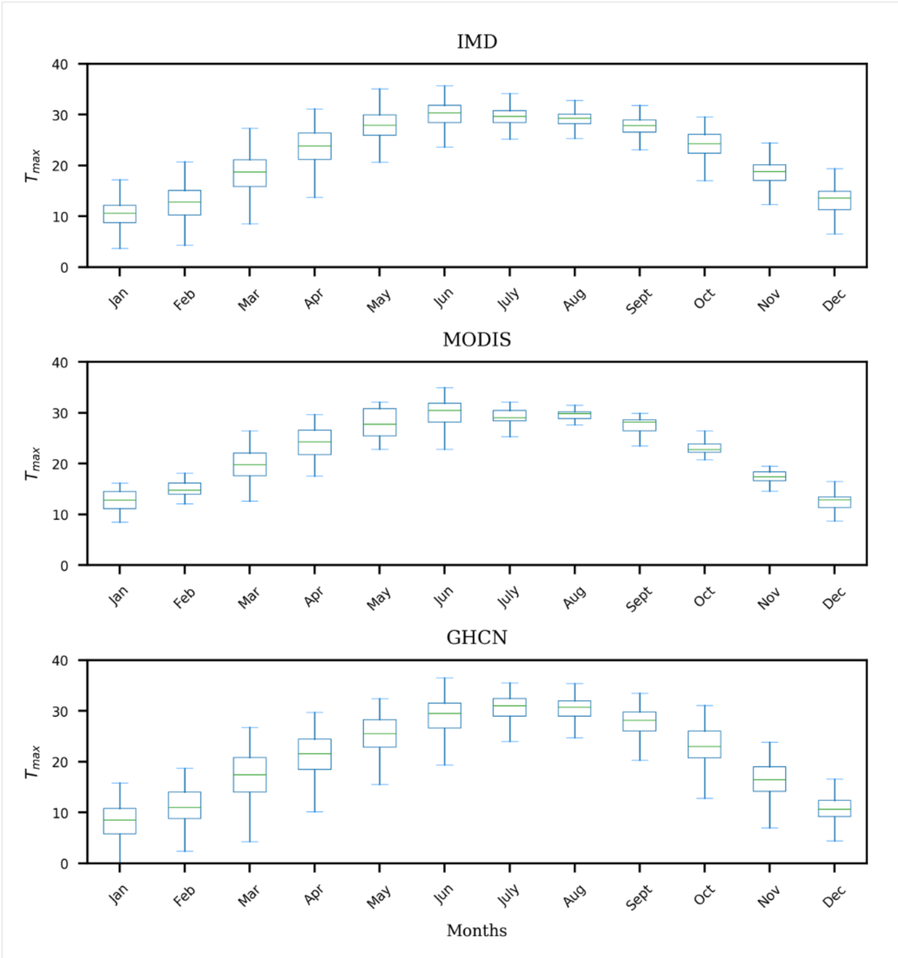

Figure S2.1. *Monthly variation of temperature based on India Meteorological Department (IMD), regional average MODIS LST, and GHCN station.*

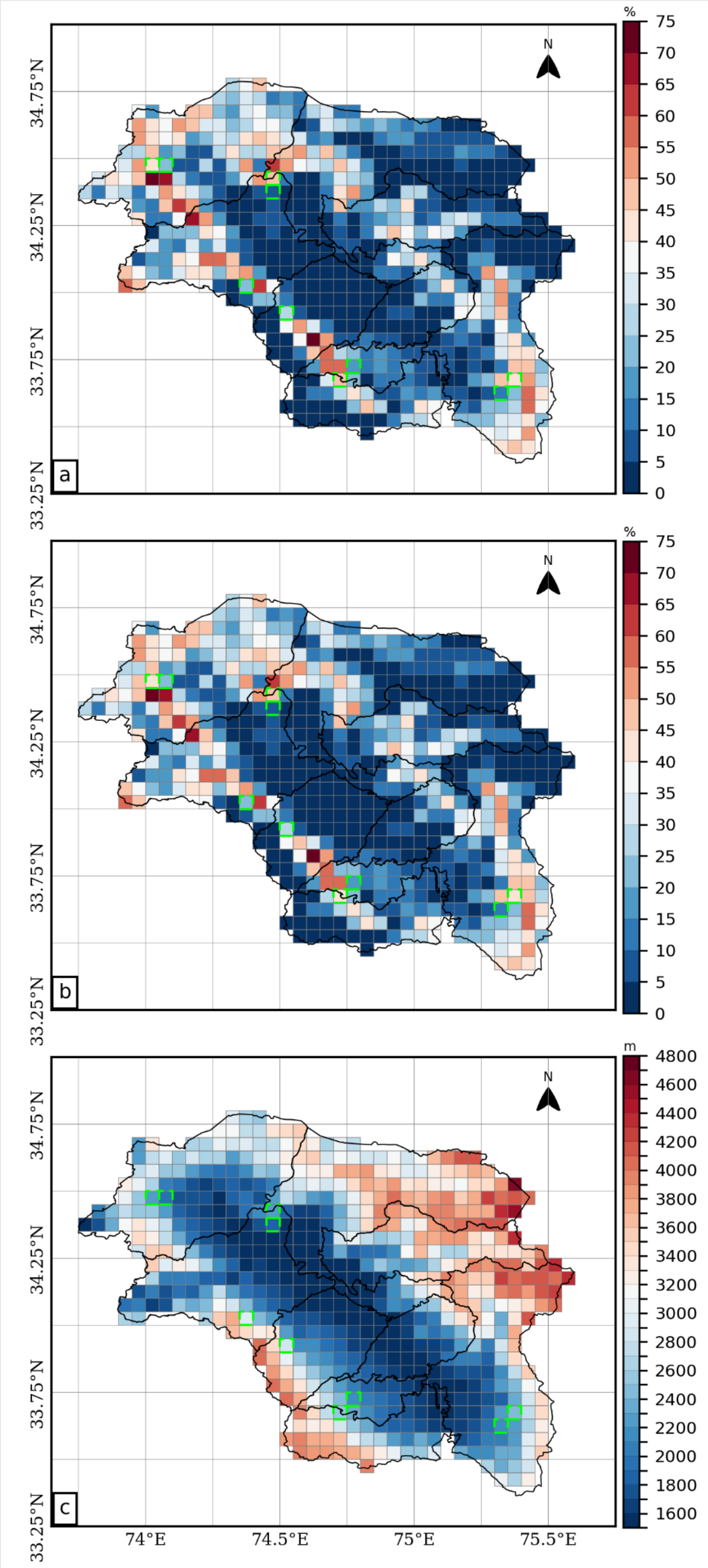
a
b
c
%
m
N
34.75°N
34.25°N
33.75°N
33.25°N
74°E
74.5°E
75°E
75.5°E
0
5
10
15
20
25
30
35
40
45
50
55
60
65
70
75
1600
1800
2000
2200
2400
2600
2800
3000
3200
3400
3600
3800
4000
4200
4400
4600
4800

Figure S2.2. *Status of forest cover in Kashmir over the period 2000–2019. (a) Forest cover (in percent) for 2000 (b) Forest cover (in percent) for 2019 and (c) Elevation for the study region; all shown at a grid resolution of 0.05°×0.05°. The higher-resolution forest cover is shown in Figure S2.14.*

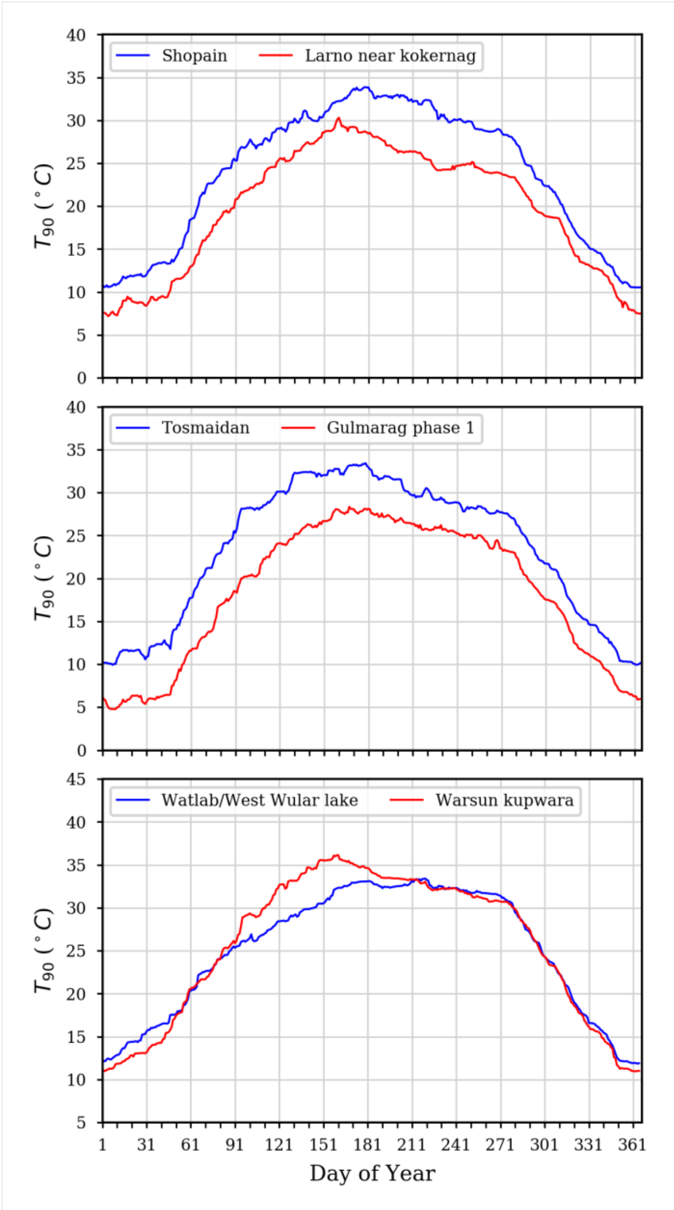

Figure S2.3. *90th-percentile of land surface temperature for the 6 selected regions over the Kashmir region. T_{90} is computed by taking the 15-day centered window for each day to increase the sample size and to reduce the anomalous high percentiles. For a calendar day, say, 08th-June we consider 01st-June to 15th-June of all years and the 90th-percentile of this set will be the 90th-percentile for 08-June.*

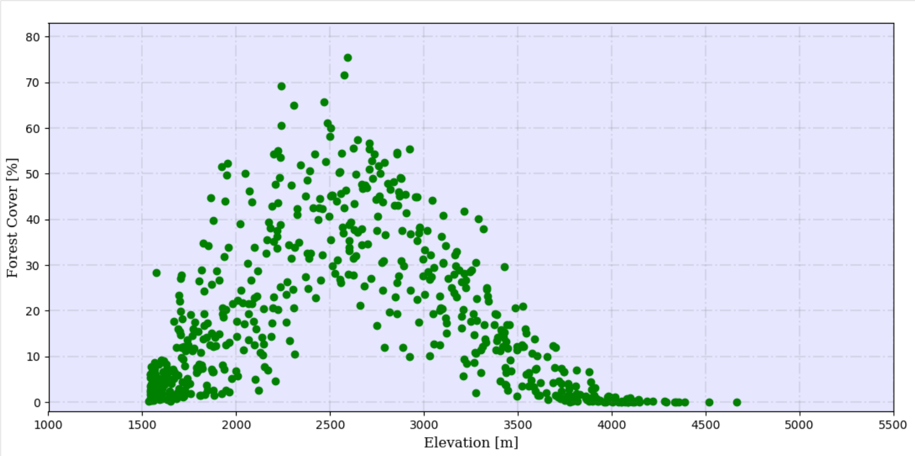

Figure S2.4. *Forest cover (in percent) of 2000 vs elevation (in m) for the study region.*

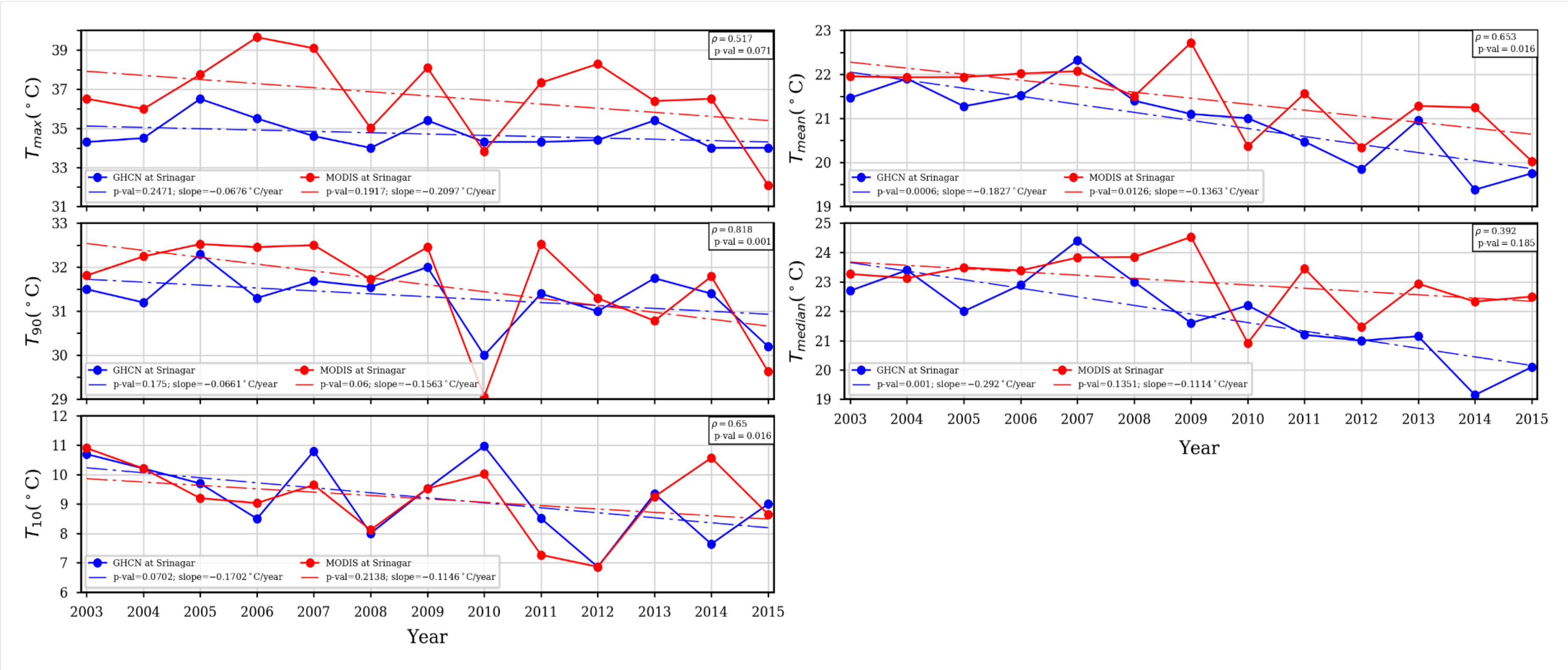

Figure S2.5. *Temporal variation of annual maximum (top left), annual mean (top right), annual 90th percentile of (middle left), annual 10th, percentile of (bottom left), and of annual median of (middle right) of GHCN and MODIS LST data at GHCN station location in Srinagar. Dashed lines represent the expected linear regression lines.*

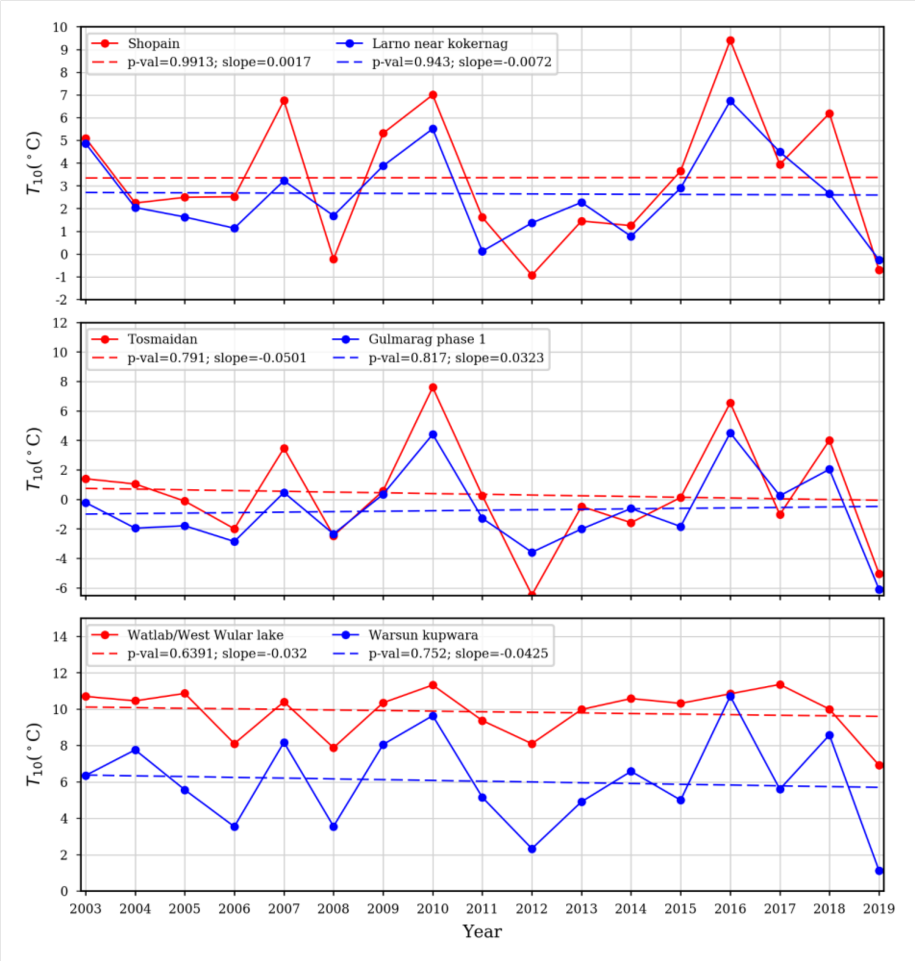

Figure S2.6. *Temporal variation of annual 10th percentile of* T_{max} *for the selected regions in Kashmir valley. Blue and red lines are for regions with no change in forest cover and loss in forest cover, respectively. Dotted lines represent the regression slope line.*

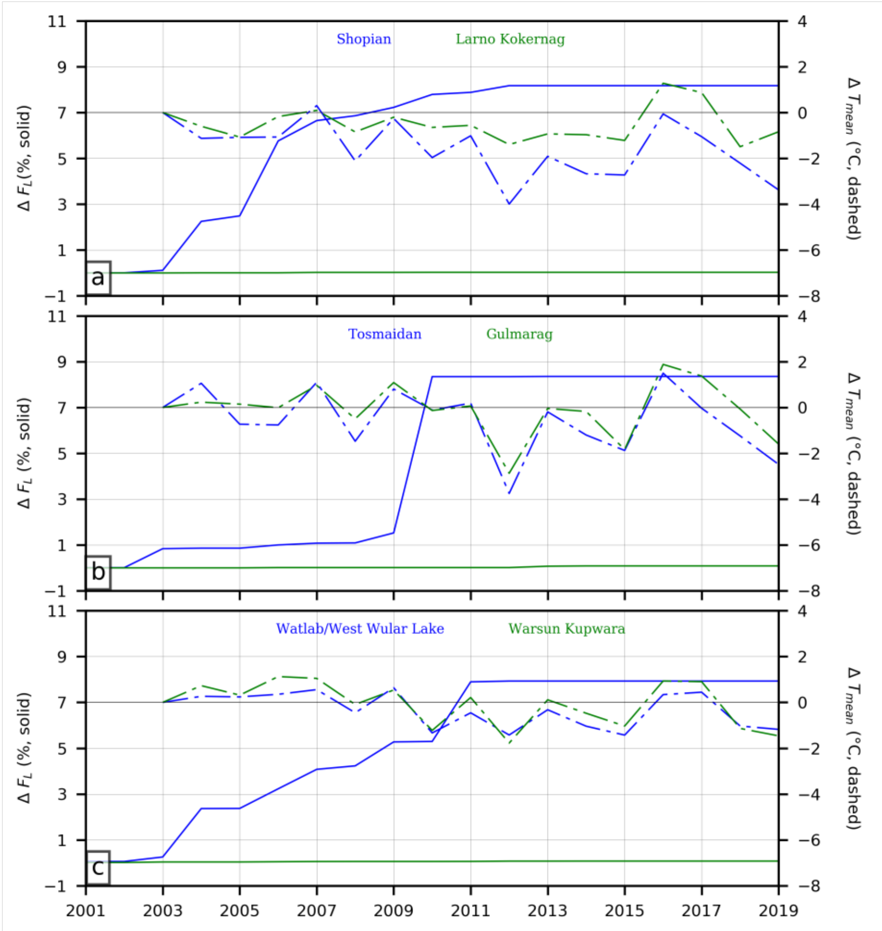

Figure S2.7. *Annual forest cover losses (ΔF_L, in percentage) from 2001−2019[left y-axis], and the annual variation of annual mean temperature (ΔT_{mean}, in ℃, averaged spatially) [right y-axis].*

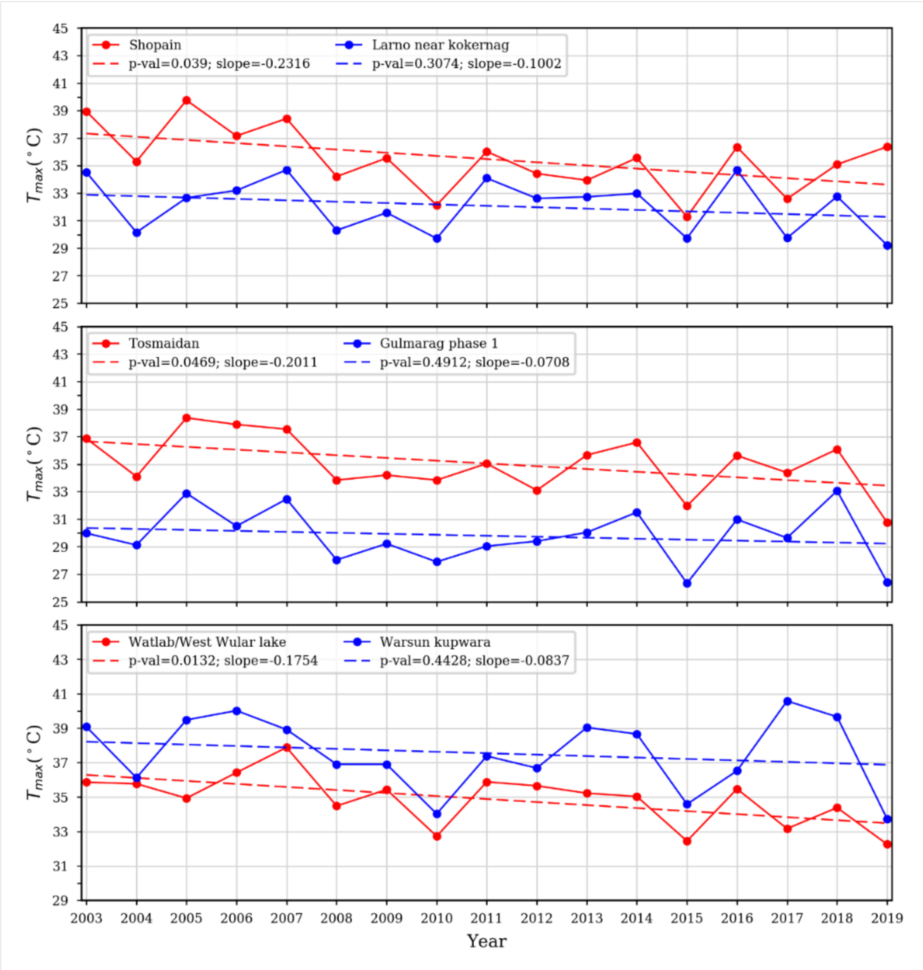

Figure S2.8. *Temporal variation of annual maximum of MODIS LST for the selected regions in Kashmir valley. Blue and red lines are for regions with no change in forest cover and loss in forest cover respectively. Dotted lines represent the regression slope line.*

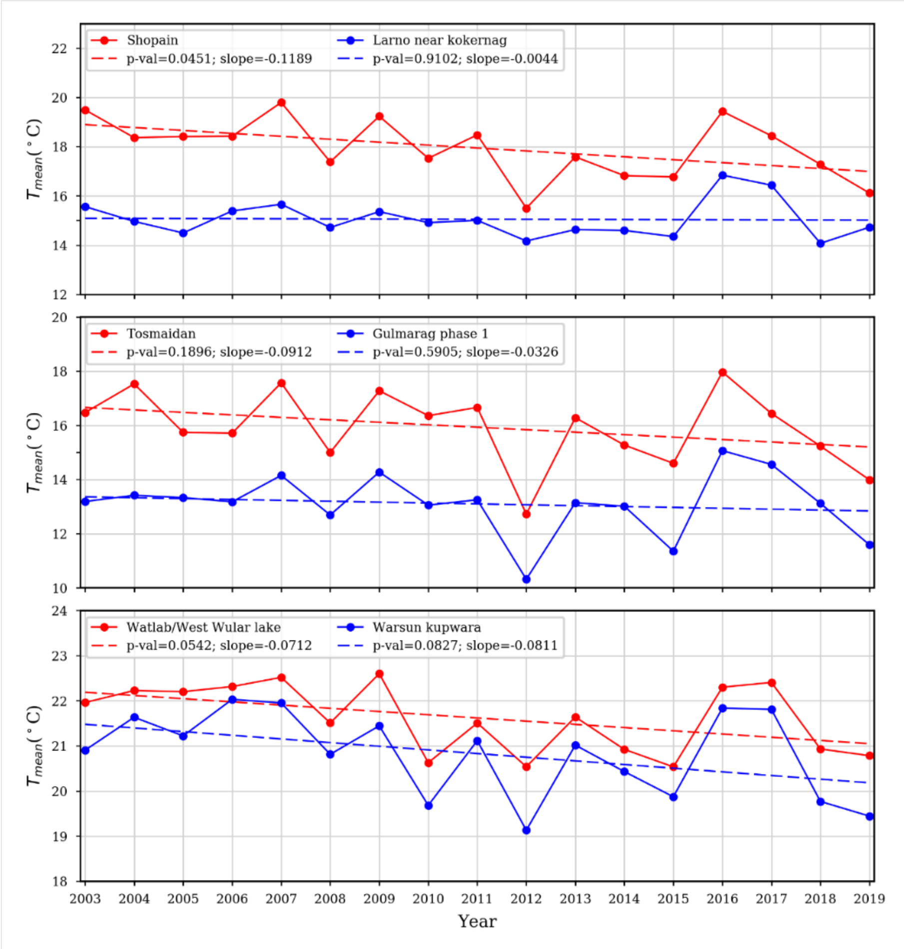

Figure S2.9. *Temporal variation of annual mean of MODIS LST for the selected regions in Kashmir valley. Blue and red lines are for regions with no change in forest cover and loss in forest cover, respectively. Dotted lines represent the regression slope line.*

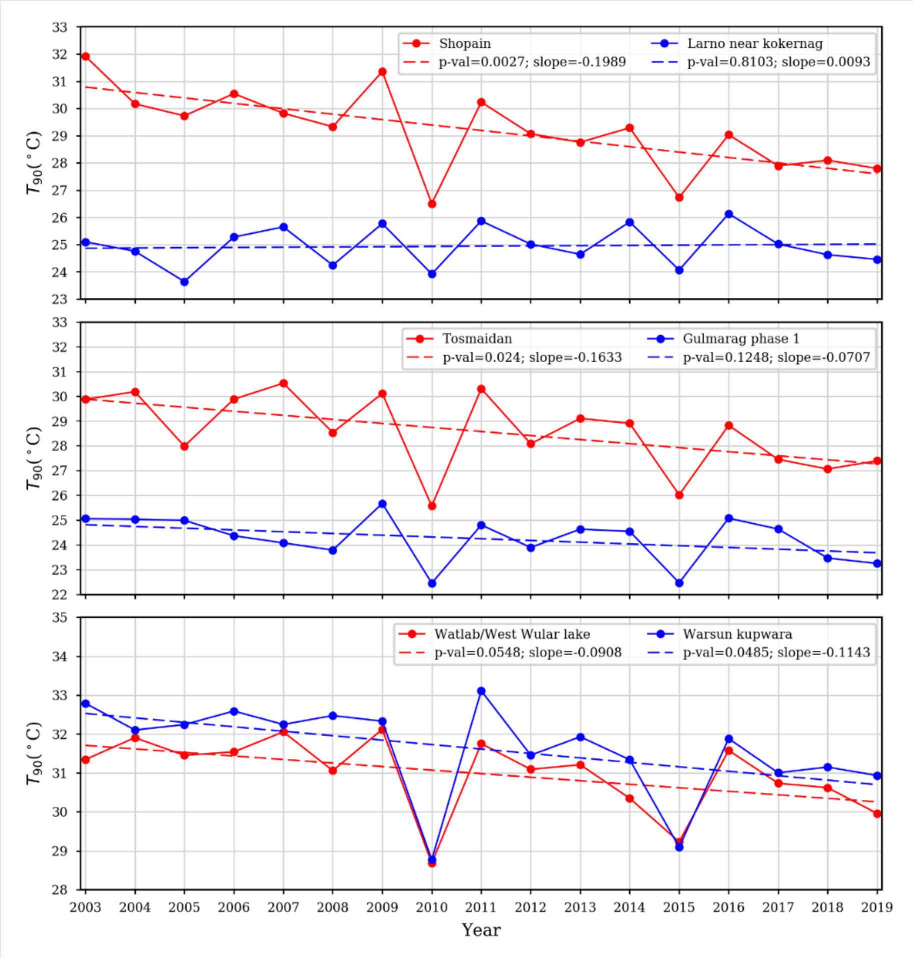

Figure S2.10. *Temporal variation of annual 90th percentile of MODIS LST for the selected regions in Kashmir valley. Blue and red lines are for regions with no change in forest cover and loss in forest cover, respectively. Dotted lines represent the regression slope line.*

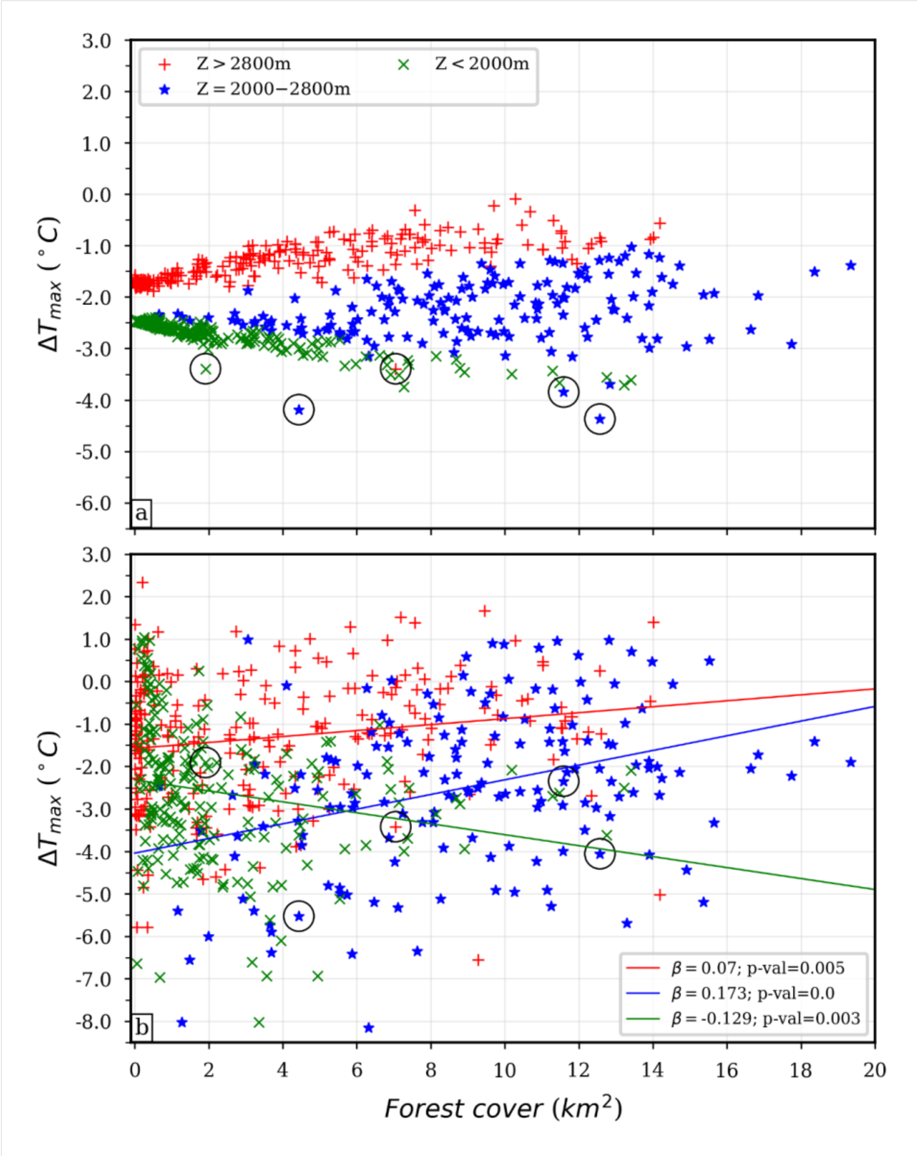

Figure S2.11. *Model expected (points in (a) and lines in (b)) and observed (points in (b)) relationship between temperature changes and forest cover in different elevation bands.*

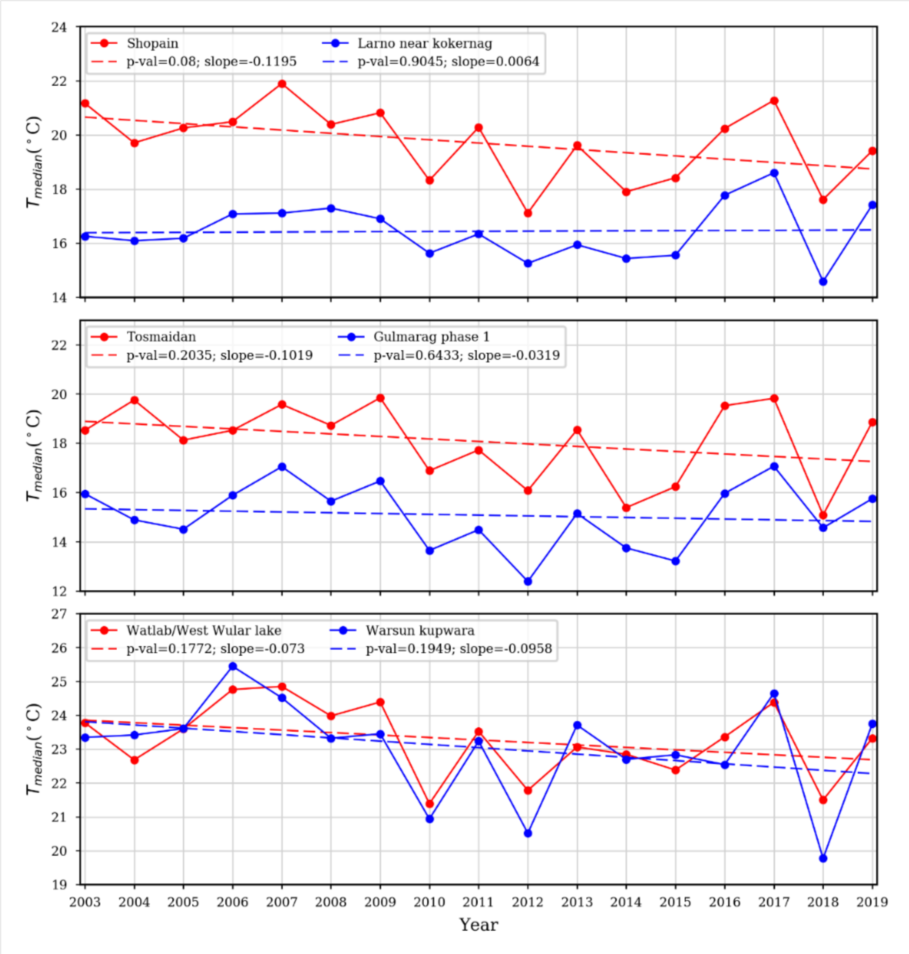

Figure S2.12. *Temporal variation of annual median of* T_{max} *for the selected regions in Kashmir valley. Blue and red lines are for regions with no change in forest cover and loss in forest cover, respectively. Dotted lines represent the regression slope line.*

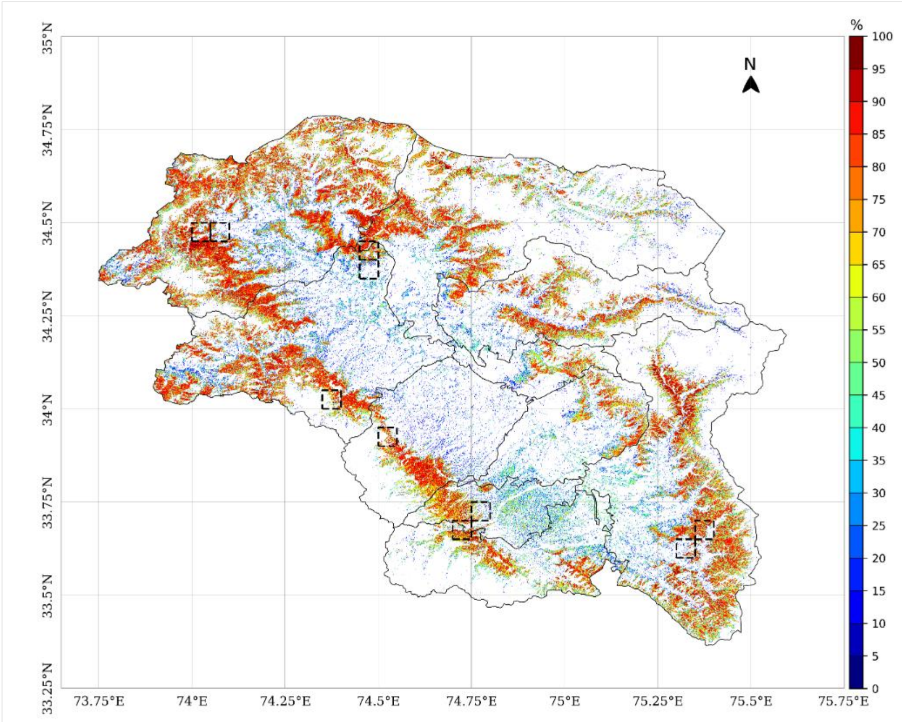

Figure S2.13. *Forest cover (in percent) for 2000 from Global Forest Change (earthenginepartners.appspot.com) (Hansen et. al. 2013), and the regions selected for analysis are highlighted as square boxes in black.*

Chapter 3 : Spatially compound drought

Executive summary

After understanding the methods for analyzing univariate extremes (droughts and heatwaves) in chapter 2, chapters 3, 4 and 5 are related to compound events. Multiple studies have explored multivariate compound extremes in the last decade, however, spatially compound events remain unexplored. In 2018, Singh *et al* (2018) found concurrent droughts in Brazil, South Africa, Southeast Asia, and India during the Global great drought, that resulted in the Great Famine. In another study, Anderson *et al* (2019) found that natural climate variability modes play an important role in global crop failure, with 1983 El-Niño resulting in the worst crop failure of modern history. This crop failure was a result of El-Niño forced concurrent drought conditions in major food producing countries which include northeast Brazil, western and southern Africa, eastern United States, and parts of southeast Asia. Althought these studies have hinted at occurrences of spatially compound droughts, but they did not explore the likelihood of such spatially compounding among different regions and physical mechanisms.

In order to answer these questions, chapter 3 discusses a novel method to investigate spatially compound droughts among IPCC AR5 reference regions. For each pair of IPCC regions, concordance probability is computed which is then compared with the concordance probability under independence. This allows us to identify the pairs of regions that have significantly higher likelihood of spatially compound droughts. A total of 17 robust concordant pairs are observed, out of which 6 pairs have more than 10000km distance between the regions and we call them teleconnections in droughts. Composite anomalies for two selected pairs revealed high-pressure blocking and climate oscillations as important drivers where El-Niño and PDO driving southeast Asia–Southern Africa teleconnection, and AO+ and PNA- driving western North America–Mediterranean teleconnection.

Precipitation deficit emerged as the initiator of these teleconnections and higher temperature anomalies work as a fuel to intensify them.

*After: **Waqar Ul Hassan** and Munir Ahmad Nayak; Global teleconnections in droughts caused by oceanic and atmospheric circulation patterns;(2021) Environmental Research. Letters. 16 014007; https://doi.org/10.1088/1748-9326/abc9e2*

Abstract

Long-duration droughts are usually tied to persistent local or remote forcings; for example, persistent droughts over California are frequently observed along with the "*ridiculously resilient ridge"* over the West Coast. It is now evident that some oceanic forcings (e.g., El–Niño Southern Oscillation [ENSO]) have *global reaches* and affect multiple regions concurrently during their progression. Here we show robust significant temporal concordances of persistent droughts in many regions, revealing multiple teleconnections (distant regions experiencing droughts concurrently), such as "western North America—Mediterranean", and "Southeast Asia—Southern Africa" teleconnections. Composite pressure and Sea Surface Temperature (SST) anomalies during concurrent droughts in western North America and the Mediterranean reveal a persistent weather regime that resembles the positive phase of Arctic Oscillation (AO) and negative phase of Pacific Decadal Oscillation (PDO). During concordant droughts of Southeast Asia and Southern Africa, composite pressure anomalies remarkably resemble the El–Niño pattern, which we infer as the leading cause of the teleconnection. The insights gained here offer a new dimension to understanding droughts and improving their long-term predictability.

3.1. Background

Droughts are ranked the highest among all-natural hazards, causing substantial damages to humans, the environment, and the economy; take, for example, the recent multi-billion-dollar droughts in California, South Africa, (Diffenbaugh *et al* 2015, Lund *et al* 2018, Simpkins 2018, Wolski 2018). Persistent droughts cause devastating damage to humans and the ecosystem health (Xu *et al* 2019, Yang *et al* 2018b), and the losses are likely to amplify in a warmer world (Su *et al* 2018), where the frequency and severity of droughts is expected to intensify (Xu *et al* 2019, Dai 2011b). Discernible changes in droughts and their associated atmospheric patterns have been reported in recent studies (Gibson *et al* 2019, Swain *et al* 2016). Often, atmospheric blocking or anticyclonic circulation [usually a part of quasi-stationary Rossby waves (Wolf *et al* 2018, Nakamura *et al* 1997)] for extended periods results in anomalously dry season in the neighbouring regions by preventing moist air from flowing into the region (García-Herrera *et al* 2019, Gibson *et al* 2019, Wise 2016). Such blocking of atmospheric flow and consequent long-duration droughts are most often established and modulated by anomalous sea surface temperatures (SSTs) and teleconnections of remote forcing, e.g., large-scale climate oscillations (Hoerling and Kumar 2003, McCabe *et al* 2004, Seager and Henderson 2016, Swain *et al* 2017, Wang *et al* 2015b, Dai 2011b). Studies over Africa, United States, Amazon and Australia (Lee and Zhang 2011, Masih *et al* 2014, McCabe *et al* 2004, Ummenhofer *et al* 2009, Yang *et al* 2018b) have noted that besides ENSO, the dominant mode of global climate variability (Dai 2011b), droughts can be attributed to direct or indirect influence of low-frequency climate variability, such as Pacific Decadal Oscillation (PDO), Atlantic Multidecadal Oscillation (AMO), the Pacific North America pattern (PNA), and North Atlantic Oscillation (NAO).

The Pacific SST anomalies modulate and are modulated by anomalies in the Atlantic and the Indian Oceans at multiple timescales ranging from months to years (Cai *et al* 2019, Kosaka and Xie 2013), and the interactions between the oceanic basins are bound to leave significant footprints in multiple regions simultaneously and sequentially. In fact, a recent study by Boers *et al* (2019) revealed temporal synchronicity of extreme precipitation between multiple distant regions. Synchronous extreme precipitation and other weather extremes of similar characteristics have been recently reported at regional and global scales (Boers *et al* 2019, Lau and Kim 2012, Hong *et al* 2011, Kripalani and Singh 1993). Studying the role of modes of climate variability on crop production variability, Anderson *et al* (2019) found that the climate modes play a significant role in regional and global crop production variability and may result in globally synchronous crop failure, for example, globally synchronous maize crop failure during 1983 El-Niño event. The fact that crop production failure (damage) across the globe is most often associated with droughts and heatwaves (Lesk *et al* 2016), which are likely to be frequent and intense in future climate (Xu *et al* 2019), raises the concern about international food security under globally synchronous droughts. These observations raise the following critical questions that we answer here, 1. Do we see temporal concordances in droughts over different regions around the globe? 2. if yes, what are the major driving factors that lead to concordances? and, 3. can they be attributed to oceanic and/or atmospheric climatic oscillations?

Here, we develop a method to quantify temporal concordancy of persistent droughts in different regions, which reveals multiple significant concordant regions. Previous studies have hinted at connections in droughts at regional scales, this study is a unifying step towards identification of teleconnections in droughts among different regions over the globe.

3.2. Data and Methods

3.2.1. Data

We used high spatial resolution gridded monthly total precipitation (P) and monthly mean temperature (T) from station-interpolated Climate Research Unit (CRU) (Harris *et al* 2014) dataset and two reanalysis datasets, Modern-Era Retrospective analysis for Research and Application, version 2 (MERRA2) (Gelaro *et al* 2017) and European Centre for Medium-Range Weather Forecasts (ECMWF) Re-Analysis fifth-generation (ERA5) (Hersbach 2016) available at spatial resolutions of ($0.5^o \times 0.5^o$), ($0.5^o \times 0.625^o$), and ($0.25^o \times 0.25^o$), respectively. CRU data from January 1901 to December 2017 are used in this analysis. MERRA2 and ERA5 precipitation and temperature data are available from 1980 to the present.

Another important variable for the calculation of the drought index used here is the available water capacity (AWC) of soil, which represents the potential moisture storage capacity of soils and mainly depends on soil texture, among other factors. Here, we used the potential soil moisture storage dataset prepared by Webb *et al* (2000), openly available at NASA's website (https://webmap.ornl.gov/ogc/dataset.jsp?ds_id=548) at $1° \times 1°$ spatial resolution with a downloading option for selecting any different spatial resolution and method of interpolation. The AWC data are downloaded at same grid resolution as that of hydrological datasets using nearest-neighbor interpolation method.

To explore the atmospheric condition causing persistent concordant droughts, we used the average monthly Sea Surface Temperature (SST), geopotential heights at 200hPa (Z_{200}) and 500hPa (Z_{500}) and mean sea level pressure (MSLP) data from ERA5 dataset (Services 2017). We also explored Outgoing Longwave Radiation (OLR) from National Oceanic and Atmospheric Administration (NOAA, Liebmann and Smith (1996)), available at https://psl.noaa.gov/data/gridded/data.interp_OLR.html.

There are various modes of internal climate variability that affect the weather systems at regional or global scales (Dunn *et al* 2017, Lee and Zhang 2011, Vicente-Serrano *et al* 2011, Dai 2011b). These internal modes of climate variability can be either intrinsic to atmosphere, which stem from natural variations in the large-scale atmospheric circulations and are usually linked with blockings, quasi-stationary Rossby waves and jet streams that have an indirect connection with the tropical SST forcing (Seager and Henderson 2016, Wang *et al* 2015b), or ocean-atmosphere couplings, in which atmospheric circulations are altered by diabatic heating and cooling of atmosphere induced by the large-scale SST anomalies which in turn influences the SST via feedback (Yang *et al* 2018a). Here, we are interested in understanding the links of concordant droughts with multiple global atmospheric oscillation patterns, such as ENSO, PDO, PNA, AO, NAO. Many indices are used to quantify the strength of ENSO due to its diverse nature; here we use the Southern Oscillation Index (SOI) to measure the strength and phase of ENSO. Besides that, we tested robustness of our results using SST-based indices available at (https://www.esrl.noaa.gov/psd/gcos_wgsp/Timeseries/). Timeseries of PNA index and other climate indices such as NAO and AO are available at NOAA's CPC website https://www.cpc.ncep.noaa.gov/products/precip/CWlink/daily_ao_index/teleconnections.shtml

3.2.2. Drought Identification

Drought indices are the primary metrics used in identifying droughts and assessing their characteristics. They usually quantify the departure of the available water (e.g., precipitation for meteorological droughts) from its long-term climatological mean. Among the many drought indices available, the self-calibrated Palmer Drought Severity Index (scPDSI) is most widely used at medium time scales of 9 to 12 months, e.g., for persistent agricultural drought and moderate hydrological drought (Dai 2011a, Vicente-Serrano *et al* 2011, van der Schrier *et al* 2013). The development of scPDSI resolved most of the shortcomings of the original Palmer Drought Severity Index (PDSI) (Palmer 1965), such as its spatial incomparability and high frequency of extreme events that are actually rare (Alley 1984). Dai, (2011a), and many studies have found scPDSI to be a reliable estimator of hydrologic and agricultural droughts. In this study, scPDSI is selected as a measure to detect and quantify droughts.

scPDSI parameters for MERRA2, ERA5 and CRU datasets are calibrated using respective monthly data for the period January 1980 to December 2017; due to the availability of longer-length observational data, another calibration period January 1930 to December 1990 for CRU was also explored. We defined a region to be in drought for a month when the scPDSI values in at least 25% grid cells in the region are below −2.0 (moderate drought) for that month. Shen *et al* (2007) used 20%, 30% and 40% of grid cells as a spatial threshold to define moderate, severe, and extreme droughts. Aadhar and Mishra (2017) also found that more than 25% of South Asia was under severe to extreme droughts in years 1982, 1987, 1992, 2002, and 2004. Persistent droughts that last for more than 12 months are considered for analyses in this study (Okin *et al* 2018). After finding the persistent drought events, a year is considered a 'drought year' when a minimum of its six months are under a persistent drought event (the rest drought months will be in previous or next year).

3.2.3. Drought probability and significant concordance

The global landmass is divided into 25 reference regions defined in the Fifth Assessment Report (AR5) of the IPCC available at https://www.ipcc-data.org/guidelines/pages/ar5_regions.html with minor modifications to Western North America (W. N. America) and Alaska because the 2011–2013 drought in California was not reproducible with these regions (See Table S3.1 and Figure S3.1 for region definition). According to Working Group 1 of the fourth assessment report of IPCC (Trenberth *et al* 2007), the land temperature has increased in recent decades; similar trends are observed in the datasets used here. The annual probability of drought for each region is estimated using equation [3.1] below. Figures S3.2-S3.3, and Table S3.3 show the annual probability of droughts in each region for the datasets used.

$$\hat{p}_i = \frac{n_i}{N} \qquad [3.1]$$

Where, n_i = number of years in drought in region i, and N = total number of years.

For each pair of regions, temporal concordance analysis is performed as follows. Two regions i and j are said to be under a concordant drought in a year if both the regions are experiencing a drought year simultaneously (e.g., Year 2010 will be a concordant drought year if both i and j are under drought in 2010), and the probability of this happening $\hat{p}_{ij}$, i. e., fraction of years in concordant droughts, can be taken as a measure of concordance between the two regions. If the regions are independent, the estimated concordance probability is $\hat{p}_i \times \hat{p}_j$. A one-tailed binomial test was carried out at 5% and 10% significance levels to test the statistical significance of the large temporal concordance for each pair of regions. The test can be written as:

$$\begin{aligned} H_o&: \hat{p}_{ij} = \hat{p}_i \times \hat{p}_j \\ H_a&: \hat{p}_{ij} > \hat{p}_i \times \hat{p}_j \end{aligned} \qquad [3.2]$$

where, H_o is the null hypothesis that drought in regions i and j are independent or concordancy is same as expected under independence assumption, and H_a is the alternate that the concurrent droughts in the two regions are higher than expected under independence assumption. In our case, we do not need to apply multiple comparison corrections, such as field significance, as the null hypothesis does not remain the same when testing different pairs of regions. Robust concordance between two regions is the one that is present in at least two datasets at 10% significance level. Here, we discuss results based on 10% significance, since the reanalysis data is only for 38 years and it is challenging to achieve small *p-values* with such small sample.

3.2.4. Underlying driving factors and connection with climate oscillations

SEA–SAF and WNA–MED robust concordances were selected to understand the factors responsible for these persistent concordant droughts. These pairs were selected because of the recent persistent droughts in these regions (Hanel *et al* 2018, Wolski 2018, Seager *et al* 2015) and large distances between the regions, signifying teleconnections in droughts. Standardized precipitation and temperature anomalies during concordant winters were analyzed to evaluate the relative influence of precipitation deficit and warm temperatures on the drought concordances. Composite geopotential height and mean sea level pressure (MSLP) anomalies (Z_{200}, Z_{500} for WNA–MED, and Z_{200}, and MSPL for SEA–SAF) for winter months during concordant drought events and 6 months before the concordant drought events were analyzed to understand the atmospheric condition leading to concordancy in droughts. Composite SST and OLR anomalies were also explored to gain further insights into the physical factors leading to the two drought concordances (Details in Supplementary section 3.2). Winter months were selected for composite anomalies calculation keeping in view the fact that if the rainy season for a region (for example, the winter season for WNA, MED) (Figure S3.4) is dry and under drought, then other months, which usually receive a lesser amount of precipitation, will most likely be under drought. Also, three out of four regions of selected pairs receive most of its precipitation during boreal winters (Figures S3.4-S3.5) and only “Southeast Asia” receives precipitation throughout the year.

We analyzed the phase and strength of various climatic modes (atmospheric and oceanic circulation mode) during the concordant droughts to explore their association with concordant droughts. Annual SOI computed by taking the average of monthly values over the year was also explored for SEA–SAF concordancy. A month or a year is said to be in El-Niño (La- Niña) phase if monthly or annual SOI is less (greater) than -0.5 (0.5).

3.3. Major Findings

3.3.1. Probability of Droughts

The approach used to identify temporal concordances requires estimation of annual probability of droughts for each region. Since scPDSI is sensitive to precipitation, temperature, and the calibration period (Karl 1986), we first compute the differences in precipitation and temperature among the different hydrologic datasets used here (Table S3.2). These differences in the input datasets and the calibration periods translate to the estimates of annual probabilities and the corresponding temporal concordances (Figures S3.2 and S3.3). Some regions, such as the Mediterranean, Central Europe, Canada and Greenland, and Southern Australia have almost similar probabilities in all the four datasets despite the variations in the data (Table S3.3), which can be attributed to similar long-term changes in precipitation and temperature observed in all datasets (Table S3.2). In general, drought probabilities in the recent decades (1980–2017, Figure S3.2) have drastically increased in most regions as compared to the historical period (1901–2017, Figure S3.3) (Diffenbaugh *et al* 2015, Trenberth *et al* 2007, Xu *et al* 2019), with some exceptions such as the Central North America, where megadroughts like dustbowl lasted for 10 years in the 1930s.

3.3.2. Robust concordances

We present significant robust concordances in Figure 3.1 and Tables S3.4–S3.5. A total of 17 (7) statistically significant and robust concordances were found at 10% (5%) significance levels. We found that some adjacent regions show robust concordance at 10% significance for example “Northern Australia and Southern Australia”, “North East Brazil and Amazon”, “East Asia and Tibet” and others. As suggested by few recent studies, such as Herrera-Estrada *et al* (2019) and Miralles *et al* (2019) droughts can self-intensify due to increased sensible heat flux and regulation of atmospheric boundary layer conditions via land-feedback mechanism, and they can self-propagate by reduced moisture transport and enhanced heat flux from the upwind drought region. Thus, the concordances observed in adjacent regions can be mainly attributed to self-intensification and self-propagation of drought events. Noteworthy, however, are the significant robust temporal concordances in the region pairs that are distant from each other, on the scale of 10000 km, for example, "Southeast Asia—Southern Africa (SEA–SAF)", "Western North America—Mediterranean (WNA–MED)", and others (Table S3.5). We call these concordances "*teleconnections in droughts*". Region pairs "Central Asia—Western Asia" and "Eastern Africa—Western Africa" bear significant concordance in almost all datasets regardless of variations among them, signifying strong temporal interaction of droughts between the regions.

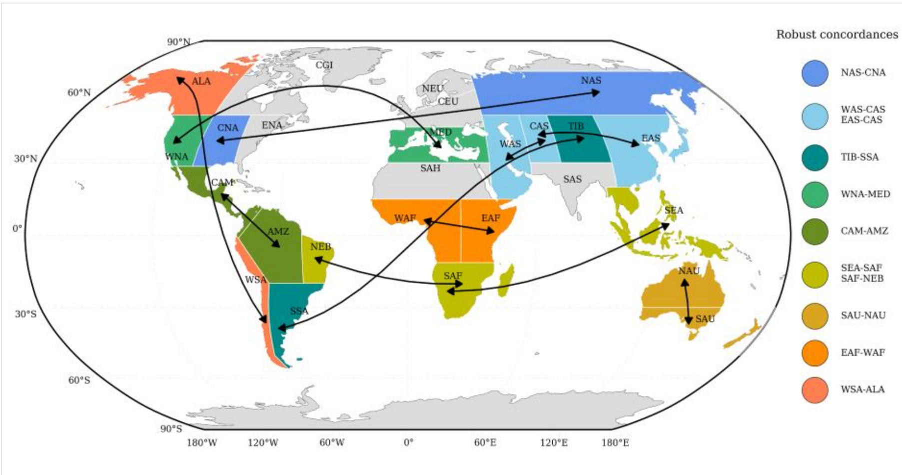

Figure 3.1. *Significant robust concordances identified. Regions with the same color represent robust concordant pairs, while the light-grey colored regions either show zero concordance or concordance is identified in only one dataset.*

Though our focus here is on significant and robust concordances, we note that some region pairs also show significant concordances individually in different datasets (Table S3.4–S3.5) and should be examined in detail in future studies.

3.3.3. Underlying driving factors and connection with climate oscillations

To explore the major driving factors, in terms of atmospheric and oceanic patterns, and to corroborate the teleconnections revealed in the previous section, we further analyzed two robust significant concordant pairs, “WNA–MED” and “SEA–SAF”. These two pairs were selected because the regions there are distant and Western North America (W. N. America) and Southern Africa (S. Africa) endured persistent severe droughts recently (Lund *et al* 2018, Wolski 2018). For WNA–MED robust pair, winter standardized precipitation and temperature anomalies are shown in Figure 3.2. From these, we observe that precipitation, as well as OLR in both regions, is roughly one standard deviation below average; whereas the temperatures in both are near normal. This suggests that the major factor for WNA–MED concordance is the deficit in precipitation. We observe a zonal band of suppressed convection over northern mid-latitudes centred over Western United States and Eastern Russia, which indicates a northward shifting of the jet stream during the teleconnection.

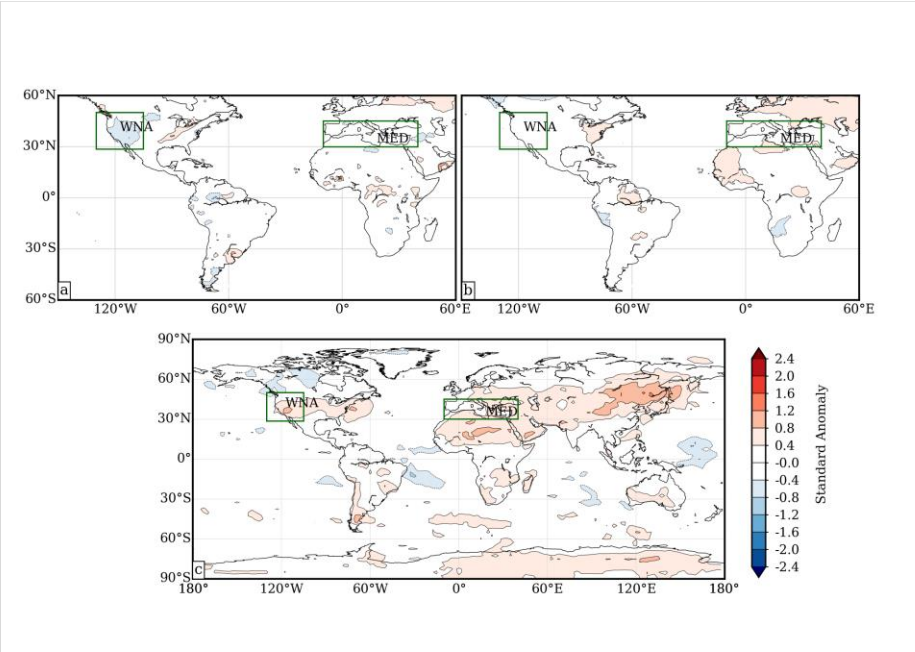

Figure 3.2. *Standardized composite anomaly during the winter concordant months of WNA–MED teleconnection. (a) Precipitation anomalies, (b) Temperature anomalies, and (c) OLR anomalies.*

For SEA–SAF pair, both precipitation deficits and warmer temperatures seem to contribute in driving the teleconnection (Figure 3.3). It has been suggested that precipitation deficits normally initiate droughts and higher temperatures tend to intensify them (Hanel et al., 2018 and Luo et al. 2017). OLR anomalies during the concordant winter months also suggest lack of cloud cover and suppressed convection over both regions. However, the pattern of deep convection in Central Pacific Ocean and suppressed convection in its western pool suggests that the teleconnections in SEA–SAF droughts happen during El–Niño periods. We also observe suppressed convection over west coast of equatorial South America and northern Brazil that may result from the descending branch of the Walker Circulation during El-Niño events (Hill *et al* 2009). In addition, enhanced deep convection is also noted over south of Northern America and subtropical southern America which is often linked with El-Niño via quasi-stationary Rossby wave train (Hill *et al* 2009, Bruick *et al* 2019).

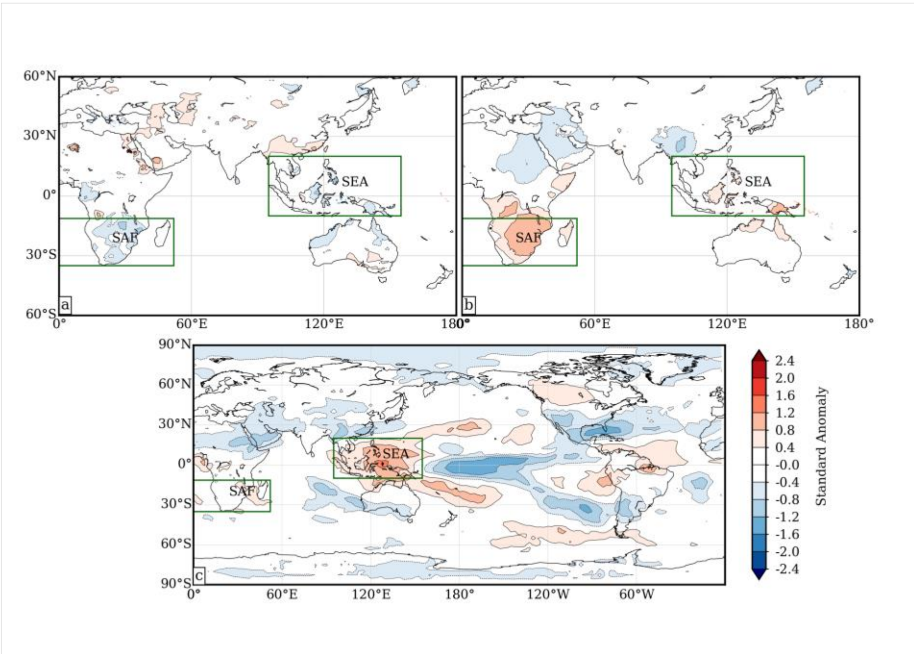

Figure 3.3. *Same as Figure 3.2, but for SEA–SAF pair.*

A peculiar pressure pattern is observed in upper atmospheric levels (at 200hPa) during winter months of WNA–MED concordant droughts (Figure 3.4). Height anomalies at 500hPa also conspicuously depict a similar pressure pattern (Figure S3.6). The persistent ridges over North Pacific and eastern Europe are often associated with the low-frequency planetary waves (Kornhuber *et al* 2019, Wang *et al* 2015b), fueled by the eddy transport of momentum and enthalpy over North

Pacific and North Atlantic Ocean (Nakamura *et al* 1997), respectively. These high-pressure systems divert and/or disrupt storm tracks and block moist air from flowing into W. North. America and Mediterranean (García-Herrera *et al* 2019, Gibson *et al* 2019, Hanel *et al* 2018, Seager *et al* 2015), resulting in below-normal precipitation and above-normal temperatures in both regions and leading to concordant droughts. Several studies have highlighted the role of tropical SST variability (such as ENSO) in the development and maintenance of high-pressure blocking (Swain *et al* 2017, Seager and Henderson 2016, Wang *et al* 2015b). Composite height anomalies (Z_{200hPa} and Z_{500hPa}) six months before concordant droughts also depict mild high-pressure systems near the west coast of W. North America and over Mediterranean favoring onset of persistent droughts in both regions (Hanel *et al* 2018, Seager *et al* 2015), which later translate to concordant drought periods (Figure S3.7).

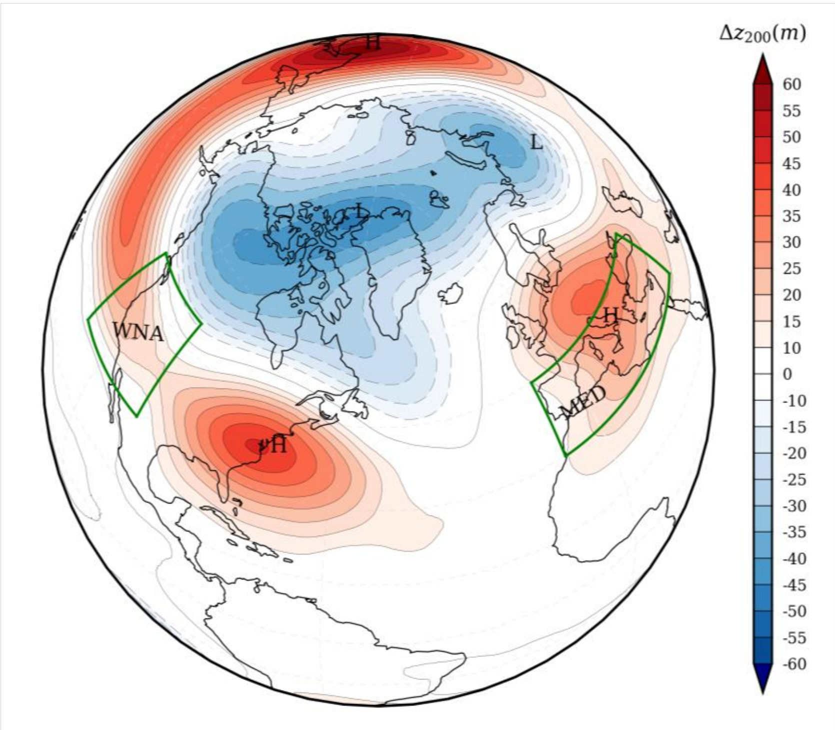

Figure 3.4. *Composite anomalies of geopotential heights at 200 hPa level during winter concordant months for WNA–MED teleconnections. Shading/contours represent composite pressure anomalies, where red shades (blue)/solid lines (dashed) correspond to above (below) normal heights. A similar figure but on cylindrical map projection is given in Figure S3.16.*

Height anomalies presented above resemble strongly with positive phase of the Artic Oscillation (AO+,), positive phase of the North Atlantic Oscillation (NAO+, a close akin to AO+ but local to Atlantic ocean (Ambaum *et al* 2001)), and negative phase of the Pacific–North American teleconnection pattern (PNA−, (Wallace and Gutzler 1981)). About 60% of concordant periods are in positive phase

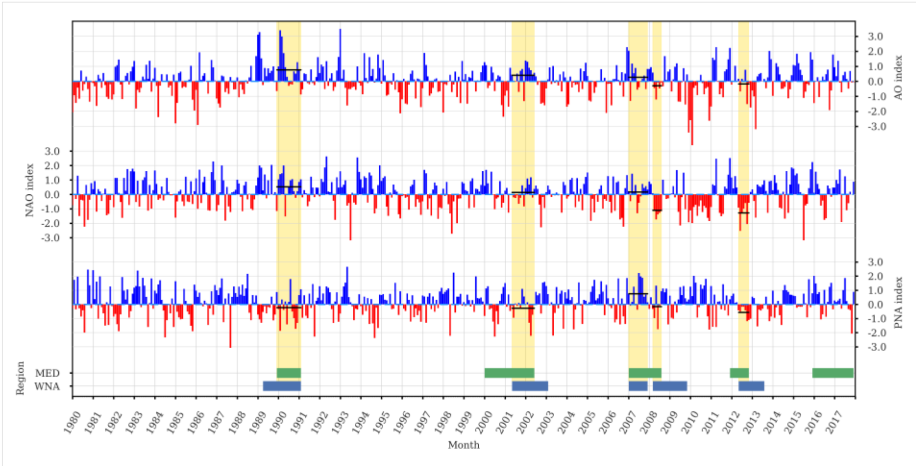

Figure 3.5. *Atmospheric teleconnection patterns AO, PNA and NAO during WNA–MED concordant droughts. About 60% (55%) of total concurrent drought months (golden column) have occurred during positive phase of AO and NAO (negative phase of PNA) (red and blue bar series, red bars represent negative index value, blue bars represent positive index value). Blue and Green horizontal bars represent persistent droughts over Western North America and Mediterranean regions, respectively. For winter concordant months see Figure S3.8.*

of AO and, as expected, a similar fraction of winters are in positive phase of NAO; in addition, negative PNA is also observed in ~60% of the concordant drought months (Figure 3.5). If we only consider concordant winters, about 70% fall in positive AO and ~50% in negative PNA (Figure S3.8). Furthermore, the SST anomalies are persistently negative near the west coast of United States and the eastern equatorial Pacific Ocean, signifying a negative PDO and near-normal phase of ENSO (McCabe *et al* 2004); offshore cold waters lead to reduced inland moisture transport from oceanic basins and tend to favor drought conditions (Figure S3.9). In addition, composite SST anomalies in Atlantic basin remarkably resemble with the positive phase of AMO. About 87% (~67%) of winter concordant months are observed during

PDO– and AMO+ (Figure S3.10). On exploring the role of ENSO in WNA–MED, we noted that about ~70% of concordant winter periods occur when ENSO is in its normal phase and remaining have a tendency to occur during weak La-Niña [considering ONI index] (Figure S3.11). From Figure 3.2, we observe mild convection in the Pacific Ocean near western pool suggesting the normal phase of ENSO and non-significant role of ENSO in WNA–MED teleconnection. These results suggest that AO+, PDO– and PNA– play a significant role in causing WNA–MED drought teleconnections. It is clear then that a coupling of multiple atmospheric patterns may explain all concordant droughts in WNA–MED, a concept similar to *weather regimes* (Baldwin and Dunkerton 2001), such as the *Western Hemisphere circulation* as an association of ridge over North Atlantic and northeast Pacific resembling NAO+ and PNA+ (Tan *et al* 2017).

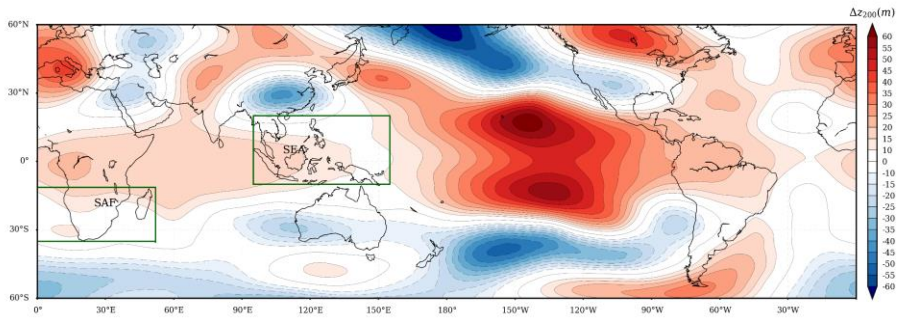

Figure 3.6. *Composite anomalies of geopotential heights at 200hPa level during winter concordant months for SEA–SAF teleconnections. Shading/contours represent composite pressure anomalies, where red shades (blue)/solid lines (dashed) correspond to above (below) normal heights. A similar figure but for the whole globe is given in Figure S3.16 for comparison with composite height of WNA–MED pair.*

Figure 3.6 shows the composite boreal winter anomalies of 200 hPa geopotential heights during the concordant drought events for SEA–SAF robust pair. This pattern remarkably resembles the warm phase ENSO, i.e., El-Niño. The anticyclonic conditions persisting over S. E. Asia and twin cyclones over Southern China and Western Australia (Adames and Wallace 2017) divert upper-level winds towards the cyclonic centres and generate easterlies in lower layers (Figure S3.12), which manifests in weakening of the Walker circulation, leading to precipitation deficits over S. E. Asia (Ropelewski and Folland 2000, Hendon 2003). The localized high-pressure ridge near and over South Africa with anticyclonic flow and decreased strength of *Angola low* (Figure S3.12) hinder the moisture inflow from southwest Indian Ocean and Southeast Atlantic ocean resulting in drying of S. Africa (Pomposi *et al* 2018, Munday and Washington 2017). Composite mean sea level pressure (MSLP) anomalies during the boreal winter months of concordant droughts again conform to El-Niño signature. Persistent warm anomalies in the central/eastern Pacific and cold anomalies in western pool during the winter concordant months (Figure S3.13) also suggest El–Niño as the major cause for SEA–SAF droughts teleconnections. Furthermore, SST anomalies near the west coast of North America are higher than the normal signifying presence of positive PDO.

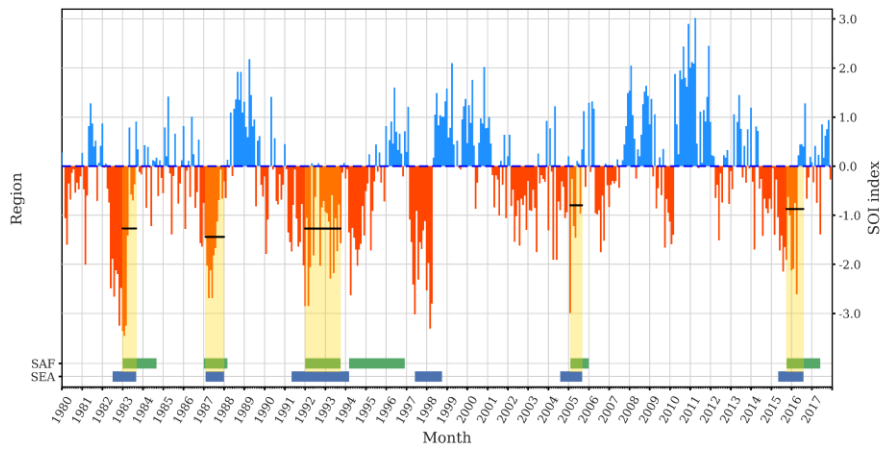

Figure 3.7. *Relationship of SEA–SAF concordant drought events with warm phase of ENSO. All temporally concurrent drought months (golden column) have occurred during negative SOI (red and blue bar series, red bars represent negative SOI, blue bars represent positive SOI), which represents warm phase of ENSO (i.e., El Niño). Blue and Green horizontal bars represent persistent droughts over Southeast Asia and South Africa regions, respectively. Similar plot at annual time scale is given in Figure S3.17.*

For validation, we examined the strength and phase of ENSO events during the concordant drought events in Figure 3.7, which shows the timeseries of Southern Oscillation Index (SOI, the atmospheric counterpart of SST-based El-Niño) and drought periods in the two regions. All concurrent drought events are observed in the second half of the El-Niño phase of ENSO with an average strength of SOI as -0.8, characterizing a moderate to extreme El-Niño. Besides the conventional well-known El-Niño (positive SST anomaly in the Eastern/Central Pacific). Kao and Yu (2000) and Ashok *et al* (2007) have recognized another type of El-Niño that has strong positive SST anomalies in central Pacific; known as "El-Niño Modoki". These studies showed that the two differ in spatial pattern, formation mechanism and influence on global climate. Composite SST anomalies during the SEA–SAF concordance are strongly positive in the eastern and central Pacific and negative in western pool and northwestern Pacific. On comparing SST anomalies of SEA–SAF pair and four dominant EOF modes of SST anomalies in tropical Pacific defined by Ashok *et al* (2007) (see Figure 2 of reference), we found that SST anomalies during SEA–SAF concordancy show remarkable resemblance with the first leading mode of SST anomalies which they call as a conventional well-known El-Niño. To assess the robustness of our results we analyzed multiple SST-based indicators of ENSO during SEA–SAF concordancy and found that all concordant droughts have occurred in El-Niño phase of ENSO (Figure S3.14). Consistent with the results from SOI index, SST-based ENSO indices also highlight the occurrence of concordant drought in the second half of strong El-Niño events. Similar results were obtained with annual SOI, where all concordant droughts are observed during El-Niño. Many studies such as Wang *et al* (2008) and Dong *et al* (2018) have noted that ENSO impact on climate is not stable and is modulated by the phase of PDO. They suggested to consider the phase of PDO when using ENSO as a predictor of climate. We explored the phase of PDO during the SEA–SAF concordant winters and observed that all concordant winters occur in positive phase of PDO (Figure S3.15), which modulates the El-Niño impacts on SEA–SAF teleconnection by amplifying the strength of high pressure over south Africa and southern Indian Ocean that in turn inhibits convection and rainfall (Wang *et al* 2014). In addition, an increased low-level (upper-level) convergence (divergence) in the central pacific during in phase PDO and El-Niño (i.e., PDO+ during El-Niño) manifests increased convection and enhanced ascending branch of walker circulation that tends to strength the atmospheric response and teleconnections of El-Niño (Wang and Liu 2016). No concordant drought is observed when PDO was out of phase with El-Niño (i.e., PDO+/PDO- during La-Niña or PDO- during El-Niño); however, concordant droughts tend to terminate when PDO is out of phase (figure not shown). Consistent with the findings of Wang *et al* (2014) and Nguyen *et al* (2020), we observed increased likelihood of concordant drought conditions in Southern Africa and Southeast Asia during PDO+ and El-Niño in comparison with El-Niño only. Out of five concordant droughts, four have delayed onset in S. Africa as compared to S. E. Asia by about six months (Figure 3.7), suggesting a delayed response of S. Africa to El-Niño, though seasonality in precipitation and other local to global factors may also be responsible (Florenchie *et al* 2003, Masih *et al* 2014). From these results, we infer that SEA–SAF teleconnection is mainly regulated by ENSO and the relationship is modulated by PDO.

3.4. Discussion and conclusions

We observed that during the historical period 1901–2017 of CRU (under calibration 1930–1990), the annual probabilities of droughts are small about “0.096” on an average as compared to the recent decades 1980–2017 (under calibration 1930–1990), where the average probability has drastically increased to '0.141', likely in response to the pronounced drier and hotter climate in response to the global climatic change. The remarkable shift in annual drought probabilities in many regions is alarming and is supported by recent findings over California and South Africa (Swain *et al* 2016, Simpkins 2018).

Precipitation deficit seemed as the main factor in the drought teleconnections of WNA–MED pair; however, we note that temperature is also important in intensifying droughts and its role is more complex, especially in snow-covered regions like WNA and Europe (Luo *et al*

2017). We observed a zonally symmetric height anomaly pattern during the concordant events of WNA–MED pair (Figure 3.4 and Figure S3.16) that suggests poleward shift of the winter jet stream and storm track from their normal positions. A stronger low-pressure system over the Arctic (polar vortex) and northward shifting of jet stream (Figure 3.4) during WNA–MED concordance, which are characteristic features of positive phase of AO, result in hot and dry conditions in the Western North America, the Mediterrenean, and some other mid-latitudinal regions. Consistent with the positive phase of AO, a positive NAO pattern is also observed but is local to the Atlantic basin and Europe. The ridiculously resilient ridge during WNA–MED concordance, a dominant cause of droughts in WNA, forms an indispensable component of the pressure pattern that remarkably resembles the negative PNA pattern. Negative phase of PDO during WNA–MED concordance suggests that off-coast cold waters near the west coast of United States may also contribute in causing precipitation deficits over WNA (McCabe *et al* 2004, Wang *et al* 2015b), and increasing the concordance likelihood in WNA–MED pair. Overall, a weather regime manifesting as a coupling of mainly AO+, NAO+, PNA–, and PDO- is hypothesized as the dominant mode of oceanic and atmospheric variability responsible WNA–MED teleconnection.

We identified a persistent high-pressure system over the tropical Pacific Ocean and twin cyclones over China and Australia during SEA–SAF concordances that result in the weakening of Walker Circulation and precipitation deficits over SEA. The pressure pattern shows a remarkable resemblance with El-Niño phase of ENSO, which is further validated by OLR and SST anomaly patterns. Positive SSTs (warm waters) near west coast of United States during concordance periods feature positive PDO as a decadal modulator of SEA–SAF teleconnection. Consistent with the findings of Ropelewski and Folland (2000) and Vicente-Serrano *et al* (2011), we found 80% of the concordant months in SEA–SAF pair during El Niño, suggesting a strong relationship between the SEA–SAF teleconnection and El Niño.

This relationship, however, is strongly dependent on the phase of PDO. We observed all concordant droughts when PDO was in phase with El Niño (i.e. PDO+ during El Niño), whereas no concordant drought was noted when PDO was out of phase with El Niño. However, concordant droughts in SEA–SAF pair tend to terminate when PDO is out of phase with El-Niño (figure not shown). The strengthening (weakening) of El-Niño impacts on SEA–SAF concordancy during PDO+ (PDO-) is consistent with the results of few recent studies such as Dong and Dai (2015), Nguyen *et al* (2020) and Wang *et al* (2014). The intensification of Walker Circulation in the central Pacific by PDO+ tends to strengthen the teleconnections of El Niño, which results in increased high pressure over South Africa, Southern Indian Ocean, and Western Pool of Pacific Ocean, and therefore, inhibits convection and rainfall over the regions (Wang *et al* 2014, Nguyen *et al* 2020). Though all concordant droughts here can be explained by El Niño dynamics alone, ignoring the phase of PDO may result in inaccurate estimation/prediction of future concordant droughts in SEA–SAF pair. Besides climatic oscillations and SST, other phenomena such as land-atmosphere feedback mechanisms, moisture transport and others may also lead to concordant droughts (Herrera-Estrada *et al* 2019, Masih *et al* 2014, Miralles *et al* 2019).

An implicit assumption in our analysis of concordancy estimation and significance tests is that annual droughts are independent events, which in some cases may not be valid since multi-year droughts are not uncommon in many regions. The seasonal variability in precipitation may affect concordant drought frequency estimation. Here, we only analyzed droughts that last more than 12 months to account for the creeping nature of droughts and administer to seasonality of precipitation.

Notwithstanding these limitations, we believe that the results presented here provide strong evidence of global teleconnections in droughts, their major driving factors, and their relationship with long-wave climatic oscillations. Our study complements the work on 'teleconnections in extreme precipitation events and globally synchronous crop failure' reported recently.

We stress that though major physical insights into the causes of teleconnections are given in this study, in-depth analysis on causal mechanisms is beyond the scope, and it is imperative to understand the physical processes underlying the observed concordances, their representation in global circulation models, and their impact on the global crop production and food security. Moreover, we recommend testing the robustness of our findings using multiple but long-term datasets.

APPENDIX-B: Supporting Information

Supplementary Text

3.1. Drought indices.

Several drought indices (Table S3.a) have been developed in recent decades to quantify various types of droughts. Here, we use the Self Calibrated Palmer Drought Severity Index (scPDSI) (Palmer 1965, Wells *et al* 2004).

Table S3.a. Types of droughts, their quantifying index, and primary moisture variables

Type of Drought	**Drought index**	**Primary variable**
Meteorological drought	SPI,	Precipitation
	SPEI, PDSI, scPDSI	Precipitation, and Temperature
Agricultural drought	CMI,	Soil moisture
Hydrological drought	SRI, SDDI	Runoff
Socio-economic drought		Water resources

3.2. Self-Calibrated Palmer Drought Severity Index (sc-PDSI)

3.2.1. Palmer Drought Severity Index (PDSI)

PDSI developed by (Palmer 1965) begins with a simple water balance method considering a 2-layer bucket model for soil moisture, a surface layer having a maximum moisture-holding capacity of 25.4mm (1 inch) and underlying layer with rest of the available water content (AWC). For every month, four potential and four actual variables are calculated (Wells *et al* 2004). Pote ntial evapotranspiration (PET) representing maximum possible outflow to the atmosphere is a critical variable. We used the Thornthwaite estimate of PET (Thornthwaite 1948) because of its simple computations and only negligible differences in the computed scPDSI when using Thornthwaite and Penman-Monteith PET estimates (Dai 2011a, Van der Schrier *et al* 2011). Calculation formulas for all the variables are given in Table S3.b and for details please refer (Palmer 1965, Alley 1984). Four water balance coefficients, which act as weighting factors for Climatically Appropriate for Existing Conditions (CAFEC) Precipitation ($\acute{P}$) are calculated from the potential and actual variables values over the calibration period as:

$$\alpha_j = \frac{\overline{ET_j}}{\overline{PET_j}}\ ;\ \beta_j = \frac{\overline{R_j}}{\overline{PR_j}}\ ;\ \gamma_j = \frac{\overline{RO_j}}{\overline{PRO_j}}\ ;\ \delta_j = \frac{\overline{L_j}}{\overline{PL_j}}$$

$$\text{where}\ , j = 1, 2, 3, \ldots, 12. \qquad [S3.1]$$

Table S3.b. Calculation formulas for potential and actual variable values.

<table>
<tr><th>Variable</th><th>Calculation formula</th><th>Terms used</th></tr>
<tr><td>Potential Loss (PL)</td><td>$PL = PL_s + PL_u$
$PL_s = \min(PET, S_s)$
$PL_u = \min\left(\frac{(PET - PL_s)S_u}{AWC}, S_u\right)$</td><td rowspan="6">$S_s =$ Available moisture in the surface layer at the beginning of the month
$S_u =$ Available moisture in the underlying layer at the beginning of the month
$PL_s =$ Potential loss in the surface layer
$PL_u =$ Potential</td></tr>
<tr><td>Potential Recharge (PR)</td><td>$PR = AWC - (S_s + S_u)$</td></tr>
<tr><td>Potential Runoff (PRO)</td><td>$PRO = AWC - PR$</td></tr>
<tr><td>Potential Evapotranspiration (PET)</td><td>Thornthwaite method (Thornthwaite 1948)</td></tr>
<tr><td>Actual Loss (L)</td><td>$L = L_s + L_u$
$L_s = \min\big((PET - P), S_s\big)$
$L_u = \min\left(\frac{\big((PET - P) - L_s\big)S_u}{AWC}, S_u\right)$</td></tr>
<tr><td>Actual Evapotranspiration (ET)</td><td>$ET = PET \quad \text{if } P > PET$
$ET = P + L \quad \text{if } P < PET$</td></tr>
</table>

Actual Recharge (R)	$R = \min(P - PET, PR)$	loss in the underlying layer L_s = Actual loss in the surface layer L_u = Actual loss in the underlying layer
Actual Runoff (RO)	$RO = P - ET - R$	

Where j ranges over calendar months and overbar represents the mean value of the j^{th} calendar month. Potential values weighted with corresponding water balance coefficients form $\acute{P}$ for each month, which is the amount of precipitation required to maintain the normal soil moisture. Computation of $\acute{P}$ uses a simple water budget model where Precipitation is equal to Evapotranspiration + Runoff $\pm$ change in soil moisture storage.

$$\acute{P} = \alpha_j PET + \beta_j PR + \gamma_j PRO - \delta_j PL \qquad [S3.2]$$

The moisture departure (d) for each month is then calculated, that is the excess or deficit of actual precipitation from CAFEC precipitation.

$$d = P - \acute{P} \qquad [S3.3]$$

The moisture departure (d) values need to be corrected to make them spatially and temporarily comparable because same d values mean different at different time and location. This correction is made by weighing d with k, which is Palmer's approximation of climate characteristic of a location. Palmer derived equations for k are as under:

$$k_j' = 1.5 \log_{10}\left(\frac{\frac{\overline{PET}_j + \bar{R}_j + \overline{RO}_j}{\bar{P}_j + \bar{L}_j} + 2.8}{D_j}\right) + 0.5 \qquad [S3.4]$$

$$k_i = \frac{17.67}{\sum_{i=1}^{12} D_j k_j'} k_i' \qquad [S3.5]$$

Where, D_j is average of absolute values of d values for j^{th} calendar month and k' is the initial approximation of climate characteristics. The value 17.69 in equation 5 is an empirical constant that Palmer derived from data of nine sites in the central United States (Palmer 1965). This limits the spatial compatibility of PDSI only to Central North America (Palmer study area), although its purpose is to make d values spatially comparable (Alley 1984).

A moisture anomaly index (Z) also known as Z- index result from the multiplication of moisture departure d and k. The Z index gives information about wetness or dryness in a single month without regard to present precipitation trends (Palmer 1965, Alley 1984).

$$Z = kd \qquad [S3.6]$$

The Palmer's general formula for the computation of the PDSI using the Z- index is as:

$$X_i = 0.897X_{i-1} + \left(\frac{1}{3}\right)Z_i \qquad [S3.7]$$

Here X_i and X_{i-1} is PDSI for current and previous month, while Z_i is moisture anomaly for the current month. The values 0.897 and $\frac{1}{3}$ are defined as duration factors that were empirically derived from data of two locations (Western Kansas and central Iowa). For more details on the computational procedure and algorithm of PDSI refer to (Palmer 1965, Alley 1984, Wells *et al* 2004).

3.2.2. Self-calibration of PDSI

(Wells *et al* 2004) developed an algorithm to replace the empirically developed climate characteristic (k) and duration factors $\left(0.897 \text{ and } \frac{1}{3}\right)$ by automatically calculated self-calibrated coefficients. scPDSI determines the duration factors for wet (p_w and q_w) and dry (p_d and q_d) spell for each location separately. The durations factors are computed using the least-squares method for both extremely wet and extremely dry condition of accumulated moisture anomaly (Z- index using initial estimate of climate characteristics ($Z = k'd$)). The calculation algorithm is discussed in detail in (Jacobi *et al* 2013). The

2nd and 98th percentile of initial estimate of PDSI computed using Z-index ($Z = k'd$) and duration factors ($p_w, p_d, q_{w,}$and q_d) is utilized in the calculation of calibrated climate characteristic (K) as follows:s

$$K_i = \begin{cases} k_i' \left(\frac{-4.00}{2^{nd}\ \text{percentile of PDSI}}\right) & \text{if } d_i < 0 \\ k_i' \left(\frac{4.00}{98^{th}\ \text{percentile of PDSI}}\right), & \text{if } d_i \geq 0 \end{cases} \qquad [S3.8]$$

The final estimate of Z-index is computed by weighting d with K (Z=Kd) that is then used for calculation of scPDSI as under:

$$\text{scPDSI} = X_i = \begin{cases} p_w X_{i-1} + q_w Z_i, & \text{if } Z_i > 0 \\ p_d X_{i-1} + q_d Z_i, & \text{if } Z_i \leq 0 \end{cases} \qquad [S3.9]$$

3.3. Underlying driving factors

The drought index used here involves both precipitation and temperature for the computation of index value. To understand the relative contribution of precipitation deficit and warmer temperature during a drought period, we computed the standardized precipitation and temperature anomalies for the same period (details given below). These anomalies give a qualitative idea about the portioning of precipitation and temperature during the drought period. Anomalies for a calendar month (say January) during concordant droughts are computed as the difference between the mean value during concordant drought months (Januarys under drought) and the mean value for remaining non-drought months (all Januarys excluding drought months). Similarly, pressure anomalies for other calendar months are calculated and the mean of winter months (October–March) represent the composite anomaly during the concordant drought events. The same procedure is adopted to compute SST, OLR anomalies and composite pressure anomalies for six months before droughts. Standardization was carried out by dividing the anomaly of each calendar month (for example, say January) by the respective standard deviation of non-drought months (all Januarys excluding drought months).

All the El-Niño event years reproduced here by monthly or annual SOI are consistent with El-Niño years defined by NOAA using

ONI index with little inconsistencies in the years when ENSO phase changes (https://origin.cpc.ncep.noaa.gov/products/analysis_monitoring/ensostuff/ONI_v5.php)

Supplementary Tables

Table S3.1. *Region definitions given in IPCC AR 5 (SREX)*

Region No.	Region name	Region
1	Alaska	Alaska/N.W. Canada
2	Greenland	Canada/Greenland/Iceland
3	W. N. America	Western North America
4	C. N. America	Central North America
5	E. N. America	Eastern North America
6	C. America/Mexico	Central America/Mexico
7	Amazon	Amazon
8	N.E. Brazil	North Eastern Brazil
9	S. America	Coast South America
10	S.E. South America	South-eastern South America
11	N. Europe	Northern Europe
12	C. Europe	Central Europe
13	Mediterranean	Southern Europe/Mediterranean
14	Sahara	Sahara
15	W. Africa	Western Africa
16	E. Africa	Eastern Africa
17	S. Africa	Southern Africa
18	N. Asia	Northern Asia
19	W. Asia	Western Asia
20	C. Asia	Central Asia
21	Tibetan	Tibetan Plateau
22	E. Asia	Eastern Asia
23	S. Asia	Southern Asia
24	S.E. Asia	South-eastern. Asia
25	N. Australia	Northern Australia
26	S. Australia	Southern Australia/New Zealand

__Table S3.2.__ Difference of P (ΔP), T (ΔT), and T (ΔET) of the datasets for the period 1980 to 2017 from CRU data over period 1930-1990.

	Datasets								
	CRU 1980-2017			**MERRA2 1980-2017**			**ERA5 1980-2017**		
Region	**ΔP (mm)**	**ΔT (°C)**	**ΔET (mm)**	**ΔP (mm)**	**ΔT (°C)**	**ΔET (mm)**	**ΔP (mm)**	**ΔT (°C)**	**ΔET (mm)**
ALA	5.76	0.99	9.57	249.13	1.28	102.85	189.02	1.22	86.91
CGI	16.17	0.62	6.71	83.97	0.28	31.92	19.68	-0.35	22.66
WNA	12.22	0.54	8.83	30.73	0.54	29.26	84.83	0.47	40.04
CNA	49.15	0.39	25.30	56.79	0.36	29.50	68.86	0.53	37.46
ENA	47.12	0.44	15.41	-18.56	-0.43	-4.49	33.66	0.27	5.99
CAM	20.72	0.44	27.51	-329.69	-1.11	-105.24	270.12	-0.69	-12.59
AMZ	5.36	0.31	38.23	-150.05	-0.45	-107.59	112.51	-0.51	-63.68
NEB	-8.91	0.57	18.23	-109.83	-0.25	-68.06	-116.84	0.25	-73.39
WSA	-25.54	0.22	-1.49	-138.57	-0.11	-35.68	714.27	-0.56	87.35
SSA	62.55	0.33	34.90	132.27	0.47	76.58	217.12	0.55	106.00
NEU	58.91	0.62	21.07	185.78	-0.42	34.90	80.65	0.27	45.66
CEU	13.47	0.82	15.55	37.33	0.00	8.50	107.40	0.52	30.67
MED	-17.76	0.62	-1.37	-63.69	-0.08	-10.00	-3.24	0.31	-2.85
SAH	-6.07	0.56	-3.81	-6.97	-0.19	-4.41	-31.63	0.11	-28.93
WAF	-53.64	0.32	-8.68	-25.14	-0.14	-68.13	-68.72	0.12	-85.70
EAF	-10.74	0.58	15.20	43.15	-0.08	-8.02	120.42	0.35	-23.98
SAF	-23.19	0.50	-5.70	24.11	0.48	-15.50	9.15	0.31	-8.94
NAS	10.91	0.97	8.32	189.96	1.12	50.28	127.78	1.41	45.26
WAS	-1.34	0.73	3.60	-45.53	0.88	-29.83	46.67	0.97	12.49
CAS	13.67	0.84	12.45	-64.13	0.91	-24.47	121.10	0.02	55.17
TIB	10.77	0.80	8.65	-27.36	1.58	-14.99	153.61	-0.03	43.44
EAS	-4.56	0.64	4.45	-90.97	0.08	-36.41	120.86	0.23	10.71
SAS	-24.91	0.42	4.45	-295.25	0.02	-108.76	110.48	-0.29	-35.72
SEA	11.75	0.32	31.24	-477.10	-1.20	-207.39	197.31	-0.79	-86.77
NAU	21.71	0.50	24.50	-23.35	0.27	-7.04	-71.28	0.47	-38.72
SAU	-15.99	0.55	7.04	-140.90	0.77	-11.64	-114.77	0.71	-14.50

Table S3.3. *Annual drought probability in the regions for different datasets and calibration periods.*

Region	Calibration period			
	Jan 1930 to Dec 1990	**Jan 1980 to Dec 2017**		
	CRU 1980-2017	**CRU 1980-2017**	**ERA5 1980-2017**	**MERRA2 1980-2017**
ALA	0.000	0.053	0.053	0.000
CGI	0.000	0.000	0.000	0.053
WNA	0.237	0.316	0.184	0.237
CNA	0.000	0.105	0.211	0.184
ENA	0.000	0.132	0.132	0.079
CAM	0.132	0.184	0.289	0.263
AMZ	0.184	0.105	0.158	0.184
NEB	0.289	0.158	0.158	0.211
WSA	0.263	0.237	0.263	0.368
SSA	0.026	0.132	0.184	0.132
NEU	0.000	0.079	0.053	0.026
CEU	0.079	0.053	0.079	0.105
MED	0.237	0.132	0.211	0.211
SAH	0.053	0.105	0.605	0.632
WAF	0.342	0.105	0.342	0.184
EAF	0.368	0.105	0.289	0.263
SAF	0.289	0.158	0.184	0.263
NAS	0.000	0.000	0.105	0.053
WAS	0.158	0.158	0.316	0.316
CAS	0.105	0.132	0.211	0.237
TIB	0.053	0.132	0.158	0.105
EAS	0.105	0.026	0.184	0.053
SAS	0.211	0.158	0.289	0.289
SEA	0.289	0.184	0.158	0.263
NAU	0.105	0.184	0.263	0.289
SAU	0.132	0.105	0.105	0.132

Table S3.4. *Concordance measures under independence assumption (expected concordance probability "value without any bracket") and observed concordance probability ("value within bracket") along with p-value ("value within square brackets") for the hypotheses given in Methods section*

		Jan 1930 - Dec 1990	**Jan 1980 - Dec 2017**		
Significant Concordant Pair	**Distance (Km)**	**CRU 1980-2017**	**CRU 1980-2017**	**MERRA2 1980-2017**	**ERA5 1980-2017**
WAS - CAS	1775.5	0.08 (0.02) [0.03]	0.08 (0.02) [0.04]	0.18 (0.07) [0.02]	0.18 (0.07) [0.01]
EAF - WAF	4005	0.18 (0.13) [0.2]	0.08 (0.01) [0.01]	0.16 (0.05) [0.01]	0.18 (0.1) [0.08]
CAM - AMZ	3834	0.08 (0.02) [0.06]	0.08 (0.02) [0.04]	0 (0.05) [1]	0.05 (0.05) [0.52]
SEA - SAF	11665	0.16 (0.08) [0.09]	0.08 (0.03) [0.1]	0.08 (0.07) [0.5]	0.03 (0.03) [0.67]
SAU - NAU	2518	0.05 (0.01) [0.1]	0.08 (0.02) [0.04]	0.08 (0.04) [0.18]	0.05 (0.03) [0.28]
CAM - NEB	6073	0.11 (0.04) [0.06]	0.05 (0.03) [0.3]	0 (0.06) [1]	0.11 (0.05) [0.09]
NEB - AMZ	2320	0.16 (0.05) [0.01]	0.05 (0.02) [0.13]	0.11 (0.04) [0.06]	0.03 (0.02) [0.62]
WNA - MED	10218	0.16 (0.06) [0.02]	0.08 (0.04) [0.21]	0.11 (0.05) [0.12]	0.11 (0.04) [0.06]
SAF - NEB	6830	0.16 (0.08) [0.09]	0.05 (0.02) [0.24]	0.11 (0.06) [0.16]	0.08 (0.03) [0.1]
TIB - SSA	16763	0.03 (0.0) [0.05]	0.05 (0.02) [0.14]	0 (0.01) [1]	0.11 (0.03) [0.02]
WSA - ALA	12268	0 (0.0) [1]	0.05 (0.01) [0.08]	0 (0) [1]	0.05 (0.01) [0.1]
SSA - WNA	10772	0.03 (0.01) [0.21]	0.13 (0.04) [0.02]	0.05 (0.03) [0.33]	0.11 (0.03) [0.04]

NAS - SSA	17403	0 (0.0) [1]	0 (0.0) [1.0]	0.05 (0.01) [0.03]	0.08 (0.02) [0.04]
TIB - CAS	1704	0 (0.01) [1]	0 (0.02) [1.0]	0.08 (0.02) [0.07]	0.11 (0.03) [0.04]
EAS - CAS	4818	0.03 (0.01) [0.35]	0 (0.0) [1.0]	0.05 (0.01) [0.08]	0.11 (0.04) [0.06]
EAS - TIB	3123	0.03 (0.01) [0.19]	0.03 (0.0) [0.12]	0.05 (0.01) [0.02]	0.16 (0.03) [0]
NAS - CNA	8765	0 (0.0) [1]	0 (0.0) [1.0]	0.05 (0.01) [0.05]	0.08 (0.02) [0.05]

Table S3.5. *Region pairs showing robust concordances at 10% and 5% significance level. Each column represents statistical significance of robust pair (✔ → significant at 5%, ✓ → significant at 10% and empty box → Not significant) for corresponding dataset.*

Robust Concordant Pair	Distance (Km)	Jan 1930 - Dec 1990	Jan 1980 - Dec 2017		
		CRU 1980-2017	**CRU 1980-2017**	**MERRA 2 1980-2017**	**ERA5 1980-2017**
WAS – CAS**	1775.5	✔	✔	✔	✔
EAF – WAF**	4005		✔	✔	✓
CAM – AMZ*	3834	✓	✔		
SEA – SAF*	11665	✓	✓		
SAU – NAU*	2518	✓	✔		
CAM – NEB*	6073	✓			✓
NEB – AMZ*	2320	✔		✓	
WNA – MED*	10218	✔			✓
SAF – NEB*	6830	✓			✓
TIB – SSA**	16763	✔			✔
WSA – ALA*	12268		✓		✓
SSA – WNA**	10772		✔		✔
NAS – SSA**	17403			✔	✔
TIB – CAS*	1704			✓	✔
EAS – CAS*	4818			✓	✓
EAS – TIB**	3123			✔	✔
NAS – CNA**	8765			✔	✔

** represents concordant pair present at least in two datasets at 5% significance level.

* represent at concordant pair present 10% significance level

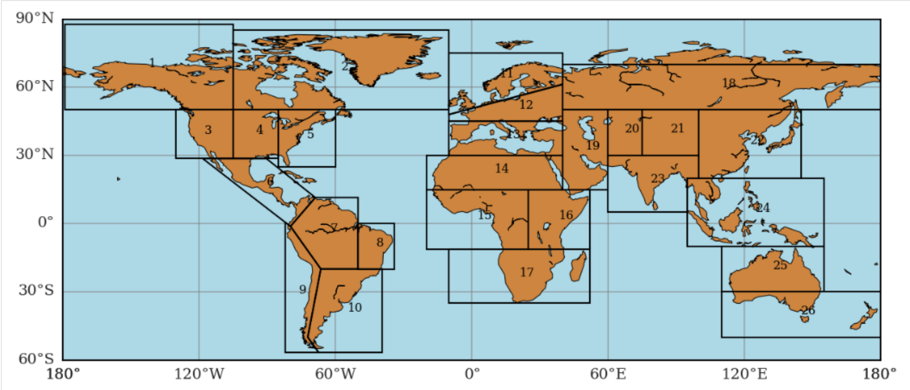

Figure S3.1. *Region defined in IPCC AR5 SREX. Minor modifications are done for Region 1 (ALA) and Region 3 WNA). Short names and full details of the regions (subcontinents and countries included in the regions) are given in Table S3.1.*

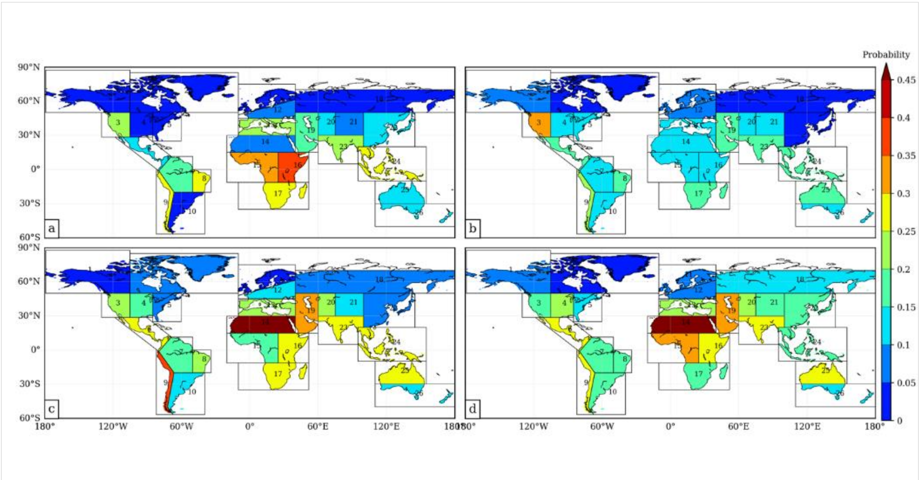

Figure S3.2. *Regional annual drought (scPDSI <-2, area under drought >25%, duration = 12 months, at least 6 months of a year are under drought) probability (a) CRU data 1980 to 2017 using calibration period Jan 1930 to Dec 1990, (b) CRU data 1980 to 2017 using calibration period Jan 1980 to Dec 2017, (c) MERRA2 data using calibration period Jan 1980 to Dec 2017, and (d) ERA5 data using calibration period Jan 1980 to Dec 2017.*

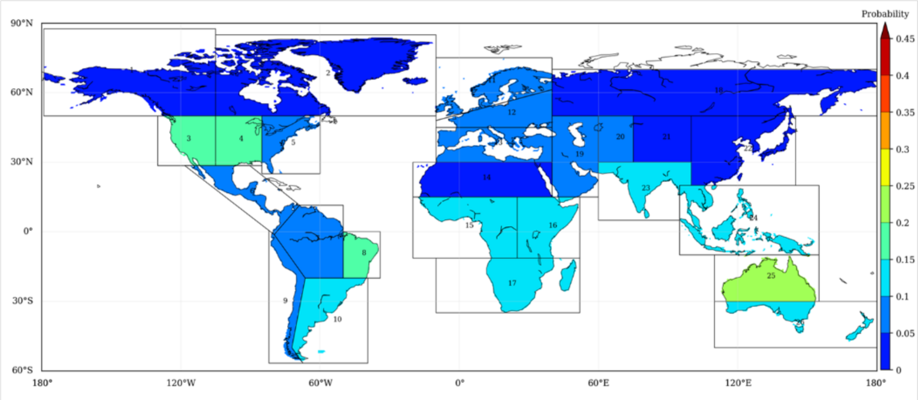

Figure S3.3. *Regional annual drought (scPDSI <-2, area under drought >25%, duration = 12 months, at least 6 months of a year are under drought) probability based on historical CRU data (Jan. 1901 to Dec. 2017, 117 years of data).*

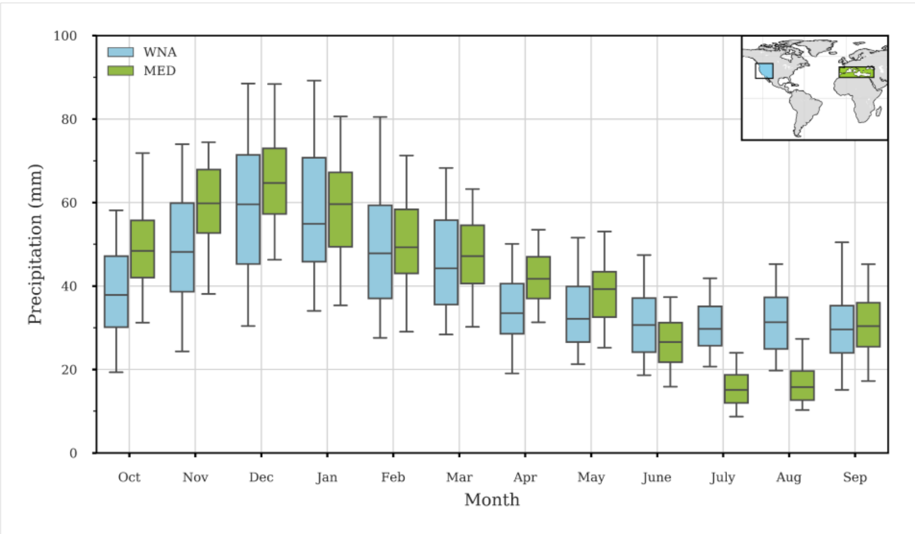

Figure S3.4. *Monthly precipitation distribution for WNA and MED regions. The upper and lower boundary of boxes corresponds to 25th and 75th percentile while as the upper and lower whiskers represent 5th and 95th percentile of precipitation of that month. The middle line of bars shows the median of monthly precipitation. Both WNA and MED lie in Northern hemisphere extra tropics and receives most of their precipitation during winter, October to March.*

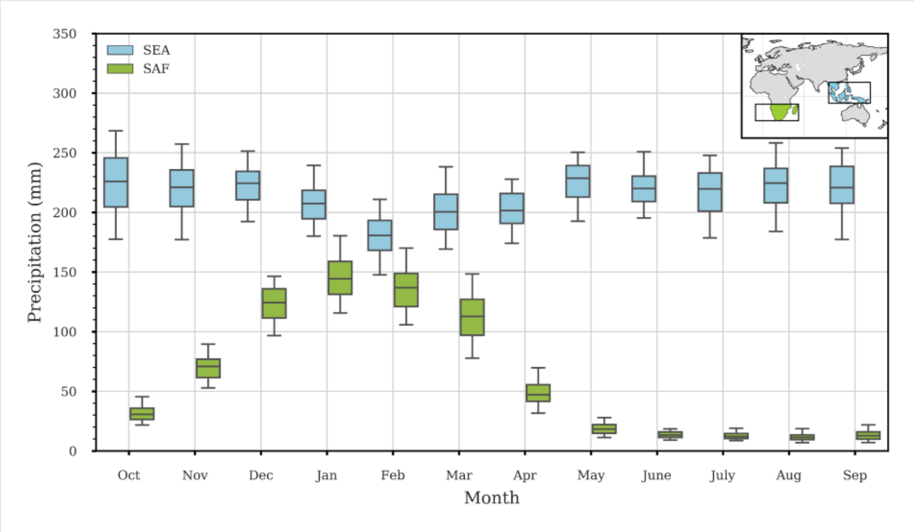

Figure S3.5. *Same as Figure S3.4 but for SEA and SAF regions. SEA has uniformly distributed precipitation throughout the year, while SAF receives most of its precipitation during October to March.*

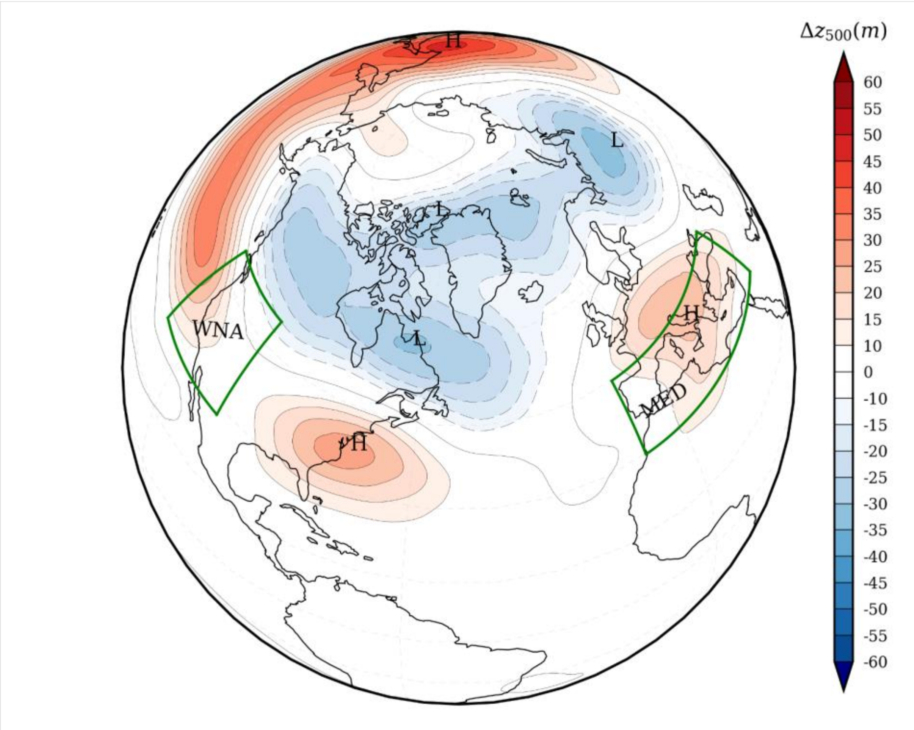

Figure S3.6. *Similar to Figure 3.4 of the main text but shows 500hPa composite winter months anomalies during concordant droughts for WNA–MED pair. Shading/contours represent average pressure anomalies during concordant winter months in "meters", red (blue)/solid (dashed) corresponds to above (below) normal geopotential height at 500hPa and inter contour spacing is 5m.*

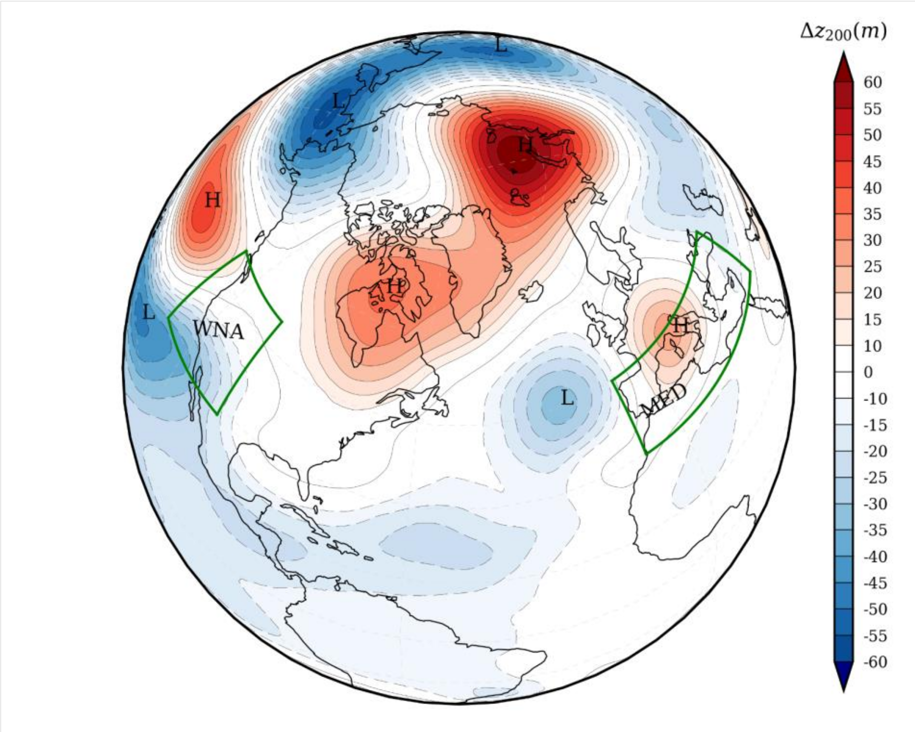

Figure S3.7. *Similar to Figure 3.4 of the main text but shows 200 hPa composite winter months anomalies 6 months before concordant droughts for WNA–MED pair.*

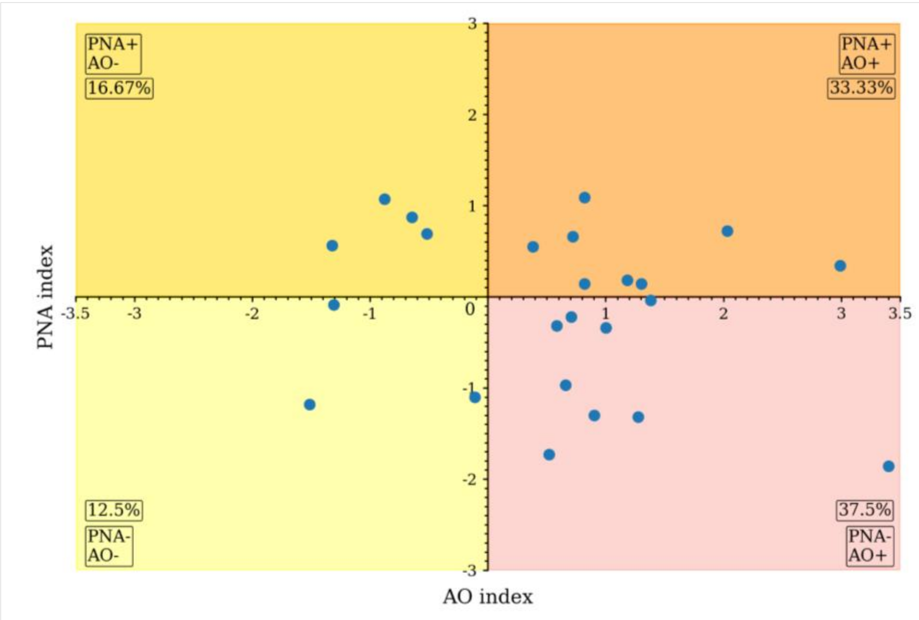

Figure S3.8. *Phase and strength of AO and PNA index during the winter concordant months of WNA–MED pair. AO is positive for about 17 months (~70%) and PNA is negative for 12 months (~50%).*

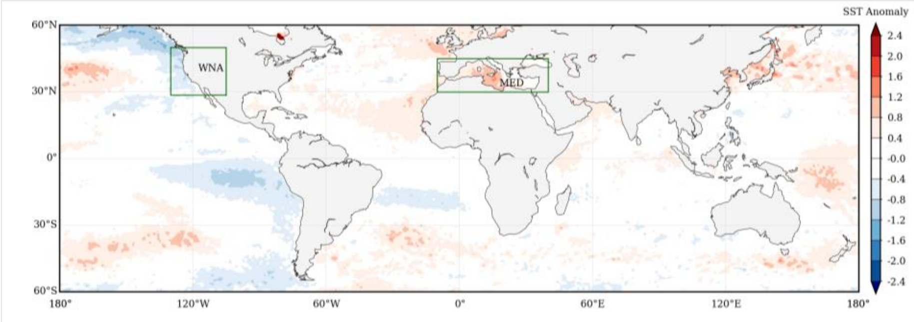

Figure S3.9. *Composite SST standard anomalies during the winter concordant months of WNA–MED teleconnection. SST anomalies are negative near the west coast of United States and equatorial eastern Pacific and positive in central and western north Pacific which strongly resembles with the negative phase of PDO and near normal La–Niña. In Atlantic Ocean, mild to normal AMO+ is observed.*

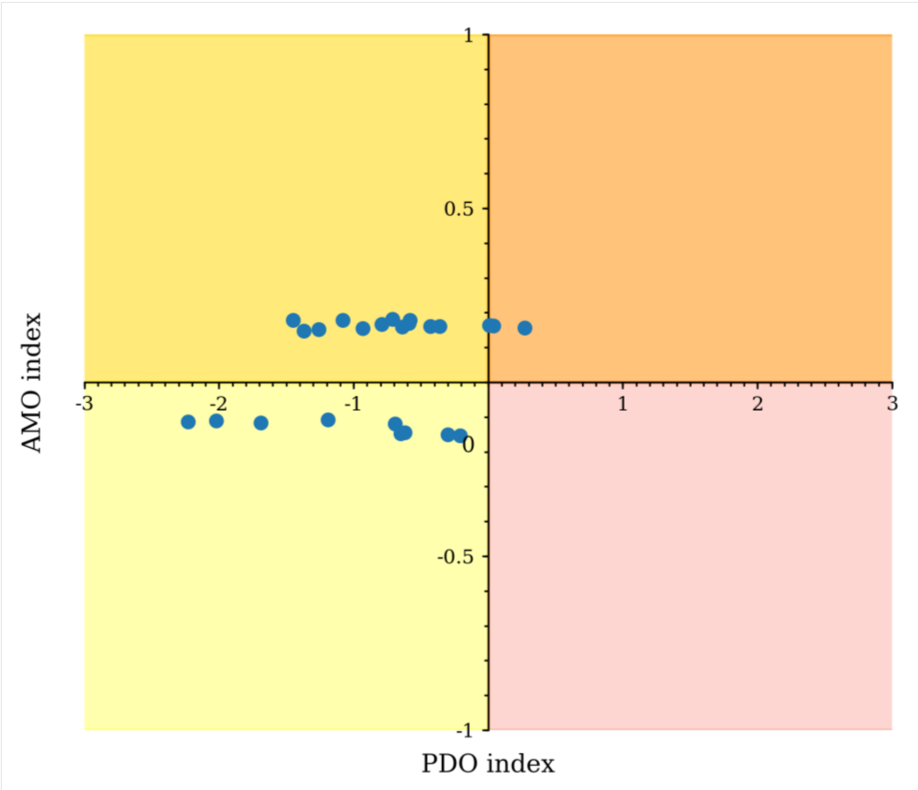

Figure S3.10. *Phase and strength of AMO and PDO index during the winter concordant months of WNA–MED pair. PDO is negative for about 21 months (~87%) and AMO is positive for 15 months (~62%).*

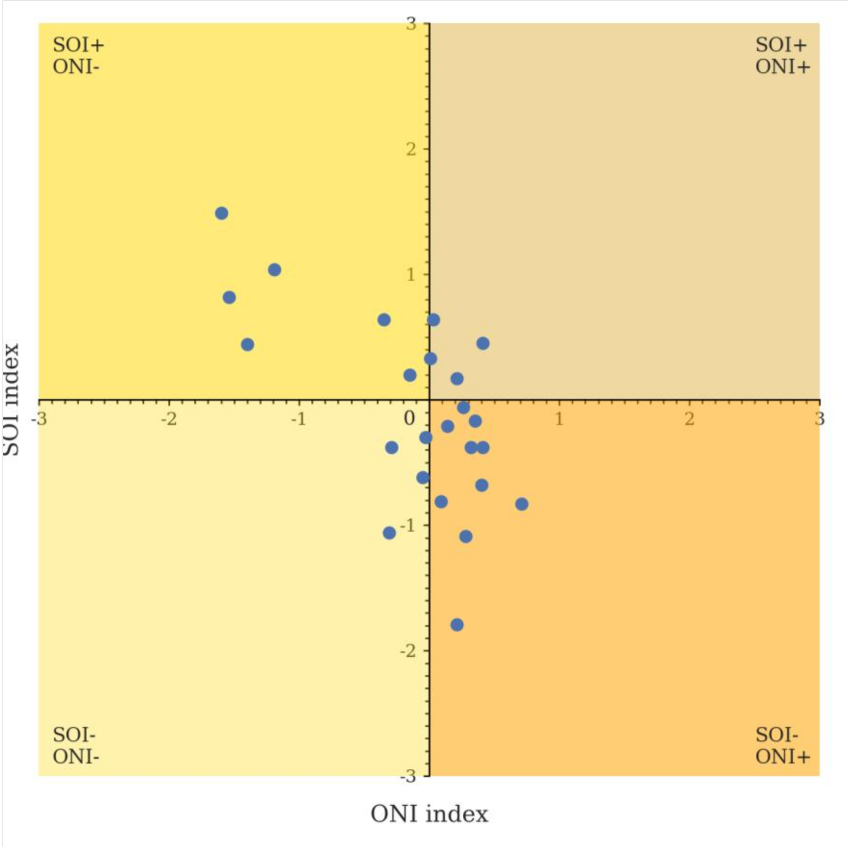

Figure S3.11. *Similar to Figure S3.9 but showing SOI and ONI index during the winter concordant months of WNA–MED pair. SOI is positive (negative) for 10 (14) months [42% (~58%)], while as ONI is positive (negative) during 14(10) months [42% (~58%)]. However, most of them (~60–80%) are in the range of -0.5 to 0.5 representing normal phase of ENSO.*

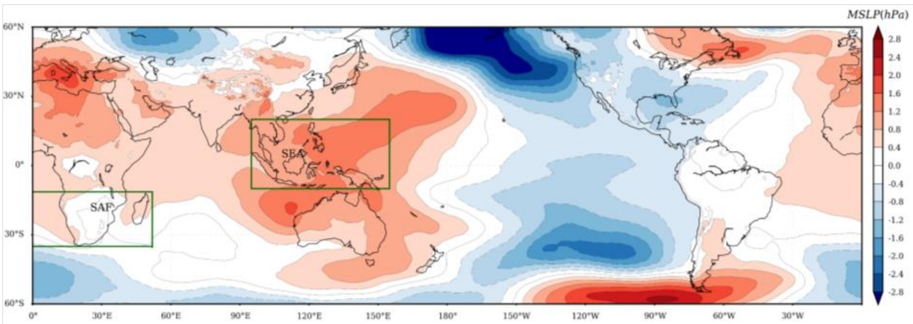

Figure S3.12. *Composite boreal winter MSLP anomalies during concordant drought events in SEA and SAF regions. Strong high pressure is observed over the western pool of Pacific Ocean and Darwin (Australia) and low pressure over the south of central Pacific Ocean and Tathti (south of central Pacific) the pattern; strongly resembles the El-Niño phase of ENSO.*

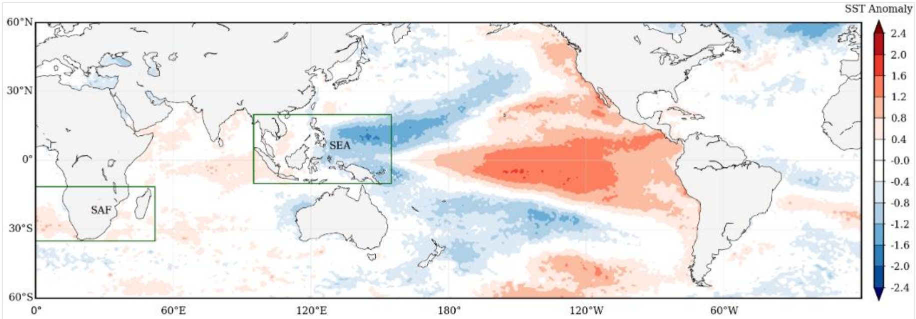

Figure S3.13. *Composite SST standard anomalies during the winter concordant months of SEA–SAF teleconnection. SST anomalies are negative near the western pool and SEA and positive in central and eastern north equatorial Pacific which is the dominant feature of El–Nino in Pacific Ocean.*

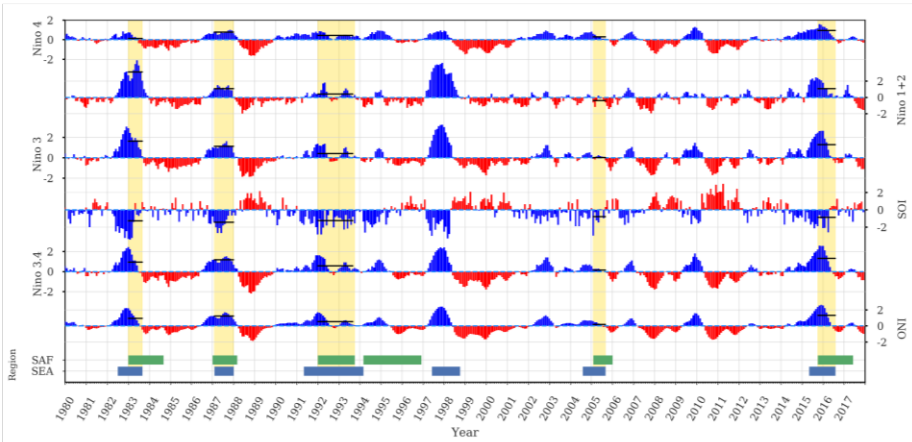

Figure S3.14. *Similar to Figure 3.7 of main text but showing the relationship of SEA–SAF concordant drought events with ENSO indices; SST based [(Oceanic Niño Index) ONI, Niño 3.4, Niño 3, Niño 1+2 and Niño 4] and atmospheric based [SOI index]. Red bars represent La-Niña and blue bars represent El-Niño Blue and Green horizontal bars represent persistent droughts over Southeast Asia and Southern Africa regions, respectively, while the golden bars highlight concordant periods. All indices highlight significant role of El-Niño in SEA–SAF concordance.*

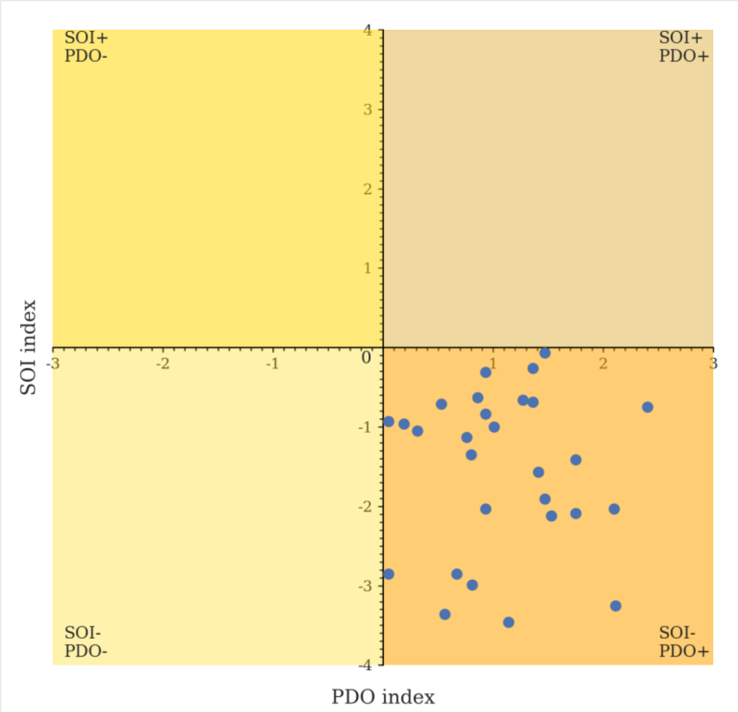

Figure S3.15. *Similar to Figure S3.10 but shows SOI and PDO index during the winter concordant months of SEA–SAF pair. PDO is positive for about all months (100%) and SOI is negative for all months. We can infer that PDO acts as a modulator for the impact of El-Nino on SEA–SAF concordance.*

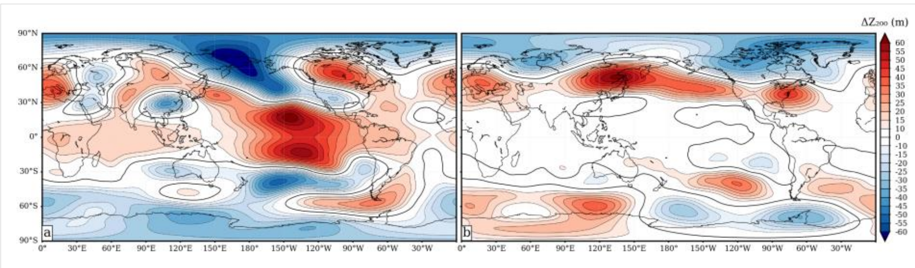

Figure S3.16*. Same as Figure 3.4 and 3.6 of the main text but on cylindrical map projection for the whole global region. (a) Composite* $\boldsymbol{Z_{200}}$ *anomalies for SEA–SAF concordance (b) Composite* $\boldsymbol{Z_{200}}$ *anomalies for WNA–MED concordance. Solid thick black line represents 0 anomaly. The patterns over Pacific-north America and Atlantic are different in two concordances.*

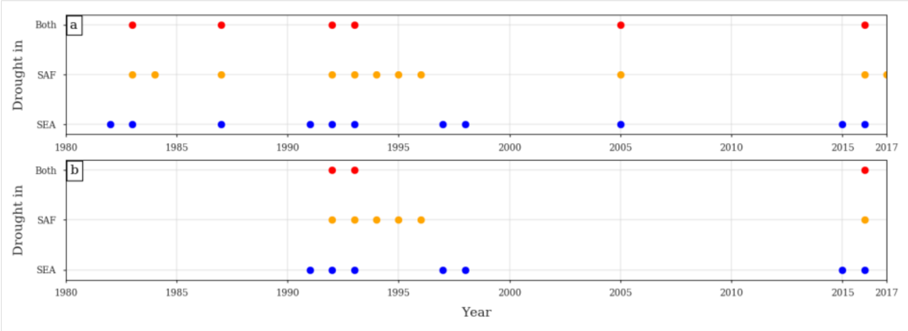

Figure S3.17. *Regional and Concordant drought years for SEA and SAF regions for the recent period (1980 to 2017). (a) CRU data with calibration period Jan. 1930 to Dec. 1990 (b) CRU data with calibration period Jan. 1980 to Dec. 2017. Out of 11 drought years in SAF, 6 years are concordant with SEA drought years which corresponds to 54% during 1930–1990 calibration of CRU data; while as calibration 1980–2017 shows 50% concordance between SEA and SAF drought years. In both calibrations, a delayed onset of concordant droughts in SAF can be observed.*

Chapter 4 : Spatially compound heatwaves: Role of ENSO

Executive summary

In chapter 3, our proposed methods revealed multiple teleconnections in persistent droughts among the IPCC AR5 regions. However, the analysis for estimation of concordances and their statistical significance was performed at annual scale. In contrast, concordances in heatwaves that usually last no longer than a week could not be estimated timescale longer than a week. In addition, Kornhuber *et al* (2019) noted concurrent heatwaves over central North America, Eastern Europe, and eastern Asia and central North America, Western Europe, and western Asia, during Rosby wave wavenumbers 5 and 7, respectively. Röthlisberger *et al* (2019) observed simultaneous warm spells over Europe, North America, and the western North Atlantic in summer 1994 during synoptic-scale recurrent Rossby waves. In a recent study by Rogers *et al* (2021a) used self-organizing maps to investigate spatially compound heatwaves (SCHs) in northern hemisphere during summer seasons of the last 4 decades and found multiple region sets that have higher probability of SCHs along with a 6-fold increase in the frequency of SCHs. However, all these studies are either event specific or limited to northern hemisphere and boreal summer. Furthermore, (Rogers *et al* 2021a) did not estimate the impacts associated with SCHs.

To answer these questions, chapter 4 estimates the SCHs globally and year-round at daily timescale. Our findings demonstrated an increase of 3% of global land in the spatial extent of the SCHs over the last 4 decades. Global heatwave days –extreme SCHs that impact more than 10 regions– in post-2000 are 8-fold higher than in pre-2000. Increasing trends in SCH suggest greater heatwave activity owing to anthropogenic climate change, but interannual variability in SCHs is likely related to changes in internal climatic variability and land cover. Multiple teleconnections in heatwaves are identified using likelihood multiplication factor, however, most of them are among the tropical regions which may be attributed to coherent warming and large-El-Nino impacts. Our findings indicate an 87.5% risk of reduced crop productivity during anomalous heatwave years. The population exposed to SCHs increased by 50% since 2000, with more exposures occurring during anomalously larger SCHs. Composite anomalies and correlation coefficients between SCHs and climate indices highighled El-Nino as the key driver of larger SCHS. Other climate oscillations also emerged important at regional scale. This analysis is an important step towards understanding the observed changes in SCEs and could serve as the basis for estimating the impacts of SCEs on various components of ecosystems such as forests and water resources including glaciers

*After: **Waqar Ul Hassan,** Munir A. Nayak, and M. F. Azam; Intensifying spatially compound heatwaves: implication to global crop production and human population; Global Environmental change. : **(Under Review)***

Abstract

Recent research has provided crucial insights on regional heatwaves, including their causal mechanisms and changes under global warming. However, detailed research on global-scale spatially compound heatwaves (SCHs) (concurrent heatwaves over multiple regions) is lacking. Here, we find statistically significant teleconnections in heatwaves and show that the frequency of global-scale SCHs and their areal extent have increased significantly, which has led to 50% increase in the population exposed to extreme heat stresses in the two most recent decades. Crop yields were reduced in most of the years of anomalous heatwaves, which often happen during El-Niños. The internal climatic variability appears to significantly influence the inter-annual variability of regional and global heatwave extents. Insights gained here are critical in better quantifying heat stress risks inflicted on socioecological systems.

4.1. Background

Heatwaves —commonly defined as multi-day events of excessive heat (Perkins and Alexander 2013b) —cause substantial damage to human health (McMichael and Lindgren 2011, Khosla *et al* 2021), environment (Xu *et al* 2020), agriculture (Kornhuber *et al* 2020, Lesk *et al* 2016), and other natural and anthropogenic systems (Rübbelke and Vögele 2011, Barriopedro *et al* 2011). These are commonly associated with anticyclonic circulations or atmospheric blockings that are often components of larger quasi-stationary Rossby waves (Petoukhov *et al* 2016, Kornhuber *et al* 2019b). Such patterns of anomalously high atmospheric pressure have intensified in the 21st century, increasing the likelihood of persistent warm spells/heatwaves (Lee *et al* 2017). In this warmer world, discernible changes in heatwaves characteristics and their associated atmospheric patterns have been noted, mainly in response to enhanced warming over high latitudes–known as Arctic amplification (Coumou *et al* 2015, 2018) and weakening of equator–pole temperature gradient (Coumou *et al* 2018). Apart from global warming, changes in heatwaves are driven by land-atmosphere feedback (Miralles *et al* 2019c, Hirsch and King 2020), land use land cover changes (Findell *et al* 2017, Ge *et al* 2022, Alkama and Cescatti 2016b, Lejeune *et al* 2018) and changes in natural climatic variability (Petoukhov *et al* 2016, Meehl and Tebaldi 2004a, Rogers *et al* 2021a, Kenyon and Hegerl 2008). Heatwaves caused ~166,000 casualties over 1998–2017 (WHO, 2022.), and 356,000 in 2019 alone (Burkart *et al* 2021). Furthermore, the global population exposed to intense heat has increased by 125 million over 2000–2016 (WHO, 2022) with 475 million additional exposures (above 1998–2005 average) in 2019 only (Burkart *et al* 2021). In July 2010, Russia experienced the century's deadliest heatwave (Hoag 2014), killing 55,000 people, destroying 25% of crops, and burning over a million hectares of land, costing the country \$15 billion (Barriopedro *et al* 2011).

Weather or climate extremes occurring concurrently in multiple remote regions, defined as spatially compound extremes (Zscheischler *et al* 2020), often result in exponential impacts compared to isolated extremes (Anderson *et al* 2019, Kornhuber *et al* 2020). Climate extremes (mainly concurrent droughts and heatwaves (Mukherjee *et al* 2020)) have decreased global and national crop productivity across the globe by 6.2% and ~10% over the periods 2000–2007 and 1964–2007, respectively (Lesk *et al* 2016). Such extreme climate-related food shocks reduce the calorie intake of millions of low-income people by 5% globally (d'Amour *et al* 2016). Spatially compound heatwaves (SCHs) reduce annual crop productivity by 4% in northern mid-latitudes and upto 11% at regional-scale based on IPCC-defined regions (Kornhuber *et al* 2020). The co-occurrences of heatwaves at multiple regions in northern mid-latitudes are often related to the circumglobal teleconnections (Kornhuber *et al* 2019b, Lee *et al* 2017, Ning and Bradley 2015), recurrent Rossby waves (Röthlisberger *et al* 2019), and persistent atmospheric blockings (Röthlisberger *et al* 2019). Such global-scale weather patterns and the associated SCHs are established and modulated by anomalous sea surface temperatures (SSTs), e.g., through El-Niño Southern Oscillation (ENSO) (Ning and Bradley 2015, Holbrook *et al* 2019, Mokhov and Smirnov 2016). ENSO has been found to influence the SSTs in other oceanic basins, thereby modulating the global oceanic and atmospheric circulations (Alexander *et al* 2002, Cai *et al* 2019b) and influencing multiple remote regions simultaneously and sequentially (Luo and Lau 2020, Lee *et al* 2021). Low-frequency climatic oscillations such as Pacific Decadal Oscillation (PDO), Atlantic Multidecadal Oscillation (AMO), and others also influence heatwaves at a circumglobal scale (Seneviratne *et al* 2021, Liu *et al* 2019, Holbrook *et al* 2019).

Studies have addressed heatwave characteristics and their driving mechanisms at global and regional scales (Meehl and Tebaldi, 2004, p. 5; Perkins et al., 2012; Perkins and Lewis, 2020; Petoukhov et al., 2016; Pfahl and Wernli, 2012; Rogers et al., 2021b; Vogel et al., 2019). However, the changes in SCHs and their spatial extent have not been explored yet on a global scale. Previous studies on SCHs are limited to a single event or specific regions (Lee *et al* 2017, Vogel *et al* 2019, Kornhuber *et al* 2020, Lee *et al* 2021), except the study by Rogers *et al* 2022, who observed a ~six-fold increase in the frequency of summer SCHs during the last four decades over the northern hemisphere (Rogers *et al* 2021a). However, this study is limited in scope to Northern hemisphere's mid-and upper-latitudes and does not consider SCHs outside summer, which is critical period for the natural environment and where faster changes in heatwaves have been documented recently (Bokhorst *et al* 2009, Flanigan *et al* 2020). Moreover, previous studies (Kornhuber *et al* 2020, 2019b, Rogers *et al* 2021a, Röthlisberger *et al* 2019) did not evaluate the impact of SCHs on crops, humans, and other components of the ecosystem, which is highlighted as an important research question in Rogers et al 2022 (Rogers *et al* 2021a). We hypothesize that SCHs impact human mortality directly by deteriorating human health and indirectly through crop productivity losses. There is an urgent need for global assessment of changes in SCHs, their casual mechanisms and the associated socio-economic damages so that the risks in future food security can be estimated rationally. To this end, our study aims at a comprehensive global assessment of the changes in SCHs, their impacts on crop yield and human population, physical drivers, and changes in the likelihood of concurrent heatwaves among different IPCC regions.

4.2. Data and Methods

4.2.1. Data

The present analysis uses daily maximum temperature (T_{max}) from the National Oceanic and Atmospheric Administration (NOAA) Climate Prediction Centre (CPC) Global Daily Temperature dataset available at a high spatial resolution of $0.5° \times 0.5°$ only over global land areas, and spans from 1st January 1979 to present. The study period for the present study is 1979 to 2020 (42 years). Daily averages of hourly Sea Surface Temperature (SST), soil moisture of top layer (0 to 7cm), and 200 hPa geo-potential height (Z_{200}) from European Centre for Medium-Range Weather Forecasts Reanalysis Fifth Generation Dataset

(ERA5 (Hersbach *et al* 2018); available at a horizontal resolution of $0.25° \times 0.25°$) are used to explore the oceanic and atmospheric conditions during spatially compound heatwaves. In addition, multiple climate oscillation indices, such as ENSO, PDO, AMO, NAO, Arctic Oscillation (AO) etc., from the NOAA CPC are employed to examine the role of internal climate variability at daily and monthly timescales. However, to distinguish between different "flavors" of El-Nino, three separate indices, namely Niño 3, Niño 3.4, and Niño 4, are used to quantify the intensity and phases of El-Niños. To analyse changes in the population exposed to compound heatwaves, gridded population data from the National Aeronautics and Space Administration (NASA) Socioeconomic Data and Applications Center (SEDAC) is used (CIESIN, 2018). Since population records before 2000 were unavailable, long-term changes in the impacts could not be investigated and due to the availability of population records after every five years, our analysis is limited to 2000, 2005, 2010, 2015, and 2020. The impacts of heatwaves on crop productivity are analyzed using the annual global crop yield dataset of Rice, Maize, Wheat, Soyabean, and Sugarcane from the Food and Agriculture Organization (FAO) for the period of 1979-2019. Moreover, the monthly crop-growing area for the selected five crops was retrieved from the MIRCA-2000 dataset, which is available at a spatial resolution of $0.5° \times 0.5°$, to compute the heatwave extent in the crop areas. This dataset provides crop-growing areas for each grid and all 12 calendar months based on the cropping area in 2000. Since the present analysis is performed at a daily time scale, we converted the monthly cropping area data to a daily time scale by considering the same crop growing area for all the days of the month.

4.2.2. Heatwave identification

Although many metrics are available to identify and quantify heatwaves, we implement the T_{max} based definition of heatwaves called CTX90 (Perkins and Alexander 2013b). For each grid cell, a heatwave is defined when the daily T_{max} is above the local daily 90th percentile of $\mathrm{T_{max}}$ distribution for consecutive three or more days and each day of this heatwave is termed a heatwave day. The 90th percentile (TX_{90}) threshold is computed locally for each grid cell and for each calendar day using a 15-day moving window of daily maximum temperatures over the period 1979–2020. In this way, spatially- and temporally-varying thresholds are adopted to identify heatwaves in all seasons and to ensure consistency across different regions. A lower bound for TX_{90} as $0°C$ is also specified to avoid the identification and inclusion of absolute cold spells as warm spells, though these days may be warmer in relative terms. This threshold is chosen to distinguish the impact of cold sub-zero conditions on crops and humans from the influence of relatively warm, above-zero temperatures. In addition, the $0°\mathrm{C}$ threshold has implications in estimating the impacts of heatwaves on snow and glaciers and segregation of false springs from freezing winters, which indirectly affect crop production. Two successive heatwaves are considered independent even if they are separated by a single non-heatwave day. Besides heatwaves, we define a dry (drought) spell as a period when the daily standardized soil moisture anomaly is less than -1 at each grid cell. The daily moisture anomalies are computed by subtracting the calendar day means from daily values, which are then divided by calendar day standard deviation to get standardized anomalies. The calendar day means and standard deviations are computed using a 15-day window.

4.2.3. Regional and Global Heatwave Days

In defining regional and spatially compound heatwave days, the global landmass (excluding Antarctica) (Iturbide *et al* 2020) is divided into 44 reference regions (Table S4.1) as in the Sixth Assessment Report (AR6) of IPCC (see IPCC AR6 reference regions). Then for each day, ***Global heatwave extent, crop-heatwave extent,*** and ***Regional heatwave extent*** are defined as the sum of the area of all grid cells under heatwave over the global land, crop growing area, and in the IPCC regions, respectively. Similarly, crop-drought extent is defined as the crop-growing area under drought conditions. A region is said to experience a ***Regional heatwave day*** if the regional heatwave extent on a given day is greater than 90th percentile of non-zero regional heatwave extents, i.e., the 90th percentile is computed only from those days that have at least one grid cell in the region under heatwave condition (see Table S4.2). The 90th percentile threshold of some regions exceeds one-fourth of regional area e.g., Western North America, Eastern Europe, Eastern Australia, among others, signifying these regions as hotspots of larger heatwaves (red-colored entries in Table S4.2). When three or more regions encounter a heatwave day concurrently (i.e., same date) and the global spatial extent under heatwaves is more than 5% of global land area (~$0.65\times 10^7\ km^2$), that day is labelled as ***compound heatwave day or spatially compound heatwave day*** for those regions.

Here, a day is defined as a ***Global heatwave day*** when the global heatwave extent exceeds $1.5 \times 10^7\ km^2$ area and at least 10 IPCC regions experience regional heatwave day simultaneously on that given day. These thresholds correspond to about 99th percentiles and are 3 standard deviations above the mean of daily global heatwave extent and regions affected, respectively. To estimate the trends for daily global heatwave extent and number of IPCC regions under a compound heatwave, Sen Kendall's slope estimator with the null hypothesis that there is no monotonic trend in the data is employed. To understand the role of internal climate variability in causing GHWDs, the global heatwave days from detrended heatwave characteristics are also explored using the corresponding thresholds of $0.73 \times 10^7\ \mathrm{km}^2$ area (~99th percentile of detrended daily global heatwave extent) and 6 regions (~99th percentile of detrended daily regions affected), respectively. A ***detrended GHWD*** is then defined when the detrended heatwave characteristics exceed the above thresholds simultaneously on a given day. Our interpretation of the role of internal climate variability is based on the assumption that the main contributions of global warming are removed by detrending, which may not the optimal procedure; however, our results are in close agreement with a recent study that used a more detailed algorithm (Rogers *et al* 2021a).

4.2.4. Composite Anomalies

The composite anomalies of SST and geo-potential height at 200 hPa during GHWDs, and for two selected concordant heatwave pairs are used to explore the atmospheric and oceanic conditions leading to the occurrence of such compound events. The composite anomaly at each grid cell is taken as the average of anomalies for all the heatwave days over the study period, where the anomaly for a heatwave day is taken as the deviation from the long-term climatological mean for that calendar day. To estimate standardized anomalies, the composite anomalies for each heatwave day are divided by the standard deviation of corresponding calendar days and then averaged.

4.2.5. Concordances in heatwaves

The probability of experiencing a regional heatwave day is estimated using equation [1] below.

$$\hat{p}_i = \frac{n_i}{N} \quad [4.1]$$

Where, n_i is the number of heatwave days in region i, and N is the total number of days in consideration (here 15341 days). Two regions (i and j) are under a concurrent heatwave day if both regions experience a regional heatwave simultaneously on the given day. For each pair of regions, the probability of concurrent heatwave day or concordance probability ($\hat{p}_{i,j}$) is the ratio of the number of concurrent heatwaves days between i and j (n_{ij}) and the total number of days under consideration (N) as shown in equation [4.2].

$$\hat{p}_{i,j} = \frac{n_{ij}}{N} \quad [4.2]$$

If the two regions are independent, the estimated concordance probability is $\hat{p}_i \times \hat{p}_j$. Likelihood multiplication factor (LMF) (Zscheischler and Seneviratne 2017) is used to illustrate the strength of concordance between each pair of regions. The LMF is the ratio of the observed concordance probability and concordance probability under the complete independence assumption. For any pair of regions i and j LMF is computed as below:

$$LMF_{ij} = \frac{\hat{p}_{i,j}}{\hat{p}_i \times \hat{p}_j} \quad [4.3]$$

The LMF varies in the range of 0 and infinity. For any pair of independent regions, LMF equals 1. If observed concordance is higher than what is expected under independence, LMF is greater than 1 and opposite is the case for LMF between 0 and 1.

Note that LMF is scaler and does not provide any information about its statistical significance. To assess the statistical significance of LMF for each regional pair, a statistical test is performed with the null hypothesis that the observed number of concurrent heatwave days can be reproduced by chance and does not require any physical relationship between the regions. To perform this, bootstrapping procedure is adopted by generating 100,000 random resamples, each of sample size 5,000, from binary RHWDs arrays for each region separately, which will eliminate the physical relationship between the regions and the temporal autocorrelation within the regions. Since the random resamples are of smaller sample size compared to the actual observation, bootstrapping method is used to produce an estimate of the observed heatwave days (sample size 5,000) while preserving the physical relationship between the regions. This was accomplished by generating an additional 100,000 resamples (sample size 5,000) by resampling all regions together based on dates. In both the cases and for all resamples, the number of concurrent heatwave days were computed for each region pair. The mean number of concurrent heatwave days (hereafter referred as "bootstrap mean", unless specified) for the second case is representative of observed concurrent heatwaves. The LMF of a region pair is considered statistically significant at 1% significance level if the number of concurrent heatwave days in at least 99% of resamples from the first case (independent case) is lesser than the number of concurrent heatwave days in the bootstrap mean. The step-by-step procedure adopted during the test is discussed in SM Text S4.4.

We also used one-tailed binomial test at 1% significance level to test the statistical significance of concordances (LMF values); where the null hypothesis is that the observed concordant probability is higher than what is expected under independence, i.e.,

$$H_o: \hat{p}_{i,j} \le \hat{p}_i \times \hat{p}_j \qquad [4.4]$$

$$H_a: \hat{p}_{i,j} > \hat{p}_i \times \hat{p}_j \qquad [4.5]$$

To test for field significance, false discovery rate (FDR) correction was applied to the p-values obtained from binomial tests (results in supplementary material).

An implicit assumption in the study lies with the estimation of concordance (i.e., LMF and binomial test), where we assume RHWDs as independent events, which in some cases may not be valid since multi-day regional heatwave events are not uncommon. In addition, the estimated frequency of RHWDs and GHWDs is sensitive to the selection of thresholds for their definition, and substantial differences are noted in the ratio of post-2000 and pre-2000 GHWDs with different thresholds, particularly between 95th and 99.5th percentile (Figure S4.12).

4.3. Results

4.3.1. Observed changes in spatially compound heatwaves

To evaluate the changes in SCHs and their associated impacts, historical changes in global heatwave extent and IPCC regions (see “Table S4.1” for region definitions and “Methods” for regional heatwave) experiencing heatwaves concurrently over 1979–2020 are presented in Figure 4.1. Significant increasing trends for both spatial extents (1.2% of global land area/decade) and number of regions (~1 region/decade) under the heatwaves are observed since 1979 (Figure 4.1a). The annual average of spatial extent of heatwaves shows a significant increase of ~5% of global land area (global land, hereafter) from 1.6% in 1979 to 6.45% in 2020, whereas the number of IPCC regions under heatwaves has increased by ~9 times (~0.46 region in

1979 to 5 regions in 2020) (Figure 4.1b). The annual average of spatial extent and number of IPCC regions under spatial compound heatwave days (SCHDs; see "Methods") have increased by ~1.8% of global land (~2.24 million km^2) and 2 regions (i.e., from 3 regions in 1979 to 5 regions in 2020), respectively (Figure 4.1b). Furthermore, the annual frequency of SCHDs has increased by 315 days (7 days in 1979 to 322 days in 2020) since 1979 (Figure 4.1c) suggesting that SCHs are virtually occurring year-round with a daily likelihood of 88%. The increase in SCHDs can be attributed to the increase in global temperatures in response to climate change (Meehl and Tebaldi 2004a, Vogel *et al* 2019, Rogers *et al* 2021a) and human-induced LULC changes (Alkama and Cescatti 2016b, Lejeune *et al* 2018). The expected risk of human exposure to SCHDs is largely determined by their variability (Figure 4.4b; discussed in detail in section 4.3.3), which has significantly amplified post-2000 compared to pre-2000 (Figure 1d). Detrending of spatial extent and number of IPCC regions in Figure 4.1d is assumed to efface the contribution of global warming to heatwave characteristics (Alexander *et al* 2018); however, its indirect impact, altering the internal climate variability, will still affect the changes in heatwave characteristics (Rogers *et al* 2021a). Increases in the variability of SCH can be related to the changes in natural modes of climate variability (Kenyon and Hegerl, 2008; Perkins et al., 2017), land use land cover changes (Ge *et al* 2022, Alkama and Cescatti 2016b, Lejeune *et al* 2018) and the interactions between global warming and natural climate variability (Rogers *et al* 2021a, Lee *et al* 2021). In general, forest removal causes increased local warming and higher variability in extreme temperatures (Ge *et al* 2022, Lejeune *et al* 2018, Cherubini *et al* 2018). However, studies have noted a complex and latitude- and altitude-dependent impact of LULC changes on temperature extremes and their variability that is largely controlled by the biophysical mechanisms (albedo and evapotranspiration) as well as the background climate (rainfall, snow, and shortwave radiation) (Alkama and Cescatti, 2016; Christidis et al., 2013; Lejeune et al., 2018; Li et al., 2015; Hassan et al., 2021).

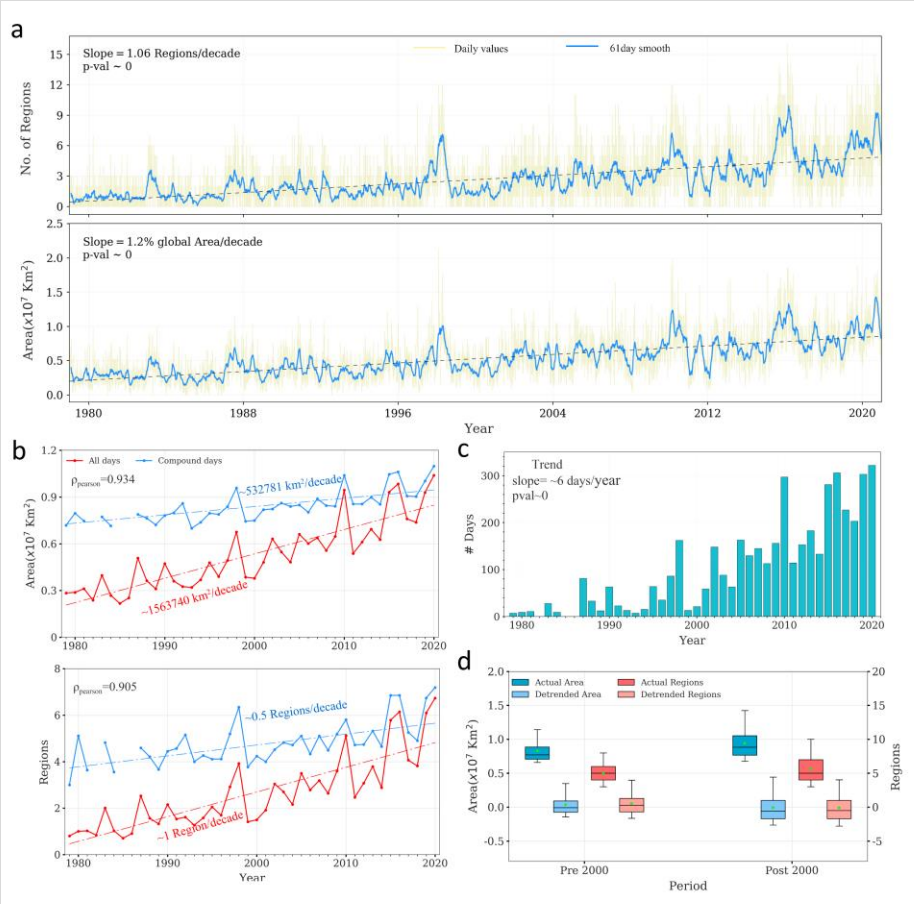

Figure 4.1. *Changes in spatially compound heatwave characteristics. Daily area (in km^2) and number of regions affected by heatwaves. (a) Number of regions (IPCC AR 6) experiencing a heatwave day (top panel) and Global land area (km^2) under heatwaves (bottom panel). The blue line represents the 61-day smoothed series. The total global land area in the 44 IPCC regions is 129.76 million km^2. (b) Annual average of the global land area and number of regions under all heatwave days (red lines) and spatially compound heatwave days (blue lines). (c) frequency of spatially compound (number of days per year that qualify the threshold for compound heatwave day). (d) Boxplot of the distribution of actual (dark color) and detrended global (light color) area and number of regions affected by spatially compound heatwaves pre-and post-2000. Boxplot whiskers correspond to 5th and 95th percentile and the lime-green dots represent the mean. F-test on monthly means of spatial extent and count of regions is used to test the statistical significance of changes in variability pre-and post-2000. All test results were significant at 5% significance. Figure S4.16 of the Supplementary Materials shows the distribution of spatial extent and number of regions affected by all heatwaves (including all SCH and non-SCH days).*

Larger compound extremes are observed to be associated with greater impacts on society and agricultural outputs; therefore, the changes in the extreme compound heatwaves that we call Global heatwaves days (GHWDs; see “Methods”) are examined. The number of GHWDs is roughly eight-fold (74 days) in post-2000 than pre-2000 (9 days) (Figure 4.2a), suggesting serious impacts of climate change on the extreme compound heatwaves. This higher number of GHWDs post-2000 can be attributed to the combined impact of global warming (Lee *et al* 2021, Vogel *et al* 2019, Kong *et al* 2020a), changes in internal climate variability (Perkins et al., 2017; Rogers et al., 2021a), aerosol trends (Van Oldenborgh *et al* 2022, Zhao *et al* 2019, Pere *et al* 2011), and land use and land cover changes (Wehrli *et al* 2019, Findell *et al* 2017, Alkama and Cescatti 2016b). To efface the contribution of global warming, GHWDs from detrended heatwave characteristics are also explored. A total of 79 days qualified the adopted thresholds for detrended GHWDs (see “Methods” for details), out of which 23 occurred pre-2000 and 56 occurred post-2000, a two-fold increase from pre-2000 period (Figure 4.2a), highlighting changes in natural climate variability as the important driver. Though more total areas affected by global heatwaves were observed pre-2000, the number of IPCC regions affected by global heatwaves does not show statistically significant change (dark color boxplots in Figure 4.2a). On contrary, the total area and number of regions affected by heatwaves during detrended GHWDs, show statistically significant (5% significance) increase post-2000 (see light color boxplots in Figure 4.2a). The variability in the areas affected by global heatwaves has significantly decreased post-2000, whereas the variability of the number of regions affected by global heatwaves shows statistically insignificant increase post-2000.

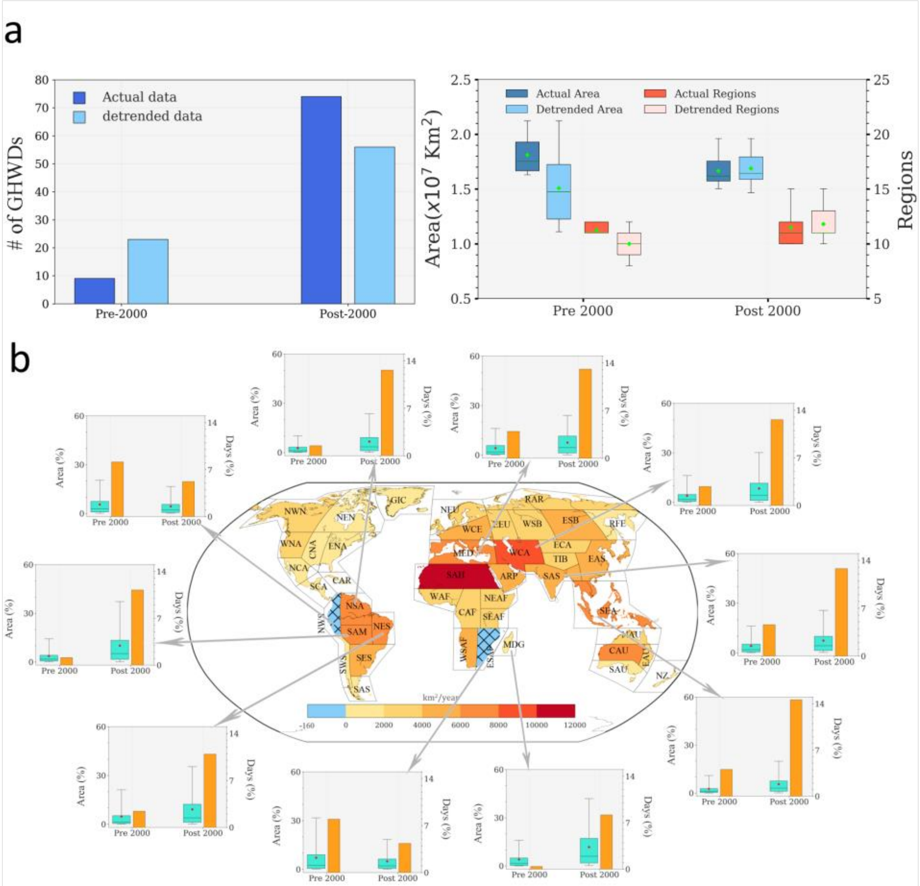

Figure 4.2. *Distribution of areal extant (km^2) and number of regions affected by GHWDs (a) Number of GHWDs pre-and post-2000 using actual (dark blue) and detrended (light blue) global heatwave extent and regions affected by heatwaves concurrently (details in Table S3) (left panel). Distribution of spatial extent and regions affected during the GHWDs pre-and post-2000 were obtained using actual (dark color) and detrended (light color) heatwave characteristics (right panel). (b) Shows the regional changes in the heatwave characteristics. The map at the center shows the trends of regional heatwave extent during 1979–2020. Hatches represent the non-significant (at 5%) trends. The inset subplots show the pre-2000 and post-2000 spatial extent and frequency of regional heatwave days for the top 10 regions (top 8 regions with the highest increase and 2 regions with a decrease in the frequency of regional heatwaves). The 'cyan' colored boxplots show the distribution of regional area affected by heatwaves as a percentage of the total area of the region and 'orange' bars show the frequency of regional heatwave days as a percentage of all days in pre-2000 period (i.e., 7670 days). Boxplot whiskers correspond to the 1st and 99th percentile. In all boxplots, the dots in boxplots represent the means.*

4.3.2. Changes in regional heatwaves and significant concordances

In agreement to increase in the global heatwave extent, all IPCC regions except ESAF (eastern south Africa) and NWS (northwestern South America), show significant increasing trends in the heatwave extents (Figure 4.2b). The large increasing trends are confined to low-latitudinal regions, where Sahara (SAH) shows the maximum increase of $\sim 12 \times 10^3\ km^2/year$. The observed increase in the spatial extent of heatwaves is likely due to enhanced global warming during the recent decades (Perkins and Lewis, 2020). Consistent with the overall global trend, higher number of regional heatwave days (RHWDs; see "Methods") post-2000 are observed in all regions except NWS and ESAF. In post-2000, the highest increase of 854 RHWDs (~7.5 times pre-2000) is observed in NSA, followed by Southeast Asia (SEA), Southern America Monsoon (SAM), and Western Central Asia (WCA) (Figure 4.2b), whereas the lowest increase is noted over Southern Australia (SAU; 98 days) (see Figure S1 for details). While increases in the frequency, duration, and intensity of heatwaves are known (Perkins and Lewis, 2020; Rogers et al., 2021a), the monthly average and variance of spatial extent of regional heatwaves also increased post-2000, implying larger risks of exposure in the warmer world post-2000.

Recent studies have noted that some regions have higher chances of encountering concurrent heatwaves (Kornhuber *et al* 2020, Vogel *et al* 2019, Röthlisberger *et al* 2019, Rogers *et al* 2021a). For instance, during a particular Rossby wave pattern central North America, Eastern Europe, and Eastern Asia experience heatwaves concurrently (Kornhuber *et al* 2020). However, studies on concurrent heatwaves are limited to the regions in the northern hemisphere (Kornhuber *et al* 2020, Vogel *et al* 2019, Röthlisberger *et al* 2019, Rogers *et al* 2021a). The present study specifically explores and quantifies the concurrent relationships (concordances) globally using pair-wise likelihood multiplication factor (LMF) and bootstrapping procedure (see "Methods"). Adjacent region pairs usually show significant concordances (Figure 4.3 and Figure S4.2), e.g., southern Australia–central Australia (SAU–CAU), SAM–NSA and others, which can be attributed to land-atmosphere feedback during heatwaves (Miralles et al., 2019) and/or absence of physical boundaries between IPCC regions. Of particular interest are the significant concordances in region pairs that are more than 10,000 km distant e.g., SEA–SAM, Russian Far East–Eastern Europe (RFE–EEU), Central Australia–Western Africa (CAU–WAF), and others (Figure 4.3 and S4.2); we call them “teleconnections in heatwaves”. The term teleconnection is used because these long-distance compound heatwaves are often governed by large-scale oceanic and atmospheric circulation such as Rossby waves, ENSO, and others (see Text S4.3). Teleconnections in heatwaves are more prevalent over tropical regions compared to subtropical and polar regions (Figure 4.3 and S4.2), where they are probably driven by coherent warming (Byrne 2021) and El-Niño impacts (Alexander *et al* 2002, Yang *et al* 2018a). The robust teleconnections present during both cooler pre-2000 and warmer post-2000 periods highlight the significant role of natural climate variability in driving these teleconnections. However, in the post-2000 warmer world, the strength of these teleconnections has reduced as measured by lower LMF values (Figure 4.3 and S4.2).

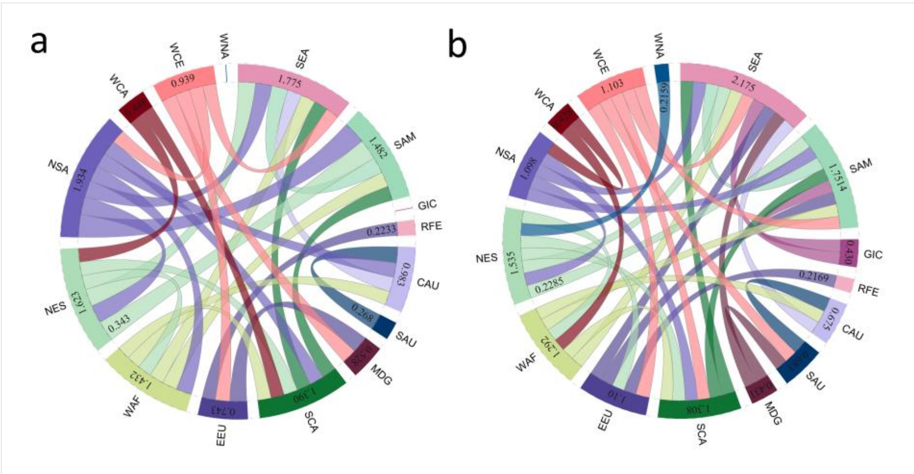

Figure 4.3. *Possible teleconnections in spatially compound heatwaves. Statistically significant concordant region pairs that experience regional heatwave days together. i.e., region pairs that have higher probability of concordant heatwaves compared to what is expected by chance. For these pairs, the likelihood multiplication factor (LMF) values are significantly higher than 1. For the period (a) Pre-2000 (b) Post-2000. The widths of the chords/links represent the LMF values of the concordance and only those concordances are shown that are statistically significant at 1% significance level. Here, we show concordances of only 15 regions. For other regions refer to Figure S4.2. The results based on binomial test and false discovery rate correction are shown in Figures S4.3 and S4.4. The numbers on the circumference and chords represent the concordance strength i.e., scaled LMF value*

($0.2 + \frac{LMF}{100}$). They are given as a scale. Interactive plots are provided for retrieving the LMF strength of all pairs. The link (Interactive_plot_Figure3) contains a folder with two sub-folders and two files. Once the folder is downloaded, the user can open the interactive plot by just opening the two files..

This reduced teleconnection strength could be attributed to the more rapid increase in the regional heatwaves than compound heatwaves. Further, the number of significant concordances for almost all IPCC regions has increased post-2000 in response to the comparable and synchronous increase in RHWDs in almost all regions (Figures 4.2b, and, S4.2). To assess the sensitivity of significant concordances to different methods, statistical significance of concordance is also estimated using binomial test and false discovery rate (FDR) (Benjamini and Yekutieli 2001) correction. The results highlight no major difference in the estimation of significant concordances at 1% significance level (Figures S4.3 and S4.4).

4.3.3. Impact on crop yield and population exposure

Despite the increases in the global temperature and frequency of weather/climate extremes, the production of global crops has nearly doubled since 1980 (Figure S4.5 and Text S4.1), mainly due to advances in irrigation, fertilizer, and genetically-modified crops (Bailey-Serres *et al* 2019). However, year-to-year variability in climate has significant impact on crop yields regionally and globally (Ray *et al* 2015). To investigate the heatwave extent-crop yield relationship, detrended annual average heatwave extent in cropping area (hereafter crop-heatwave extent) and annual yields (Figure 4.4a) are used to estimate the correlations. The monthly cropping area for each of the selected crops is obtained from MIRCA 2000 (Portmann *et al* 2010). The detrended crop-heatwave extent is negatively correlated with Rice ($\rho^{**} = -0.4445$), Wheat ($\rho^{**} = -0.3398$), Maize ($\rho^{*} = -0.1046$), and

---

** represents the value is statistically significant at 5% significance

* represents the value is not statistically significant

Sugarcane ($\rho* = -0.0559$), signifying a decrease in the yield with increase in crop-heatwave extent, and positively correlated with Soya ($\rho* = 0.1714$). The positive correlation of Soya may be due to its higher critical temperature of reproductive growth (Hatfield *et al* 2011, Gourdji *et al* 2013). Heatwaves typically have a direct impact on crop yield by damaging the crop's enzymes, tissues, and flowers, or by reducing photosynthesis. Indirectly, crop loss can be due to water stress (dryness or drought) in response to soil moisture deficits and/or increased vapor pressure deficit, both of which typically happen concurrently with heatwaves and amplify their overall impacts. To understand and segregate the impact of heatwaves and dryness on crop yield, we estimated the probability of yield loss during positive crop-heatwave extent (see Methods) years, positive crop-drought extent years (see Methods), and compound extent years (i.e., years with positive crop-heatwave extent and positive crop-drought extent). In general, roughly 50% of the positive anomalous crop-heatwave extent years (shown as pink bars in Figure 4.4a), irrespective of drought extent, result in reduced crop yield [Rice =61.1%, Wheat= 56.2%, Maize=43.75%, Sugarcane=57.14%, and Soya=36.84%] out of which ~15% of years have yield loss only because of positive crop-heatwave extent, i.e., when crop-drought extent was less than normal [Rice =22.2%, Wheat= 6.25%, Maize=18.75%, Sugarcane=7.14%, and Soya=15.79%] (Figure 4.4a). In addition, 14 out of 16 (i.e., 87.5%) positive anomalous global heatwave extent years (shown as golden bars in Figure S4.6) have resulted in reduced crop yield of at least two of the five selected crops (Figure S4.6). Furthermore, we used a multiple linear regression model to estimate the sensitivity of yield to the changes in the crop-heatwave and crop-drought extent (details in Text S4.1). The results show that, except Soya, all the selected crops experience declines in yield as the crop-heatwave extent increases. For every 1% rise in crop-heatwave extent, Maize suffers the greatest losses of 0.65% (with respect to long-term mean yield), followed by Rice (0.5%), Wheat (0.48%), and Sugarcane (0.3%) (details in text S4.1).

Heatwaves are often tagged as 'silent killers' (Loughnan 2014) as they impact human life in a variety of ways (McMichael and Lindgren 2011). More frequent heatwaves not only deteriorate quality of life but also result in more casualties (Rogers *et al* 2021b). Regardless of vigorous population growth in the recent decades (Tripathi *et al* 2019), a general increase in the population affected by

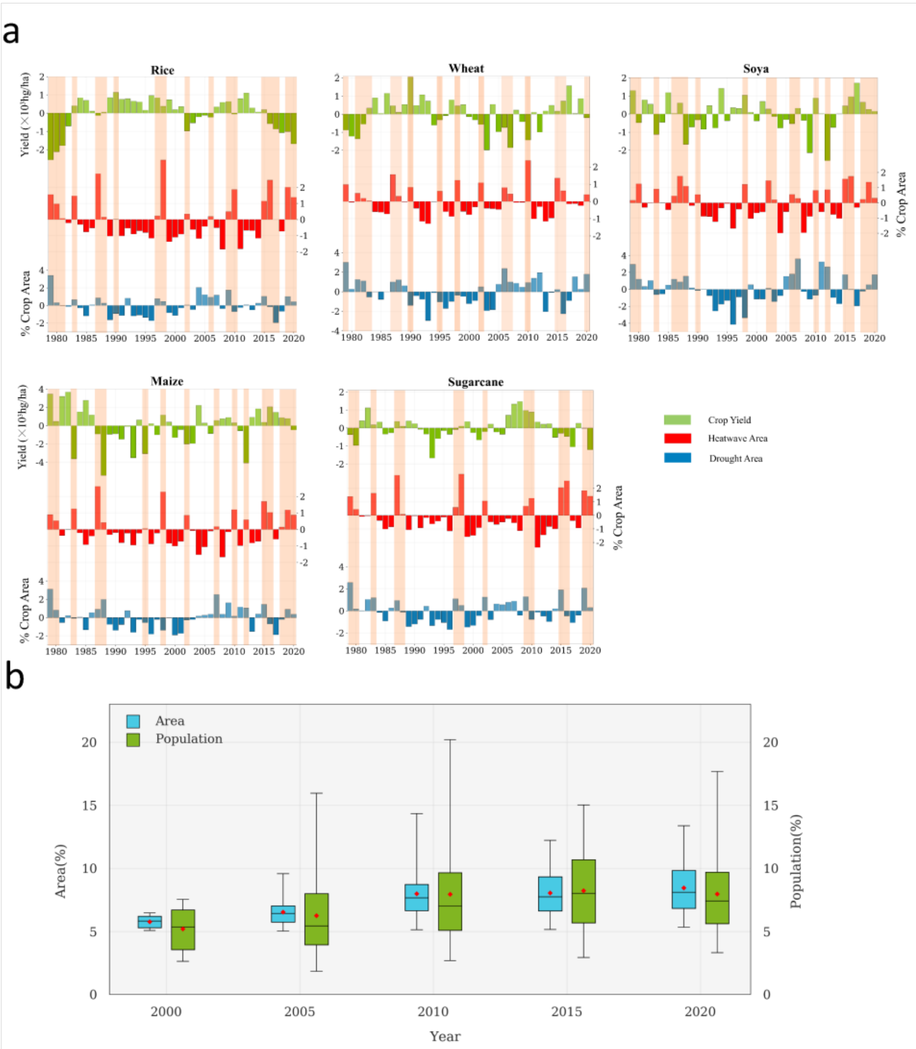

Figure 4.4. *Impact of compound heatwaves on global crop yield and human population. (a) impacts of heatwaves on crops. The red and blue color bars represent the crop-heatwave and crop-drought extents, respectively. Crop-drought extent represents the indirect impact of heatwaves or direct impact of moisture stress. All values are anomalies with respect to trend i.e., expected value for that year ($\hat{y}$; estimated using linear regression). The crop-heatwave and crop-drought area used is*

the average of the daily area affected during the year and are given as the percentage of the annual average crop-growing area. The pink bars highlight the years that have positive heatwave extent irrespective of drought extent conditions. (b) Impact of SCHs on human population. Blue and green colors represent the distribution of land area (% of total global land area) and population (% of the total global population for that year, see Table S4 for population of each year) affected by compound heatwaves. Boxplot whiskers correspond to 1 and 99th percentile. The numbers in the parenthesis are spearman's correlation coefficients. Correlation coefficients for 2010, 2015, and 2020 are significant at 5%. A similar figure for the population affected by the heatwaves during all days in Figure S4.17

the heatwaves is found due to expanding spatial extent of SCHs (Figure 4.4b). In addition, the variability in population exposure to SCHs is primarily driven by the variability of their spatial extent. The population exposure to the SCHs has increased by 2.8% during the period 2000–2020 (from 5.2% in 2000 to 8% in 2020), which is about 50% of the population affected in 2000, in response to ~2.7% increase in the heatwave extent post-2000 (Figure 4.4b). Statistically significant correlation between daily heatwave extent and population affected by SCHs after 2010 also highlights increased exposure of population to heatwave impacts during the larger SCHs.

4.3.4. Variability in global heatwave extent mainly driven by ENSO

Although global warming has increased spatially compound extremes, their interannual variability is mainly driven by the internal climate variability and/or large-scale climate modes (Rogers *et al* 2021a, Kenyon and Hegerl 2008). The relationships between heatwaves and climatic modes are complex and are modulated by the presence of other climatic modes (Hassan and Nayak 2020, Wang 2019, Mokhov and Smirnov 2016). Spearman's rank correlation coefficient is used to quantify the monotonic relationship between spatial extent of heatwaves (globally and regionally) and several known climate oscillations (Figure S4.7). Positive correlations of global heatwaves with ENSO, Dipole Moment Index (DMI), AMO, and East Atlantic (EA) highlight that larger heatwaves are expected during their positive phases (Figure S4.7). At regional scale, the positive phases of these indices also correspond to larger extents of heatwaves in tropical regions. Similar results are obtained at seasonal scale with more intense and widespread relationships during boreal summer and autumn (Figure S4.8). Recent studies have highlighted ENSO as the major driver of spatially compound droughts globally (Hassan and Nayak 2020, Singh *et al* 2021). Our results point to larger global land areas under SCHs during the El-Niño (warm phase of ENSO).

ENSO —the dominant mode of inter-annual climate variability— modulates and is modulated by the climate modes in the Atlantic (e.g., AMO) and Indian Ocean (IOD) (Mokhov and Smirnov 2016, Wang 2019), and is the most understood and efficiently predicted climate mode (Tang *et al* 2018). Notwithstanding this, recent studies have recognized different types of El-Niño, namely Warm pool (El-Nino Modoki), Cold tongue, and Mixed El-Niño, that exhibit contrasting spatial patterns and impacts on the global climate (Kug *et al* 2009). Thus, we mainly focus on the relationship between different flavors of ENSO and compound heatwaves (Figures 4.5a, S4.9, and Text S4.2). Most often, the periods of larger heatwave extent (positive values, i.e., values above the trend line) and the higher number of regions affected coincide with the positive phase of Niño indices (i.e., El-Niño phase). In addition, the strong or extreme El-Niño events [index value > 1.0] are uniquely associated with anonymously larger spatial extent (1σ above mean) heatwaves (Figure 5a and *S9*). However, a 90 to 110 days lag is noticed between heatwave characteristics and El-Niño events (Figure S4.10). Furthermore, the occurrence of top ten prominent heatwaves (annotated in Figure 4.5a) is observed during the El-Niño or within the lag period.

4.3.5. Large-scale atmospheric and oceanic anomalies during GHWDs

Knowing the potential impacts of global heatwaves, it is important to understand the physical state of the ocean and atmosphere leading to such disastrous heatwave events. To this end, the composites of SST and 200-hPa geopotential height anomalies during GHWDs are shown (Figures 4.5b and S4.11, respectively). The SST anomalies revealed above-normal SSTs over the equatorial, Northeastern Pacific Ocean, and most of the Indian Ocean. Positive anomalies over the central pacific, particularly over Niño 3.4 region, signify El-Niño conditions over the Pacific. In addition to El-Niño, higher SSTs are noted near the west coast of US which hints at the co-occurrence of El-Niño and positive phase PDO during the GHWDs.

The 200-hPa height anomalies during the GHWDs remarkably resemble the El-Niño pattern over the Pacific Ocean (Figure S11). The persistent high pressure/anticyclonic condition over most of the tropics along with high pressure blocking over the Mediterranean, Northern polar fridge, and south of the Andes prevent air and moisture intrusion and warm air extrusion from these regions, thus increasing the air temperature over land (hereafter, air temperature), which is further often amplified by land-atmosphere feedback (Miralles *et al* 2019c, Hirsch and King 2020). In addition, a Rossby wave-like pattern can be noticed over both hemispheres resembling negative North Atlantic Oscillation (NAO) over North Atlantic Ocean and Europe. Furthermore, the composite height anomalies during SCHDs in two robust teleconnections namely RFE–EEU and CAU–WAF are explored to gain insights into the physical mechanisms of these teleconnections. The height anomalies reveal the presence of persistent and anomalously high pressure (atmospheric blocking) over the teleconnected regions that exceed their climatology by about one standard deviation (Figures S4.12 and S4.15). These blocks divert the storm track, favour downwelling of air masses, and reduce cloud cover, which together with land-air interaction increases the air temperature abnormally (Pfahl and Wernli 2012) (see other details in “SM Text S4.3”).

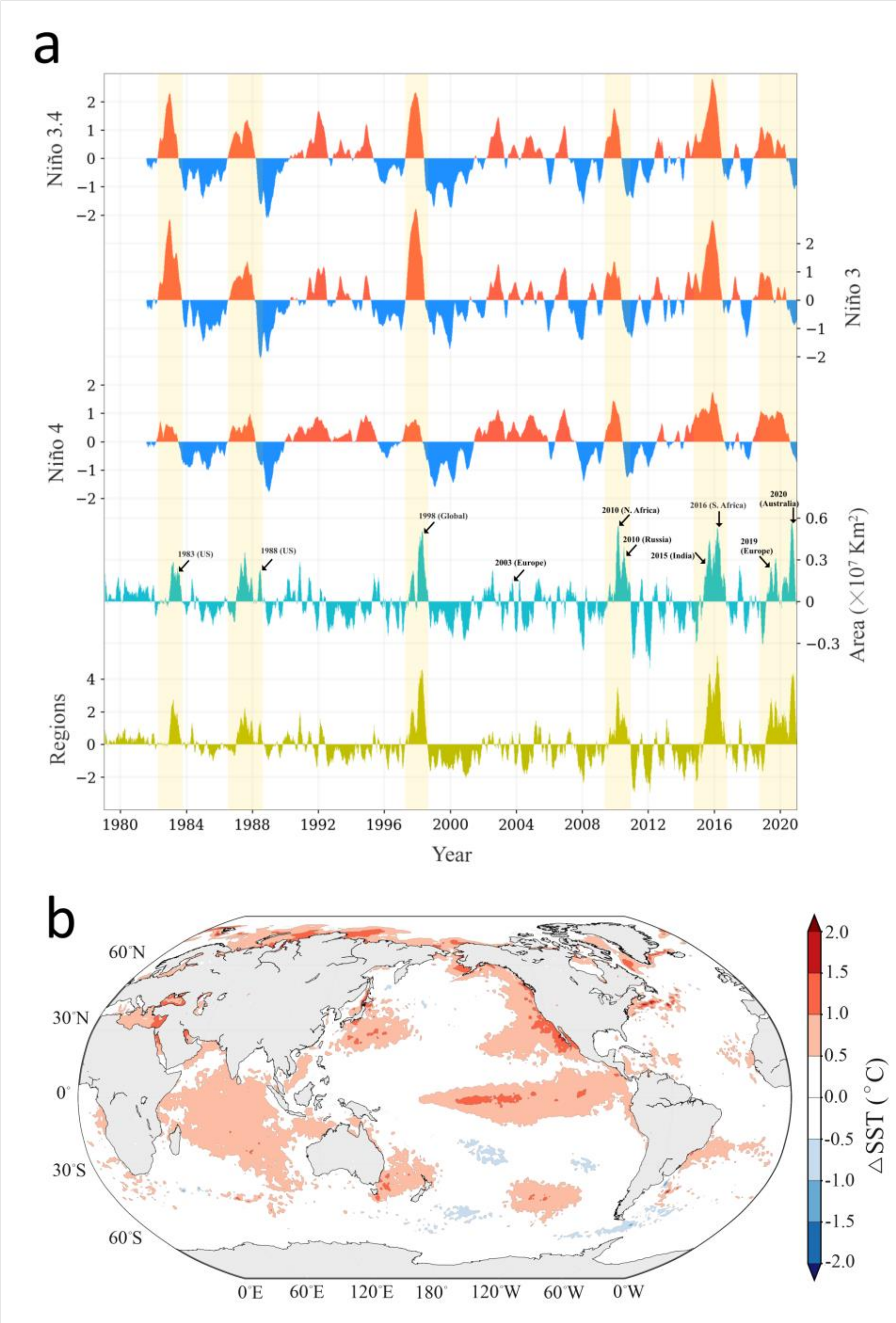

Figure 4.5. *Role of ENSO variability on spatially compound and Global heatwaves. (a) The bottom panel (olive bars) represent the variation of the detrended daily number of regions experiencing heatwaves. Light blue bars (Second panel from bottom) show the variation of the detrended daily area under heatwave. The top three panels show different indices for ENSO quantification. Red color signifies El-Niño and blue color represent La-Niña. The data plotted is 61-day smoothed (moving averages). Here, three indices of ENSO are used to represent different types of El-Niños e.g., Niño 4 is the best index to measure warm pool El-Niño (El-Niño Modoki) and Niño 3 is considered better in quantifying cold -tongue El-Niño. The complex type of El-Niño is quantified by Niño 3.4. The annotations show the top 10 prominent*

heatwaves (that have affected widespread areas and caused mass mortality and socio-economical damage (source: WHO)) during the study period. The golden bars represent the period of exceptionally larger heatwaves that occur during El-Niño events. A similar figure using monthly averages (average of daily values of each month) is shown in Supplementary Materials Figure S4.9 (b) shows the composite SST anomalies during the GHWDs. Composite anomalies were computed by averaging the anomalies of GHWD with respect to their calendar days.

4.4. Conclusions

This study revealed alarming rates of increase in the spatial extent of heatwaves at global and regional scales. The increasing trends in SCH highlight larger heatwave activity due to anthropogenic climate change, while the enhanced variability in global heatwave extent is more likely due to the changes in internal climate variability (Kenyon and Hegerl, 2008; Perkins et al., 2017) and land cover (Ge *et al* 2022, Alkama and Cescatti 2016b, Lejeune *et al* 2018). In addition to the role of climate change and climate variability, Alkama et al 2016 (Alkama and Cescatti 2016b) and Jun et al 2022 (Ge *et al* 2022) noted that forest cover clearing significantly increases the mean and variability of temperature and its extremes. Indistinguishably, the increase in GHWDs can also be attributed to climate change, though their interannual/interdecadal variability is primarily driven by natural climate variability. Furthermore, the heatwaves of anomalously larger spatial extent, which affect multiple regions concurrently, pose threat to global food security and affect the human population disproportionally. Our results suggest ~50% likelihood of reduced crop yield during anomalously positive crop-heatwave extent years out of which ~15% likelihood is related SCHs and rest could due be combination of SCHs and other confounding factors such as moisture deficit. In addition, results highlighted ~87.5% likelihood of reduced crop yield (in at least two of the selected crops) during anomalously positive heatwave extent years. The population exposed to SCHs also showed a 50% increase during the last two decades with more exposures during anomalously larger extent SCHs. An increase in the number of significant concordances in heatwaves in a warmer post-2000 period could be an early warning of larger and highly impactful global heatwaves in future.

Consistent with the previous studies that claim El-Niño events as a major driver of large-scale drying, increased air temperatures, and compound droughts (Hassan and Nayak 2020, Kenyon and Hegerl 2008, Singh *et al* 2021), the larger SCHs are found during El-Niño events are found. The SST and height anomalies during GHWDs remarkably resemble El-Niño conditions which strengthens our conclusion of larger SCHs during El-Niño events. Besides El-Niño, other climatic modes (e.g., AMO, DMI, PDO and others) also play a significant role in driving the changes in SCHs by modulating the regional heatwave characteristics and ENSO impacts via atmospheric bridges.

Understanding changes in SCHs and their impacts on multiple sectors of our environment are critical for devising preventive measures before mitigating them becomes too costly. We strongly believe that our analyses are important steps towards understanding the observed changes in global heatwave extent, teleconnections in heatwaves, SCHs, and their impacts on crops and humans. Although major physical insights into the causes of spatially compound heatwaves and pairwise concordances are discussed in this study, further in-depth analyses of the individual teleconnections, their reduced teleconnection strength post-2000, and their casual mechanisms are imperative for estimating their behaviour in future climate and their representation in global circulation models. This study could serve as the basis for estimating the impacts of SCHs on various ecosystems such as forests and water resources including glaciers (Azam *et al* 2021).

APPENDIX-C: Supporting Information

Supplementary Text

4.1. Impact of heatwaves on crops productivity

Despite the increase in global temperatures and frequency of weather extremes, the global production of crops has nearly doubled (~1.8 times) during 1979–2019. For example, the yield of maize, wheat, and rice has increased from 33847hg/ha, 18522hg/ha, and 26591hg/ha to 58238hg/ha, 35468hg/ha, and 46618hg/ha at a rate of 675.4hg/ha, 380.1hg/ha, and 463.5hg/ha per year, respectively (see Figure S5). This increase in crop yield is mainly an outcome of Avant-garde irrigation systems, advanced fertilizers, improved seeds, and genetically modified crops post green revolution (Bailey-Serres *et al* 2019). However, year-to-year variability in climate has significant impacts on crop yields regionally and globally (Ray *et al* 2015). In order to investigate such relationship between the compound heatwave extent and crop yield, which are showing an overall significant increase, we use detrended (difference of observed value [y] and estimated value [$\hat{y}$] from linear regression) annual average heatwave extent and annual yield (main text Figure 4a). Moreover, we observed that the decrease in crop production in response to higher heatwave extents usually occurs when ENSO is in the El-Niño phase (Figure 5a and S5). Furthermore, the decreases are higher during the extreme El-Niño years (index value >1).

We also explored the sensitivity of the crop yield to the cropping heatwave extent and cropping drought extent using a multiple linear regression model. A strong correlation between the drought and heatwave extent was observed which necessitated the use of an interaction term in the model. The mathematical formulation of the final model is as below:

$$Yield_i = \alpha + \beta_{hw} HW_i + \beta_{dr} DR_i + \beta_{inter} HW_i * DR_i + \epsilon_i$$

$$\epsilon_i \sim N(0, \sigma^2) \qquad \text{[S4.1]}$$

Where HW_i and DR_i are the cropping heatwave and drought extents (as the percentage of total cropping area) for ith year, α is the model intercept, β_{hw} and β_{dr} are the main effects and β_{inter} is the interaction effect. The main effect β_{hw} represent the change in the yield with every 1% change in cropping heatwave extent when there is no contribution from drought conditions. In contrast, the interaction effect β_{inter} represent the change in the yield with every 1% change in cropping heatwave extent that depends on drought conditions. Using the annual yield, cropping heatwave extent, and cropping drought extent for the selected five crops, the estimated model coefficients are as follows:

Crop	α *(hg/ha)*	β_{hw}*(hg/ha)*	β_{dr}*(hg/ha)*	β_{inter}*(hg/ha)*
Rice	34.8	-197.56	-200.63	-62.63
Wheat	73.3	-127.1	-237.4	-169.1
Maize	47.1	-288.9	136.8	-130.5
Sugarcane	1045	-1971	3801	-1400
Soya	70.35	133	-116	-121

The results revealed a general decrease in the yield of all crops, with an increase in the crop-heatwave extent, and crop-drought extent. However, the decreases are heterogeneous and depend on the crop type. Maize shows the maximum decrease of 197.56 hg/ha followed by Rice, Wheat, and Sugarcane for every 1% increase in the crop-heatwave extent (β_{hw} column). In contrast, the crop-dought extent reduces yield in Rice, Wheat and soya only (β_{dr} column). More importantly, all crops show yield loss when both crop-heatwave extent and crop-drought extent increase simultaneously (β_{inter} column).

4.2. ENSO drives the variability in global heatwave extent

We explored the role of large-scale climatic oscillations in modulating the spatially compound heatwaves by calculating spearman's correlation between spatial extent of heatwaves and climate oscillations. We find statistically significant influence of ENSO, AMO, DMI (Dipole moment index), EA (East Atlantic), and NAO on the variability of global heatwave extents at monthly (Figure S7) and seasonal scales (Figure S8). However, more intense and widespread relationships during boreal summer and autumn are observed. The positive correlation coefficients between heatwave extent and climate oscillation highlight that larger spatial extents are observed during positive phases of these climatic oscillations. The spatial extent of heatwaves in tropical regions is strongly and positively influenced during the positive phase of ENSO, DMI, EA and AMO. Consistent with the previous observations (Tachibana *et al* 2010, Drouard *et al* 2019), we observed a larger area under heatwaves in Europe (NEU, WCE, EEU) during the positive phase of NAO and AO. Furthermore, some climate modes showed a strong seasonality in their impacts. For example, western Pacific (WP) and PNA showed a widespread negative relationship (most regions showing significant negative correlation) during summers, whereas during other seasons we notice that only a few regions are affected by these modes. Above all, we observed a larger global land area under heatwaves during the El-Niño (warm phase of ENSO) phase.

Previous studies have recognized different types of El-Niño, namely Warm pool (El-Nino Modoki), Cold tongue, and Mixed El-Niño, that exhibit contrasting spatial patterns and impacts on the global climate (Kug *et al* 2009). The strength and phase of these three flavours of El-Niño are best quantified by Niño 4, Niño 3, and Niño 3.4, respectively (Kug *et al* 2009). All three indices are consistent in showing the phase of ENSO, however, they vary in intensity (Figure 5a and S8). In a warmer world, we observe a decrease in the intensity of Niño 3 (cold tongue) El-Niño while Niño 4 (El-Niño Modoki) shows an increase (Lee and McPhaden 2010b, Yang *et al* 2018a). We explicitly explored the relationship between the different flavours of ENSO and compound heatwave characteristics (extent and regions affected) at daily (discussed in main text) and monthly time scales (Figure S9). We observe that most periods of larger heatwave extent (positive values) and the larger number of regions affected coincide with the positive phase of Niño indices (i.e., El-Niño phase). During pre-2000 period larger heatwaves are mostly caused by cold-tongue El-Niños, whereas the recent larger SCHs are linked to mixed and El-Niño Modoki.

4.3. Significant concordances in the heatwave and their underlying physical mechanism

To gain insights into the physical mechanisms driving the occurrences of concurrent heatwaves, we selected two teleconnections, one from each hemisphere (RFE–EEU and CAU–WAF. Composite geo-potential height anomalies for RFE–EEU concordant pair revealed persistent high pressure blocking over RFE and EEU, respectively, that are more than 1 standard deviation above the mean (Figure S12 and S15). The pattern resembles remarkably omega block over EEU. In addition, a Rossby wave pattern is also apparent during these days. Similarly, we find anomalously high pressure blocking in vicinity of CAU and over WAF during the concordant heatwaves of CAU–WAF pair (Figures S10 and S11). The composite height anomalies also highlighted the presence of a Rossby wave during these events. In both cases, the high-pressure blockings prevent the outflux of hot air and influx of moist and cold air which results in further accumulation of heat in the region via increased Bowen's ratio. As previous studies have noted an increase in such atmospheric blockings in future, we thus can expect more frequent concurrent heatwaves in future. Furthermore, we also explored the SST and geopotential composite anomalies during the concurrent heatwaves in three tropical regions (SEA–NES–WSAF), which show teleconnections among each other. The composite anomalies remarkably resemble the El-Niño conditions over the tropical Pacific Ocean (Figure S18) highlighting El-Niño as the major driver of compound heatwaves in these regions, which is also in agreement with the previous studies (Alexander *et al* 2002, Hassan and Nayak 2020, Lee and McPhaden 2010b). A similar pattern of composite anomalies was noted by Hassan *et al* (2020) during the concurrent droughts and warm anomalies in southeast Asia and southern Africa (Hassan and Nayak 2020).

4.4. Bootstrapping algorithm

Step 1: For each IPCC reference region (44 regions) we have a daily binary vector of 15341 days, where "1" represents a regional heatwave day and "0" represents no heatwave day. We combine all the vectors into a matrix "X" (15341×44).

Step 2: We apply bootstrapping method (with replacement) on time axis of each column of matrix "X" to generate 100,000 alternate time-series, each of sample size 5,000. The time sequence is not preserved and, in every resampling, the samples are selected randomly with replacement. All these resamples are then stored in a three-dimensional array "X^*" ($5{,}000 \times 44 \times 100{,}000$). The number of concurrent heatwave days for each region pair and each resample is calculated and stored in a three-dimensional array "A" ($44 \times 44 \times 100{,}000$). We then compute the 99th percentile of the number of concurrent heatwave days for each region pair (i.e., 99th along 3rd dimension of array A), which we store as array "Z^*" (44×44). This array Z^* represents the 99th quantile of concurrent heatwave days under complete independence.

Step 3: Since we generated the random sample of size 5000 only in *step 2,* we could not use the actual observed number of concurrent heatwaves, instead we use bootstrapping to obtain a more reliable estimate of observed number of concurrent heatwaves from a sample size of 5000 (i.e., mean from resampled time-series). To perform this, we generate 100000 resamples each of sample size 5000 by resampling the entire rows of matrix X rather than elements of a column and name that resampled matrix as $Y^*(5000 \times 44 \times 100000)$. This row-wise resampling was performed to preserve the connectedness between regional heatwave days. Similar to *Step 2*, we compute the number of concurrent heatwave days for region pairs and stored them in an array B ($44 \times 44 \times 100000$). We then compute the mean number of heatwave days for each pair of regions (Z (44×44)) from the array B (i.e., mean of 100000 resamples), which we assume represents the population estimates of the observed number of concurrent heatwave days for the selected sample size of 5000.

Step 4: To test the null hypothesis that the observed number of concurrent heatwave days can be generated by chance, we compared array Z and Z^*, where every element represents a region pair. For example, Z_{ij} and Z^*_{ij} corresponds to the estimate of observed (population mean) concurrent heatwave days and 99th percentile of the number of concurrent heatwave days under independent assumption between region i and j, respectively. For any pair of regions i and j, if Z_{ij} is higher than Z^*_{ij}, then there is evidence to reject the null hypothesis at 1% significance level.

Supplementary Tables

Table S4.1. *Region definition as given in IPCC AR6. See IPCC AR6 reference regions for further details*

Short name	Region name
GIC	Greenland, Iceland,
NWN	Northwestern North America
NEN	Northeastern North America
WNA	Western North America
CNA	Central North America
ENA	Eastern North America
NCA	Northern Central America
SCA	Southern Central America
CAR	Caribbean
NWS	Northwestern South America
NSA	Northern South America
NES	Northeastern South America
SAM	South America Monsoon
SWS	Southwestern South America
SES	Southeastern South America
SSA	Southern South America
NEU	Northern Europe
WCE	Western and Central Europe
EEU	Eastern Europe
MED	Mediterranean
SAH	Sahara
WAF	Weastern Africa
CAF	Central Africa
NEAF	Northeastern Africa
SEAF	Southeastern Africa
WSAF	Wastern South Africa
ESAF	Eastern South Africa
MDG	Madagascar
RAR	Russian-Arcitic
WSB	Western Siberia
ESB	Eastern Siberia
RFE	Russian Far east
WCA	Western Central Asia
ECA	Eastern Central Asia
TIB	Tibetan-plateau
EAS	Eastern Asia
ARP	Arabian peninsula
SAS	Southern Asia
SEA	Southeast Asia
NAU	Northern Australia
CAU	Central Australia
EAU	Eastern Australia
SAU	Southern Australia
NZ	New Zealand

Table S4.2. *Regional land area and areal thresholds for defining regional heatwaves. The red highlighted values demonstrate that these regions are hotspots for larger heatwaves*

Region	**Total Area (km^2)**	**90th percentile Threshold (km^2)**	**Threshold as percent of Total area (%)**
GIC	472215.1	75889.6	16.07
NWN	5075286.5	800794.3	15.78
NEN	4198442.0	573405.2	13.66
WNA	2660467.3	693629.6	**26.07**
CNA	2680814.0	632803.4	23.60
ENA	3038773.5	602344.8	19.82
NCA	2018376.9	372066.3	18.43
SCA	975162.5	170651.2	17.50
CAR	227568.4	42266.7	18.57
NWS	2053488.1	267760.0	13.04
NSA	4342215.0	617024.8	14.21
NES	2701294.3	597495.0	22.12
SAM	2971875.0	611871.1	20.59
SWS	1020144.6	158242.3	15.51
SES	3752028.8	803317.8	21.41
SSA	733449.5	211885.0	**28.89**
NEU	1913023.5	432647.5	22.62
WCE	3309365.0	851403.4	**25.73**
EEU	2704219.8	923581.5	**34.15**
MED	4116021.0	664494.0	16.14
SAH	9146104.0	1413569.4	15.46
WAF	3012935.3	421050.1	13.97
CAF	4618361.0	474526.4	10.27
NEAF	2965824.0	371934.3	12.54
SEAF	2010807.3	323685.9	16.10
WSAF	2925237.8	590959.3	20.20
ESAF	2812284.0	454227.8	16.15
MDG	590793.0	155570.2	**26.33**
RAR	4230268.0	633282.7	14.97
WSB	4102670.0	904295.3	22.04
ESB	5553635.5	972207.3	17.51
RFE	2656924.3	369972.3	13.92
WCA	5055177.5	909683.3	18.00
ECA	2765177.5	732997.1	**26.51**
TIB	2270747.5	463035.2	20.39
EAS	5052078.0	750465.6	14.85
ARP	2763696.0	486956.3	17.62
SAS	4156777.3	637910.2	15.35
SEA	4152421.5	478935.5	11.53
NAU	1627421.9	445130.6	**27.35**
CAU	3533648.3	756796.6	21.42
EAU	1006141.8	369471.6	**36.72**
SAU	1511959.5	320746.8	21.21
NZ	272024.9	70422.9	**25.89**

Table S4.3*. Dates of Global Heatwave days from actual and detrended observations (we noted that 63 GHWDs from detrended heatwave extents conform with GHWDs from actual heatwave extents)*

Actual	Detrended	Actual	Detrended	Actual	Detrended
	3/24/1980	4/19/2010	4/19/2010	4/25/2016	
	7/24/1987		4/20/2010	4/26/2016	4/26/2016
	7/25/1987	6/20/2010	6/20/2010	4/27/2016	
	11/4/1990	8/2/2011	8/2/2011	5/17/2016	5/17/2016
	11/5/1990	2/8/2015	2/8/2015	5/18/2016	
	11/6/1990	2/9/2015		6/6/2016	
	1/2/1997	8/20/2015	8/20/2015	6/26/2019	6/26/2019
2/2/1998	2/2/1998	9/11/2015	9/11/2015	6/28/2019	
2/3/1998	2/3/1998	9/24/2015		9/25/2019	
2/4/1998	2/4/1998	10/14/2015	10/14/2015	9/26/2019	9/26/2019
2/5/1998	2/5/1998	10/15/2015		9/27/2019	9/27/2019
	2/6/1998	12/23/2015		9/28/2019	9/28/2019
	2/7/1998	12/24/2015	12/24/2015	9/29/2019	9/29/2019
	4/6/1998	1/9/2016		9/30/2019	9/30/2019
	4/7/1998	2/14/2016	2/14/2016	10/1/2019	10/1/2019
	4/12/1998	2/15/2016	2/15/2016	3/12/2020	3/12/2020
	4/13/1998	2/16/2016	2/16/2016	3/13/2020	3/13/2020
4/14/1998	4/14/1998	2/17/2016	2/17/2016	8/16/2020	
4/15/1998	4/15/1998	2/18/2016	2/18/2016	8/17/2020	8/17/2020
4/16/1998	4/16/1998	2/19/2016	2/19/2016	8/18/2020	8/18/2020
4/17/1998	4/17/1998	2/25/2016		8/19/2020	8/19/2020
4/18/1998	4/18/1998	2/27/2016		8/20/2020	
	4/20/1998	2/28/2016	2/28/2016	9/12/2020	
	3/28/2007	2/29/2016	2/29/2016	9/13/2020	9/13/2020
2/16/2010	2/16/2010	3/1/2016	3/1/2016	9/14/2020	
2/17/2010	2/17/2010	3/2/2016	3/2/2016	9/24/2020	9/24/2020
2/18/2010	2/18/2010	3/3/2016	3/3/2016	9/25/2020	9/25/2020
2/19/2010	2/19/2010	3/4/2016	3/4/2016	10/1/2020	
2/20/2010	2/20/2010	4/7/2016		10/2/2020	10/2/2020
3/12/2010	3/12/2010	4/8/2016		10/9/2020	10/9/2020
3/13/2010	3/13/2010	4/20/2016	4/20/2016	10/15/2020	10/15/2020
3/14/2010	3/14/2010	4/21/2016	4/21/2016	10/17/2020	10/17/2020
3/15/2010	3/15/2010	4/22/2016	4/22/2016	10/18/2020	10/18/2020

Table S4.4. *Global land area and total population for the five years after from FAO and NASA respectively*

Year	**Area (km^2)**	**Population (No. of persons)**
2000	129757346.0	6026036700
2005	129757346.0	6383455700
2010	129757346.0	6813492000
2015	129757346.0	7329886000
2020	129757346.0	7969444400

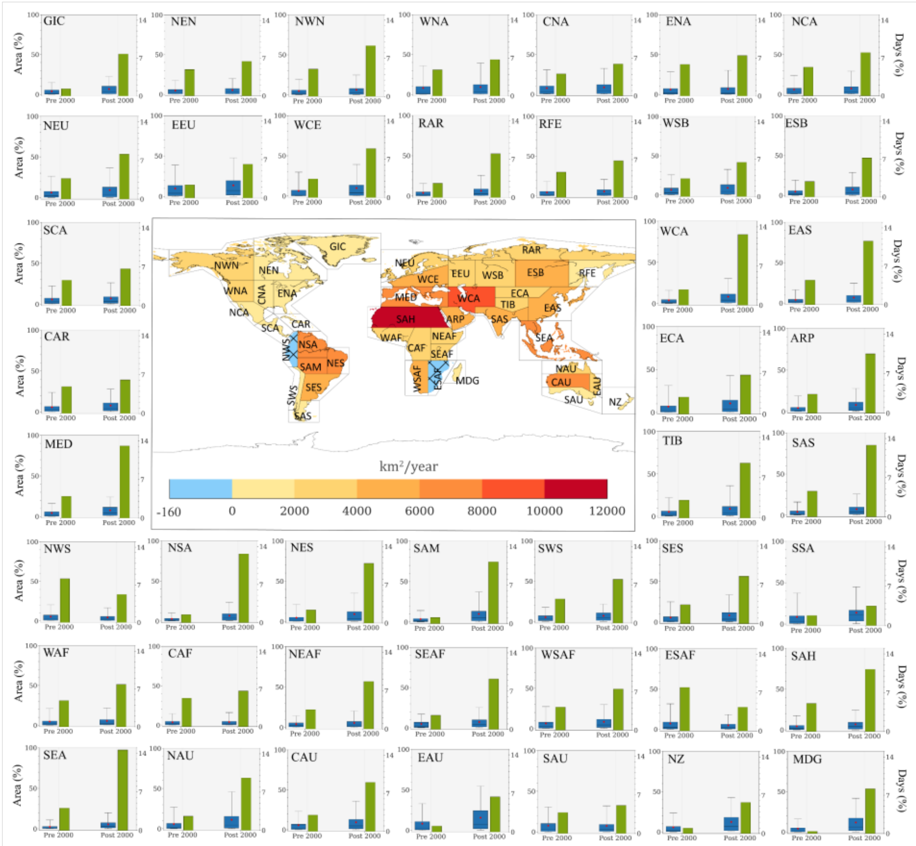

Figure S4.1. *Similar to Figure 4.2b but shows the changes in regional heatwave extent and RHWDs for all 44 IPCC references regions*

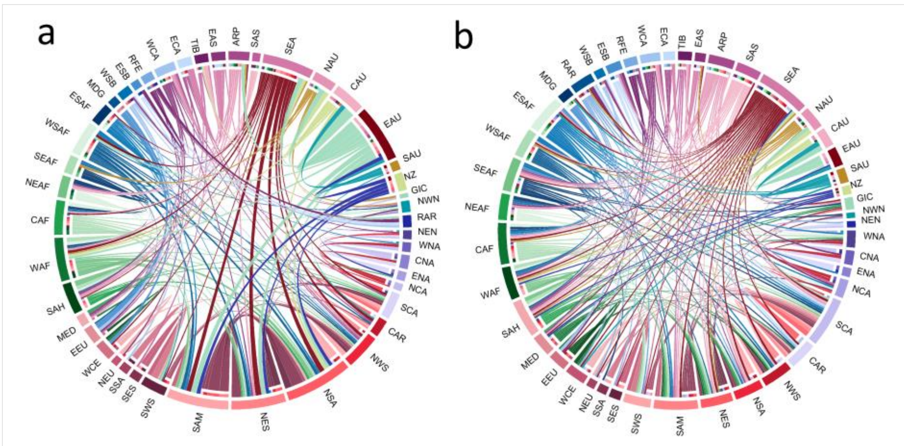

Figure S4.2. *Same as Figure 4.3 of main text but for all the 44 regions. (a) Pre-2000 (b)Post-2000*

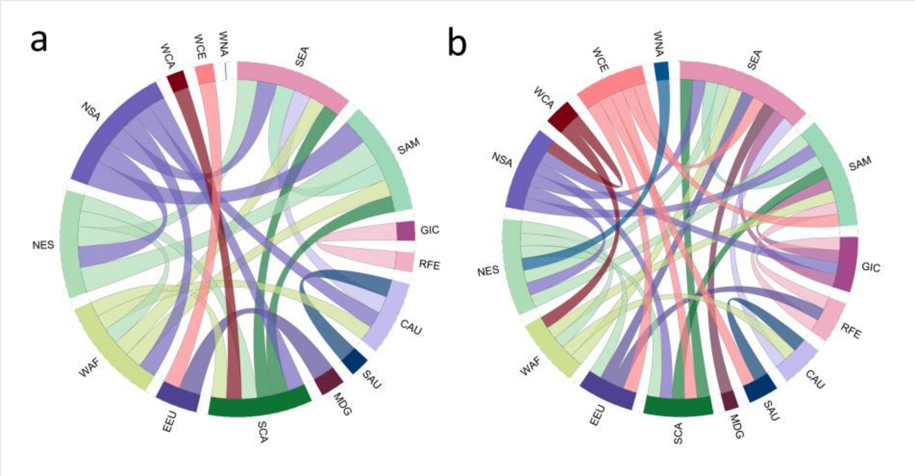

Figure S4.3. *Same as Figure 4.3 of main text. Binomial test is used for testing the statistical significance of concordances at 1% significance level. Also, false discovery rate correction is applied for field significance. Here we show only 15 regions. (a) Pre-2000 (b)Post-2000*

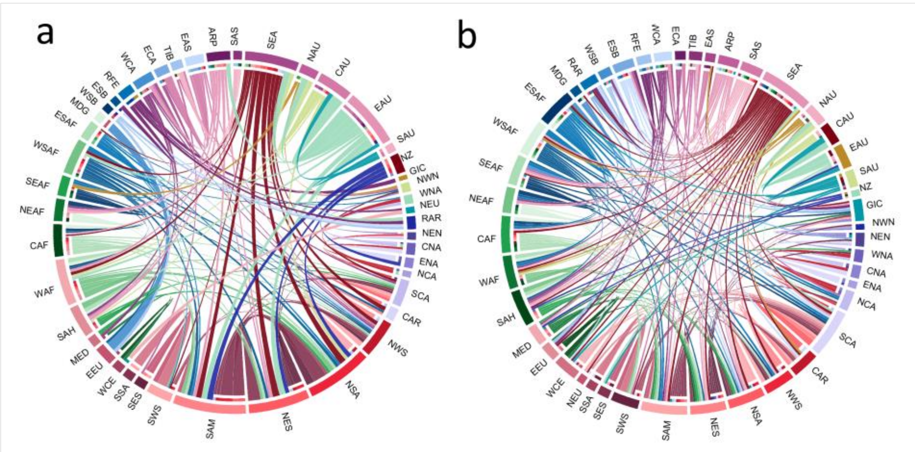

Figure S4.4. *Same as Figure S4.3 but for all the 44 regions. (a) Pre-2000 (b)Post-2000*

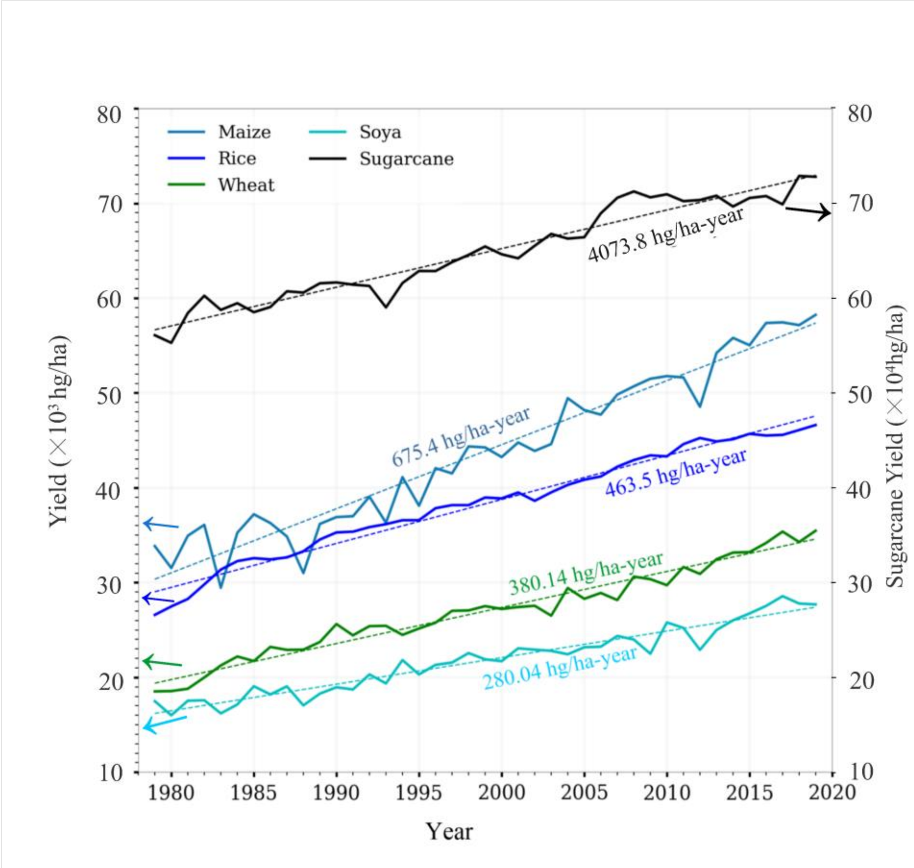

Figure S4.5. *Trends in the crop yield data obtained from FAO. The sugarcane yield is scaled by 10 to bring it in the range of other crops yields.*

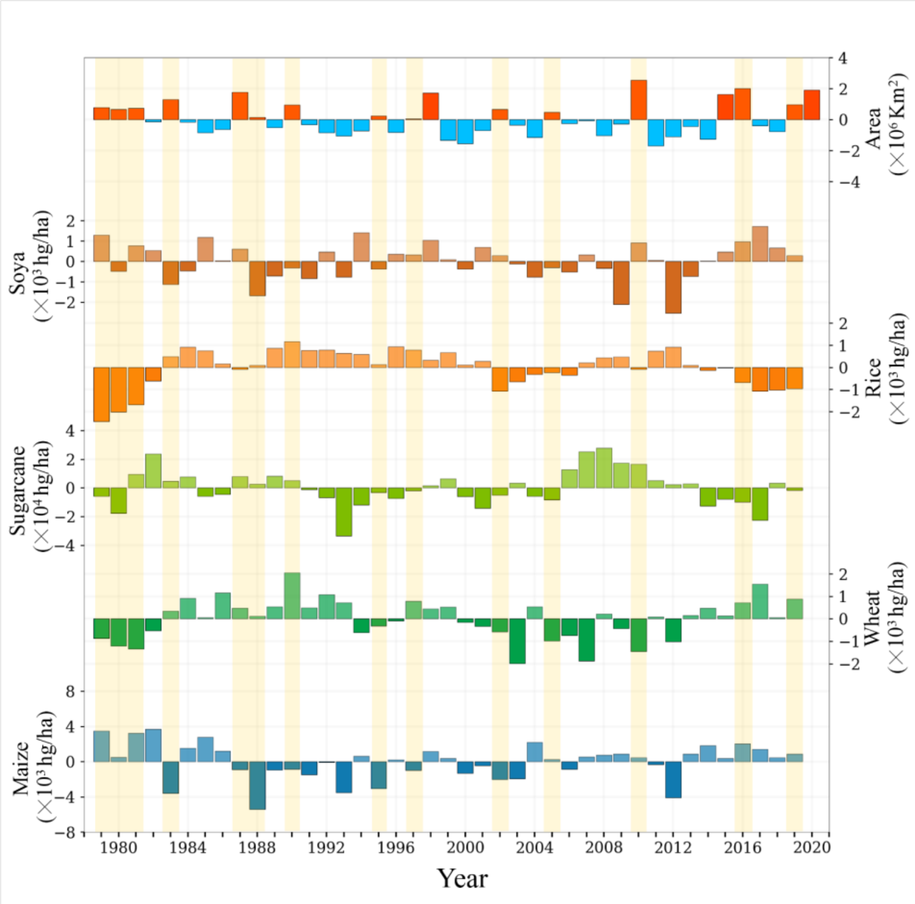

Figure S4.6. *Similar to Figure 4a but the heatwave extent is the global heatwave extent. Impact of heatwaves on crop yield. All values are anomalies with respect to trend i.e., expected value for that year ($\hat{y}$; estimated using linear regression). The area used is the average of the daily area affected during the year. The golden bars highlight the years that have a deficit (compared to estimated yield for that year) in yield for at least two of the selected crops during anomalously higher heatwave areas (higher compared to estimated extent for that year).*

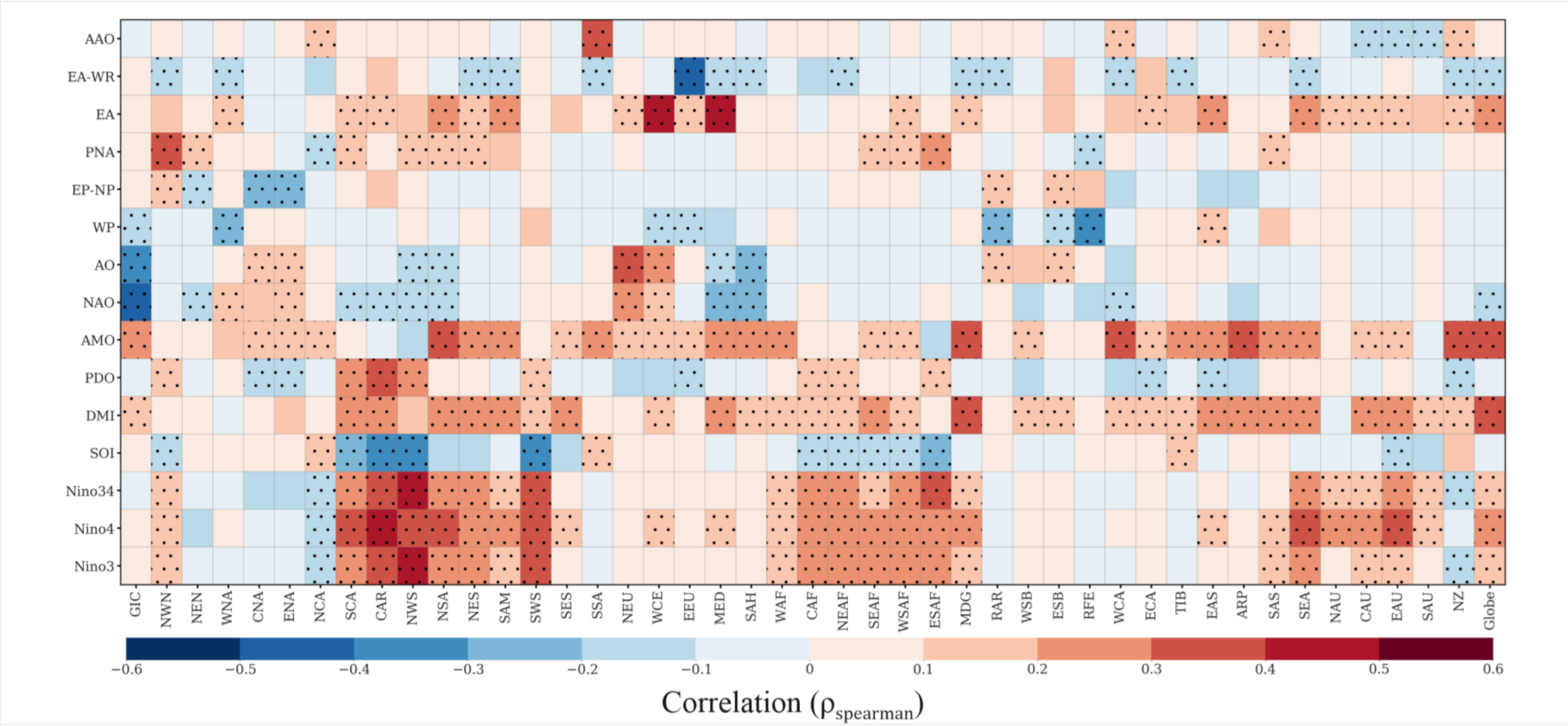

Figure S4.7. *Correlation between monthly average heatwave areal extent for regional and global heatwaves, and monthly climate indices (y-axis) during the period (1979 to 2020). The correlation coefficients are calculated using spearman's correlation. The dotted boxes represent statistical significance at 1%.*

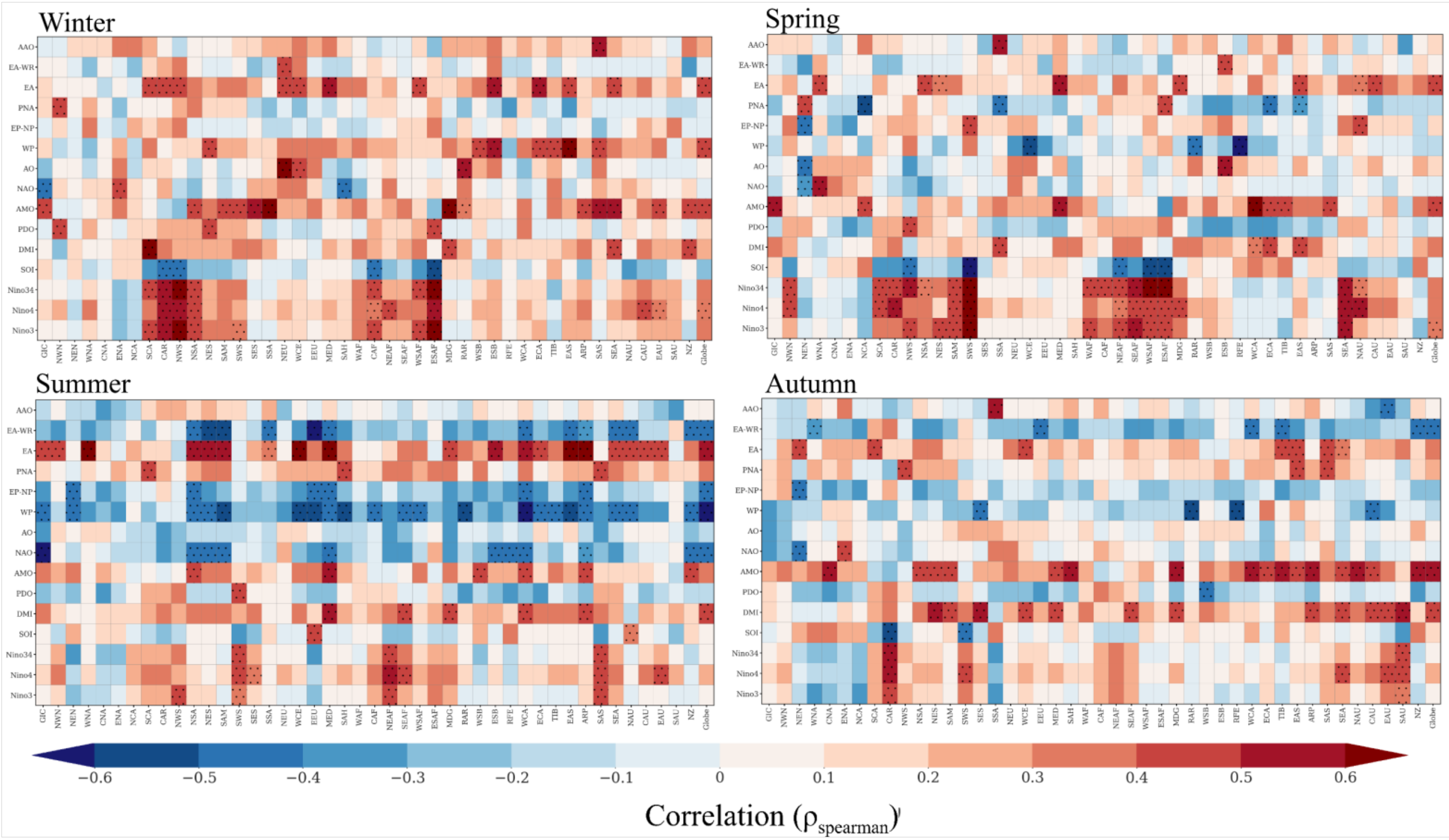

Figure S4.8. *Same as Figure S4.7 but for seasonal averages.*

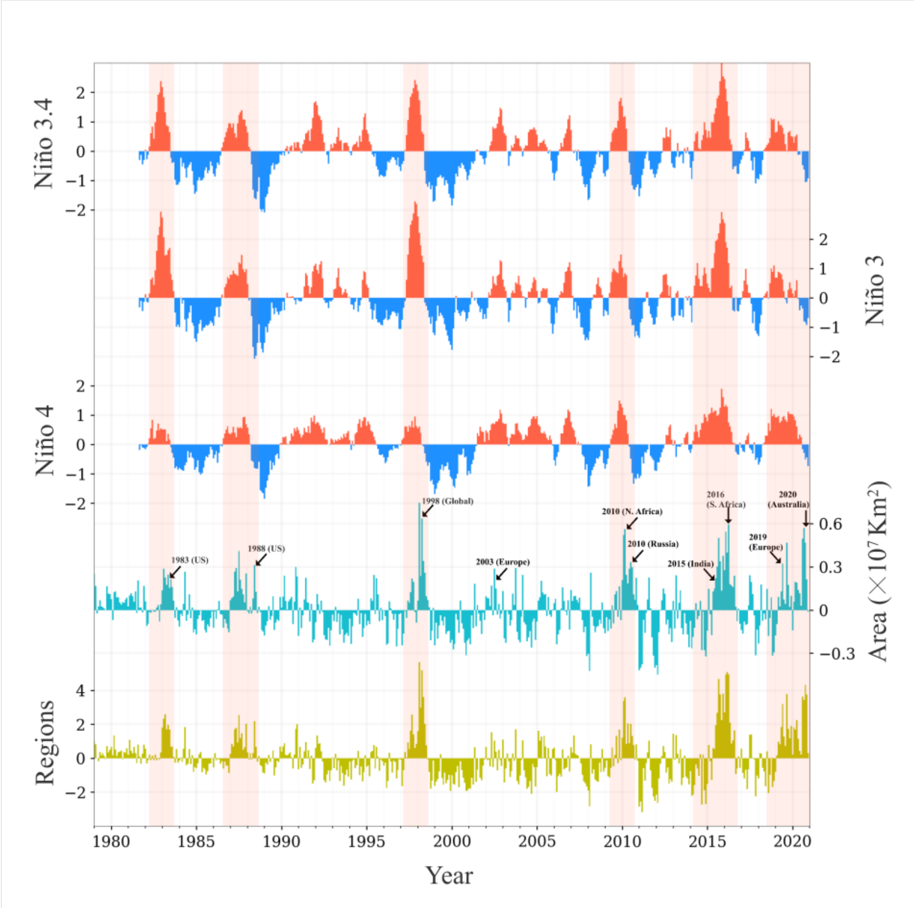

***Figure S4.9**. Similar to Figure 4.5a of the main text but the values are averaged at a monthly time scale.*

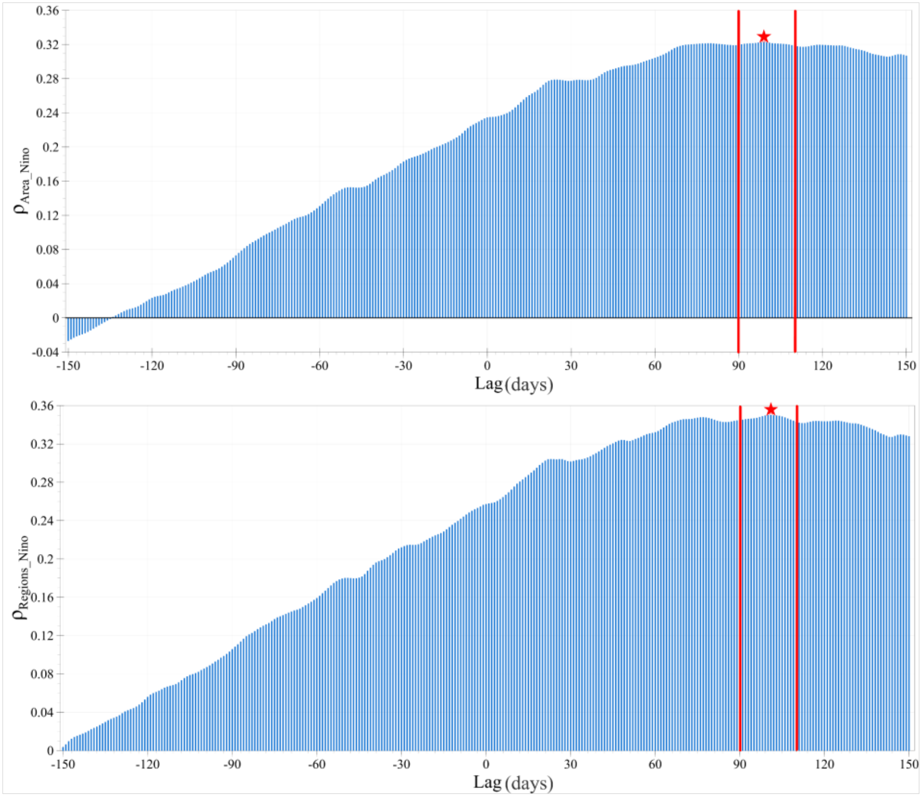

Figure S4.10. *Cross-correlation between heatwave characteristics and Niño index. The blue bars show the Pearson correlation between daily global heatwave extent and Niño 3.4 (top panel) and between daily number of regions affected and Niño 3.4(bottom panel) at different time lags. The vertical red lines give the range of lags (days) that correspond to the maximum correlation values and the red star highlights the maximum correlation value*

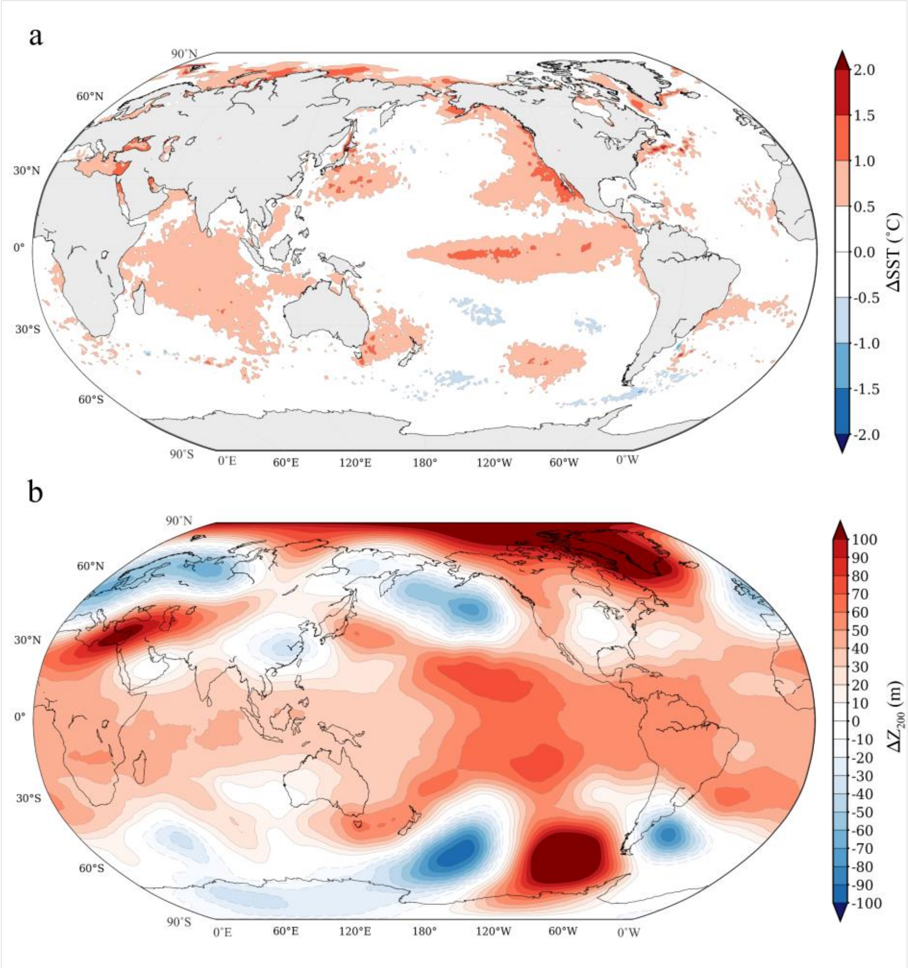

Figure S4.11. *Atmospheric and oceanic conditions during global heatwave days. Composite anomalies during global heatwave days. (a) SST anomalies during the global heatwave days (same as Figure 4.5b of main text) (b) Geopotential height anomalies at 200hpa during global heatwave days. Composite anomalies were computed by averaging the anomalies of GHWD w.r.t their calendar days.*

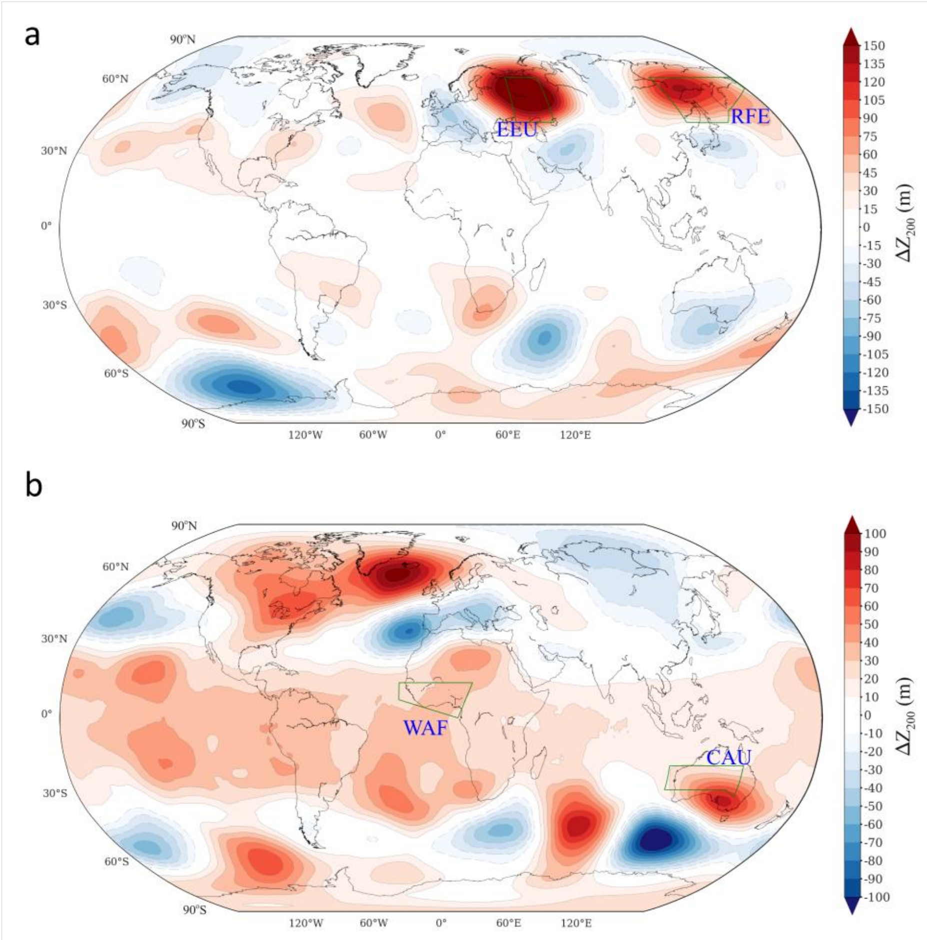

***Figure S4.12**. Composite geopotential height anomalies at 200hpa (in m) for the two teleconnection pairs (a) RFE–EEU pair and (b) CAU–WAF pair. Red and Blue colours represent the high and low pressures.*

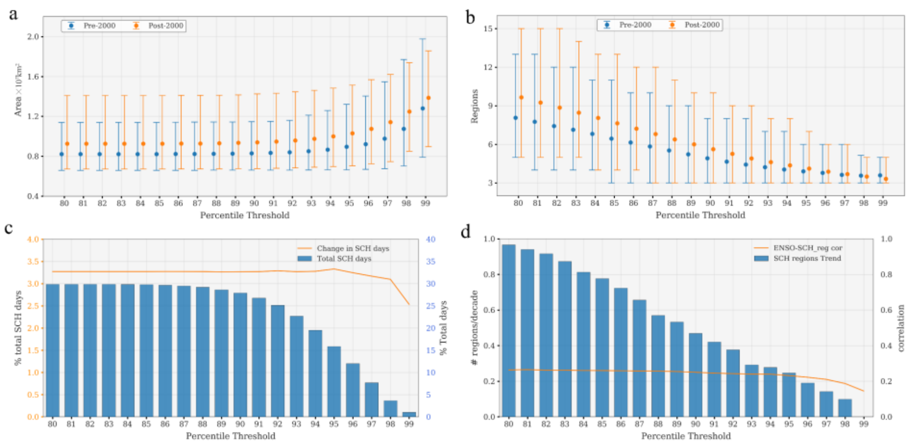

***Figure S4.13**. Sensitivity of SCH characteristics and regional heatwaves to the selection of thresholds for heatwave definition. Change in the pre- and post-2000 distribution of SCHs characteristics for different thresholds, area (a) regions (b). The dots correspond to mean and the whiskers correspond to the 5th and 95th percentiles. (c) total number of SCHs days during the period 1979-2020 (blue bars) is given as the percentage of the total number of days. The orange line shows the* *change in the annual average frequency of SCH days pre-and post-2000; the values are represented as the percentage of total SCH days. (d) sensitivity of the trend in the number of regions affected by the SCHs (bars) and the line plot gives the correlation values between the Niño 3.4 index and the number of regions affected by heatwaves. All trend and correlation values are significant at 5%, except the trend corresponding to 99th percentile*

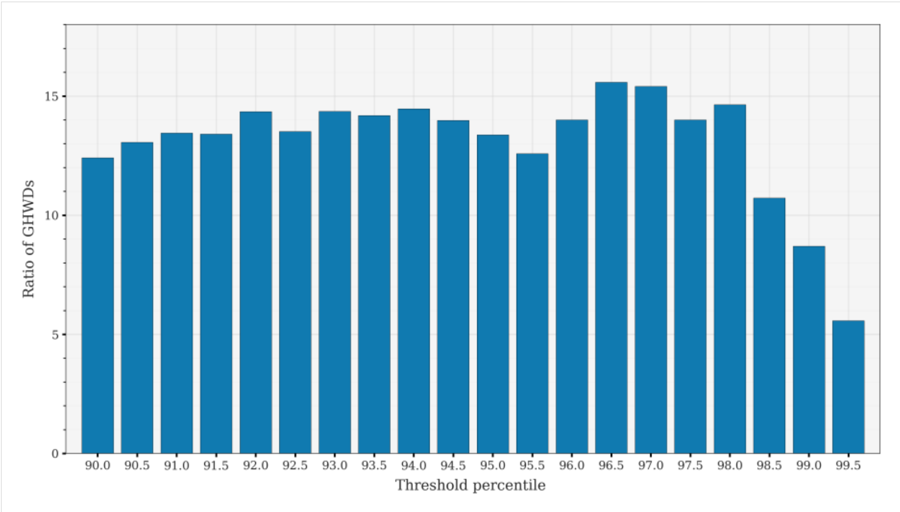

Figure S4.14. *Ratio of post- and pre-2000 GHWDs for different threshold percentiles (same threshold percentiles for global heatwave extent and number of regions affected by heatwaves) adopted to define GHWDs.*

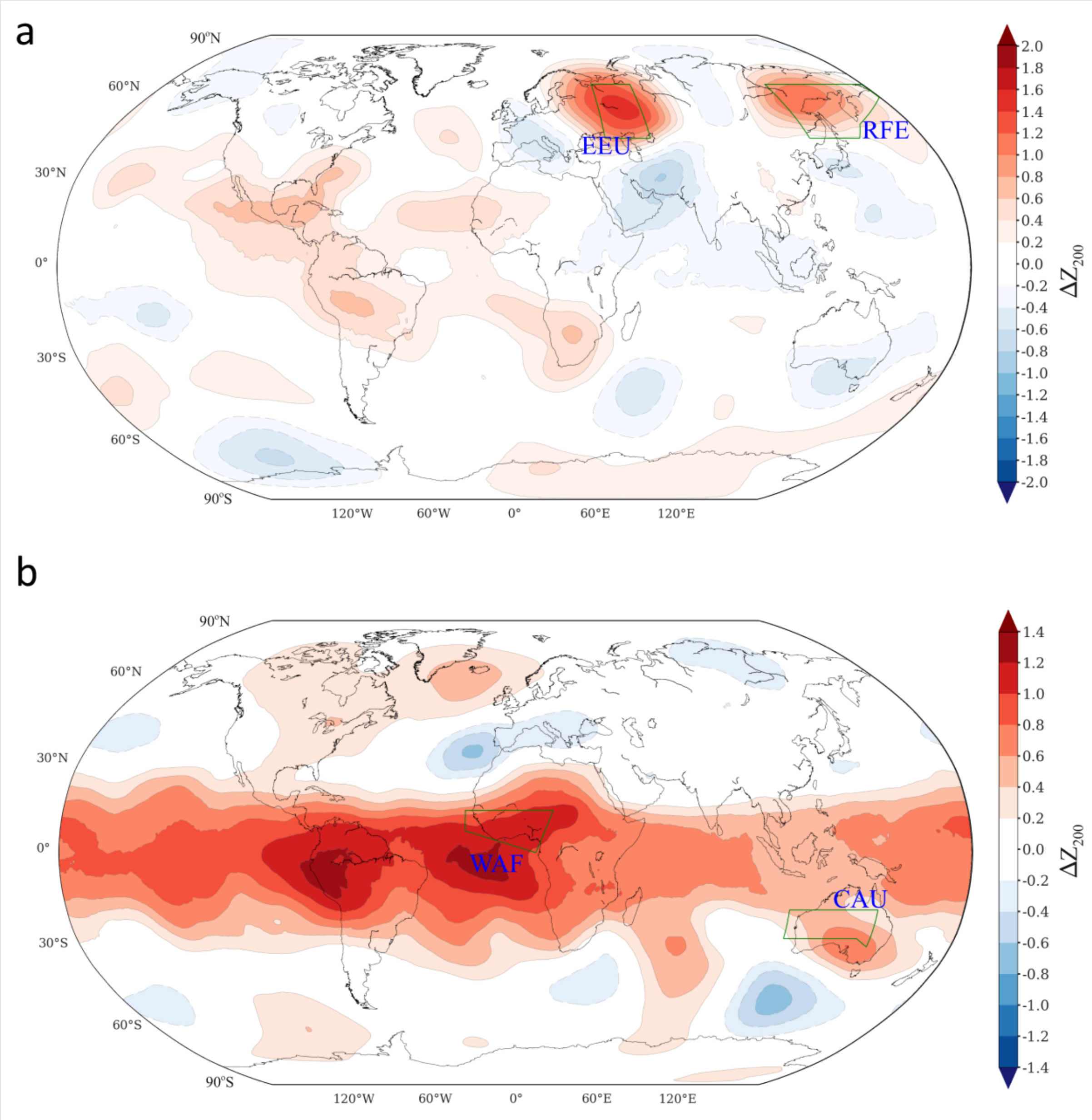

Figure S4.15. *Same as Figure S4.12 but anomalies are standardized.*

.

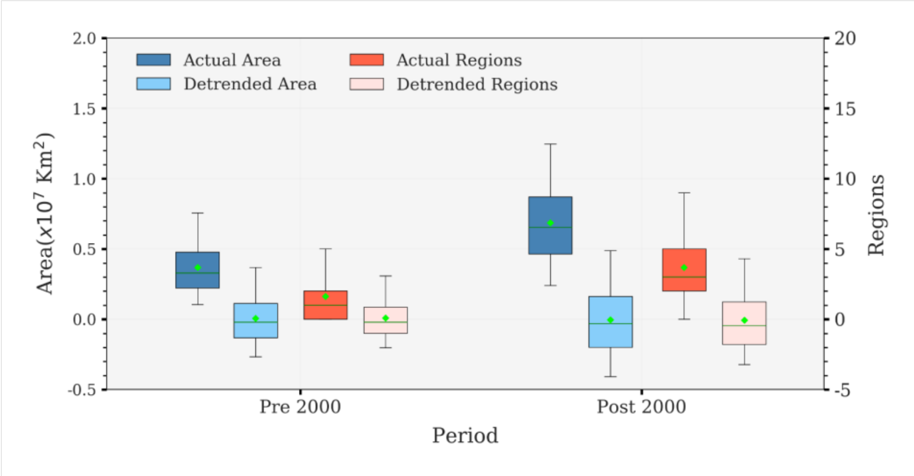

Figure S4.16. *Same as Figure 4.1d but the distributions are for global area and number of regions affected by heatwaves (i.e., all days are included) pre-and post-2000. Whiskers correspond to 5th and 95th percentile and green dots represent mean.*

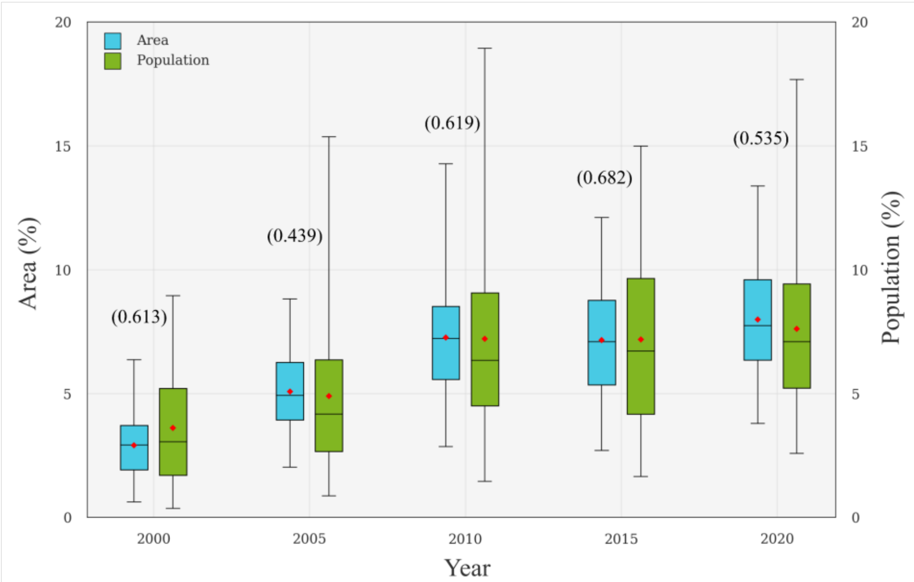

Figure S4.17. *Same as Figure 4.4b of main text but using all heatwave days.*

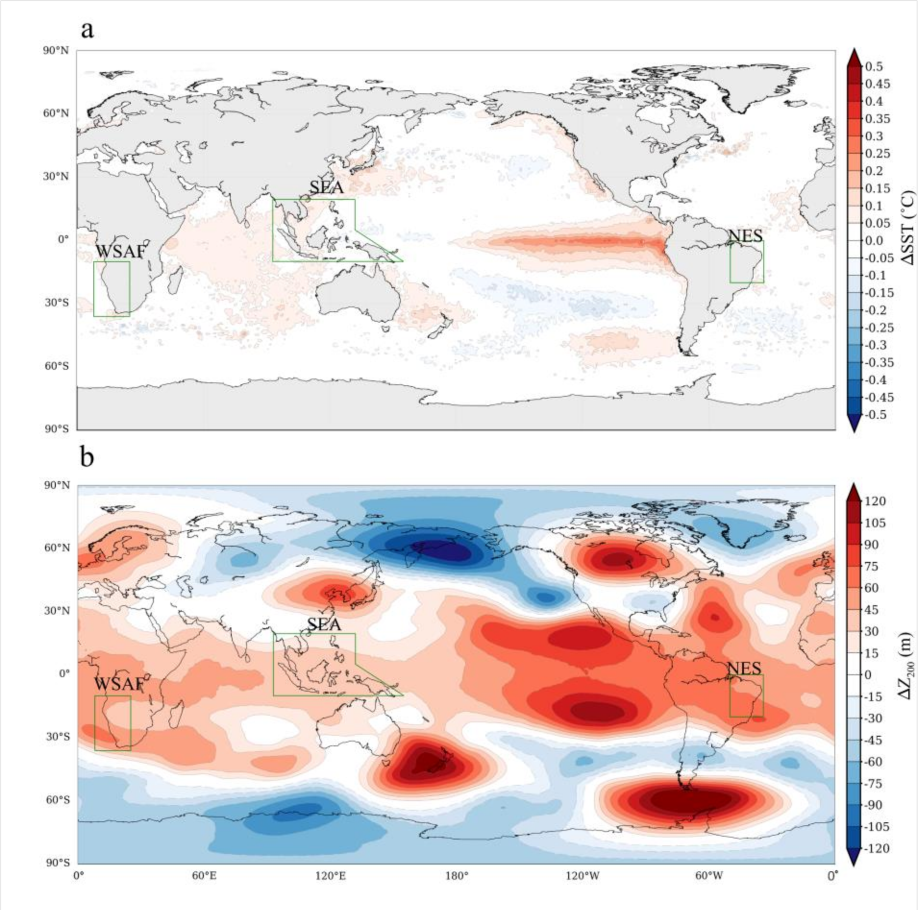

Figure S4.18. *Composite anomalies during concordant heatwaves days in NES–SEA–WSAF. (a) composite SST anomalies (b) composite geopotential height anomalies at 200 hPa.*

Chapter 5 : Spatially compounding of multivariate extremes: Role of climatic variability

Executive summary

Identification of the regions that show a significantly higher likelihood of experiencing droughts or heatwaves together in Chapters 3 and 4 allowed us to identify the regions that possess higher likelihood of spatially compound CDHWs (SC-CDHW) in Chapter 5. SC-CDHW is a special type of spatially compound multivariate extreme (SCME) where the multivariate extreme is compound drought and heatwave. These SCMEs are more damaging than univariate SCEs as they represent two-way compounding of extremes (spatial and variable). Although univariate SCEs have been relatively explored (Chapters 3 and 4 and references and few more studies), SCMEs have not been explored till date. Previous studies on CDHWs, however, have indirectly hinted at the co-occurrence of CDHWs in multiple regions during El-Nino events (Hao *et al* 2018, Feng *et al* 2019, Feng and Hao 2021, Mukherjee *et al* 2020). Hao *et al* (2018) found higher probability of CDHWs in northern South America, Southern Africa, Southeast Asia, and Australia during El-Nino events. Moreover, Mukherjee *et al* (2020) noted significant positive relationship between El-Nino and CDHWs days over multiple regions, suggesting higher likelihood of SC-CDHWs during El-Nino in these regions.

To answer these questions, Chapter 5 of this thesis identifies the regions that show significant concordance in CDHWs and develop a model that could estimate the probability of SCEs or SCMEs based on the climatic conditions (given by climate indices). Using weekly drought and heatwaves we find an intimidating increase in the number of IPCC AR6 regions that are experiencing droughts, heatwaves, and CDHWs concurrently. The highest trend is shown by heatwaves which also control the trend in CDHWs. Multiple CDHW concordances are observed, with the majority occurring in nearby regions, and the land-atmosphere feedback is most likely responsible. Long-distance teleconnections in CDHWs are usually driven by large-scale climatic oscillation such as ENSO. Two long-distance concordant (NSA–SEA, and NSSA–MDG) pairs are selected for in-depth analysis of physical mechanisms and role of climatic oscillations. Higher transitional probabilities between drought, heatwaves, and CDHWs in Northern South America (NSA) throughout both (winter and summer) seasons highlight strong land-atmosphere feedback and precipitation–temperature dependence while as lower transitional probabilities in Southeast Asia and Madagascar indicate weak precipitation–temperature dependency and land-atmosphere feedback in these island regions. Both logistic model and composite anomalies indicated El-Nino as the dominant driver, whereas AO seemed to have a significant impact on NSA–MDG pair. When El-Nino intensity rises from moderate to exceptional, our model estimated an increase in the probability of CS-CDHWs from 0.008 to 0.9 in NSA–SEA and from 0.005 to 0.97 in NSA–MDG. The model developed for SC-CDHW could be used for all SCEs and potentially could predict the SCEs with little improvements.

After: ***Waqar Ul Hassan*** *Munir A. Nayak and M. F. Azam; Spatially compounding of multivariate hazards: role of climate oscillations and land-atmosphere interaction:* ***(In preparation)***

Abstract

Compound droughts and heatwaves –droughts and heatwaves occurring simultaneously in a region– cause serious socio-ecological damage. The impacts, however, are epidemic when these CDHWs co-occur at multiple locations. Recent studies have addressed CDHW but their spatial compounding is yet to be understood. In this Chapter, we use weekly precipitation and maximum temperature data to explore spatially compound multivariate events at global scale. Our analysis shows an unprecedented rise in the number of IPCC regions experiencing spatially compound droughts, heatwaves, and CDHWs. We find that the increasing trend of spatially compound CDHWs (SC-CDHWs) is mainly driven by the trend in heatwaves. LMF analysis revealed multiple concordances in CDHWs, with majority among adjacent regions, and are likely driven by land-atmosphere feedback. Many long-distance SC-CDHWs, which are tens of thousands of kilometres distant, are driven by large-scale atmospheric and oceanic teleconnections, such as ENSO.

The stronger transitional probabilities between drought, heatwaves, and CDHWs in Northern South America (NSA) during both (winter and summer) seasons emphasize strong land-atmosphere feedback and precipitation–temperature dependency. On the other hand, the lower transitional probabilities in Southeast Asia (SEA) and Madagascar (MDG) highlight weak precipitation–temperature dependence and land-atmosphere feedback. The logistic models for the two selected teleconnections identified El Niño as a primary driver of SC-CDHWswhile AO appears to play an important role in NSA–MDG teleconnection. Composite SST and 200hpa height anomalies also demonstrated El-Nino as the key driver of these teleconnections. We estimate that the chance of an SC-CDHW increase from 0.008 to 0.9 in NSA–SEA and 0.005 to 0.97 in NSA–MDG when El Niño intensity increases from moderate (Nino3.4=1) to exceptional (Nino=3).

5.1. Background

Droughts, heatwaves, and their concurrence has increased dramatically in the last few decades, particularly in response to anthropogenic climate change (Diffenbaugh *et al* 2015, Feng *et al* 2021, Mazdiyasni and AghaKouchak 2015, Wu *et al* 2019). The co-occurrence of these extremes over a geographic region is commonly termed as "*multivariate compound events*" (Zscheischler *et al* 2020) or simply "*compound events*" (Leonard *et al* 2014). Compound droughts and heatwaves (CDHWs) have received lot of attention in the last decade (Mukherjee *et al* 2020, Wu *et al* 2021, Wu and Jiang 2022, Wu *et al* 2019, Hao *et al* 2019). These events are often associated with multiple adverse socio-ecological impacts that include reduction in crop productivity (Ciais *et al* 2005, Feng *et al* 2019, Haqiqi *et al* 2021, Wegren 2011), an increase in wildfire occurrence (Jones *et al* 2020, Yoon *et al* 2015), reduction in quality of life, and adverse implications to human health including deaths (Poumadere *et al* 2005, Vogel *et al* 2019).

The occurrence of CDHWs is triggered by two major physical mechanisms: the land-atmosphere feedback loop (Hirsch *et al* 2019, Miralles *et al* 2019) and the persistent ocean-atmospheric circulation (Hao *et al* 2018, Mukherjee *et al* 2020, Seneviratne *et al* 2012). Drought causes dry soils, clear sky, and increased sun irradiation. A dry soil inhibits or ceases evapotranspiration, limiting latent heat cooling (Berg *et al* 2014, Hirsch *et al* 2019), and extra solar energy is converted to sensible heat flux, which raises temperatures and worsens heatwaves (Miralles *et al* 2019). These energy budget abnormalities are connected to atmospheric blockings, anticyclonic cyclonic circulations, and low-level wind divergence (Mukherjee *et al* 2020, Dong *et al* 2018b). These anticyclonic circulations and blockings last longer than usual over a region, allowing the droughts and heatwave to intensify and expand to become a CDHW event by increasing temperature, evapotranspiration and diverting cold, moist air (Dong *et al* 2018b, Pfahl and Wernli 2012, Schneidereit *et al* 2012). For example, during the summer 2010 drought, the persistent subtropical high/ anticyclonic pattern over Russia lead to increased evapotranspiration during the initial period that resulting in the severe soil moisture deficiency (severe drought) and anomalously increase in air temperature due to prolonged increase in sensible heat fluxes (severe heatwave) (Hong *et al* 2011, Schneidereit *et al* 2012).

Climatic oscillations, such as ENSO, PDO, NAO, and others, drive the formation and propagation of these large-scale atmospheric anomalies including sub-tropical high-pressure patterns, and stationary blocking zones and play a significant role in the occurrence of CDHWs (Hao *et al* 2019, 2019, 2018). El-Niño is found to cause summer season compound dry and hot events in most of the tropical regions, particularly in Northern South America, Central and Southern Africa, Australia, and Southeast Asia (Hao *et al* 2018, Mukherjee *et al* 2020). Hao *et al* (2019) built a logistic model to predict the global CDHW and discovered that ENSO skillfully predicted the spatiotemporal variability of CDHWs across the globe. Mukherjee *et al* (2020) developed a Poisson Generalized linear model (GLM) to understand the role of climate oscillations in causing the CDHWs at the global scale and noted that ENSO strongly impacts CDHW events in the Southern Hemisphere during the austral summer and autumn, whereas PDO influences CDHWs in Western North America during the boreal summer. Multiple regional studies have also highlighted the relationship between the occurrence of CDHWs and low frequency climate oscillations (Wu *et al* 2019, Hao *et al* 2018, Reddy *et al* 2022, Feng and Hao 2021). Wu *et al* (2019) discovered a statistically significant positive correlation of spatial extent of compound extremes in China with AMO. It was also observed that NAO- and EA/WR- had a substantial influence, while ENSO did not. PDO and NAO significantly impact regional CDHWs with higher CDHW activity over much of Europe during NAO+ (Hao et al., 2019). In a recent study, Reddy *et al* (2022) found increased frequency, duration, and severity of CDHWs during strong El Niño phases in northeast Australia compared to neutral ENSO and IOD conditions; however, the increases are intense and widespread over

Eastern Australia when strong El Niño phases co-occur with strong IOD+.

Weather or climate extremes occurring simultaneously in multiple remote regions, defined as spatially compound extremes (Zscheischler *et al* 2020), are more dangerous compared to multivariate compound events as they may cause global food and water crisis (Haqiqi *et al* 2021, Anderson *et al* 2019). For example, the concurrent droughts in multiple food-producing countries including Brazil, India, South Africa, and Southeast Asia, during the Global drought of 1876–1877 caused 50 million casualties and resulted in the Great Global Famine (Singh *et al* 2018). Singh *et al* (2022) observed a ninefold increase in the agricultural land and population exposed to spatially compound droughts. The co-occurrences of droughts and/or heatwaves in multiple regions across the globe are often related to the atmospheric and oceanic circulation anomalies (Ding and Wang 2005, Hassan and Nayak 2020, Kornhuber *et al* 2020, Rogers *et al* 2021a, Singh *et al* 2021), recurrent Rossby waves (Röthlisberger *et al* 2019), and persistent atmospheric blockings (Röthlisberger *et al* 2019, Pfahl and Wernli 2012). For example, the simultaneous warm spells over Europe, North America, and the Western North Atlantic in summer 1994 resulted from synoptic-scale recurrent Rossby waves (Röthlisberger *et al* 2019). Such global-scale weather patterns and the associated spatially compound events are established and modulated by anomalous sea surface temperatures and atmospheric teleconnections of remote forcings, e.g., large-scale climate oscillations such as ENSO (Alexander *et al* 2002, Hassan and Nayak 2020, Herceg-Bulić *et al* 2017, Luo and Lau 2020, Singh *et al* 2021). The Pacific SST anomalies (i.e., ENSO) influence the evolution of SST anomalies in other oceanic basins and modulate the global atmospheric circulations (Alexander *et al* 2002, Cai *et al* 2019a). These ocean-atmosphere interactions are bound to influence multiple remote regions simultaneously and/or sequentially (Luo and Lau 2020, Lee *et al* 2021). In addition, the low-frequency climate oscillations such as NAO, PDO, AMO, PNA, and others are also found to influence spatially compound droughts or heatwaves at a more regional scale (Hassan and Nayak 2020, Mukherjee *et al* 2020, Rogers *et al* 2021a, Singh *et al* 2021).

In the last few years, monitoring and modelling of risk associated with compound events have garnered significant attention (de Brito 2021, Zscheischler *et al* 2020). Multiple studies have attempted to develop methods to quantify the risk and impacts arising from compound events (de Brito 2021, Hao *et al* 2018, Haqiqi *et al* 2021, Pfahl and Wernli 2012); however, the research on spatially compound events is in its initial stages with only a limited studies available. These studies either consider spatial compounding of droughts (Hassan and Nayak 2020, Singh *et al* 2021) or spatial compounding in heatwaves (Kornhuber *et al* 2020, Rogers *et al* 2021a) in isolation. Moreover, some global studies on CDHWs have hinted toward the occurrence of CDHWs in multiple regions during El-Niño.

These observations and multiplication of impacts due to spatially compounding highlight the need for a global assessment of spatially compound multivariate extremes (here, spatially compound CDHWs), so that their impacts and risks to future food security can be estimated rationally. To this end the following questions are answered in this Chapter: (1) How often are spatial compounding of CDHW observed? (2) What regions show higher likelihood of these events? (3) What are the contributions of different climate oscillations? (4) Develop a model to estimate the probability of SCE given the climatic conditions?

5.2. Data and Methods

5.2.1. Data

High-resolution (spatial resolution of $0.5° \times 0.5°$) daily precipitation and maximum temperature (T_{max}) from the National Oceanic and Atmospheric Administration (NOAA) Climate Prediction Centre (CPC) for the period 1st January 1979 to 31st Dec 2020 (i.e., 42 years) are used in this analysis. Here, the analysis is performed at weekly time scale by aggregating the daily precipitation to weekly totals and daily temperature to weekly averages. Sea Surface Temperature (SST) and 200hPa geo-potential height (Z_{200}) from European Centre for Medium-Range Weather Forecasts Reanalysis Fifth Generation Dataset (ERA5(Service (C3S) 2017) available at a horizontal resolution of $0.25° \times 0.25°$ are used to explore the oceanic and atmospheric conditions during spatially compound CDHWs. In addition, standard climate oscillation indices, such as Niño 3.4 and Niño 4 (ENSO), NAO, AO, PNA, and AAO from the WHO's climexp and NOAA CPC (http://climexp.knmi.nl/selectdailyindex) and (Climate Prediction Center: Teleconnections - Archive of Daily Indices (noaa.gov)) are examined for their role in SC-CDHWs.

5.2.2. Identification of dominant CDHW season

In this study, global land mass (excluding Antarctica) is divided into 44 reference regions as per IPCC AR6. For each region, we computed regional average of daily precipitation and temperature. Afterwards, total number of wet days and average weekly temperature for each calendar week are calculated. For example, for the first calendar week of the year, i.e., 1–7 Jan of all the years, we calculated the number of days that have precipitation more than 2mm. Same procedure was applied to temperature but instead of defining hot days, we calculated average temperature for calendar weeks. For each region, we identified the dominant season of precipitation and temperature using circular statistics, which include circular mean, mean resultant length, and circular standard deviation. Circular statistics are often used to identify the seasonality in hydrological variables (Villarini 2016). For precipitation, we use circular mean to represent the time of the year that is expected to have on an average maximum frequency of wet days (rainfall $\geq$ 2mm). Mean resultant length gives the strength of seasonality given by the mean, while as standard deviation gives scatter of the data around the mean. Circular statistics for each region are then calculated for both precipitation and temperature. In a region, we define a dominant season for precipitation or temperature as the period of the year that is given by one standard deviation on both sides of circular means (i.e., circular mean $\pm$ one standard deviation).

A compound drought and heatwave represent the concurrence of precipitation deficit and high temperatures; however, precipitation deficit should not be confused with the aridity or dry season i.e., season which hardly receives any rainfall. Therefore, we limited our analysis of drought and heatwaves to the common period of dominant seasons for precipitation and temperature, i.e., intersection of dominant seasons of precipitation and temperature. This common period also represents the dominant season for CDHW occurrence as it has more likelihood of actual droughts and heatwaves occurrences.

5.2.3. Identification of Droughts, Heatwaves and CDHWs

We used weekly SPI and CTX90pct to define weekly droughts and heatwaves at each grid cell. In addition, the calculation of SPI in each region is limited to the grid cells and calendar weeks that have at most 30% of years (13 years) with zero precipitation or climatological filling. For heatwaves, although CTX90pct needs to be computed on daily data (algorithm discussed in previous Chapters), we computed it on a weekly scale. The 90th percentile (TX_{90}) threshold is computed locally for each grid cell and each calendar week using a 3-week moving window of weekly average of daily maximum temperatures over the period 1979–2020. We specify a lower bound for TX_{90} as $0°C$ to avoid the identification and inclusion of frost spells as warm spells. At each grid cell, a week is defined as a drought when the weekly SPI is less than -0.8 and a heatwave week is defined when weekly $T_{max} - TX_{90}$ exceeds 0.

After identifying grid cell droughts and heatwaves, for each region and for each week, *Regional drought extent* and *Regional heatwave extent* are computed as the sum of the area of all grid cells in the regions that are experiencing drought week and heatwave week, respectively. A region is said to experience a regional drought week when the regional drought extent on a given week is greater than 80th percentile of non-zero regional drought extents. The 80th percentile is computed only from those weeks that have at least one grid cell in the region under drought conditions. Same procedure is used to define regional heatwave week. Then we define a regional CDHW week if a region experiences a regional drought week and regional heatwave week concurrently.

When two or more regions encounter a regional CDHW week concurrently (i.e., same week), we call that week a ***Spatially compound CDHW week*** or ***spatially compound CDHW event (SC-CDHW)***.

5.2.4. Probability estimation

The probability of experiencing a regional extreme week (drought, heatwave, and CDHW) is estimated using equation (5.1) below.

$$\hat{p}_i = \frac{n_i}{N} \tag{5.1}$$

where, n_i is the number of extreme event weeks in region i, and N is the total number of weeks in consideration (based on the dominant season). Two regions (i and j) are under a spatially compound extreme event, say spatially compound CDHW, if both regions experience a regional CDHW event simultaneously on the given week. For each pair of regions, the probability of experiencing SC-CDHW week or concordance probability $(\hat{p}_{i,j})$ is the ratio of the number of SC-CDHW weeks between i and j (n_{ij}) and the total number of weeks under consideration (N) as shown in equation (5.2).

$$\hat{p}_{i,j} = \frac{n_{ij}}{N} \tag{5.2}$$

If the two regions are independent, the estimated concordance probability is $\hat{p}_i \times \hat{p}_j$. We used the likelihood multiplication factor (LMF) to illustrate the strength of concordance between each pair of regions. The LMF is the ratio of the observed concordance probability and concordance probability under the complete independence assumption. For any pair of regions i and j LMF is computed as below:

$$LMF_{ij} = \frac{\hat{p}_{i,j}}{\hat{p}_i \times \hat{p}_j} \tag{5.3}$$

The LMF varies in the range of 0 and infinity. For any pair of independent regions, LMF equals 1. If observed concordance is higher than what is expected under independence, LMF is greater than 1 and for the opposite case, LMF is between 0 and 1.

Notably, LMF is a scaler and provides no information on its statistical significance. To determine the statistical significance of LMF for each pair of regions, a statistical test is conducted under the null hypothesis that the observed number of SC-CDHW weeks may be recreated by chance and do not need any physical link between the regions. To do this, a bootstrapping method is used in a way similar to that described in the preceding chapter (Chapter 4), but with a lower sample size (500) for each resample generated.

5.2.5. Composite Anomalies

The composite anomalies of SST and geopotential height at 200hPa during two selected SC-CDHW pairs are used to investigate the atmospheric and oceanic characteristics that contribute to the occurrence of such spatially compound extremes. The composite anomaly for each grid cell is the average of the anomalies for all SC-CDHW weeks throughout the research period, where the anomaly for a SC-CDHW is the departure from the long-term climatological mean for that calendar week. To estimate standardized anomalies, the composite anomalies for each SC-CDHW week are divided by the standard deviation of the corresponding calendar weeks before being averaged.

5.2.6. Transitional probabilities and Logistic regression model

The transitional probabilities for any pair of extreme events represent the conditional probabilities of an extreme given another extreme is already there. These extremes can be same or different and can be occurring in same or different regions. The transitional probabilities on the same day and one day after are used in this study, and are computed as in equations 5.4 and 5.5, respectively.

$$p(EX_1|EX_2)_t = \frac{\sum(EX_{1,t} \times EX_{2,t})}{\sum(EX_{2,t})} \qquad (5.4)$$

$$p(EX_1|EX_2)_{t-i} = \frac{\Sigma(EX_{1,t} \times EX_{2,t-1})}{\Sigma(EX_{2,t-1})} \quad (5.5)$$

Where, $p(EX_1|EX_2)_t$, represent the probability of week *"t"* being extreme 1 (EX_1; say drought) week given week *"t"* is extreme 2 (EX_2; say heatwave) week also and $p(EX_1|EX_2)_{t-1}$ is the probability of a week *"t"* being EX_1 week given that week *"t-1"* was EX_2 week. *"t"* stand for *t*th week.

The logistic regression is a special form of the Generalized Linear Model (Lindsey 2000) and is used to model binary data (takes only 0 and 1) based on a set of continuous and/or categorical independent variables. However, it does not make much sense to fit continuous data to binary outcomes, rather, it is preferred to model the conditional probabilities of successes *(Y=1)* as a function of independent variables *(X)* i.e., $P(Y=1|X=X_t)$. As the outcome are probabilities, they are bound to be in the range of 0 and 1. The conditional probability of success in a logistic model is modelled as logit inverse function of the log-odds (or log(odds)), where odds are defined as the ratio of likelihood of success divided by the likelihood of failure. The mathematical formulation of model is shown below:

$$P(Y_i = 1|X_i) = p_i = logit^{-1}(log(odds)) \quad (5.6)$$

$$odds = \frac{p_i}{1-p_i} \quad (5.7)$$

Where, Y_i, X_i represent the set dependent (in our case, binary array of SC-CDHWs) and of independent variables (i.e., climate oscillation indices in our case) for a particular week, p_i is the probability of success given the independent variables. The logit inverse function, which transforms the continuous values into a range of (0,1), is mathematically written as:

$$logit^{-1}(a) = \frac{e^a}{1+e^a} \quad [5.8]$$

In logistic regression the log(odds) is given by the linear combination of the independent variables as is shown below:

$$log(odds) = \log\left(\frac{p_i}{1+p_i}\right) = Z_i = logit\ (p_i) \qquad [5.9]$$

$$Z_i = \alpha + \sum \beta_i X_i + \epsilon_i \qquad [5.10]$$

β_i are the slope corresponding to X_i. α and ϵ are the intercept and residuals.

5.3. Results

5.3.1. Dominant CDHW seasons

The dominant seasons of precipitation and temperature for each IPCC region are identified based on the circular mean (direction) and circular standard deviation. The circular distribution of precipitation (wet) days and temperature are shown in Figures 5.1 and 5.2, respectively. Northern hemisphere regions, except few regions such as WNA, MED, and ARP have boreal summer (May-Sep) as the dominant season of precipitation (top 3 rows of Figure 5.1), and boreal winter is the dominant season for the Southern hemisphere (bottom 2 rows of Figure 5.1). Some Equatorial regions such as SEA, NSA, and NWS receive precipitation throughout the year and show no dominant seasonality (fourth row of Figure 5.1). Tropical African regions receive most of their precipitation in boreal summer while tropical South American regions highlighted boreal winter as their dominant season.

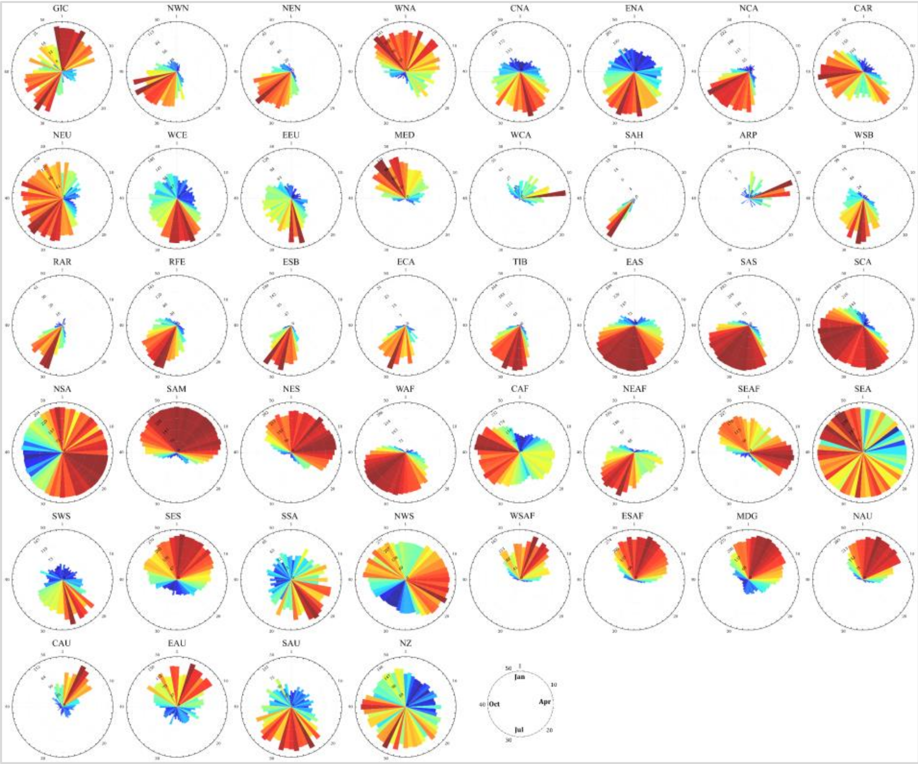

Figure 5.1. *Regional seasonality in precipitation for IPCC AR6 regions. The numbers on the circumference correspond to the calendar week and the radial bars show the number of wet days during that calendar week. Red and blue colors show the wetter and drier periods, respectively, for that region. In some tropical regions, the difference between maximum and minimum number of wet days is small, so we consider the entire year as their dominant season for precipitation.*

In contrast to precipitation, temperature show more homogenous seasonality (Figure 5.2). All boreal regions have summer as the dominant season for warm temperatures (more than 20 ° C), with exception of polar regions such as GIC, while as all the Southern hemisphere regions show warm temperature dominance during boreal winter (Nov-Mar). Tropical regions, however, show year-round warm temperatures with no dominant seasonality. Similar results for both precipitation and temperature are reported in Iturbide *et al* (2020) and IPCC AR6. As stated in the methods section of this Chapter, dominant season for CDHWs is the common period of dominant season in precipitation and temperature. Based on the dominant seasons of precipitation and temperature, we find that almost all regions of Northern hemisphere (greater than 0°N), except WNA and MED, have their common dominant period within the extended 5-month summer season (i.e., mid-May to mid-Sept). In contrast, Southern hemispheric regions, excluding NZ and SAU, showed extended 5-month boreal winter (first-Nov to end-Mar) as their dominant season for CDHWs. Moreover, some tropical regions where no apparent seasonality is observed in precipitation and temperature show both seasons as their dominant seasons for CDHWs.

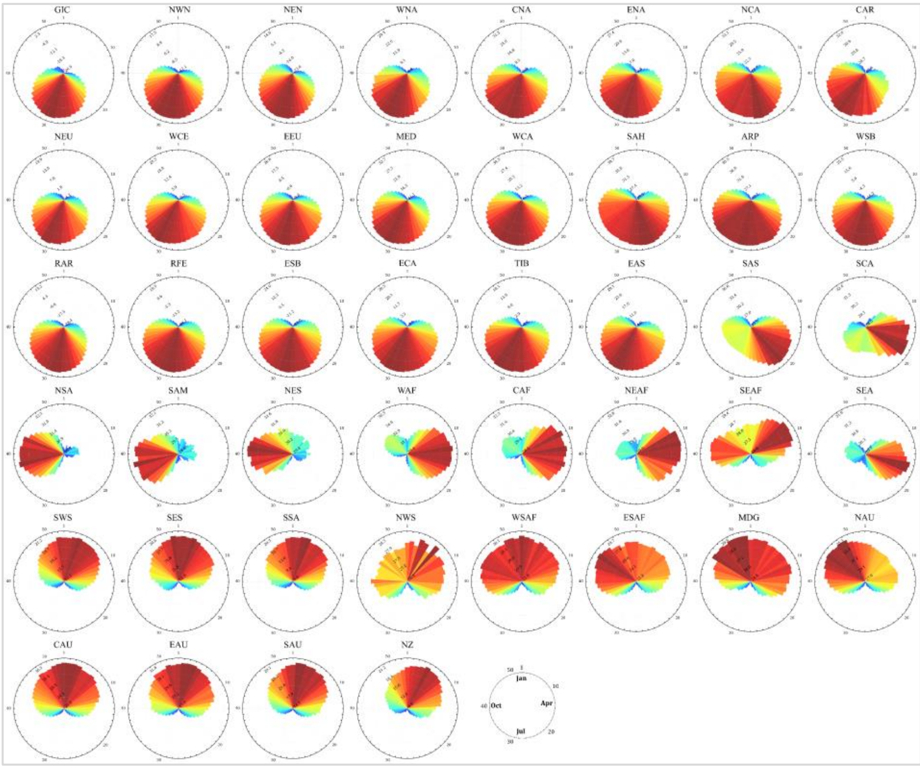

Figure 5.2. *Same as Figure 5.2 but for temperature. The radial bars show the magnitude of the temperature during that week. Red and blue colors show the period hotter and cooler periods respectively for that region. Here, the value at the centre of the circle is not same for all regions. In tropical regions, the minimum temperature is always more than 20°C and difference between maximum and minimum temperature is small, so they are considered hot throughout the year.*

Furthermore, we find that some regions, mostly tropical regions with no appearent seasonality and those that show exceptions to hemispheric seasonality highlighted 3-month spring (Mar to May) and 3-month Autumn (mid-Sep to mid-Nov) as their dominant seasons for CDHWs. The complete list of regions and their dominant season for CDHWs is given in Table 5.1.

Table 5.1. *IPCC AR6 regions and their dominant seasons for occurrence of CHDWs. Here regions show entire year as dominant season for CDHW, however, we have divided the year into seasons to perform seasonal analysis.*

S. No.	***Summer***	***Winter***	***Spring***	***Autumn***
1	GIC	NWS	NWS	WNA
2	NWN	NSA	NSA	SCA
3	NEN	NES	NES	CAR
4	CAN	SAM	SAM	NWS
5	ENA	SES	SSA	NSA
6	NCA	CAF	CAF	SAM
7	SCA	SEAF	SEAF	MED
8	CAR	WSAF	WCA	CAF
9	NSA	ESAF	ARP	SEA
10	NEU	MDG	SEA	SAU
11	WCE	SEA		NZ
12	EEU	NAU		
13	SAH	CAU		
14	WAF	EAU		
15	CAF			
16	NEAF			
17	RAR			
18	WSB			
19	ESB			
20	RFE			
21	ECA			
22	TIB			
23	EAS			
24	SAS			
25	SEA			

5.3.2. Changes in CDHWs

After identifying the dominant season(s) for each IPCC region, regional extreme (drought, heatwave, and CDHW) weeks are identified (see Methods). It is important to mention that regional extreme weeks for any IPCC region are defined during their dominant seasons(s) for CDHWs only. Then the number of regions that experience spatially compound events concurrently are computed. Annual average of the weekly number of IPCC regions that experience spatially compound droughts, heatwaves, and CDHWs are shown in Figure 5.3. Statistically significant increasing trends (at 5% significance) are observed in all the three types of extremes considered here. Droughts show the lowest increasing trend of only 2.4 regions per century. In contrast, heatwave regions are increasing much faster with an increasing rate of 11.2

regions per century, i.e., on an average one additional region experiences the SCH in every 10 years. This faster increase in heatwaves is mainly an outcome of increased global warming in response of anthropogenic climate change (Christidis *et al* 2015, Trenberth *et al* 2007, Perkins-Kirkpatrick and Lewis 2020) and is consistent with previous studies on heatwaves at regional and global scale (Perkins-Kirkpatrick and Lewis 2020, Holbrook *et al* 2019, Perkins *et al* 2012). The increasing trend in SC-CDHWs, however, lies between the trend in droughts and heatwaves, with a rate of 4.2 regions per century. This trend in SC-CDHWs is mostly driven by the trend in the heatwaves (Figure 5.3). Moreover, the increase in the SCHs and SC-CDHWs is more faster in post-2000 compared to pre-2000, which can provide evidence that climate change is the main driver of these trends.

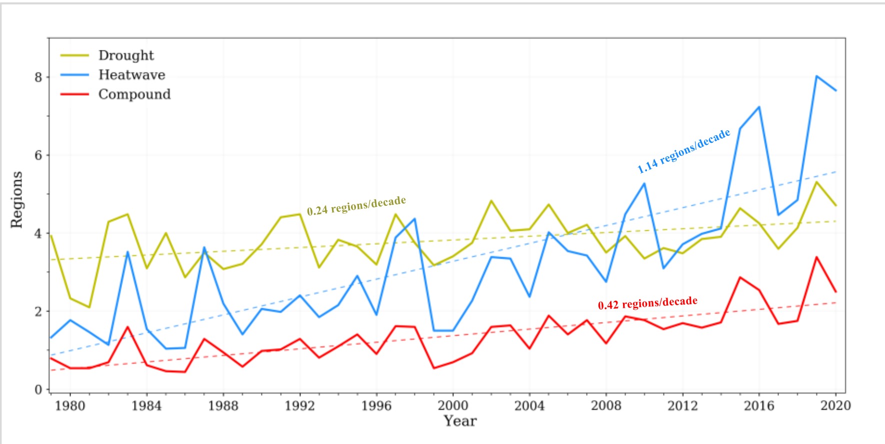

Figure 5.3. *Changes in the extent (number of regions) of the droughts, heatwaves and CDHWs. Annual time-series of the number of IPCC regions that are affected by regional droughts (green line), heatwaves (blue line), and CDHWs (red line). The dotted lines show the linear trends estimated from Man-Kendall test at 5% significance.*

5.3.3. Concordances in CDHWs

As most of IPCC regions have boreal summer or winter as their dominant season for the occurrence of CDHW, these two seasons are selected for further analysis. We find summer and winter as dominant seasons for CDHWs in 25 and 14 IPCC regions, respectively (Table 5.1). Multiple studies have observed occurrences of droughts or heatwaves in multiple regions simultaneously (Hassan and Nayak 2020, Singh *et al* 2021, Kornhuber *et al* 2020, Rogers *et al* 2021a) and some studies have also hinted at the occurrence of CDHWs in many tropical regions during El-Niño (Hao *et al* 2018, Feng *et al* 2019, Feng and Hao 2021). We explicitly explore and quantify the spatial concordances in CDHWs using pairwise LMF during summer and winter seasons. Adjacent region pairs usually show significant concordances during both seasons (Figure 5.4), e.g., southern Australia–central Australia (SAU–CAU), SAM–NSA and others, which can be mainly attributed to land-atmosphere feedback and/or absence of physical boundaries between the regions (Miralles *et al* 2019, Hirsch and King 2020, Schumacher *et al* 2019). Significant concordances in region pairs that are more than 10,000 km apart are of special relevance. e.g., SEA–NSA, Western Central Europe–Northern Caribbean (WCE–NCA), NSA–Madagascar (NSA–MDG), Eastern Australia–Southeast South America (EAU–SES), and others (Figure 5.4); we call these "*spatially compound CDHW pairs*" or *"Teleconnections in CDHWs"*. Compared to subtropical and polar locations, teleconnections in CDHWs are more common in tropical regions, where they are probably triggered by coherent warming (Byrne 2021) and El-Niño impacts (Alexander *et al* 2002, Yang *et al* 2018a). In addition, regions in Southern America (NSA, SAM, NES) and Australia (NAU, CAU, EAU) show the highest number of concordances due to the large impact of ENSO on regional CDHWs. These long-distance concordances in CDHWs highlight the role of large-scale climate oscillation and/or natural climate variability in driving these teleconnections. Previous studies have also noted climate oscillations as an important driver of long-distance teleconnections in droughts (Hassan and Nayak 2020, Singh *et al* 2021) and heatwaves (Chapter 4 and (Kornhuber *et al* 2020, Rogers *et al* 2021a)).

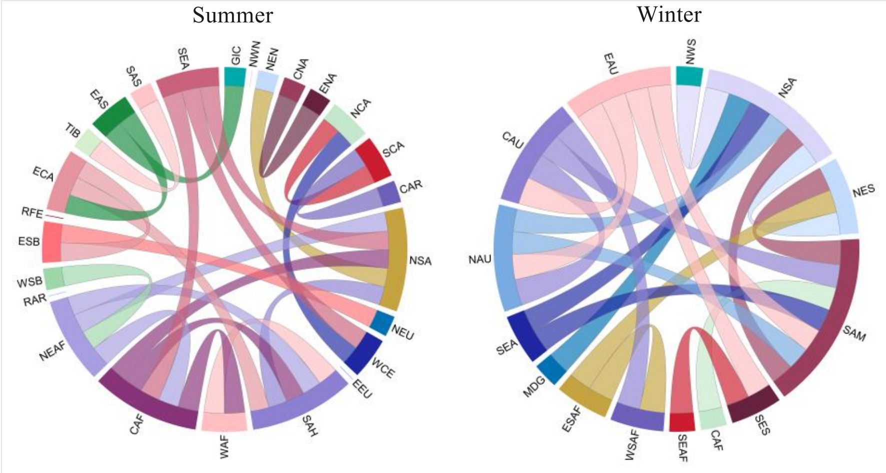

Figure 5.4. *Statistically significant concordances in SC-CDHWs. Region pairs that often experience regional CDHWs weeks together, i.e., region pairs that have higher probability of concordant CDHWS compared to what is expected by chance or LMF are significantly higher than 1. During (a) summer season and (b) winter Season. The widths of the chords/links represent the likelihood multiplication factor of the concordance and only those concordances are shown that are statistically significant at 5% significance level.*

5.3.4. Transitional probability

Among the identified teleconnections in CDHWs, NSA–SEA (during summer) and NSA–MDG (during winter) are selected for further investigation on transitional probabilities and role of climate oscillations. The higher transitional probability, of the order of 0.4, from drought to heatwave and vice-versa in NSA during both the seasons (summer and winter) highlights strong positive dependence between droughts and heatwaves (or negative precipitation–temperature dependence) and significant role of land-atmosphere interaction in causing the CDHW events (Figure 5.5). Adler *et al* (2008) and Feng and Hao (2021) also noted higher negative correlation between precipitation and temperature in NSA. While as other two regions SEA (during summer) and MDG (during winter) have relatively lower transitional probabilities, which could be because these regions are small islands and are covered by seas on all sides. In addition, the precipitation–correlation is also relatively weak (Adler *et al* 2008, Feng and Hao 2021) highlighting weak land-atmosphere feedback. Moreover, we find higher transitional probabilities of heatwaves in SEA given drought or heatwave in NSA and vice-versa, which clearly indicats strong dependence between the heatwaves in the two regions. This pair of regions was also identified as teleconnections in heatwaves (see Figure S4.2). A similar but weak dependence is also observed in other pair of regions (NSA–MDG) (Figure 5.5). This long-distance relationship between the extremes suggests strong important role of large-scale oceanic or atmospheric teleconnection that leads to the compounding of extremes.

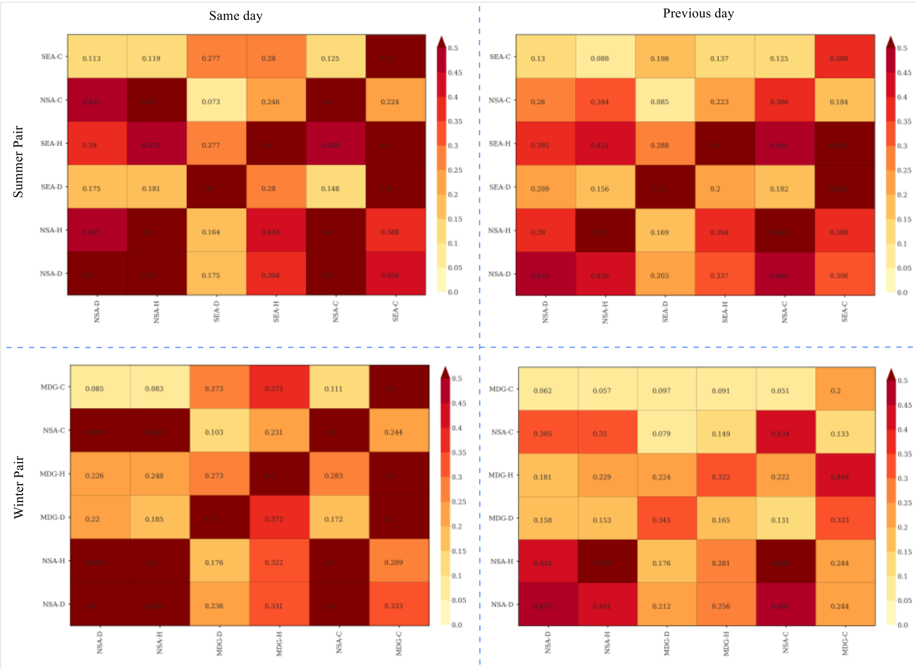

Figure 5.5. *Transitional probabilities between droughts, heatwaves, and CDHWs. (Top panels) for NSA–SEA pair on the same day (left top), on the next day (right-top), and (bottom panels) NSA–MDG on the same day (bottom left), next day (bottom right). The darker color represents higher chances of occurrence of an extreme given other is already there.*

5.3.5. Estimating the probability of spatially compound CDHWs

Two logistic regression models are developed, one for each pair, to identify the potential climatic oscillations and to estimate the probability of SC-CDHW week given the specific climatic conditions (in terms of climate indices). In this study, we used weekly averages Niño index of ENSO (one that gives the maximum R^2), NAO or AO (as they are highly correlated), PNA, and AAO. The estimated linear combination of the independent variables (i.e., estimated log-odds) in the logistic regression model for NSA–SEA and NSA–MDG pairs are given in equations 5.11 and 5.12, respectively. The model for NSA–SEA pair highlighted Niño 3.4 as the only potential driver (significant at 5%) of the teleconnection. The model has the R^2 of 0.48.

$$logit\ (p) = Z = -8.2524^{**}\ + 3.491 \times Niño3.4^{**}$$
$$-0.83 \times PNA + 0.7 \times AO + 1.016\ AAO \qquad (5.11)$$

On the other hand, the logistic model for NSA–MDG pair illustrated Niño 4 and AO as the potential drivers at 5% significance. This model, however, had a higher R^2 of 0.68.

$$logit\ (p) = \log(odds) = Z = -10.803^{**}\ + 5.589 \times Niño4^{**}$$
$$-2.805 \times PNA - 1.146 \times AO^{*} + 0.554\ AAO \qquad (5.12)$$

On examining and interpreting the model coefficients, we find that both models show almost 0 odds (ratio of probability of success to failure= e^Z) under normal conditions of the climate oscillations used (i.e., all climate indices are fixed at 0). In NSA–SEA model an increase of 1 unit in Niño3.4 increases the odds (odd-ratio) by 32 times when other climate oscillations are in normal phase, which means that positive phase of ENSO (i.e., El-Niño) has a strong impact on the occurrence of SC-CDHWs in NSA and SEA. Similarly, a unit increase in AO and AAO increases the odds by 1 and 1.76 times respectively. However, PNA decreases the odds by 1.3 times. The logistic model for NSA–MDG reveals Niño 4 as the primary driver and estimates an increase of ~267 times in the odds of SC-CDHW by just 1 unit increase in Niño 4 index. Thus, highlighting El-Niño Modoki as the major contributor to SC-CDHW in NSA and MDG. AAO increases the odds by only 70%. Unlike Niño and AAO, PNA and AO decrease the odds by ~15.5 and 2.15 times respectively, meaning more chances of SC-CDHW during their negative phase.

Based on the models discussed above, we find that the probability of SC-CDHW week in NSA–SEA pair increase from 0.008 to 0.902, when Niño 3.4 changes from 1 (moderate El-Niño) to 3

** Significant at 1% significance

* Significant at 5% significance

(exceptional El-Niño) (Figure 5.6a) after fixing other variables. Similarly, after fixing other variables the probability of SC-CDHW in NSA–MDG pair increase sharply from 0.0054 to 0.997 when Niño 4 changes from 1 (moderate) to 3 (exceptional El-Niño) (Figure 5.6b).

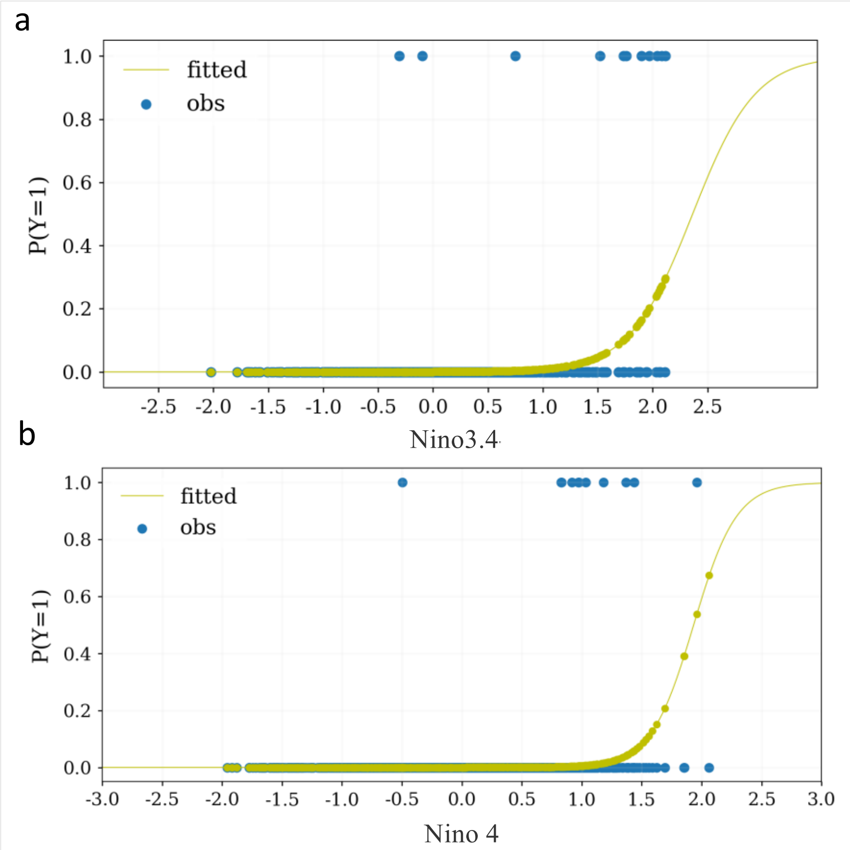

Figure 5.6. *Probability of SC-CDHW (P(Y=1)) estimated by the logistic regression model for (a) NSA–SEA pair and (b) NSA–MDG pair. The blue dots represent the observed occurrence of SC-CDHW week and the green dots represent the estimated probability of occurrence of SC-CDHW week for that value of Nino index. Green line is the fitted line for the non-observed values of Niño index. While plotting these probabilities only intercept and Niño index are used in the model.*

5.3.6. Oceanic and atmospheric anomalies during NSA–SEA pair

To further understand the physical mechanisms that are driving these strong concordances and to verify the role of potential climate oscillations suggested by the model, we computed the composite SST and 200hpa height anomalies during the SC-CDHWs weeks in NSA–SEA pair (Figure 5.7 top panel). Over the equatorial, northeastern Pacific Ocean and the majority of the tropical Atlantic Ocean, SST anomalies were above normal. Positive anomalies in the eastern and central Pacific, particularly in the Niño 3 and 3.4 regions, imply El Niño conditions. Higher SSTs over the west coast of the United States imply positive PDO phase co-occurring with the El-Niño during the SC-CDHWs. The SST anomalies in the tropical Atlantic are strikingly similar to the positive Atlantic Meridional Mode (Figure 5.7 top panel).

Over the Pacific Ocean, the 200hPa height anomalies approximate the El Niño pattern, although the pattern is rather faint (Figure 5.7 bottom panel). The persistent high pressure/anticyclonic condition over the majority of the tropics, as well as high pressure over southeast Asia and tropical southern America, diverts cold air and moisture away from these regions and prevents warm air extrusion, thereby increasing the air temperature, which is frequently amplified by land-atmosphere feedback. Additionally, the pressure pattern over the North Pacific and the United States closely resembles a negative PNA (Figure 5.7 bottom panel). In addition, distinct positive AO/NAO and AAO patterns may be seen over the North Atlantic and the South Pole, respectively. Both hemispheres also exhibit Rossby wave-like patterns with a wave number of 4.

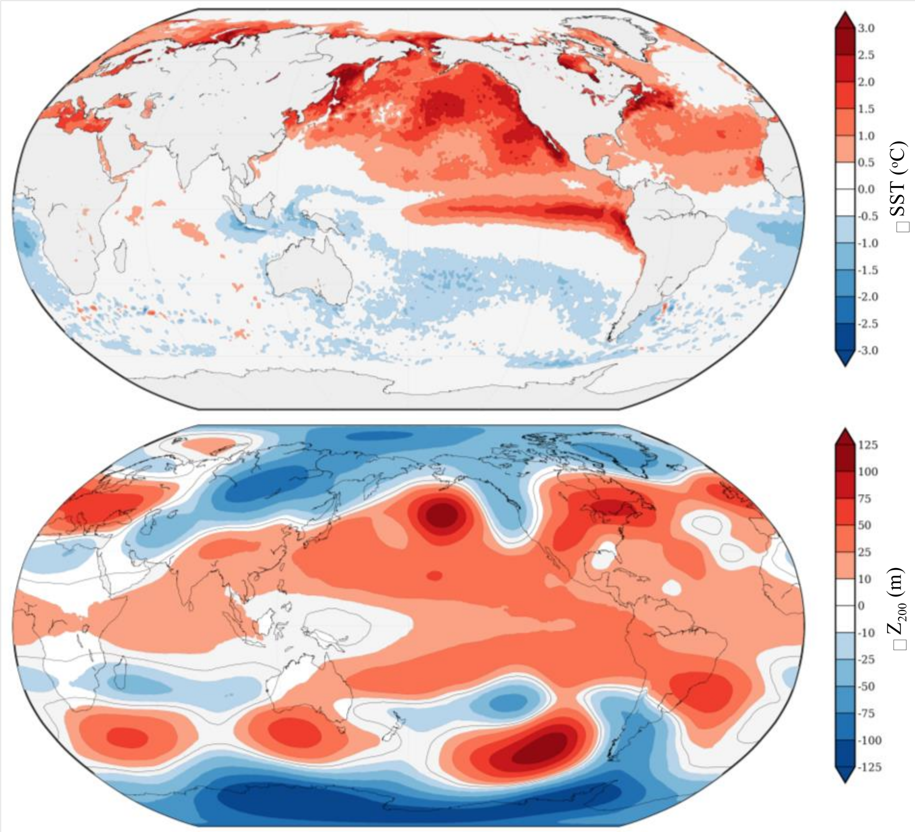

Figure 5.7. *Composite SST and 200hpa Height anomalies during the SC-CDHW for NSA–SEA pair. Red and blue color show the positive and negative anomalies, respectively.*

5.4. Conclusions

Using high-resolution gridded observations of weekly precipitation and weekly maximum temperature, we present the first comprehensive global analysis of spatially compound multivariate events (here multivariate events are compound drought and heatwaves) during the last 4 decades (1979–2020). Our results reveal an alarming rate of increase in the number of the IPCC AR6 regions that experience drought, heatwaves, and/or CDHWs simultaneously. The observed trend in heatwaves is the highest and controls the trend in CDHWs and are often attributed to anthropogenic climate change (King and Harrington 2018); however, natural climate change and internal climate variability also play a significant role (Rogers *et al* 2021a). These increasing trends in the number of regions experiencing spatially compound extremes (droughts, heatwaves or CDHWs) are more concerning as compound extremes often result in global crop failures and food insecurity (Kornhuber *et al* 2020, Singh *et al* 2021). Our LMF analysis depicts multiple significant concordant pairs; however, most of these concordances are in adjacent regions and appear driven mainly by local land-atmosphere feedback. Several long-distance teleconnections in CDHWs are also found that are usually driven by the large-scale atmospheric and oceanic teleconnection, such as ENSO.

The higher transitional probabilities between drought, heatwaves, and CDHWs in NSA during both seasons (winter and summer) highlight significant negative dependence between precipitation and temperature and strong land-atmosphere feedback. In contrast, the lower transitional probabilities in the SEA and MDG, which are small island regions, are limited by the relatively weak negative precipitation-temperature dependence and land-atmosphere-feedback (Trenberth and Shea 2005, Adler *et al* 2008). Moreover, the logistic models for both teleconnections revealed El-Niño as the potential driver of spatially compounding in CDHWs. Negative AO also emerged as the significant driver of NSA–MDG teleconnection. The logistic models estimated that the probability of SC-CDHW week increases from 0.008 to 0.9 and 0.005 to 0.97 in NSA–SEA and NSA–MDG, respectively when El-Niño intensity increases from moderate (index value=1) to exceptional (index value=3). Composite anomalies for the NSA–SEA pairs verified the presence of El-Niño, AO+, PNA-, and AAO+ patterns during the spatially compound CDHW weeks. In addition, the composite anomalies also highlight presence of positive PDO and Atlantic meridional mode. Besides that, a Rossby wave pattern is also visible.

The identification of regional drought and heatwave weeks depends strongly on the selection of threshold (80 percentile adopted there). We also estimated heatwaves at weekly timescale which is not the best procedure, however, our analysis estimated all the observed heatwaves. An underlying assumption in the analysis is that each CDHW week is an independent event, which may not be applicable in most circumstances since multi-week regional CDHW occurrences are not uncommon when estimating the LMF across area pairs. Furthermore, we only used a few climatic oscillations in our model which could limit the efficiency of the model.

Regardless of assumptions and constraints, we believe our findings are a vital step toward understanding and quantifying spatial compounding in multivariate events on a global scale. With the use of climatic oscillations and weather regimes, we built a model that might predict spatially complex extremes efficiently. Major physical insights into spatially compound CDHWs are discussed in this study, but an in-depth analysis into the causal mechanisms is essential for understanding spatially compound CDHWs and pairwise regional concordances, their future climate change, and their representation in global circulation models.

Chapter 6 : General conclusions and Future Implications

6.1. Conclusions

Weather and climate extremes are often associated with negative and disastrous consequences. These impacts amplify and have serious implications on society and the ecosystem when the extremes co-occur in space and/or time i.e., compound extremes. In recent decades, extreme events are increasing in frequency, intensity, and duration due to anthropogenic climate change in response to increased emission of greenhouse gases. Univariate extremes have been explored extensively at regional and global scales, however, the compound extremes remained relatively understudied. According to IPCC SREX (2012) compounding of extremes can occur in both space and time but most of the studies on compound extremes considered synchronization in time only. Hence, the spatially compound extremes remained unexplored (till 2018).

A rapidly expanding literature on climate and weather extremes, mainly related to monitoring and prediction of extremes, has investigated the contribution of anthropogenic climate change, climate variability, and other local factors. Droughts are usually identified by the indices that measure the departure of a hydrological variable from its climatological average and characterize drought events by their duration, intensity, severity, and frequency. In order to clearly understand the concept of droughts, a smaller region i.e., India was selected for an in-depth review of different monitoring and prediction methods and to show how these methods have evolved with time. Climatic oscillations for instance ENSO, IOD, and NAO have significant impact on the occurrence of droughts over India and their inclusion in prediction models has resulted in remarkable improvement in the prediction skill of droughts; however, the large degree of spatial variability in ISMR and droughts limits the efficient predictions to finer spatiotemporal resolution resolutions. In addition, the relationship between droughts and climate oscillations is non-stationary and due to global warming, the atmospheric teleconnections and their associated precipitations patterns are also changing.

On the other hand, for the understanding and monitoring of heatwaves, this study selects a smaller region in the complex terrains of Himalayas (i.e., the Kashmir valley) that is deficit in the literature on heatwaves. The in-situ observations (station, gridded, satellite) are sparse and have missing data. In that case, we developed a method, based on CTX90pct index, to estimate the annual heatwave frequency as heatwave proxy in the data-limited areas of Himalayas and observed a large-scale decreasing trend in heatwaves and maximum temperature. A method developed to segregate temperature changes due to global and local changes revealed a large-scale regional decrease of $2°C$ over last 17 years (2003–2019) in response to global climate change. These temperature changes are locally modulated by the extent of urbanization, forest cover, and elevation. The locations with large-scale forest cover loss over the study period have more steeper decrease highlighting that deforestation amplifies the anthropogenic climate change over the region.

After understanding the concepts, definitions, and characteristics of droughts and heatwaves, this study then identifies and quantifies the spatially compound of droughts among different IPCC AR 5 regions. The droughts were identified using monthly sc-PDSI index and only persistent droughts –that last at least one year– were used for the analysis of spatial compounding analysis. 17 pairs of regions showed robust significant concordances (i.e., significant spatial compounding) in persistent droughts out of which 6 pairs were teleconnections in droughts –the regions of teleconnection pair are more 10000 kms distant. Two robust teleconnections pairs, "SEA–SAF" and "WNA–MED", were selected to understand the oceanic and atmospheric conditions during the spatially compound droughts. SEA–SAF pair highlighted El-Niño and positive PDO as the major driver of spatially compound droughts and all compound drought months occurred during

El-Niño and PDO+. Moreover, the compound droughts in SAF begin six months later than in SEA, suggesting a delayed response to El-Niño in SAF. Alternatively, the spatially compound droughts in WNA–MED pair occur during a specific weather regime that resembles the combination of positive AO/NAO, negative PNA, positive AMO, and negative PNA. Almost 60% of the compound drought months have happened during the PNA- and AO+ and ~80% of droughts months are during PDO-. These insights emphasize the importance of climatic oscillations in producing long-distance spatially compounded droughts.

Droughts may last months or years, but heatwaves last just a few days or weeks and have a major but immediate effect on agriculture and human health, potentially leading to a severe economic catastrophe. Like droughts, heatwaves also show teleconnections as they are also driven by similar physical mechanisms (i.e., anticyclonic circulations, evapotranspiration deficit, and increased sensible heat fluxes). In chapter 4, this study discusses the methods that help in identifying the global-scale spatially compound heatwaves (teleconnections in heatwaves) based on daily CTX90pct index. The results reveal alarming rates of increase in the spatial extent of heatwaves at global and regional scales. Over the last four decades, the area impacted by compound heatwaves has expanded by 3% of global land area and 4 IPCC regions, respectively, which is in close agreement with the IPCC AR6. Multiple teleconnections in heatwaves are discovered using the likelihood multiplication factor (LMF), where two or more distant places (greater than 10000km away) have a high risk of compound heatwaves. Post-2000, the frequency of large-scale SCHs (i.e., global heatwave days) increased by seven-fold, resulting in a fifty percent increase in population exposure to heatwaves. Positively anomalous heatwave years, which typically happen during El Nio, have 87.5% chance of reducing crop production of at least two crops. Moreover, teleconnections in heatwaves are increasing in a warmer climate, which might provide as an early warning of greater and more devastating global heatwaves in the future. While SCHs are caused by a variety of climate oscillations, El-Niño is indeed their primary source of energy. More frequently than not during El-Niño episodes, severe global heatwaves that have a significant effect on human life and agriculture are observed. Internal climatic variability has led to considerable increases in annual variations in global heatwaves' spatial extents, which has exponentially increased the risk of agricultural losses and human fatality, in addition to trends caused by global warming.

Compound events is a relatively new concept in climate research that remains less explored compared to univariate extremes. Spatially compounding of univariate extremes (droughts or heatwaves) has gained popularity in recent years (after 2018), however, spatially compound multivariate events –co-occurrence of multivariate compound events at different locations– have not been explored at all. Although such events are rear but their potential impacts are more devastating. In Chapter 5, this thesis discusses a method to quantify the likelihood of spatial compounding in compound droughts and heatwaves among the IPCC AR 6 regions. A logistic model developed to estimate the probability of such events is also explained in this chapter. Weekly SPI and weekly CTX90pct are used to identify the droughts, heatwaves, and CDHWs. The results show an alarming increase in the number of regions that suffer CDHWs at the same time. As a result of the observed rise in heatwaves, we can clearly see the influence of human climate change on severe CDHW and their concurrences, although they are not only attributed to climate change but also to internal climatic variability. Multiple significant concordant pairs of SC-CDHW were found via LMF analysis, however, most were found in adjacent regions and caused by local land-atmosphere feedbacks. The long-distance teleconnections in CDHWs, which are often driven by large-scale atmospheric and oceanic teleconnections, such as ENSO, are of more concern. The greater transitional probabilities between drought, heatwaves, and CDHWs in NSA during both seasons (winter and summer) emphasize strong negative precipitation-temperature dependency and land-atmosphere feedbacks. In contrast, the lower transitional probabilities in the SEA and MDG are constrained by the comparatively weak negative correlation between precipitation and temperature and weak land-atmosphere feedback. The logistic models for both teleconnections identified El Niño as a primary driver of spatial compounding in CDHWs. Other climate oscillations (PMNA, AO, and AAO) also play an important role though not statistically significant. The chance of a SC-CDHW week increases from 0.008 to 0.9 in NSA–SEA and 0.005 to 0.97 in NSA–MDG when El Niño intensity increases from moderate (index=1) to exceptional (index=3).

Overall, this thesis on spatially compound extremes noted a worrisome increase in the extent of the global land and the number of IPCC regions that are experiencing droughts, heatwaves and/or CDHWs concurrently, which is in close agreement with chapter 11 of IPCC AR6. The methods developed here are employed for droughts, heatwaves, and CDHWs but they could be used for any extreme. A novel model developed to estimate the probability of spatially compound CDHWs based on climatic oscillations, could be implemented as a potential tool for prediction of spatially compound extremes with little improvement. Moreover, the spatially compounding in majority of the long-distance teleconnections are driven, directly or indirectly, by ENSO via atmospheric bridges and modulation of other climatic oscillations.

6.2. Future Implications

This thesis explicitly explored and quantified spatially compound droughts, heatwaves and CDHWs among the IPCC regions and identified physical mechanisms responsible for spatial compounding in these extremes. The results from this thesis provide important insights into the role of climatic oscillations/natural variability in driving the spatial compounding of extremes. Although this analysis improved the science of compound weather and climate extremes, especially spatially compound extremes, which are the deadliest compound extreme, it also highlighted some major gaps in the field of monitoring and modelling compound extremes at a global scale. Based on the research challenges identified and highlighted, following could be the potential future works on spatially compound extremes.

- In this study, the spatial compounding of a single variable, such as droughts, heatwaves, or CDHWs, is examined at one time. However, future research must account for the spatial compounding of several extremes, such as the simultaneous occurrence of drought in one location and flooding in another, for instance, the 2010 Russian heatwave and Pakistan flood.
- This thesis analyzed the spatially compounding of extremes on predefined regions in IPCC AR 5 and AR6 that sometimes may blur the actual teleconnections that could be between the regions which are the combinations of parts from IPCC regions. For example, most of the tropical south American regions (NSA, NES and SAM) show teleconnection with North Australia and southeast Asia, highlighting that a combination of some parts for instance NSA, NES, and SAM shows the teleconnection with a bigger region defined by combination of SEA and NAU. In that case, a need for a more efficient method is highlighted that does not require predefined regions and possibly identifies the regions that show temporal synchronization using ML/AI.
- Even though this thesis emphasizes the role of climate variability and oscillations, it will be critical to conduct a more thorough investigation into how climate change will affect the spatial compounding of extremes in future climate and socio-economic scenarios.
- Additionally, this thesis attributes the spatial compounding in adjacent regions to land-atmospheric interaction (i.e., self-intensification and self-propagation), but it does not examine the role of land-atmosphere (LA) interaction and other local or global factors. In this situation, a detailed investigation of the roles played by local factors, atmospheric circulations, and LA interactions could make a significant contribution to science's understanding of the spread of spatial compounding.

- Although this thesis explored the role of climate oscillations on compound extremes for some of the selected teleconnections in extremes, it is important to investigate which concordant pairs are driven by physical/causal pathways and which are driven by confounding factors. Also, the need to explore the relative contribution of causal networks and confounding factors for the spatial compounding of extremes in future studies is highlighted.
- The variability in the Pacific, Atlantic and Indian Oceans have been found to interact and influence each other and their remote teleconnections through interbasin interactions and ocean-atmosphere couplings. The remote influence of these inter-basin interactions is not always in phase thereby could either amplify or mute the resulting teleconnection of these forcings. Based on these observations, a more comprehensive analysis is recommended to examine the role of these pantropical interactions in modulating the concurrent extremes. In addition, these pantropical interactions have been observed to improve seasonal-decadal predictions; however, it is imperative to explore the influence of their representation on the sub-seasonal forecast skill of extremes, particularly compound extremes.
- Even though the thesis carefully investigated the role of climate oscillations of extremes and compound extremes, it does not include any analysis for examining the feedback of climate oscillations to extremes. Moreover, there is no available literature on the feedback of climate oscillations and extremes. Hence, it is crucial to explore the feedback of climate oscillations, such as ENSO, AO, NAO, and others to the regional and spatially compound extremes in future studies.
- The present thesis provides insights into the physical mechanisms of concurrent droughts, heatwaves and CDHWs, however, we stress the need for an in-depth analysis of causal mechanisms to understand the physical mechanism driving these compound events by using large ensemble climate model simulations such as SMILEs. It is

also critical to explore the representation of these spatial connections in seasonal forecasting systems and how their representation will impact the forecasting skill of these models.

- Compound extremes may inflict catastrophic harm to crops, humans, and the environment. When it comes to the effects of spatially compound extremes on agricultural production and human populations, a short investigation was conducted in this thesis, despite its primary emphasis on the understanding of spatially compound extremes and their causative mechanisms. However, because of the wide range of effects that spatially compound extremes may have, a comprehensive study of the effects of spatially compound extremes on our environment is urgently needed.

REFERENCES

Aadhar S and Mishra V 2017 High-resolution near real-time drought monitoring in South Asia *Scientific data* **4** 170145

Abhilash S, Sahai A K, Borah N, Chattopadhyay R, Joseph S, Sharmila S, De S, Goswami B N and Kumar A 2014a Prediction and monitoring of monsoon intraseasonal oscillations over Indian monsoon region in an ensemble prediction system using CFSv2 *Climate dynamics* **42** 2801–15

Abhilash S, Sahai A K, Pattnaik S and De S 2013 Predictability during active break phases of Indian summer monsoon in an ensemble prediction system using climate forecast system *Journal of Atmospheric and Solar-Terrestrial Physics* **100** 13–23

Abhilash S, Sahai A K, Pattnaik S, Goswami B N and Kumar A 2014b Extended range prediction of active-break spells of Indian summer monsoon rainfall using an ensemble prediction system in NCEP Climate Forecast System *International Journal of Climatology* **34** 98–113

Acharya N, Chattopadhyay S, Mohanty U C, Dash S K and Sahoo L N 2013a On the bias correction of general circulation model output for Indian summer monsoon *Meteorological Applications* **20** 349–56

Acharya N, Singh A, Mohanty U C, Nair A and Chattopadhyay S 2013b Performance of general circulation models and their ensembles for the prediction of drought indices over India during summer monsoon *Natural hazards* **66** 851–71

Adames Á F and Wallace J M 2017 On the tropical atmospheric signature of El Niño *Journal of the Atmospheric Sciences* **74** 1923–39

Adarsh S and Janga Reddy M 2019 Evaluation of trends and predictability of short-term droughts in three meteorological subdivisions of India using multivariate EMD-based hybrid modelling *Hydrological Processes* **33** 130–43

Adler R F, Gu G, Wang J-J, Huffman G J, Curtis S and Bolvin D 2008 Relationships between global precipitation and surface temperature on interannual and longer timescales (1979–2006) *Journal of Geophysical Research: Atmospheres* **113**

AghaKouchak A 2015 A multivariate approach for persistence-based drought prediction: Application to the 2010–2011 East Africa drought *Journal of Hydrology* **526** 127–35

Aghakouchak A, Chiang F, Huning L S, Love C A, Mallakpour I, Mazdiyasni O, Moftakhari H, Papalexiou S M, Ragno E and Sadegh M 2020 Climate Extremes and Compound Hazards in a Warming World *Annual Review of Earth and Planetary Sciences* **48** 519–48

Akhter J, Das L, Meher J K and Deb A 2018 Uncertainties and time of emergence of multi-model precipitation projection over homogeneous rainfall zones of India *Climate Dynamics* **50** 3813–31

Alexander L V, Uotila P and Nicholls N 2009 Influence of sea surface temperature variability on global temperature and precipitation extremes *Journal of Geophysical Research: Atmospheres* **114**

Alexander M A, Bladé I, Newman M, Lanzante J R, Lau N-C and Scott J D 2002 The atmospheric bridge: The influence of ENSO teleconnections on air–sea interaction over the global oceans *Journal of climate* **15** 2205–31

Alexander M A, Scott J D, Friedland K D, Mills K E, Nye J A, Pershing A J, Thomas A C and Carmack E C 2018 Projected sea surface temperatures over the 21st century: Changes in the mean, variability and extremes for large marine ecosystem regions of Northern Oceans *Elementa: Science of the Anthropocene* **6**

Alkama R and Cescatti A 2016a Biophysical climate impacts of recent changes in global forest cover *Science* **351** 600–4

Alkama R and Cescatti A 2016b Biophysical climate impacts of recent changes in global forest cover *Science* **351** 600–4

Alley W M 1984 The Palmer drought severity index: limitations and assumptions *Journal of climate and applied meteorology* **23** 1100–9

Ambaum M H, Hoskins B J and Stephenson D B 2001 Arctic oscillation or North Atlantic oscillation? *Journal of Climate* **14** 3495–507

d'Amour C B, Wenz L, Kalkuhl M, Steckel J C and Creutzig F 2016 Teleconnected food supply shocks *Environmental Research Letters* **11** 035007

Anderson M C, Zolin C A, Sentelhas P C, Hain C R, Semmens K, Yilmaz M T, Gao F, Otkin J A and Tetrault R 2016 The Evaporative Stress Index as an indicator of agricultural drought in Brazil: An assessment based on crop yield impacts *Remote Sensing of Environment* **174** 82–99

Anderson W B, Seager R, Baethgen W, Cane M and You L 2019 Synchronous crop failures and climate-forced production variability *Science advances* **5** eaaw1976

Anon Heatwaves Online: https://www.who.int/westernpacific/health-topics/heatwaves

Arblaster J M and Alexander L V 2012 The impact of the El Niño-Southern Oscillation on maximum temperature extremes *Geophysical Research Letters* **39**

Ashok K, Behera S K, Rao S A, Weng H and Yamagata T 2007a El Niño Modoki and its possible teleconnection *Journal of Geophysical Research: Oceans* **112**

Ault T R 2020 On the essentials of drought in a changing climate *Science* **368** 256–60

Azad S and Rajeevan M 2016 Possible shift in the ENSO-Indian monsoon rainfall relationship under future global warming *Scientific reports* **6** 20145

Azam M F, Kargel J S, Shea J M, Nepal S, Haritashya U K, Srivastava S, Maussion F, Qazi N, Chevallier P and Dimri A P 2021 Glaciohydrology of the himalaya-karakoram *Science* **373** eabf3668

Bailey-Serres J, Parker J E, Ainsworth E A, Oldroyd G E and Schroeder J I 2019 Genetic strategies for improving crop yields *Nature* **575** 109–18

Bala G, Caldeira K, Wickett M, Phillips T J, Lobell D B, Delire C and Mirin A 2007 Combined climate and carbon-cycle effects of large-scale deforestation *Proceedings of the National Academy of Sciences* **104** 6550–5

Baldwin M P and Dunkerton T J 2001 Stratospheric harbingers of anomalous weather regimes *Science* **294** 581–4

Barnston A G and Livezey R E 1987 Classification, Seasonality and Persistence of Low-Frequency Atmospheric Circulation Patterns *Monthly Weather Review* **115** 1083–126

Barriopedro D, Fischer E M, Luterbacher J, Trigo R M and García-Herrera R 2011 The hot summer of 2010: redrawing the temperature record map of Europe *Science* **332** 220–4

Barton Y, Giannakaki P, Von Waldow H, Chevalier C, Pfahl S and Martius O 2016 Clustering of regional-scale extreme precipitation events in southern Switzerland *Monthly Weather Review* **144** 347–69

Benjamini Y and Yekutieli D 2001 The control of the false discovery rate in multiple testing under dependency *Annals of statistics* 1165–88

Berg A, Lintner B R, Findell K L, Malyshev S, Loikith P C and Gentine P 2014 Impact of soil moisture–atmosphere interactions on surface temperature distribution *Journal of Climate* **27** 7976–93

Berman J D, Ebisu K, Peng R D, Dominici F and Bell M L 2017 Drought and the risk of hospital admissions and mortality in older adults in western USA from 2000 to 2013: a retrospective study *The Lancet Planetary Health* **1** e17–25

Bevacqua E, Maraun D, Hobæk Haff I, Widmann M and Vrac M 2017 Multivariate statistical modelling of compound events via pair-copula constructions: analysis of floods in Ravenna (Italy) *Hydrology and Earth System Sciences* **21** 2701–23

Bhat M A, Romshoo S A and Beig G 2017 Aerosol black carbon at an urban site-Srinagar, Northwestern Himalaya, India: Seasonality, sources, meteorology and radiative forcing *Atmospheric Environment* **165** 336–48

Bifulco M and Ranieri R 2017 Impact of drought on human health *European Journal of Internal Medicine* **46** e9–10

Bjerknes J 1969 Atmospheric teleconnection from the tropical Pacific *Mon. Wea. Rev* **97** 103–72

Black E, Blackburn M, Harrison G, Hoskins B and Methven J 2004 Factors contributing to the summer 2003 European heatwave *Weather* **59** 217–23

B\lażejczyk K, Jendritzky G, Bröde P, Fiala D, Havenith G, Epstein Y, Psikuta A and Kampmann B 2013 An introduction to the universal thermal climate index (UTCI) *Geographia Polonica* **86** 5–10

Boers N, Goswami B, Rheinwalt A, Bookhagen B, Hoskins B and Kurths J 2019 Complex networks reveal global pattern of extreme-rainfall teleconnections *Nature* **566** 373–7

Bokhorst S F, Bjerke J W, Tømmervik H, Callaghan T V and Phoenix G K 2009 Winter warming events damage sub-Arctic vegetation: consistent evidence from an experimental manipulation and a natural event *Journal of Ecology* **97** 1408–15

Bonan G B 2001 Observational evidence for reduction of daily maximum temperature by croplands in the Midwest United States *Journal of Climate* **14** 2430–42

Borah N, Sahai A K, Chattopadhyay R, Joseph S, Abhilash S and Goswami B N 2013 A self-organizing map–based ensemble forecast system for extended range prediction of active/break cycles of Indian summer monsoon *Journal of Geophysical Research: Atmospheres* **118** 9022–34

Borah P J, Venugopal V, Sukhatme J, Muddebihal P and Goswami B N 2020 Indian monsoon derailed by a North Atlantic wavetrain *Science* **370** 1335–8

Boston A 2013 Delivering a secure electricity supply on a low carbon pathway *Energy Policy* **52** 55–9

de Brito M M 2021 Compound and cascading drought impacts do not happen by chance: A proposal to quantify their relationships *Science of the Total Environment* **778** 146236

Bröde P, Fiala D, B\lażejczyk K, Holmér I, Jendritzky G, Kampmann B, Tinz B and Havenith G 2012 Deriving the operational procedure for the Universal Thermal Climate Index (UTCI) *International journal of biometeorology* **56** 481–94

Bruick Z S, Rasmussen K L, Rowe A K and McMurdie L A 2019 Characteristics of Intense Convection in Subtropical South America as Influenced by El Niño–Southern Oscillation *Monthly Weather Review* **147** 1947–66

Bryant E A 1991 Natural hazards

Budd G M 2008 Wet-bulb globe temperature (WBGT)—its history and its limitations *Journal of science and medicine in sport* **11** 20–32

Burkart K G, Brauer M, Aravkin A Y, Godwin W W, Hay S I, He J, Iannucci V C, Larson S L, Lim S S and Liu J 2021 Estimating the cause-specific relative risks of non-optimal temperature on daily mortality: a two-part modelling approach applied to the Global Burden of Disease Study *The Lancet* **398** 685–97

Byrne M P 2021 Amplified warming of extreme temperatures over tropical land *Nature Geoscience* **14** 837–41

Byun H-R and Wilhite D A 1999 Objective quantification of drought severity and duration *Journal of climate* **12** 2747–56

Cai W, Wu L, Lengaigne M, Li T, McGregor S, Kug J-S, Yu J-Y, Stuecker M F, Santoso A and Li X 2019a Pantropical climate interactions *Science* **363** eaav4236

Cai W, Wu L, Lengaigne M, Li T, McGregor S, Kug J-S, Yu J-Y, Stuecker M F, Santoso A and Li X 2019b Pantropical climate interactions *Science* **363**

Capotondi A, Wittenberg A T, Newman M, Di Lorenzo E, Yu J-Y, Braconnot P, Cole J, Dewitte B, Giese B and Guilyardi E 2015 Understanding ENSO diversity *Bulletin of the American Meteorological Society* **96** 921–38

Castro-Díez Y, Pozo-Vázquez D, Rodrigo F S and Esteban-Parra M J 2002 NAO and winter temperature variability in southern Europe *Geophysical Research Letters* **29** 1-1-1–4

Center for International Earth Science Information Network - CIESIN - Columbia University 2018 Gridded Population of the World, Version 4 (GPWv4): Basic Demographic Characteristics, Revision 11 NASA Socioeconomic Data and Applications Center (SEDAC) Online: https://doi.org/10.7927/H46M34XX

Chapman S C, Watkins N W and Stainforth D A 2019 Warming trends in summer heatwaves *Geophysical Research Letters* **46** 1634–40

Charney J G and Shukla J 1981 *Predictability of monsoons. Monsoon Dynamics, J. Lighthill and RP Pearce, Eds* (Cambridge University Press)

Cherubini F, Huang B, Hu X, Tölle M H and Strømman A H 2018 Quantifying the climate response to extreme land cover changes in Europe with a regional model *Environmental Research Letters* **13** 074002

Christian J I, Basara J B, Otkin J A, Hunt E D, Wakefield R A, Flanagan P X and Xiao X 2019 A methodology for flash drought identification: application of flash drought frequency across the United States *Journal of Hydrometeorology* **20** 833–46

Christidis N, Jones G S and Stott P A 2015 Dramatically increasing chance of extremely hot summers since the 2003 European heatwave *Nature Climate Change* **5** 46–50

Christidis N, Stott P A, Hegerl G C and Betts R A 2013 The role of land use change in the recent warming of daily extreme temperatures *Geophysical Research Letters* **40** 589–94

Ciais P, Reichstein M, Viovy N, Granier A, Ogée J, Allard V, Aubinet M, Buchmann N, Bernhofer C and Carrara A 2005 Europe-wide reduction in primary productivity caused by the heat and drought in 2003 *Nature* **437** 529–33

Coelho C A, de Oliveira C P, Ambrizzi T, Reboita M S, Carpenedo C B, Campos J L P S, Tomaziello A C N, Pampuch L A, Custódio M de S and Dutra L M M 2016 The 2014 southeast Brazil austral summer drought: regional scale mechanisms and teleconnections *Climate Dynamics* **46** 3737–52

Coumou D, Di Capua G, Vavrus S, Wang L and Wang S 2018 The influence of Arctic amplification on mid-latitude summer circulation *Nature Communications* **9** 1–12

Coumou D, Lehmann J and Beckmann J 2015 The weakening summer circulation in the Northern Hemisphere mid-latitudes *Science* **348** 324–7

Council A M S 2004 AMS statement on meteorological drought *Bulletin of the American Meteorological Society* **85** 771–3

Crausbay S D, Ramirez A R, Carter S L, Cross M S, Hall K R, Bathke D J, Betancourt J L, Colt S, Cravens A E and Dalton M S 2017 Defining ecological drought for the twenty-first century *Bulletin of the American Meteorological Society* **98** 2543–50

Crosson W L, Al-Hamdan M Z, Hemmings S N J and Wade G M 2012 A daily merged MODIS Aqua–Terra land surface temperature data set for the conterminous United States *Remote Sensing of Environment* **119** 315–24

Dai A 2011a Characteristics and trends in various forms of the Palmer Drought Severity Index during 1900–2008 *Journal of Geophysical Research: Atmospheres* **116**

Dai A 2011b Drought under global warming: a review *Wiley Interdisciplinary Reviews: Climate Change* **2** 45–65

Dai Y, Feldstein S B, Tan B and Lee S 2017 Formation mechanisms of the Pacific–North American teleconnection with and without its canonical tropical convection pattern *Journal of Climate* **30** 3139–55

Dar G H and Khuroo A A 2020 *Biodiversity of the Himalaya: Jammu and Kashmir State* vol 18 (Singapore: Springer Singapore)

Davin E L and De Noblet Ducoudré N 2010 Climatic impact of global-scale deforestation: Radiative versus nonradiative processes *Journal of Climate* **23** 97–112

Davis S J, Caldeira K and Matthews H D 2010 Future CO2 emissions and climate change from existing energy infrastructure *Science* **329** 1330–3

Di Capua G, Kretschmer M, Runge J, Alessandri A, Donner R V, van Den Hurk B, Vellore R, Krishnan R and Coumou D 2019 Long-lead statistical forecasts of the Indian summer monsoon rainfall based on causal precursors *Weather and Forecasting* **34** 1377–94

Di Sante F, Coppola E, Farneti R and Giorgi F 2019 Indian Summer Monsoon as simulated by the regional earth system model RegCM-ES: the role of local air–sea interaction *Climate dynamics* **53** 759–78

Dibike Y B and Coulibaly P 2005 Hydrologic impact of climate change in the Saguenay watershed: comparison of downscaling methods and hydrologic models *Journal of hydrology* **307** 145–63

Diffenbaugh N S, Swain D L and Touma D 2015 Anthropogenic warming has increased drought risk in California *Proceedings of the National Academy of Sciences* **112** 3931–6

Dijkstra H A, Te Raa L, Schmeits M and Gerrits J 2006 On the physics of the Atlantic multidecadal oscillation *Ocean Dynamics* **56** 36–50

Ding Q and Wang B 2005 Circumglobal teleconnection in the Northern Hemisphere summer *Journal of climate* **18** 3483–505

Ding Q and Wang B 2009 Predicting extreme phases of the Indian summer monsoon *Journal of Climate* **22** 346–63

Ding Y, Hayes M J and Widhalm M 2011 Measuring economic impacts of drought: a review and discussion *Disaster Prevention and Management: An International Journal*

Doesken N J, McKee T B and Kleist J D 1991 Development of a surface water supply index for the western United States *Climatology report; 91-3*

Dong B and Dai A 2015 The influence of the interdecadal Pacific oscillation on temperature and precipitation over the globe *Climate Dynamics* **45** 2667–81

Dong B, Dai A, Vuille M and Timm O E 2018a Asymmetric modulation of ENSO teleconnections by the interdecadal Pacific oscillation *Journal of Climate* **31** 7337–61

Dong L, Mitra C, Greer S and Burt E 2018b The dynamical linkage of atmospheric blocking to drought, heatwave and urban heat island in southeastern US: A multi-scale case study *Atmosphere* **9** 33

Dosio A, Mentaschi L, Fischer E M and Wyser K 2018 Extreme heat waves under 1.5 C and 2 C global warming *Environmental research letters* **13** 054006

Drouard M, Kornhuber K and Woollings T 2019 Disentangling dynamic contributions to summer 2018 anomalous weather over Europe *Geophysical Research Letters* **46** 12537–46

Duan S-B, Li Z-L, Li H, Göttsche F-M, Wu H, Zhao W, Leng P, Zhang X and Coll C 2019 Validation of Collection 6 MODIS land surface temperature product using in situ measurements *Remote sensing of environment* **225** 16–29

Dunn R J, Hurst D F, Gobron N and Willett K M 2017 Global Climate [in 'State of the Climate in 2016'] *Bull. Amer. Meteor. Soc* **98** 5–62

Dutta R and Maity R 2020a Spatial variation in long-lead predictability of summer monsoon rainfall using a time-varying model and global climatic indices *International Journal of Climatology*

Dutta R and Maity R 2018 Temporal evolution of hydroclimatic teleconnection and a time-varying model for long-lead prediction of Indian summer monsoon rainfall *Scientific reports* **8** 1–10

Dutta R and Maity R 2020b Temporal networks-based approach for nonstationary hydroclimatic modeling and its demonstration with streamflow prediction *Water Resources Research* **56** e2020WR027086

Egger J 1978 Dynamics of blocking highs *Journal of Atmospheric sciences* **35** 1788–801

Eltahir E A 1992 Drought frequency analysis of annual rainfall series in central and western Sudan *Hydrological sciences journal* **37** 185–99

Fayaz A, Shafiq M U, Singh H and Ahmed P 2020 Assessment of spatiotemporal changes in land use/land cover of North Kashmir Himalayas from 1992 to 2018 *Model. Earth Syst. Environ.* **6** 1189–200

Feng S and Hao Z 2021 Quantitative contribution of ENSO to precipitation-temperature dependence and associated compound dry and hot events *Atmospheric Research* **260** 105695

Feng S, Hao Z, Zhang X and Hao F 2019 Probabilistic evaluation of the impact of compound dry-hot events on global maize yields *Science of the Total Environment* **689** 1228–34

Feng Y, Liu W, Sun F and Wang H 2021 Changes of compound hot and dry extremes on different land surface conditions in China during 1957–2018 *International Journal of Climatology* **41** E1085–99

Fernández-Martínez M, Sardans J, Chevallier F, Ciais P, Obersteiner M, Vicca S, Canadell J G, Bastos A, Friedlingstein P and Sitch S 2019 Global trends in carbon sinks and their relationships with CO 2 and temperature *Nature Climate Change* **9** 73–9

Findell K L, Berg A, Gentine P, Krasting J P, Lintner B R, Malyshev S, Santanello J A and Shevliakova E 2017 The impact of anthropogenic land use and land cover change on regional climate extremes *Nature communications* **8** 1–10

Fischer E M and Schär C 2010 Consistent geographical patterns of changes in high-impact European heatwaves *Nature Geoscience* **3** 398–403

Fischer E M, Seneviratne S I, Vidale P L, Lüthi D and Schär C 2007 Soil moisture–atmosphere interactions during the 2003 European summer heat wave *Journal of Climate* **20** 5081–99

Flanigan N P, Bandara R, Wang F, Jastrzębowski S, Hidayati S N and Walck J L 2020 Germination responses to winter warm spells and warming vary widely among woody plants in a temperate forest *Plant Biology* **22** 1052–61

Florenchie P, Lutjeharms J R, Reason C, Masson S and Rouault M 2003 The source of Benguela Niños in the south Atlantic Ocean *Geophysical Research Letters* **30**

Fogt R L and Marshall G J 2020 The Southern Annular Mode: variability, trends, and climate impacts across the Southern Hemisphere *Wiley Interdisciplinary Reviews: Climate Change* **11** e652

Fu C and Fletcher J O 1985 The relationship between Tibet-tropical ocean thermal contrast and interannual variability of Indian monsoon rainfall *Journal of Applied Meteorology and Climatology* **24** 841–7

Gadgil S and Gadgil S 2006 The Indian monsoon, GDP and agriculture *Economic and political weekly* 4887–95

Gadgil S, Rajeevan M and Nanjundiah R 2005 Monsoon prediction—why yet another failure *Curr. Sci* **88** 1389–400

Gadgil S and Sajani S 1998 Monsoon precipitation in the AMIP runs *Climate Dynamics* **14** 659–89

Gadgil S and Srinivasan J 2011 Seasonal prediction of the Indian monsoon *Curr. Sci* **100** 343–53

Gadgil S, Srinivasan J, Nanjundiah R S, Kumar K K, Munot A A and Kumar K R 2002 On forecasting the Indian summer monsoon: the intriguing season of 2002 *Current Science* **83** 394–403

Gadgil S, Vinayachandran P N, Francis P A and Gadgil S 2004 Extremes of the Indian summer monsoon rainfall, ENSO and equatorial Indian Ocean oscillation *Geophysical Research Letters* **31**

Ganguli P and Reddy M J 2014 Ensemble prediction of regional droughts using climate inputs and the SVM–copula approach *Hydrological Processes* **28** 4989–5009

García-Herrera R, Garrido-Perez J M, Barriopedro D, Ordóñez C, Vicente-Serrano S M, Nieto R, Gimeno L, Sorí R and Yiou P 2019 The European 2016/17 Drought *Journal of Climate* **32** 3169–87

Ge J, Liu Q, Zan B, Lin Z, Lu S, Qiu B and Guo W 2022 Deforestation intensifies daily temperature variability in the northern extratropics *Nature communications* **13** 1–15

Gelaro R, McCarty W, Suárez M J, Todling R, Molod A, Takacs L, Randles C A, Darmenov A, Bosilovich M G and Reichle R 2017 The modern-era retrospective analysis for research and applications, version 2 (MERRA-2) *Journal of Climate* **30** 5419–54

Ghosh S, Das D, Kao S-C and Ganguly A R 2012 Lack of uniform trends but increasing spatial variability in observed Indian rainfall extremes *Nature Climate Change* **2** 86–91

Ghosh S and Katkar S 2012 Modeling uncertainty resulting from multiple downscaling methods in assessing hydrological impacts of climate change *Water resources management* **26** 3559–79

Gibbs W J 1975 Drought-its definition, delineation and effects. *Drought. Lectures presented at the twenty-sixth session of the WMO Executive Committee.* 1–39

Gibson P B, Waliser D E, Guan B, DeFlorio M J, Ralph F M and Swain D L 2019 Ridging associated with drought across the Western and Southwestern United States: characteristics, trends and predictability sources *Journal of Climate*

Gong D and Wang S 1998 Antarctic oscillation: concept and applications *Chinese Science Bulletin* **43** 734–8

Good E J, Ghent D J, Bulgin C E and Remedios J J 2017 A spatiotemporal analysis of the relationship between near-surface air temperature and satellite land surface temperatures using 17 years of data from the ATSR series *Journal of Geophysical Research: Atmospheres* **122** 9185–210

Gore M, Abiodun B J and Kucharski F 2020 Understanding the influence of ENSO patterns on drought over southern Africa using SPEEDY *Climate Dynamics* **54** 307–27

Gorelick N, Hancher M, Dixon M, Ilyushchenko S, Thau D and Moore R 2017 Google Earth Engine: Planetary-scale geospatial analysis for everyone *Remote Sensing of Environment* **202** 18–27

Goswami B B and Goswami B N 2017 A road map for improving dry-bias in simulating the South Asian monsoon precipitation by climate models *Climate Dynamics* **49** 2025–34

Goswami B N, Madhusoodanan M S, Neema C P and Sengupta D 2006a A physical mechanism for North Atlantic SST influence on the Indian summer monsoon *Geophysical Research Letters* **33**

Goswami B N, Venugopal V, Sengupta D, Madhusoodanan M S and Xavier P K 2006b Increasing trend of extreme rain events over India in a warming environment *Science* **314** 1442–5

Goswami B N and Xavier P K 2003 Potential predictability and extended range prediction of Indian summer monsoon breaks *Geophysical Research Letters* **30**

Gourdji S M, Sibley A M and Lobell D B 2013 Global crop exposure to critical high temperatures in the reproductive period: historical trends and future projections *Environmental Research Letters* **8** 024041

Government of Jammu and Kashmi Department of Forest and India water Portal 2011 Jammu and Kashmir state forest policy 2010 Online: http://jkforest.gov.in/pdf/Approved_Forest_Policy_28jan11.pdf

Grotjahn R, Black R, Leung R, Wehner M F, Barlow M, Bosilovich M, Gershunov A, Gutowski W J, Gyakum J R and Katz R W 2016 North American extreme temperature events and related large scale meteorological patterns: a review of statistical methods, dynamics, modeling, and trends *Climate Dynamics* **46** 1151–84

Grotjahn R and Huynh J 2018 Contiguous US summer maximum temperature and heat stress trends in CRU and NOAA Climate Division data plus comparisons to reanalyses *Scientific reports* **8** 1–18

Guerrero B 2012 The impact of agricultural drought losses on the Texas Economy *Briefing Paper Updated* **4**

Habib U 2017 TRENDS OF URBANIZATION IN JAMMU AND KASHMIR *International Journal of Research in Economics and Social Sciences (IJRESS)* **7**

Haile G G, Tang Q, Li W, Liu X and Zhang X 2020 Drought: Progress in broadening its understanding *WIREs Water* **7** 1–25

Hanel M, Rakovec O, Markonis Y, Máca P, Samaniego L, Kyselý J and Kumar R 2018 Revisiting the recent European droughts from a long-term perspective *Scientific reports* **8** 1–11

Hanigan I C, Butler C D, Kokic P N and Hutchinson M F 2012 Suicide and drought in new South Wales, Australia, 1970–2007 *Proceedings of the National Academy of Sciences* **109** 13950–5

Hansen M C, Potapov P V, Moore R, Hancher M, Turubanova S A, Tyukavina A, Thau D, Stehman S V, Goetz S J, Loveland T R, Kommareddy A, Egorov A, Chini L, Justice C O and Townshend J R G 2013 High-resolution global maps of 21st-century forest cover change *Science* **342** 850–3

Hansen M, Potapov P, Margono B, Stehman S, Turubanova S and Tyukavina A 2014 Response to comment on "High-resolution global maps of 21st-century forest cover change" *Science* **344** 981–981

Hao Z and AghaKouchak A 2014 A Nonparametric Multivariate Multi-Index Drought Monitoring Framework *Journal of Hydrometeorology* **15** 89–101

Hao Z, AghaKouchak A and Phillips T J 2013 Changes in concurrent monthly precipitation and temperature extremes *Environmental Research Letters* **8** 034014

Hao Z, Hao F, Singh V P and Zhang X 2018 Quantifying the relationship between compound dry and hot events and El Niño–southern Oscillation (ENSO) at the global scale *Journal of Hydrology* **567** 332–8

Hao Z, Hao F, Xia Y, Singh V P and Zhang X 2019 A monitoring and prediction system for compound dry and hot events *Environmental Research Letters* **14** 114034

Haqiqi I, Grogan D S, Hertel T W and Schlenker W 2021 Quantifying the impacts of compound extremes on agriculture *Hydrology and Earth System Sciences* **25** 551–64

Harpold A, Dettinger M D and Rajagopal S 2017 Defining snow drought and why it matters *Eos, Earth and Space Science News* **98**

Harris I, Jones P D, Osborn T J and Lister D H 2014 Updated high-resolution grids of monthly climatic observations–the CRU TS3. 10 Dataset *International journal of climatology* **34** 623–42

Hassan W U and Nayak M A 2020 Global teleconnections in droughts caused by oceanic and atmospheric circulation patterns *Environmental Research Letters* **16** 014007

ul Hassan W, Nayak M A and Lyngwa R V 2021 Recent changes in heatwaves and maximum temperatures over a complex terrain in the Himalayas *Science of The Total Environment* **794** 148706

Hatfield J L, Boote K J, Kimball B A, Ziska L H, Izaurralde R C, Ort D, Thomson A M and Wolfe D 2011 Climate impacts on agriculture: implications for crop production *Agronomy journal* **103** 351–70

Heim Jr R R 2002 A review of twentieth-century drought indices used in the United States *Bulletin of the American Meteorological Society* **83** 1149–66

Hendon H H 2003 Indonesian rainfall variability: Impacts of ENSO and local air–sea interaction *Journal of Climate* **16** 1775–90

Herbst J, Mason K, Byard R W, Gilbert J D, Charlwood C, Heath K J, Winskog C and Langlois N E 2014 Heat-related deaths in Adelaide, South Australia: Review of the literature and case findings–An Australian perspective *Journal of forensic and legal medicine* **22** 73–8

Herceg-Bulić I, Mezzina B, Kucharski F, Ruggieri P and King M P 2017 Wintertime ENSO influence on late spring European climate: the stratospheric response and the role of North Atlantic SST *International Journal of Climatology* **37** 87–108

Hernández A, Martin-Puertas C, Moffa-Sánchez P, Moreno-Chamarro E, Ortega P, Blockley S, Cobb K M, Comas-Bru L, Giralt S and Goosse H 2020 Modes of climate variability: Synthesis and review of proxy-based reconstructions through the Holocene *Earth-Science Reviews* **209** 103286

Herrera-Estrada J E, Martinez J A, Dominguez F, Findell K L, Wood E F and Sheffield J 2019 Reduced moisture transport linked to drought propagation across North America *Geophysical Research Letters* **46** 5243–53

Hersbach H 2016 The ERA5 Atmospheric Reanalysis.

Hersbach H, Bell B and Berrisford P 2018 ERA5: Fifth generation of ECMWF atmospheric reanalyses of the global climate *Copernicus Climate Change Service Climate Data Store (CDS)*

Hill K J, Taschetto A S and England M H 2009 South American rainfall impacts associated with inter-El Niño variations *Geophysical Research Letters* **36**

Hingray B and Saïd M 2014 Partitioning internal variability and model uncertainty components in a multimember multimodel ensemble of climate projections *Journal of Climate* **27** 6779–98

Hirsch A L, Evans J P, Di Virgilio G, Perkins-Kirkpatrick S E, Argüeso D, Pitman A J, Carouge C C, Kala J, Andrys J and Petrelli P 2019 Amplification of Australian heatwaves via local land-atmosphere coupling *Journal of Geophysical Research: Atmospheres* **124** 13625–47

Hirsch A L and King M J 2020 Atmospheric and land surface contributions to heatwaves: an Australian perspective *Journal of Geophysical Research: Atmospheres* **125** e2020JD033223

Ho M, Kiem A S and Verdon-Kidd D C 2012 The Southern Annular Mode: a comparison of indices *Hydrology and Earth System Sciences* **16** 967–82

Hoag H 2014 Russian summer tops 'universal'heatwave index *Nature* **16**

Hoerling M and Kumar A 2003 The perfect ocean for drought *Science* **299** 691–4

Hoerling M, Kumar A, Dole R, Nielsen-Gammon J W, Eischeid J, Perlwitz J, Quan X-W, Zhang T, Pegion P and Chen M 2013 Anatomy of an extreme event *Journal of Climate* **26** 2811–32

Holbrook N J, Scannell H A, Gupta A S, Benthuysen J A, Feng M, Oliver E C, Alexander L V, Burrows M T, Donat M G and Hobday A J 2019 A global assessment of marine heatwaves and their drivers *Nature Communications* **10** 1–13

Hong C, Hsu H, Lin N and Chiu H 2011 Roles of European blocking and tropical-extratropical interaction in the 2010 Pakistan flooding *Geophysical Research Letters* **38**

Hu Y and Jia G 2010 Influence of land use change on urban heat island derived from multi-sensor data *International Journal of Climatology* **30** 1382–95

Hubeny J. Bradford, King John W., and Reddin Mike 2011 Northeast US precipitation variability and North American climate teleconnections interpreted from late Holocene varved sediments *Proceedings of the National Academy of Sciences* **108** 17895–900

Hudson D, Marshall A G and Alves O 2011 Intraseasonal forecasting of the 2009 summer and winter Australian heat waves using POAMA *Weather and Forecasting* **26** 257–79

Hulley G C, Dousset B and Kahn B H 2020 Rising trends in heatwave metrics across Southern California *Earth's Future* **8** e2020EF001480

Huning L S and AghaKouchak A 2020 Global snow drought hot spots and characteristics *Proceedings of the National Academy of Sciences* **117** 19753–9

Hurrell J W and Deser C 2010 North Atlantic climate variability: the role of the North Atlantic Oscillation *Journal of marine systems* **79** 231–44

Husain M 1987 *Geography of Jammu & Kashmir State* (Rejesh Publications)

Im E-S, Pal J S and Eltahir E A 2017 Deadly heat waves projected in the densely populated agricultural regions of South Asia *Science advances* **3** e1603322

Iturbide M, Gutiérrez J M, Alves L M, Bedia J, Cerezo-Mota R, Cimadevilla E, Cofiño A S, Di Luca A, Faria S H and Gorodetskaya I V 2020 An update of IPCC climate reference regions for subcontinental analysis of climate model data: definition and aggregated datasets *Earth System Science Data* **12** 2959–70

Jacobi J, Perrone D, Duncan L L and Hornberger G 2013 A tool for calculating the Palmer drought indices *Water Resources Research* **49** 6086–9

Jain S, Scaife A A and Mitra A K 2019 Skill of Indian summer monsoon rainfall prediction in multiple seasonal prediction systems *Climate Dynamics* **52** 5291–301

Jamei Y, Rajagopalan P and Sun Q C 2019 Spatial structure of surface urban heat island and its relationship with vegetation and built-up areas in Melbourne, Australia *Science of the total environment* **659** 1335–51

Jones M W, Smith A, Betts R, Canadell J G, Prentice I C and Le Quéré C 2020 Climate change increases risk of wildfires *ScienceBrief Review* **116** 117

Ju J and Slingo J 1995 The Asian summer monsoon and ENSO *Quarterly Journal of the Royal Meteorological Society* **121** 1133–68

Justice C O, Townshend J R G, Vermote E F, Masuoka E, Wolfe R E, Saleous N, Roy D P and Morisette J T 2002 An overview of MODIS Land data processing and product status *Remote sensing of Environment* **83** 3–15

Kanda N, Negi H S, Rishi M S and Kumar A 2020 Performance of various gridded temperature and precipitation datasets over Northwest Himalayan Region *Environmental Research Communications* **2** 085002

Kao H-Y and Yu J-Y 2009 Contrasting eastern-Pacific and central-Pacific types of ENSO *Journal of Climate* **22** 615–32

Karl T R 1986 The sensitivity of the Palmer Drought Severity Index and Palmer's Z-index to their calibration coefficients including potential evapotranspiration *Journal of Climate and Applied Meteorology* **25** 77–86

Kashid S S, Ghosh S and Maity R 2010 Streamflow prediction using multi-site rainfall obtained from hydroclimatic teleconnection *Journal of Hydrology* **395** 23–38

Kashid S S and Maity R 2012 Prediction of monthly rainfall on homogeneous monsoon regions of India based on large scale circulation patterns using Genetic Programming *Journal of Hydrology* **454** 26–41

Kelley C P, Mohtadi S, Cane M A, Seager R and Kushnir Y 2015 Climate change in the Fertile Crescent and implications of the recent Syrian drought *Proceedings of the national Academy of Sciences* **112** 3241–6

Kenyon J and Hegerl G C 2008 Influence of modes of climate variability on global temperature extremes *Journal of Climate* **21** 3872–89

Keshavamurty R N 1982 Response of the atmosphere to sea surface temperature anomalies over the equatorial Pacific and the teleconnections of the Southern Oscillation *Journal of the Atmospheric Sciences* **39** 1241–59

Keyantash J and Dracup J A 2002 The quantification of drought: an evaluation of drought indices *Bulletin of the American Meteorological Society* **83** 1167–80

Khosla R, Jani A and Perera R 2021 Health risks of extreme heat *bmj* **375**

Kiem A S, Johnson F, Westra S, van Dijk A, Evans J P, O'Donnell A, Rouillard A, Barr C, Tyler J, Thyer M, Jakob D, Woldemeskel F, Sivakumar B and Mehrotra R 2016 Natural hazards in Australia: droughts *Climatic Change* **139** 37–54

King A D and Harrington L J 2018 The inequality of climate change from 1.5 to 2 C of global warming *Geophysical Research Letters* **45** 5030–3

King A D, Pitman A J, Henley B J, Ukkola A M and Brown J R 2020 The role of climate variability in Australian drought *Nat. Clim. Chang.* **10** 177–9

Kjellstrom T 2016 Impact of climate conditions on occupational health and related economic losses: a new feature of global and urban health in the context of climate change *Asia Pacific Journal of Public Health* **28** 28S-37S

Köhn-Reich L and Bürger G 2019 Dynamical prediction of Indian monsoon: Past and present skill *International Journal of Climatology* **39** 3574–81

Kong D, Gu X, Li J, Ren G and Liu J 2020a Contributions of global warming and urbanization to the intensification of human-perceived heatwaves over China *Journal of Geophysical Research: Atmospheres* **125** e2019JD032175

Kong Q, Guerreiro S B, Blenkinsop S, Li X-F and Fowler H J 2020b Increases in summertime concurrent drought and heatwave in Eastern China *Weather and Climate Extremes* **28** 100242

Kornhuber K, Coumou D, Vogel E, Lesk C, Donges J F, Lehmann J and Horton R M 2020 Amplified Rossby waves enhance risk of concurrent heatwaves in major breadbasket regions *Nature Climate Change* **10** 48–53

Kornhuber K, Osprey S, Coumou D, Petri S, Petoukhov V, Rahmstorf S and Gray L 2019 Extreme weather events in early summer 2018 connected by a recurrent hemispheric wave-7 pattern *Environmental Research Letters* **14** 054002

Kornhuber K, Petoukhov V, Karoly D, Petri S, Rahmstorf S and Coumou D 2017 Summertime planetary wave resonance in the Northern and Southern Hemispheres *Journal of Climate* **30** 6133–50

Kosaka Y and Xie S-P 2013 Recent global-warming hiatus tied to equatorial Pacific surface cooling *Nature* **501** 403–7

Kovats R S and Kristie L E 2006 Heatwaves and public health in Europe *European journal of public health* **16** 592–9

Kripalani R H and Singh S V 1993 Large scale aspects of India-China summer monsoon rainfall *Advances in Atmospheric Sciences* **10** 71–84

Krishna Kumar K, Hoerling M and Rajagopalan B 2005 Advancing dynamical prediction of Indian monsoon rainfall *Geophysical Research Letters* **32**

Kueh M T, Lin C Y, Chuang Y J, Sheng Y F and Chien Y Y 2017 Climate variability of heat waves and their associated diurnal temperature range variations in Taiwan *Environmental Research Letters* **12** 074017

Kug J-S, Jin F-F and An S-I 2009 Two types of El Niño events: cold tongue El Niño and warm pool El Niño *Journal of climate* **22** 1499–515

Kulkarni M A, Acharya N, Kar S C, Mohanty U C, Tippett M K, Robertson A W, Luo J-J and Yamagata T 2012 Probabilistic prediction of Indian summer monsoon rainfall using global climate models *Theoretical and Applied Climatology* **107** 441–50

Kumar K K, Rajagopalan B and Cane M A 1999 On the weakening relationship between the Indian monsoon and ENSO *Science* **284** 2156–9

Kumar K K, Rajagopalan B, Hoerling M, Bates G and Cane M 2006 Unraveling the mystery of Indian monsoon failure during El Niño *Science* **314** 115–9

Kumar R, Mishra V, Buzan J, Kumar R, Shindell D and Huber M 2017 Dominant control of agriculture and irrigation on urban heat island in India *Scientific reports* **7** 1–10

Lamb P J and Peppler R A 1987 North Atlantic Oscillation: concept and an application *Bulletin of the American Meteorological Society* **68** 1218–25

Latif M, Groetzner A and Frey H 1996 El Hermanito: El Nino`s overlooked little brother in the Atlantic Online: https://www.osti.gov/etdeweb/biblio/397149

Lau W K and Kim K-M 2012 The 2010 Pakistan flood and Russian heat wave: Teleconnection of hydrometeorological extremes *Journal of Hydrometeorology* **13** 392–403

Le Tertre A, Lefranc A, Eilstein D, Declercq C, Medina S, Blanchard M, Chardon B, Fabre P, Filleul L and Jusot J-F 2006 Impact of the 2003 heatwave on all-cause mortality in 9 French cities *Epidemiology* 75–9

Lean J and Warrilow D A 1989 Simulation of the regional climatic impact of Amazon deforestation *Nature* **342** 411–3

Lee H and Zhang D 2011 Relationship between NAO and drought disasters in northwestern China in the last millennium *Journal of Arid Environments* **75** 1114–20

Lee J, Mast J C and Dessler A E 2021 The effect of forced change and unforced variability in heat waves, temperature extremes, and associated population risk in a CO 2-warmed world *Atmospheric Chemistry and Physics* **21** 11889–904

Lee M-H, Lee S, Song H-J and Ho C-H 2017 The recent increase in the occurrence of a boreal summer teleconnection and its relationship with temperature extremes *Journal of Climate* **30** 7493–504

Lee T and McPhaden M J 2010a Increasing intensity of El Niño in the central-equatorial Pacific *Geophysical Research Letters* **37**

Lee T and McPhaden M J 2010b Increasing intensity of El Niño in the central-equatorial Pacific *Geophysical Research Letters* **37**

Lee X, Goulden M L, Hollinger D Y, Barr A, Black T A, Bohrer G, Bracho R, Drake B, Goldstein A and Gu L 2011 Observed increase in local cooling effect of deforestation at higher latitudes *Nature* **479** 384–7

Lejeune Q, Davin E L, Gudmundsson L, Winckler J and Seneviratne S I 2018 Historical deforestation locally increased the intensity of hot days in northern mid-latitudes *Nature climate change* **8** 386–90

Leonard M, Westra S, Phatak A, Lambert M, van den Hurk B, McInnes K, Risbey J, Schuster S, Jakob D and Stafford-Smith M 2014 A compound event framework for understanding extreme impacts *Wiley Interdisciplinary Reviews: Climate Change* **5** 113–28

Lesk C, Rowhani P and Ramankutty N 2016 Influence of extreme weather disasters on global crop production *Nature* **529** 84–7

L'Heureux M 2019 The Pacific-North American Pattern: the stomach sleeper of the atmosphere *NOAA Climate. gov*

Li M, Yao Y, Simmonds I, Luo D, Zhong L and Chen X 2020 Collaborative impact of the NAO and atmospheric blocking on European heatwaves, with a focus on the hot summer of 2018 *Environmental Research Letters* **15** 114003

Li S, Wang Y and Gao Y 2009 A review of the researches on the Atlantic Multidecadal Oscillation (AMO) and its climate influence. *Transactions of Atmospheric Sciences* **32** 458–65

Li Y, Zhao M, Mildrexler D J, Motesharrei S, Mu Q, Kalnay E, Zhao F, Li S and Wang K 2016 Potential and actual impacts of deforestation and afforestation on land surface temperature *Journal of Geophysical Research: Atmospheres* **121** 14–372

Li Y, Zhao M, Motesharrei S, Mu Q, Kalnay E and Li S 2015a Local cooling and warming effects of forests based on satellite observations *Nature communications* **6** 1–8

Li Y, Zhao M, Motesharrei S, Mu Q, Kalnay E and Li S 2015b Local cooling and warming effects of forests based on satellite observations *Nature communications* **6** 1–8

Li Z, He P, Zhu J, Chen H, Zeng G and Deng W 2019 Improving the simulation of East Asian summer monsoon with mesoscale enhancement in an AGCM *Climate dynamics* **53** 225–36

Liebmann B and Smith C A 1996 Description of a complete (interpolated) outgoing longwave radiation dataset *Bulletin of the American Meteorological Society* **77** 1275–7

Lin L, Chen C and Luo M 2018 Impacts of El Niño–Southern Oscillation on heat waves in the Indochina peninsula *Atmospheric Science Letters* **19** e856

Lindsey J K 2000 *Applying generalized linear models* (Springer Science & Business Media)

Liu B, Siu Y L and Mitchell G 2016 Hazard interaction analysis for multi-hazard risk assessment: a systematic classification based on hazard-forming environment *Natural Hazards and Earth System Sciences* **16** 629–42

Liu B, Zhu C, Su J, Ma S and Xu K 2019 Record-breaking northward shift of the western North Pacific subtropical high in July 2018 *Journal of the Meteorological Society of Japan. Ser. II*

Lobell D B and Field C B 2007 Global scale climate–crop yield relationships and the impacts of recent warming *Environmental research letters* **2** 014002

López-Moreno J I and Vicente-Serrano S M 2008 Positive and negative phases of the wintertime North Atlantic Oscillation and drought occurrence over Europe: a multitemporal-scale approach *Journal of Climate* **21** 1220–43

Lorenz E N 1951 Seasonal and irregular variations of the Northern Hemisphere sea-level pressure profile *Journal of Atmospheric Sciences* **8** 52–9

Lorenz R, Jaeger E B and Seneviratne S I 2010 Persistence of heat waves and its link to soil moisture memory *Geophysical Research Letters* **37**

Loughnan M 2014 Heatwaves are silent killers *Geodate* **27** 7–10

Lu H, Wu Y, Li Y and Liu Y 2017 Effects of meteorological droughts on agricultural water resources in southern China *Journal of Hydrology* **548** 419–35

Lund J, Medellin-Azuara J, Durand J and Stone K 2018 Lessons from California's 2012–2016 drought *Journal of Water Resources Planning and Management* **144** 04018067

Luo L, Apps D, Arcand S, Xu H, Pan M and Hoerling M 2017 Contribution of temperature and precipitation anomalies to the California drought during 2012–2015 *Geophysical Research Letters* **44** 3184–92

Luo M and Lau N-C 2020 Summer heat extremes in northern continents linked to developing ENSO events *Environmental Research Letters* **15** 074042

Luyssaert S, Schulze E-D, Börner A, Knohl A, Hessenmöller D, Law B E, Ciais P and Grace J 2008 Old-growth forests as global carbon sinks *Nature* **455** 213–5

Lyon B 2009 Southern Africa summer drought and heat waves: observations and coupled model behavior *Journal of Climate* **22** 6033–46

Maity R and Kashid S S 2011 Importance analysis of local and global climate inputs for basin-scale streamflow prediction *Water Resources Research* **47**

Maity R and Kashid S S 2010 Short-term basin-scale streamflow forecasting using large-scale coupled atmospheric–oceanic circulation and local outgoing longwave radiation *Journal of Hydrometeorology* **11** 370–87

Maity R and Nagesh Kumar D 2006 Bayesian dynamic modeling for monthly Indian summer monsoon rainfall using El Nino–Southern Oscillation (ENSO) and Equatorial Indian Ocean Oscillation (EQUINOO) *Journal of Geophysical Research: Atmospheres* **111**

Maity R and Nagesh Kumar D 2008 Probabilistic prediction of hydroclimatic variables with nonparametric quantification of uncertainty *Journal of Geophysical Research: Atmospheres* **113**

Maity R, Suman M and Verma N K 2016 Drought prediction using a wavelet based approach to model the temporal consequences of different types of droughts *Journal of Hydrology* **539** 417–28

Malik A and Brönnimann S 2018 Factors affecting the inter-annual to centennial timescale variability of Indian summer monsoon rainfall *Climate dynamics* **50** 4347–64

Malik A, Kumar A and Singh R P 2019 Application of heuristic approaches for prediction of hydrological drought using multi-scalar streamflow drought index *Water Resources Management* **33** 3985–4006

Mandal V, De U K and Basu B K 2007 Precipitation forecast verification of the Indian summer monsoon with intercomparison of three diverse regions *Weather and forecasting* **22** 428–43

Mantua N J and Hare S R 2002 The Pacific decadal oscillation *Journal of oceanography* **58** 35–44

Mares I, Mares C and Mihailescu M 2002 NAO impact on the summer moisture variability across Europe *Physics and Chemistry of the Earth, Parts A/B/C* **27** 1013–7

Marino G P, Kaiser D P, Gu L and Ricciuto D M 2011 Reconstruction of false spring occurrences over the southeastern United States, 1901–2007: an increasing risk of spring freeze damage? *Environmental Research Letters* **6** 024015

Marquardt D W 1980 Comment: You should standardize the predictor variables in your regression models *Journal of the American Statistical Association* **75** 87–91

Marshall A G, Hudson D, Wheeler M C, Alves O, Hendon H H, Pook M J and Risbey J S 2014 Intra-seasonal drivers of extreme heat over Australia in observations and POAMA-2 *Climate dynamics* **43** 1915–37

Martínez-Fernández J, González-Zamora A, Sánchez N and Gumuzzio A 2015 A soil water based index as a suitable agricultural drought indicator *Journal of Hydrology* **522** 265–73

Mascioli N R, Previdi M, Fiore A M and Ting M 2017 Timing and seasonality of the United States 'warming hole' *Environmental Research Letters* **12** 034008

Masih I, Maskey S, Mussá F and Trambauer P 2014 A review of droughts on the African continent: a geospatial and long-term perspective *Hydrology and Earth System Sciences* **18** 3635

Matsueda M 2011 Predictability of Euro-Russian blocking in summer of 2010 *Geophysical Research Letters* **38**

Matzarakis A and Nastos P T 2011 Human-biometeorological assessment of heat waves in Athens *Theoretical and applied climatology* **105** 99–106

Mazdiyasni O and AghaKouchak A 2015 Substantial increase in concurrent droughts and heatwaves in the United States *Proceedings of the National Academy of Sciences* **112** 11484–9

McCabe G J, Palecki M A and Betancourt J L 2004 Pacific and Atlantic Ocean influences on multidecadal drought frequency in the United States *Proceedings of the National Academy of Sciences* **101** 4136–41

McGregor G R, Bessmoulin P, Ebi K and Menne B 2015 *Heatwaves and health: guidance on warning-system development.* (WMOP)

McKechnie A E, Hockey P A and Wolf B O 2012 Feeling the heat: Australian landbirds and climate change

McKee T B, Doesken N J and Kleist J 1993 The relationship of drought frequency and duration to time scales *Proceedings of the 8th Conference on Applied Climatology* vol 17 (Boston) pp 179–83

McMichael A J and Lindgren E 2011 Climate change: present and future risks to health, and necessary responses *Journal of internal medicine* **270** 401–13

Meehl G A and Tebaldi C 2004 More intense, more frequent, and longer lasting heat waves in the 21st century *Science* **305** 994–7

Meehl G A, Tebaldi C, Teng H and Peterson T C 2007 Current and future US weather extremes and El Niño *Geophysical Research Letters* **34**

Menne M J, Durre I, Vose R S, Gleason B E and Houston T G 2012 An overview of the global historical climatology network-daily database *Journal of Atmospheric and Oceanic Technology* **29** 897–910

Mildrexler D J, Zhao M and Running S W 2011 A global comparison between station air temperatures and MODIS land surface temperatures reveals the cooling role of forests *Journal of Geophysical Research: Biogeosciences* **116**

Miralles D G, Gentine P, Seneviratne S I and Teuling A J 2019 Land–atmospheric feedbacks during droughts and heatwaves: state of the science and current challenges *Annals of the New York Academy of Sciences* **1436** 19

Miralles D G, Teuling A J, Van Heerwaarden C C and Vilà-Guerau de Arellano J 2014 Mega-heatwave temperatures due to combined soil desiccation and atmospheric heat accumulation *Nature geoscience* **7** 345–9

Mishra A K and Desai V R 2005 Drought forecasting using stochastic models *Stochastic Environmental Research and Risk Assessment* **19** 326–39

Mishra A K, Desai V R and Singh V P 2007 Drought forecasting using a hybrid stochastic and neural network model *Journal of Hydrologic Engineering* **12** 626–38

Mishra A K, Dwivedi S and Di Sante F 2021 Performance of the RegCM-MITgcm Coupled Regional Model in Simulating the Indian Summer Monsoon Rainfall *Pure and Applied Geophysics* **178** 603–17

Mishra A K and Singh V P 2010 A review of drought concepts *Journal of hydrology* **391** 202–16

Mishra V 2015 Climatic uncertainty in Himalayan water towers *Journal of Geophysical Research: Atmospheres* **120** 2689–705

Mishra V, Ambika A K, Asoka A, Aadhar S, Buzan J, Kumar R and Huber M 2020 Moist heat stress extremes in India enhanced by irrigation *Nature Geoscience* **13** 722–8

Mishra V and Cherkauer K A 2010 Retrospective droughts in the crop growing season: Implications to corn and soybean yield in the Midwestern United States *Agricultural and Forest Meteorology* **150** 1030–45

Mishra V, Mukherjee S, Kumar R and Stone D A 2017 Heat wave exposure in India in current, 1.5 C, and 2.0 C worlds *Environmental Research Letters* **12** 124012

Mishra V, Shah R and Thrasher B 2014 Soil moisture droughts under the retrospective and projected climate in India *Journal of Hydrometeorology* **15** 2267–92

Mishra V, Smoliak B V, Lettenmaier D P and Wallace J M 2012 A prominent pattern of year-to-year variability in Indian Summer Monsoon Rainfall *Proceedings of the National Academy of Sciences* **109** 7213–7

Mitchell J M 1976 An overview of climatic variability and its causal mechanisms *Quaternary Research* **6** 481–93

Mo K C and Schemm J E 2008 Relationships between ENSO and drought over the southeastern United States *Geophysical Research Letters* **35** 1–5

Mohanty U C, Nageswararao M M, Sinha P, Nair A, Singh A, Rai R K, Kar S C, Ramesh K J, Singh K K and Ghosh K 2019 Evaluation of performance of seasonal precipitation prediction at regional scale over India *Theoretical and Applied Climatology* **135** 1123–42

Mokhov I I and Smirnov D A 2016 Relation between the variations in the global surface temperature, El Niño/La Niña phenomena, and the Atlantic Multidecadal Oscillation *Doklady Earth Sciences* vol 467 (Springer) pp 384–8

Mukherjee S, Ashfaq M and Mishra A K 2020 Compound drought and heatwaves at a global scale: The role of natural climate variability-associated synoptic patterns and land-surface energy budget anomalies *Journal of Geophysical Research: Atmospheres* **125** e2019JD031943

Mukherjee S, Mishra A and Trenberth K E 2018 Climate change and drought: a perspective on drought indices *Current Climate Change Reports* **4** 145–63

Muller J C-Y 2014 Adapting to climate change and addressing drought–learning from the Red Cross Red Crescent experiences in the Horn of Africa *Weather and Climate Extremes* **3** 31–6

Muluneh A, van Loon E, Bewket W, Keesstra S, Stroosnijder L and Burka A 2017 Effects of long-term deforestation and remnant forests on rainfall and temperature in the Central Rift Valley of Ethiopia *Forest Ecosystems* **4** 1–17

Munday C and Washington R 2017 Circulation controls on southern African precipitation in coupled models: The role of the Angola low *Journal of Geophysical Research: Atmospheres* **122** 861–77

Murari K K and Ghosh S 2019 Future Heat Wave Projections and Impacts *Climate Change Signals and Response* 91–107

Murari K K, Ghosh S, Patwardhan A, Daly E and Salvi K 2015 Intensification of future severe heat waves in India and their effect on heat stress and mortality *Regional Environmental Change* **15** 569–79

Murari K K, Sahana A S, Daly E and Ghosh S 2016 The influence of the El N iño Southern Oscillation on heat waves in India *Meteorological Applications* **23** 705–13

Nairn J R and Fawcett R J 2015 The excess heat factor: a metric for heatwave intensity and its use in classifying heatwave severity *International journal of environmental research and public health* **12** 227–53

Nakamura H, Nakamura M and Anderson J L 1997 The role of high-and low-frequency dynamics in blocking formation *Monthly Weather Review* **125** 2074–93

Nasipuri P, Majumdar T J and Mitra D S 2006 Study of high-resolution thermal inertia over western India oil fields using ASTER data *Acta Astronautica* **58** 270–8

Nayak S, Maity S, Singh K S, Nayak H P and Dutta S 2021 Influence of the Changes in Land-Use and Land Cover on Temperature over Northern and North-Eastern India *Land* **10** 52

Nayak S and Mandal M 2019a Examining the impact of regional land use and land cover changes on temperature: the case of Eastern India *Spatial Information Research* **27** 601–11

Nayak S and Mandal M 2019b Impact of land use and land cover changes on temperature trends over India *Land Use Policy* **89** 104238

New M, Todd M, Hulme M and Jones P 2001 Precipitation measurements and trends in the twentieth century *International*

Journal of Climatology: A Journal of the Royal Meteorological Society **21** 1889–922

Newman M, Alexander M A, Ault T R, Cobb K M, Deser C, Di Lorenzo E, Mantua N J, Miller A J, Minobe S and Nakamura H 2016 The Pacific decadal oscillation, revisited *Journal of Climate* **29** 4399–427

Nguyen P-L, Min S-K and Kim Y-H 2020 Combined impacts of the El Niño-Southern Oscillation and Pacific Decadal Oscillation on global droughts assessed using the standardized precipitation evapotranspiration index *International Journal of Climatology*

Nicholson S E 2014 A detailed look at the recent drought situation in the Greater Horn of Africa *Journal of Arid Environments* **103** 71–9

Ning L and Bradley R S 2015 Winter climate extremes over the northeastern United States and southeastern Canada and teleconnections with large-scale modes of climate variability *Journal of climate* **28** 2475–93

Nitschke M, Tucker G R, Hansen A L, Williams S, Zhang Y and Bi P 2011 Impact of two recent extreme heat episodes on morbidity and mortality in Adelaide, South Australia: a case-series analysis *Environmental Health* **10** 1–9

de Noblet-Ducoudré N, Boisier J-P, Pitman A, Bonan G B, Brovkin V, Cruz F, Delire C, Gayler V, Van den Hurk B and Lawrence P J 2012 Determining robust impacts of land-use-induced land cover changes on surface climate over North America and Eurasia: results from the first set of LUCID experiments *Journal of Climate* **25** 3261–81

Nobre C A, Marengo J A, Seluchi M E, Cuartas L A and Alves L M 2016 Some characteristics and impacts of the drought and water crisis in Southeastern Brazil during 2014 and 2015 *Journal of Water Resource and Protection* **8** 252–62

Okin G S, Dong C, Willis K S, Gillespie T W and MacDonald G M 2018 The impact of drought on native southern California vegetation: Remote sensing analysis using MODIS-derived time series *Journal of Geophysical Research: Biogeosciences* **123** 1927–39

Oleson K W, Bonan G B, Levis S and Vertenstein M 2004 Effects of land use change on North American climate: impact of surface datasets and model biogeophysics *Climate Dynamics* **23** 117–32

Page A, Morrell S and Taylor R 2002 Suicide and political regime in New South Wales and Australia during the 20th century *Journal of Epidemiology & Community Health* **56** 766–72

Palmer T N, Branković Č, Viterbo P and Miller M J 1992 Modeling interannual variations of summer monsoons *Journal of climate* **5** 399–417

Palmer W C 1965a *Meteorological drought* vol 30 (US Department of Commerce, Weather Bureau)

Palmer W C 1965b *Meteorological drought* vol 30 (US Department of Commerce, Weather Bureau)

Parker T J, Berry G J, Reeder M J and Nicholls N 2014 Modes of climate variability and heat waves in Victoria, southeastern Australia *Geophysical Research Letters* **41** 6926–34

Parthasarathy B and Pant G B 1985 Seasonal relationships between Indian summer monsoon rainfall and the Southern Oscillation *Journal of climatology* **5** 369–78

Partridge T F, Winter J M, Osterberg E C, Hyndman D W, Kendall A D and Magilligan F J 2018 Spatially distinct seasonal patterns and forcings of the US warming hole *Geophysical Research Letters* **45** 2055–63

Pere J-C, Mallet M, Pont V and Bessagnet B 2011 Impact of aerosol direct radiative forcing on the radiative budget, surface heat fluxes, and atmospheric dynamics during the heat wave of summer 2003 over western Europe: A modeling study *Journal of Geophysical Research: Atmospheres* **116**

Perkins S E 2015 A review on the scientific understanding of heatwaves-Their measurement, driving mechanisms, and changes at the global scale *Atmospheric Research* **164–165** 242–67

Perkins S E and Alexander L V 2013b On the measurement of heat waves *Journal of climate* **26** 4500–17

Perkins S E, Alexander L V and Nairn J R 2012a Increasing frequency, intensity and duration of observed global heatwaves and warm spells *Geophysical Research Letters* **39**

Perkins S E, Alexander L V and Nairn J R 2012b Increasing frequency, intensity and duration of observed global heatwaves and warm spells *Geophysical Research Letters* **39**

Perkins S E, Argüeso D and White C J 2015 Relationships between climate variability, soil moisture, and Australian heatwaves *Journal of Geophysical Research: Atmospheres* **120** 8144–64

Perkins-Kirkpatrick S E, Fischer E M, Angélil O and Gibson P B 2017 The influence of internal climate variability on heatwave frequency trends *Environmental Research Letters* **12** 044005

Perkins-Kirkpatrick S E and Lewis S C 2020a Increasing trends in regional heatwaves *Nature communications* **11** 1–8

Perkins-Kirkpatrick S E and Lewis S C 2020b Increasing trends in regional heatwaves *Nature communications* **11** 1–8

Peters A J, Walter-Shea E A, Ji L, Vina A, Hayes M and Svoboda M D 2002 Drought monitoring with NDVI-based standardized vegetation index *Photogrammetric engineering and remote sensing* **68** 71–5

Peterson T C and Vose R S 1997 An overview of the Global Historical Climatology Network temperature database *Bulletin of the American Meteorological Society* **78** 2837–50

Petoukhov V, Petri S, Rahmstorf S, Coumou D, Kornhuber K and Schellnhuber H J 2016 Role of quasiresonant planetary wave dynamics in recent boreal spring-to-autumn extreme events *Proceedings of the National Academy of Sciences* **113** 6862–7

Pezza A B, Van Rensch P and Cai W 2012 Severe heat waves in Southern Australia: synoptic climatology and large scale connections *Climate Dynamics* **38** 209–24

Pfahl S and Wernli H 2012 Quantifying the relevance of atmospheric blocking for co-located temperature extremes in the Northern Hemisphere on (sub-) daily time scales *Geophysical Research Letters* **39**

Philander S G H 1983 El Nino southern oscillation phenomena *Nature* **302** 295–301

Pillai P A, Rao S A, Ramu D A, Pradhan M and George G 2018 Seasonal prediction skill of Indian summer monsoon rainfall in NMME models and monsoon mission CFSv2 *International Journal of Climatology* **38** e847–61

Pitman A J, Avila F B, Abramowitz G, Wang Y P, Phipps S J and de Noblet-Ducoudré N 2011 Importance of background climate in determining impact of land-cover change on regional climate *Nature Climate Change* **1** 472–5

Pokhrel S, Hazra A, Chaudhari H S, Saha S K, Paulose F, Krishna S, Krishna P M and Rao S A 2018 Hindcast skill improvement in Climate Forecast System (CFSv2) using modified cloud scheme *Int. J. Climatol* **38** 2994–3012

Pomposi C, Funk C, Shukla S, Harrison L and Magadzire T 2018 Distinguishing southern Africa precipitation response by strength of El Niño events and implications for decision-making *Environmental Research Letters* **13** 074015

Portmann F T, Siebert S and Döll P 2010 MIRCA2000—Global monthly irrigated and rainfed crop areas around the year 2000: A new high-resolution data set for agricultural and hydrological modeling *Global biogeochemical cycles* **24**

Poumadere M, Mays C, Le Mer S and Blong R 2005 The 2003 heat wave in France: dangerous climate change here and now *Risk Analysis: an International Journal* **25** 1483–94

Prakash S, Norouzi H, Azarderakhsh M, Blake R, Prigent C and Khanbilvardi R 2018 Estimation of consistent global microwave land surface emissivity from AMSR-E and AMSR2 observations *Journal of Applied Meteorology and Climatology* **57** 907–19

Preethi B, Kripalani R H and Kumar K K 2010 Indian summer monsoon rainfall variability in global coupled ocean-atmospheric models *Climate dynamics* **35** 1521–39

Quiring S M 2009 Monitoring drought: an evaluation of meteorological drought indices *Geography Compass* **3** 64–88

Rabenhorst M C 2005 Biologic zero: a soil temperature concept *Wetlands* **25** 616–21

Rafiq M, Rashid I and Romshoo S A 2016 Estimating land surface temperature and its lapse rate over Kashmir Valley Using MODIS Data *Geostatistical and geospatial approaches for the characterization of natural resources in the environment* (Springer) pp 723–8

Raina A N 2002 Geography of Jammu & Kashmir State *Radha Krishan Anand & Co., Pacca Danga, Jammu*

Rajeevan M and Pai D S 2007 On the El Niño-Indian monsoon predictive relationships *Geophysical Research Letters* **34**

Rajeevan M, Pai D S, Dikshit S K and Kelkar R R 2004 IMD's new operational models for long-range forecast of southwest monsoon rainfall over India and their verification for 2003 *Current Science* 422–31

Rajeevan M, Pai D S, Kumar R A and Lal B 2007 New statistical models for long-range forecasting of southwest monsoon rainfall over India *Climate Dynamics* **28** 813–28

Rajeevan M, Unnikrishnan C K and Preethi B 2012 Evaluation of the ENSEMBLES multi-model seasonal forecasts of Indian summer monsoon variability *Climate Dynamics* **38** 2257–74

Ramu D A, Rao S A, Pillai P A, Pradhan M, George G, Rao D N, Mahapatra S, Pai D S and Rajeevan M 2017 Prediction of seasonal summer monsoon rainfall over homogenous regions of

India using dynamical prediction system *Journal of Hydrology* **546** 103–12

Ramu D A, Sabeerali C T, Chattopadhyay R, Rao D N, George G, Dhakate A R, Salunke K, Srivastava A and Rao S A 2016 Indian summer monsoon rainfall simulation and prediction skill in the CFSv2 coupled model: Impact of atmospheric horizontal resolution *Journal of Geophysical Research: Atmospheres* **121** 2205–21

Rao S A, Pillai P A, Pradhan M and Srivastava A 2019 Seasonal prediction of Indian summer monsoon in India: The past, the present and the future *MAUSAM* **70** 265–76

Rasmusson E M and Carpenter T H 1982 Variations in tropical sea surface temperature and surface wind fields associated with the Southern Oscillation/El Niño *Monthly Weather Review* **110** 354–84

Rathore L S and Maini P 2008 Economic impact assessment of agro-meteorological advisory service of NCMRWF *National Centre for Medium Range Weather Forecasting, Ministry of Earth Sciences, GOI*

RATNA D Sikka S B 2011 On improving the ability of a high-resolution atmospheric general circulation model for dynamical seasonal prediction of the extreme seasons of the Indian summer monsoon

Ratna S B, Sikka D R, Dalvi M and Venkata Ratnam J 2011 Dynamical simulation of Indian summer monsoon circulation, rainfall and its interannual variability using a high resolution atmospheric general circulation model *International journal of climatology* **31** 1927–42

Ratnam J V, Behera S K, Ratna S B, Rajeevan M and Yamagata T 2016 Anatomy of Indian heatwaves *Scientific reports* **6** 1–11

Ray D K, Gerber J S, MacDonald G K and West P C 2015 Climate variation explains a third of global crop yield variability *Nature communications* **6** 1–9

Reason C J C 2017 Climate of southern Africa *Oxford Research Encyclopedia of Climate Science*

Reddy P J, Perkins-Kirkpatrick S E, Ridder N N and Sharples J J 2022 Combined role of ENSO and IOD on compound drought and heatwaves in Australia using two CMIP6 large ensembles *Weather and Climate Extremes* 100469

Rickard D S and Fitzgerald P D 1969 The estimation and occurrence of agricultural drought *Journal of Hydrology (New Zealand)* 11–6

Robine J-M, Cheung S L K, Le Roy S, Van Oyen H, Griffiths C, Michel J-P and Herrmann F R 2008 Death toll exceeded 70,000 in Europe during the summer of 2003 *Comptes rendus biologies* **331** 171–8

Robinson P J 2001 On the definition of a heat wave *Journal of Applied Meteorology and Climatology* **40** 762–75

Rogers C D, Kornhuber K, Perkins-Kirkpatrick S E, Loikith P C and Singh D 2021a Six-fold increase in historical Northern Hemisphere concurrent large heatwaves driven by warming and changing atmospheric circulations *Journal of Climate* 1–39

Rogers C D, Ting M, Li C, Kornhuber K, Coffel E D, Horton R M, Raymond C and Singh D 2021b Recent Increases in Exposure to Extreme Humid-Heat Events Disproportionately Affect Populated Regions *Geophysical Research Letters* **48** e2021GL094183

Rohini P, Rajeevan M and Srivastava A K 2016 On the variability and increasing trends of heat waves over India *Scientific reports* **6** 1–9

Romshoo S A, Rafiq M and Rashid I 2018 Spatio-temporal variation of land surface temperature and temperature lapse rate over mountainous Kashmir Himalaya *Journal of Mountain Science* **15** 563–76

Ropelewski C and Folland C 2000 Prospects for the prediction of meteorological drought *Drought: a global assessment* **1** 21–40

Rössler O, Froidevaux P, Börst U, Rickli R, Martius O and Weingartner R 2014 Retrospective analysis of a nonforecasted rain-on-snow flood in the Alps–a matter of model limitations or unpredictable nature? *Hydrology and Earth System Sciences* **18** 2265–85

Röthlisberger M, Frossard L, Bosart L F, Keyser D and Martius O 2019 Recurrent synoptic-scale Rossby wave patterns and their effect on the persistence of cold and hot spells *Journal of Climate* **32** 3207–26

Rübbelke D and Vögele S 2011 Impacts of climate change on European critical infrastructures: the case of the power sector *Environmental science & policy* **14** 53–63

Rummukainen M 2012 Changes in climate and weather extremes in the 21st century *Wiley Interdisciplinary Reviews: Climate Change* **3** 115–29

Ruprich-Robert Y, Delworth T, Msadek R, Castruccio F, Yeager S and Danabasoglu G 2018 Impacts of the Atlantic multidecadal variability on North American summer climate and heat waves *Journal of Climate* **31** 3679–700

Russo S, Marchese A F, Sillmann J and Immé G 2016 When will unusual heat waves become normal in a warming Africa? *Environmental Research Letters* **11** 054016

Russo S, Sillmann J and Sterl A 2017 Humid heat waves at different warming levels *Scientific reports* **7** 1–7

Ryu J H and Hayhoe K 2015 Large-scale processes relevant to extreme hot and dry summer conditions in the South Central US: Comparing observations with CMIP5 simulations *AGU Fall Meeting Abstracts* vol 2015 pp A51H-0165

Sadegh M, Moftakhari H, Gupta H V, Ragno E, Mazdiyasni O, Sanders B, Matthew R and AghaKouchak A 2018 Multihazard scenarios for analysis of compound extreme events *Geophysical Research Letters* **45** 5470–80

Saha M, Mitra P and Nanjundiah R S 2017 Deep learning for predicting the monsoon over the homogeneous regions of India *Journal of Earth System Science* **126** 54

Sahai A K, Abhilash S, Chattopadhyay R, Borah N, Joseph S, Sharmila S and Rajeevan M 2015 High-resolution operational monsoon forecasts: an objective assessment *Climate Dynamics* **44** 3129–40

Sahai A K, Soman M K and Satyan V 2000 All India summer monsoon rainfall prediction using an artificial neural network *Climate dynamics* **16** 291–302

Sahastrabuddhe R, Ghosh S, Saha A and Murtugudde R 2019 A minimalistic seasonal prediction model for Indian monsoon based on spatial patterns of rainfall anomalies *Climate Dynamics* **52** 3661–81

Sahoo B B, Jha R, Singh A and Kumar D 2019 Long short-term memory (LSTM) recurrent neural network for low-flow hydrological time series forecasting *Acta Geophysica* **67** 1471–81

Sajani S, Nakazawa T, Kitoh A and Rajendran K 2007 Ensemble simulation of Indian summer monsoon rainfall by an atmospheric general circulation model *Journal of the Meteorological Society of Japan. Ser. II* **85** 213–31

Sakai A and Fujita K 2017 Contrasting glacier responses to recent climate change in high-mountain Asia *Scientific reports* **7** 1–8

Saseendran S A, Singh S V, Rathore L S and Das S 2002 Characterization of weekly cumulative rainfall forecasts over meteorological subdivisions of India using a GCM *Weather and Forecasting* **17** 832–44

Schär C 2016 The worst heat waves to come *Nature Climate Change* **6** 128–9

Schär C, Vidale P L, Lüthi D, Frei C, Häberli C, Liniger M A and Appenzeller C 2004 The role of increasing temperature variability in European summer heatwaves *Nature* **427** 332–6

Schatz J and Kucharik C J 2015 Urban climate effects on extreme temperatures in Madison, Wisconsin, USA *Environmental Research Letters* **10** 094024

Schneidereit A, Schubert S, Vargin P, Lunkeit F, Zhu X, Peters D H and Fraedrich K 2012 Large-scale flow and the long-lasting blocking high over Russia: Summer 2010 *Monthly Weather Review* **140** 2967–81

van der Schrier G, Barichivich J, Briffa K and Jones P 2013 A scPDSI-based global data set of dry and wet spells for 1901–2009 *Journal of Geophysical Research: Atmospheres* **118** 4025–48

Schumacher D, Keune J and Miralles D 2020 Atmospheric heat and moisture transport to energy-and water-limited ecosystems *Annals of the New York Academy of Sciences*

Schumacher D L, Keune J, Van Heerwaarden C C, de Arellano J V-G, Teuling A J and Miralles D G 2019a Amplification of mega-heatwaves through heat torrents fuelled by upwind drought *Nature Geoscience* **12** 712–7

Schumacher D L, Keune J, Van Heerwaarden C C, de Arellano J V-G, Teuling A J and Miralles D G 2019b Amplification of mega-heatwaves through heat torrents fuelled by upwind drought *Nature Geoscience* **12** 712–7

Seager R and Henderson N 2016 On the Role of Tropical Ocean Forcing of the Persistent North American West Coast Ridge of Winter 2013/14 *J. Climate* **29** 8027–49

Seager R, Hoerling M, Schubert S, Wang H, Lyon B, Kumar A, Nakamura J and Henderson N 2015 Causes of the 2011–14 California drought *Journal of Climate* **28** 6997–7024

Seneviratne S I, Donat M G, Pitman A J, Knutti R and Wilby R L 2016 Allowable CO 2 emissions based on regional and impact-related climate targets *Nature* **529** 477–83

Seneviratne S I, Lüthi D, Litschi M and Schär C 2006 Land–atmosphere coupling and climate change in Europe *Nature* **443** 205–9

Seneviratne S I, Zhang X, Adnan M, Badi W, Dereczynski C, Di Luca A, Vicente-Serrano S M, Wehner M and Zhou B 2021 11 Chapter 11: Weather and climate extreme events in a changing climate

Seneviratne S, Nicholls N, Easterling D, Goodess C, Kanae S, Kossin J, Luo Y, Marengo J, McInnes K and Rahimi M 2012 Changes in climate extremes and their impacts on the natural physical environment

Service (C3S) C C C 2017 *ERA5: Fifth generation of ECMWF atmospheric reanalyses of the global climate, Copernicus Climate Change Service Climate Data Store (CDS)*

Shafiq M U, Rasool R, Ahmed P and Dimri A P 2019a Temperature and precipitation trends in Kashmir Valley, north western Himalayas *Theoretical and Applied Climatology* **135** 293–304

Shafiq M ul, Ahmed P, Islam Z ul, Joshi P K and Bhat W A 2019b Snow cover area change and its relations with climatic variability in Kashmir Himalayas, India *Geocarto International* **34** 688–702

Shah D and Mishra V 2020 Integrated Drought Index (IDI) for drought monitoring and assessment in India *Water Resources Research* **56** e2019WR026284

Shah R D and Mishra V 2015 Seasonal drought prediction in India *Proceedings of the American Geophysical Union. Fall Meeting*

Shah R D and Mishra V 2016 Utility of Global Ensemble Forecast System (GEFS) reforecast for medium-range drought prediction in India *Journal of Hydrometeorology* **17** 1781–800

Shah R, Sahai A K and Mishra V 2017 Short to sub-seasonal hydrologic forecast to manage water and agricultural resources in India. *Hydrology & Earth System Sciences* **21**

Sharifnezhadazizi Z, Norouzi H, Prakash S, Beale C and Khanbilvardi R 2019 A global analysis of land surface temperature diurnal cycle using MODIS observations *Journal of Applied Meteorology and Climatology* **58** 1279–91

Shashikanth K, Madhusoodhanan C G, Ghosh S, Eldho T I, Rajendran K and Murtugudde R 2014 Comparing statistically downscaled simulations of Indian monsoon at different spatial resolutions *Journal of Hydrology* **519** 3163–77

Sheffield J, Andreadis K M, Wood E F and Lettenmaier D P 2009 Global and continental drought in the second half of the twentieth century: severity–area–duration analysis and temporal variability of large-scale events *Journal of Climate* **22** 1962–81

Shen C, Wang W-C, Hao Z and Gong W 2007 Exceptional drought events over eastern China during the last five centuries *Climatic Change* **85** 453–71

Shrivastava S, Kar S C, Sahai A K and Sharma A R 2018 Identification of drought occurrences using ensemble predictions up to 20-days in advance *Water resources management* **32** 2113–30

Shukla S and Wood A W 2008 Use of a standardized runoff index for characterizing hydrologic drought *Geophysical research letters* **35**

Sigauke C and Nemukula M M 2020 Modelling extreme peak electricity demand during a heatwave period: A case study *Energy Systems* **11** 139–61

Simpkins G 2018 Running dry *Nature Climate Change* **8** 369–369

Sims D A, Rahman A F, Cordova V D, El-Masri B Z, Baldocchi D D, Bolstad P V, Flanagan L B, Goldstein A H, Hollinger D Y, Misson L, Monson R K, Oechel W C, Schmid H P, Wofsy S C and Xu L 2008 A new model of gross primary productivity for North American ecosystems based solely on the enhanced vegetation index and land surface temperature from MODIS *Remote Sensing of Environment* **112** 1633–46

Singh A, Acharya N, Mohanty U C, Robertson A W and Mishra G 2012a On the predictability of Indian summer monsoon rainfall in general circulation model at different lead time *Dynamics of atmospheres and oceans* **58** 108–27

Singh A, Kulkarni M A, Mohanty U C, Kar S C, Robertson A W and Mishra G 2012b Prediction of Indian summer monsoon rainfall (ISMR) using canonical correlation analysis of global circulation model products *Meteorological Applications* **19** 179–88

Singh A, Thakur S and Adhikary N C 2020 Influence of climatic indices (AMO, PDO, and ENSO) and temperature on rainfall in the Northeast Region of India *SN Applied Sciences* **2** 1–15

Singh D, Seager R, Cook B I, Cane M, Ting M, Cook E and Davis M 2018 Climate and the Global Famine of 1876–78 *Journal of Climate* **31** 9445–67

Singh J, Ashfaq M, Skinner C B, Anderson W B, Mishra V and Singh D 2022 Enhanced risk of concurrent regional droughts with increased ENSO variability and warming *Nature Climate Change* **12** 163–70

Singh J, Ashfaq M, Skinner C B, Anderson W B and Singh D 2021 Amplified risk of spatially compounding droughts during co-occurrences of modes of natural ocean variability *npj Climate and Atmospheric Science* **4** 1–14

Singh P and Borah B 2013 Indian summer monsoon rainfall prediction using artificial neural network *Stochastic environmental research and risk assessment* **27** 1585–99

Singh R and AchutaRao K 2019 Quantifying uncertainty in twenty-first century climate change over India *Climate dynamics* **52** 3905–28

Singh S, Ghosh S, Sahana A S, Vittal H and Karmakar S 2017 Do dynamic regional models add value to the global model projections of Indian monsoon? *Climate dynamics* **48** 1375–97

Singh V, Jain S K and Singh P K 2019 Inter-comparisons and applicability of CMIP5 GCMs, RCMs and statistically downscaled NEX-GDDP based precipitation in India *Science of the Total Environment* **697** 134163

Sinha P, Mohanty U C, Kar S C, Dash S K, Robertson A W and Tippett M K 2013 Seasonal prediction of the Indian summer monsoon rainfall using canonical correlation analysis of the NCMRWF global model products *International Journal of Climatology* **33** 1601–14

Smith D M, Cusack S, Colman A W, Folland C K, Harris G R and Murphy J M 2007 Improved surface temperature prediction for the coming decade from a global climate model *science* **317** 796–9

Snyder P K, Delire C and Foley J A 2004 Evaluating the influence of different vegetation biomes on the global climate *Climate Dynamics* **23** 279–302

Sobrino J A, García-Monteiro S and Julien Y 2020 Surface Temperature of the Planet Earth from Satellite Data over the Period 2003–2019 *Remote Sensing* **12** 2036

Sohrabi M M, Ryu J H, Abatzoglou J and Tracy J 2015 Development of soil moisture drought index to characterize droughts *Journal of Hydrologic Engineering* **20** 04015025

Song F and Zhou T 2014 Interannual variability of East Asian summer monsoon simulated by CMIP3 and CMIP5 AGCMs: Skill dependence on Indian Ocean–western Pacific anticyclone teleconnection *Journal of Climate* **27** 1679–97

Sperber K R and Palmer T N 1996 Interannual tropical rainfall variability in general circulation model simulations associated with the Atmospheric Model Intercomparison Project *Journal of Climate* **9** 2727–50

Sridevi C, Singh K K, Suneetha P, Durai V R and Kumar A 2020 Rainfall forecasting skill of GFS model at T1534 and T574 resolution over India during the monsoon season *Meteorology and Atmospheric Physics* **132** 35–52

Srivastava A K, Rajeevan M and Kulkarni R 2002 Teleconnection of OLR and SST anomalies over Atlantic Ocean with Indian summer monsoon *Geophysical research letters* **29** 125–1

Srivastava A, Rao S A, Pradhan M, Pillai P A and Prasad V S 2020 Gain of one-month lead time in seasonal prediction of Indian summer monsoon prediction: comparison of initialization strategies *Theoretical and Applied Climatology* 1–14

Srivastava A, Rao S A, Rao D N, George G and Pradhan M 2017 Structure, characteristics, and simulation of monsoon low-pressure systems in CFS v2 coupled model *Journal of Geophysical Research: Oceans* **122** 6394–415

Steptoe H, Jones S E O and Fox H 2018 Correlations between extreme atmospheric hazards and global teleconnections: implications for multihazard resilience *Reviews of Geophysics* **56** 50–78

Stone B, Hess J J and Frumkin H 2010 Urban form and extreme heat events: are sprawling cities more vulnerable to climate change than compact cities? *Environmental health perspectives* **118** 1425–8

Strobach E and Bel G 2017 The contribution of internal and model variabilities to the uncertainty in CMIP5 decadal climate predictions *Climate Dynamics* **49** 3221–35

Stull R 2011 Wet-bulb temperature from relative humidity and air temperature *Journal of applied meteorology and climatology* **50** 2267–9

Sturm M, Douglas T, Racine C and Liston G E 2005 Changing snow and shrub conditions affect albedo with global implications *Journal of Geophysical Research: Biogeosciences* **110**

Su B, Huang J, Fischer T, Wang Y, Kundzewicz Z W, Zhai J, Sun H, Wang A, Zeng X and Wang G 2018 Drought losses in China might double between the 1.5 C and 2.0 C warming *Proceedings of the National Academy of Sciences* **115** 10600–5

Sun C, Li J and Ding R 2016 Strengthening relationship between ENSO and western Russian summer surface temperature *Geophysical Research Letters* **43** 843–51

Surendran S, Gadgil S, Francis P A and Rajeevan M 2015 Prediction of Indian rainfall during the summer monsoon season on the basis of links with equatorial Pacific and Indian Ocean climate indices *Environmental Research Letters* **10** 094004

Swain D L, Horton D E, Singh D and Diffenbaugh N S 2016 Trends in atmospheric patterns conducive to seasonal precipitation and temperature extremes in California *Science Advances* **2** e1501344

Swain D L, Singh D, Horton D E, Mankin J S, Ballard T C and Diffenbaugh N S 2017 Remote Linkages to Anomalous Winter Atmospheric Ridging Over the Northeastern Pacific *Journal of Geophysical Research: Atmospheres* **122** 12,194-12,209

Tachibana Y, Nakamura T, Komiya H and Takahashi M 2010 Abrupt evolution of the summer Northern Hemisphere annular mode and its association with blocking *Journal of Geophysical Research: Atmospheres* **115**

Tallaksen L M and Van Lanen H A 2004 *Hydrological drought: processes and estimation methods for streamflow and groundwater* (Elsevier)

Tan E and Unal Y S 2003 Impact Of NAO To Winter Precipitation And Temperature Variability Over Turkey 626

Tan X, Bao M, Hartmann D L and Ceppi P 2017 The role of synoptic waves in the formation and maintenance of the Western Hemisphere circulation pattern *Journal of Climate* **30** 10259–74

Tang Y, Zhang R-H, Liu T, Duan W, Yang D, Zheng F, Ren H, Lian T, Gao C and Chen D 2018 Progress in ENSO prediction and predictability study *National Science Review* **5** 826–39

Thompson D W and Wallace J M 2000 Annular modes in the extratropical circulation. Part I: Month-to-month variability *Journal of climate* **13** 1000–16

Thompson D W and Wallace J M 2001 Regional climate impacts of the Northern Hemisphere annular mode *Science* **293** 85–9

Thompson D W and Wallace J M 1998 The Arctic Oscillation signature in the wintertime geopotential height and temperature fields *Geophysical research letters* **25** 1297–300

Thornthwaite C W 1948 An approach toward a rational classification of climate *Geographical review* **38** 55–94

Tilloy A, Malamud B D, Winter H and Joly-Laugel A 2019 A review of quantification methodologies for multi-hazard interrelationships *Earth-Science Reviews* **196** 102881

Tiwari A D and Mishra V 2019 Prediction of reservoir storage anomalies in India *Journal of Geophysical Research: Atmospheres* **124** 3822–38

Tokarczyk T 2013 Classification of low flow and hydrological drought for a river basin *Acta Geophysica* **61** 404–21

Trenberth K E 2001 Climate variability and global warming *Science* **293** 48–9

Trenberth K E and Shea D J 2005 Relationships between precipitation and surface temperature *Geophysical Research Letters* **32**

Trenberth K, Jones P, Ambenje P, Bojariu R, Easterling D, Tank A K, Parker D, Rahimzadeh F, Renwick J and Rusticucci M 2007 Observations: surface and atmospheric climate change. Chapter 3 *Climate change* 235–336

Tripathi A D, Mishra R, Maurya K K, Singh R B and Wilson D W 2019 Estimates for world population and global food availability for global health *The role of functional food security in global health* (Elsevier) pp 3–24

Ummenhofer C C, England M H, McIntosh P C, Meyers G A, Pook M J, Risbey J S, Gupta A S and Taschetto A S 2009 What causes southeast Australia's worst droughts? *Geophysical Research Letters* **36**

Ummenhofer C C, Sen Gupta A, Briggs P R, England M H, McIntosh P C, Meyers G A, Pook M J, Raupach M R and Risbey J S 2011 Indian and Pacific Ocean influences on southeast Australian drought and soil moisture *Journal of Climate* **24** 1313–36

UNCCD 2022 Land and Drought | UNCCD Online: https://www2.unccd.int/issues/land-and-drought

UNISDR C 2015 The human cost of natural disasters: A global perspective

Urban M, Eberle J, Hüttich C, Schmullius C and Herold M 2013 Comparison of satellite-derived land surface temperature and air temperature from meteorological stations on the pan-Arctic Scale *Remote Sensing* **5** 2348–67

Van der Schrier G and Barkmeijer J 2007 North American 1818–1824 drought and 1825–1840 pluvial and their possible relation to the atmospheric circulation *Journal of Geophysical Research: Atmospheres* **112**

Van der Schrier G, Jones P and Briffa K 2011 The sensitivity of the PDSI to the Thornthwaite and Penman-Monteith parameterizations for potential evapotranspiration *Journal of Geophysical Research: Atmospheres* **116**

Van Lanen H A J and Peters E 2000 Definition, effects and assessment of groundwater droughts *Drought and drought mitigation in Europe* (Springer) pp 49–61

Van Loon A F 2015 Hydrological drought explained *Wiley Interdisciplinary Reviews: Water* **2** 359–92

Van Loon A F and Laaha G 2015 Hydrological drought severity explained by climate and catchment characteristics *Journal of hydrology* **526** 3–14

Van Loon A F, Stahl K, Di Baldassarre G, Clark J, Rangecroft S, Wanders N, Gleeson T, Van Dijk A I, Tallaksen L M and Hannaford J 2016 Drought in a human-modified world: reframing drought definitions, understanding, and analysis approaches *Hydrology and Earth System Sciences* **20** 3631–50

Van Oldenborgh G J, Wehner M F, Vautard R, Otto F E, Seneviratne S I, Stott P A, Hegerl G C, Philip S Y and Kew S F 2022 Attributing and projecting heatwaves is hard: we can do better *Earth's Future* **10** e2021EF002271

Vautard R, Gobiet A, Jacob D, Belda M, Colette A, Déqué M, Fernández J, García-Díez M, Goergen K and Güttler I 2013 The simulation of European heat waves from an ensemble of regional climate models within the EURO-CORDEX project *Climate Dynamics* **41** 2555–75

Veena K, Parammasivam K M and Venkatesh T N 2020 Urban Heat Island studies: Current status in India and a comparison with the International studies *Journal of Earth System Science* **129** 1–15

Vicente Serrano S M, López-Moreno J I, Beguería S, Lorenzo-Lacruz J, Azorin-Molina C and Morán-Tejeda E 2012 Accurate computation of a streamflow drought index (American Society of Civil Engineers)

Vicente-Serrano S M, Beguería S and López-Moreno J I 2010 A multiscalar drought index sensitive to global warming: the standardized precipitation evapotranspiration index *Journal of climate* **23** 1696–718

Vicente-Serrano S M, Beguería S, Lorenzo-Lacruz J, Camarero J J, López-Moreno J I, Azorin-Molina C, Revuelto J, Morán-Tejeda E and Sanchez-Lorenzo A 2012 Performance of drought indices for ecological, agricultural, and hydrological applications *Earth Interactions* **16** 1–27

Vicente-Serrano S M, López-Moreno J I, Gimeno L, Nieto R, Morán-Tejeda E, Lorenzo-Lacruz J, Beguería S and Azorin-Molina C 2011 A multiscalar global evaluation of the impact of ENSO on droughts *Journal of Geophysical Research: Atmospheres* **116**

Vicente-Serrano S M, López-Moreno J I, Lorenzo-Lacruz J, Kenawy A E, Azorin-Molina C, Morán-Tejeda E, Pasho E, Zabalza J, Beguería S and Angulo-Martínez M 2011 The NAO impact on droughts in the Mediterranean region *Hydrological, socioeconomic and ecological impacts of the north Atlantic oscillation in the mediterranean region* (Springer) pp 23–40

Villarini G 2016 On the seasonality of flooding across the continental United States - ScienceDirect *Adv. in Water Res.* 80–91

Vinayachandran P N, Francis P A and Rao S A 2009 Indian Ocean dipole: processes and impacts *Current trends in science* **46** 569–89

Vinayachandran P N, Iizuka S and Yamagata T 2002 Indian Ocean dipole mode events in an ocean general circulation model *Deep Sea Research Part II: Topical Studies in Oceanography* **49** 1573–96

Vins H, Bell J, Saha S and Hess J J 2015 The mental health outcomes of drought: a systematic review and causal process diagram *International journal of environmental research and public health* **12** 13251–75

Vishnu S, Francis P A, Ramakrishna S and Shenoi S S C 2019 On the relationship between the Indian summer monsoon rainfall and the EQUINOO in the CFSv2 *Climate Dynamics* **52** 1263–81

Vogel M M, Zscheischler J, Wartenburger R, Dee D and Seneviratne S I 2019 Concurrent 2018 hot extremes across Northern Hemisphere due to human-induced climate change *Earth's future* **7** 692–703

Wada Y, Van Beek L P, Wanders N and Bierkens M F 2013 Human water consumption intensifies hydrological drought worldwide *Environmental Research Letters* **8** 034036

Wahl T, Jain S, Bender J, Meyers S D and Luther M E 2015 Increasing risk of compound flooding from storm surge and rainfall for major US cities *Nature Climate Change* **5** 1093–7

Walker G T 1924 Correlations in seasonal variations of weather. I. A further study of world weather *Mem. Indian Meteorol. Dep.* **24** 275–332

Wallace J M and Gutzler D S 1981 Teleconnections in the geopotential height field during the Northern Hemisphere winter *Monthly Weather Review* **109** 784–812

Wan, Zhengming, Hook, Simon and Hulley, Glynn 2015 MYD11C1 MODIS/Aqua Land Surface Temperature/Emissivity Daily L3 Global 0.05Deg CMG V006 Online: https://lpdaac.usgs.gov/products/myd11c1v006/

Wan Z 2008 New refinements and validation of the MODIS land-surface temperature/emissivity products *Remote sensing of Environment* **112** 59–74

Wang B, Ding Q, Fu X, Kang I-S, Jin K, Shukla J and Doblas-Reyes F 2005a Fundamental challenge in simulation and prediction of summer monsoon rainfall *Geophysical Research Letters* **32**

Wang B, Webster P J and Teng H 2005b Antecedents and self-induction of active-break south Asian monsoon unraveled by satellites *Geophysical Research Letters* **32**

Wang B, Xiang B, Li J, Webster P J, Rajeevan M N, Liu J and Ha K-J 2015a Rethinking Indian monsoon rainfall prediction in the context of recent global warming *Nature communications* **6** 1–9

Wang C 2019 Three-ocean interactions and climate variability: a review and perspective *Climate Dynamics* **53** 5119–36

Wang C and Picaut J 2004 Understanding ENSO physics—A review *Earth's Climate: The Ocean–Atmosphere Interaction, Geophys. Monogr* **147** 21–48

Wang C, Wang Z-H, Wang C and Myint S W 2019a Environmental cooling provided by urban trees under extreme heat and cold waves in US cities *Remote sensing of environment* **227** 28–43

Wang H, Kumar A, Wang W and Xue Y 2012a Seasonality of the Pacific decadal oscillation *Journal of climate* **25** 25–38

Wang L, Chen W and Huang R 2008 Interdecadal modulation of PDO on the impact of ENSO on the East Asian winter monsoon *Geophysical Research Letters* **35**

Wang S, Huang J, He Y and Guan Y 2014 Combined effects of the Pacific decadal oscillation and El Nino-southern oscillation on global land dry–wet changes *Scientific reports* **4** 6651

Wang S S-Y, Kim H, Coumou D, Yoon J-H, Zhao L and Gillies R R 2019b Consecutive extreme flooding and heat wave in Japan: Are they becoming a norm? *Atmospheric Science Letters* **20** e933

Wang S-Y, Hipps L, Gillies R R and Yoon J-H 2015b Probable causes of the abnormal ridge accompanying the 2013–2014 California drought: ENSO precursor and anthropogenic warming footprint *Geophysical Research Letters* 3220–6

Wang W, Zhou W, Li X, Wang X and Wang D 2016 Synoptic-scale characteristics and atmospheric controls of summer heat waves in China *Climate dynamics* **46** 2923–41

Wang X and Liu H 2016 PDO modulation of ENSO effect on tropical cyclone rapid intensification in the western North Pacific *Climate Dynamics* **46** 15–28

Wang X Y, Barnett A G, Yu W, FitzGerald G, Tippett V, Aitken P, Neville G, McRae D, Verrall K and Tong S 2012b The impact of heatwaves on mortality and emergency hospital admissions from non-external causes in Brisbane, Australia *Occupational and environmental medicine* **69** 163–9

Webb R, Rosenzweig C E and Levine E R 2000 Global soil texture and derived water-holding capacities (Webb et al.) *ORNL DAAC*

Wegren S K 2011 Food security and Russia's 2010 drought *Eurasian Geography and Economics* **52** 140–56

Wehrli K, Guillod B P, Hauser M, Leclair M and Seneviratne S I 2019 Identifying key driving processes of major recent heat waves *Journal of Geophysical Research: Atmospheres* **124** 11746–65

Wells N, Goddard S and Hayes M J 2004 A self-calibrating Palmer drought severity index *Journal of Climate* **17** 2335–51

White C J, Hudson D and Alves O 2014 ENSO, the IOD and the intraseasonal prediction of heat extremes across Australia using POAMA-2 *Climate dynamics* **43** 1791–810

Wilhite D A 2000 Drought as a natural hazard: concepts and definitions

Wilhite D A and Glantz M H 1985 Understanding: the drought phenomenon: the role of definitions *Water international* **10** 111–20

Wise E K 2016 Five centuries of US West Coast drought: Occurrence, spatial distribution, and associated atmospheric circulation patterns *Geophysical Research Letters* **43** 4539–46

Wolf G, Brayshaw D J, Klingaman N P and Czaja A 2018 Quasi-stationary waves and their impact on European weather and extreme events *Quarterly Journal of the Royal Meteorological Society* **144** 2431–48

Wolski P 2018 How severe is Cape Town's "Day Zero" drought? *Significance* **15** 24–7

Wright C K, De Beurs K M and Henebry G M 2014 Land surface anomalies preceding the 2010 Russian heat wave and a link to the North Atlantic oscillation *Environmental Research Letters* **9** 124015

Wu H and Wilhite D A 2004 An operational agricultural drought risk assessment model for Nebraska, USA *Natural Hazards* **33** 1–21

Wu X, Hao Z, Hao F and Zhang X 2019 Variations of compound precipitation and temperature extremes in China during 1961–2014 *Science of the Total Environment* **663** 731–7

Wu X, Hao Z, Tang Q, Zhang X, Feng S and Hao F 2021 Population exposure to compound dry and hot events in China under 1.5 and 2° C global warming *International Journal of Climatology* **41** 5766–75

Wu X and Jiang D 2022 Probabilistic impacts of compound dry and hot events on global gross primary production *Environmental Research Letters* **17** 034049

Wyatt M G, Kravtsov S and Tsonis A A 2012 Atlantic multidecadal oscillation and Northern Hemisphere's climate variability *Climate Dynamics* **38** 929–49

Xu C, McDowell N G, Fisher R A, Wei L, Sevanto S, Christoffersen B O, Weng E and Middleton R S 2019 Increasing impacts of extreme droughts on vegetation productivity under climate change *Nature Climate Change* **9** 948–53

Xu H, Xiao J and Zhang Z 2020 Heatwave effects on gross primary production of northern mid-latitude ecosystems *Environmental Research Letters* **15** 074027

Yadav R K, Srinivas G and Chowdary J S 2018 Atlantic Niño modulation of the Indian summer monsoon through Asian jet *NPJ Climate and Atmospheric Science* **1** 1–11

Yang S, Li Z, Yu J-Y, Hu X, Dong W and He S 2018a El Niño–Southern Oscillation and its impact in the changing climate *National Science Review* **5** 840–57

Yang Y, Saatchi S S, Xu L, Yu Y, Choi S, Phillips N, Kennedy R, Keller M, Knyazikhin Y and Myneni R B 2018b Post-drought decline of the Amazon carbon sink *Nature communications* **9** 1–9

Yevjevich V M 1967 *Objective approach to definitions and investigations of continental hydrologic droughts, An* PhD Thesis (Colorado State University. Libraries)

Yin J, Gentine P, Zhou S, Sullivan S C, Wang R, Zhang Y and Guo S 2018 Large increase in global storm runoff extremes driven by climate and anthropogenic changes *Nature Communications* **9** 1–10

Yoon J-H, Wang S-Y S, Gillies R R, Hipps L, Kravitz B and Rasch P J 2015 2. Extreme fire season in California: A glimpse into the future? *Bulletin of the American Meteorological Society* **96** S5–9

Zargar A, Sadiq R, Naser B and Khan F I 2011 A review of drought indices *Environmental Reviews* **19** 333–49

Zaz S N, Romshoo S A, Krishnamoorthy R T and Viswanadhapalli Y 2019 Analyses of temperature and precipitation in the Indian Jammu and Kashmir region for the 1980–2016 period: implications for remote influence and extreme events *Atmospheric Chemistry and Physics* **19** 15–37

Zhang L, Zhou T, Klingaman N P, Wu P and Roberts M 2018 Effect of horizontal resolution on the representation of the global monsoon annual cycle in AGCMs *Advances in Atmospheric Sciences* **35** 1003–20

Zhang M, Lee X, Yu G, Han S, Wang H, Yan J, Zhang Y, Li Y, Ohta T and Hirano T 2014a Response of surface air temperature to small-scale land clearing across latitudes *Environmental Research Letters* **9** 034002

Zhang P, Bounoua L, Imhoff M L, Wolfe R E and Thome K 2014b Comparison of MODIS land surface temperature and air temperature over the continental USA meteorological stations *Canadian Journal of Remote Sensing* **40** 110–22

Zhao A, Bollasina M A and Stevenson D S 2019 Strong influence of aerosol reductions on future heatwaves *Geophysical Research Letters* **46** 4913–23

Zickfeld K, Arora V K and Gillett N P 2012 Is the climate response to CO2 emissions path dependent? *Geophysical Research Letters* **39**

Zscheischler J, Martius O, Westra S, Bevacqua E, Raymond C, Horton R M, van den Hurk B, AghaKouchak A, Jézéquel A and Mahecha M D 2020 A typology of compound weather and climate events *Nature reviews earth & environment* **1** 333–47

Zscheischler J and Seneviratne S I 2017 Dependence of drivers affects risks associated with compound events *Science advances* **3** e1700263

Zscheischler J, Westra S, Van Den Hurk B J, Seneviratne S I, Ward P J, Pitman A, AghaKouchak A, Bresch D N, Leonard M and Wahl T 2018 Future climate risk from compound events *Nature Climate Change* **8** 469–77

Zuo J, Pullen S, Palmer J, Bennetts H, Chileshe N and Ma T 2015 Impacts of heat waves and corresponding measures: A review *Journal of Cleaner Production* **92** 1–12